A study of fluctuations in the multiparticle production at ultra-relativistic high energy collisions

A
THESIS

SUBMITTED TO THE UNIVERSITY OF JAMMU
FOR
THE AWARD OF THE DEGREE OF

DOCTOR OF PHILOSOPHY
IN
PHYSICS

by

Sheetal Sharma

Department of Physics
University of Jammu, Jammu Tawi
J&K – 180006 (INDIA)
(July 2024)

DEDICATED

To

MY PARENTS

DEPARTMENT OF PHYSICS, UNIVERSITY OF JAMMU JAMMU TAWI-180006

CERTIFICATE

It is certified that **Ms. Sheetal Sharma**, worked under my supervision and the work is worthy of consideration for the award of Ph.D. degree in Physics. It is further certified that:

1. the thesis embodies the work of the candidate herself. It is original and not copied from any other source;
2. the candidate worked under my supervision for the period required under statutes;
3. the candidate has put in the required attendance in the Department of Physics, University of Jammu, Jammu during the period of research;
4. the candidate fulfills all the requirements of the UGC-MSP-2016 regulations;
5. the candidate has fulfilled the statutory conditions as laid down in Section 18 of the statutes governing the degree of Doctor of Philosophy.

(**Prof. Arun Bharti**)
Head
Department of Physics
University of Jammu
Jammu

(**Prof. Ramni Gupta**)
Research Supervisor
Department of Physics
University of Jammu
Jammu

PLAGIARISM CERTIFICATE

I, **Sheetal Sharma**, D/o Sh. Pawan Kumar Sharma, hereby declare that the work reported in this thesis entitled "**A study of fluctuations in the multi-particle production at ultra-relativistic high energy collisions**" is entirely done by me under the supervision of Prof. Ramni Gupta, Department of Physics, University of Jammu. The work undertaken by me in this thesis is original and has not been copied from other sources without due acknowledgement. I also ascertain that no part of this thesis is presented elsewhere for the award of any degree or diploma of any University or Institution. Moreover, this thesis is having 9% degree of plagiarism as per the DrillBit analysis report.

Dated: **(Sheetal Sharma)**

(**Prof. Arun Bharti**)
Head
Department of Physics
University of Jammu
Jammu

(**Prof. Ramni Gupta**)
Research Supervisor
Department of Physics
University of Jammu
Jammu

No: JU/DLJ/24/1002
Dtd - 9-7-24

DrillBit

The Report is Generated by DrillBit Plagiarism Detection Software

Submission Information

Author Name	Sheetal Sharma
Title	Ph.D
Paper/Submission ID	2088827
Submitted by	sahi_vikram@yahoo.com
Submission Date	2024-07-08 10:29:11
Total Pages, Total Words	130, 30547
Document type	Thesis

8/7/24

08/07/24

Result Information

Similarity **9 %**

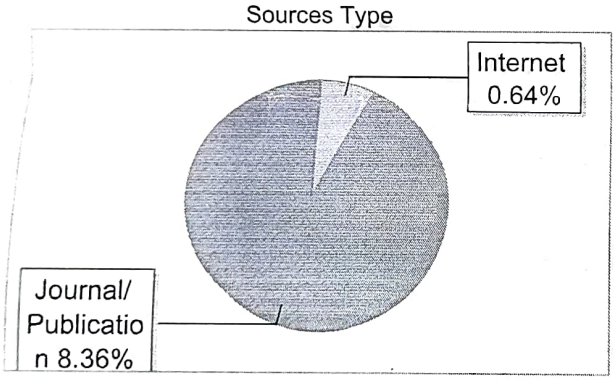

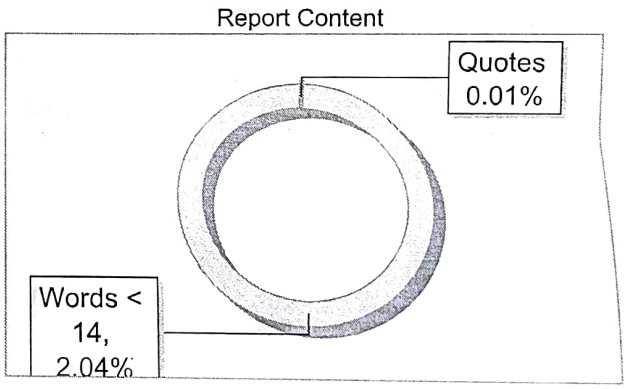

Exclude Information

Quotes	Excluded
References/Bibliography	Excluded
Source: Excluded < 14 Words	Excluded
Excluded Source	**0 %**
Excluded Phrases	Not Excluded

Database Selection

Language	English
Student Papers	Yes
Journals & publishers	Yes
Internet or Web	Yes
Institution Repository	Yes

A Unique QR Code use to View/Download/Share Pdf File

LIBRARIAN
DHANVANTRI LIBRARY
UNIVERSITY OF JAMMU.

Head
Department of Physics
University of Jammu
Jammu-180 006

DECLARATION

I, Sheetal Sharma, declare that the thesis entitled "**A study of fluctuations in the multiparticle production at ultra-relativistic high energy collisions**"submitted for the award of the degree of Doctor of Philosophy is a record of the research work carried out by me in the Department of Physics, University of Jammu, under the guidance of Prof. Ramni Gupta. The work is original and has not been copied from any other sources without due acknowledgement and having 9% degree of plagiarism as per the DrillBit analysis report.

Dated: **(Sheetal Sharma)**

(**Prof. Arun Bharti**)
Head
Department of Physics
University of Jammu
Jammu

(**Prof. Ramni Gupta**)
Research Supervisor
Department of Physics
University of Jammu
Jammu

ACKNOWLEDGMENTS

First and foremost, I thank the Almighty God for his blessings to complete my research successfully. I am grateful for the strength He gave me to overcome challenges and stay determined. I would like to express my immense gratitude to all the people who have contributed to this thesis directly or indirectly. Without their constant support and motivation, the work carried out for this thesis would have never been completed.

I would like to express my sincere and deepest gratitude and respect to my supervisor Prof. Ramni Gupta for providing guidance and support throughout the entire period of my research. I consider myself fortunate enough for getting this opportunity to pursue my research under her guidance. I sincerely thank her for her encouragement, constant motivation to accept challenges in research thus, always pointing me in the right direction during the entire period of my research.

My sincere thanks to Prof. Arun Bharti, Head of the Department of Physics, for providing the necessary infrastructure for this work. I express my heartfelt gratitude to Prof. Anju Bhasin, HEP Group Incharge, for her invaluable support and encouragement. Additionally, I am grateful to Er. Anik Gupta for his time to time help for the accomplishment of this work. My sincere thanks to Prof. Sanjeev Singh Sambyal for all the encouragement. I am also thankful to Er. Sanjay Mahajan, Dr. Saroj Nayak and Dr. Renu Bala for their help and good wishes. I would also like to extend my thanks to all the faculty members in the Department of Physics for their academic support and encouragement throughout the entire period. I want to thank the financial support from Department of Science and Technology (DST), Govt. of India, New Delhi.

I am privileged to participate in one of the experiments at the Large Hadron Collider, ALICE. I am deeply grateful to Dr. Marco Van Leeuwen (Spokesperson, ALICE), Dr. Luciano Musa (former Spokesperson, ALICE), Dr. Bedangadas Mohanty (Deputy Spokesperson, ALICE), and Dr. Zubayer Ahammed (ALICE-India Spokesperson) for their support in various matters. I want to extend my gratitude to the ALICE collaboration Physics Working Group(PWG) and Physics

Analysis Group(PAG) conveners: Dr. Mesut Arslandok, Dr. Igor Altsybeev, Dr. Tapan Nayak, Dr. Ante Bilandzic, Dr. Sumit Basu for their valuable suggestions, comments and helpful physics discussions to proceed with this work. I would like to extend my heartfelt thanks to everyone in the ALICE collaboration who has directly or indirectly contributed to the data-taking efforts at the LHC. I consider it a privilege to have had the opportunity to contribute to service tasks within ALICE as a O2 hyperloop operator. I would like to express my gratitude to the TRD project leader for giving me the opportunity to work on quality control for the TRD detector.

My sincere thanks to all my seniors Dr. Rohni Sharma, Dr. Randhir Singh and Dr. Meenakshi Sharma for their help and guidance. My sincere acknowledgement goes to my fellow lab-mates of the High Energy Physics lab for making my PhD life cheerful with their constant support. My sincere thanks to Ashish, Balwan, Binti di, Haider, Mahima, Mokshi, Nasir, Pratibha, Salman, Soom Raj, Touseef, Upasana, Vikash and Zarina.

I would also like to express my gratitude to all my friends from school, college, and university for their constant motivation and support throughout my PhD journey. I would also like to thank my sister Surbhi, who is also my roommate, for all the wonderful moments we spent together at the hostel.

Last but not the least, I would like to thank my parents and family for their unconditional support and motivation. Without the support, love and encouragement of my mother, this would not have been possible.

(Sheetal Sharma)

ABSTRACT

In the Standard Model, the fundamental theory describing strong interactions between colour-charged objects (quarks and gluons) is quantum chromodynamics (QCD). A feature of strong interactions is the asymptotic freedom according to which the interaction between colour charged objects weaken as they approach each other. In contrast, the potential between these particles increases as they move apart due to the property called colour confinement. Quarks and gluons, the basic degrees of freedom of the strong interactions are confined within the hadrons but are expected to be deconfined at extremely high temperature or pressure, forming a new state of matter called the quark-gluon plasma (QGP). QCD predicts phase transition from the hadronic phase to the deconfined phase of quarks and gluons as a function of thermodynamic parameters. As per the broadly accepted Big-Bang theory, QGP is a primordial form of matter that is considered to have existed for a few microseconds after the birth of the universe, potentially contributing to the formation of various elements in the present universe. It is also speculated that, due to high pressure, the cores of neutron stars may reach the necessary densities to have matter in the QGP form.

Relativistic heavy-ion collisions in the laboratory provide a means to study and characterize the properties of QGP as these may result into the creation of this hot and dense medium resembling a liquid like state where quarks and gluons move freely. The experimental confirmation of QGP formation has been reported by RHIC (Relativistic Heavy Ion Collider) at BNL, USA and by LHC (Large Hadron Collider) at CERN, Geneva. To locate the critical point of the nuclear matter phase diagram, to know about the order of quark to hadron and hadron to quark phase transition, to characterize the nature of matter at high energies and densities are among some of the main goals of these big experimental facilities. While the theoretical approach of studying QGP properties is challenging due to the non-applicability of the perturbative QCD to the strongly interacting systems characterized by large coupling constant and colour confinement, the experimental studies face challenges due to the short lifetime of this medium formed in the heavy-ion collisions. Lattice QCD offers valuable information on QGP

properties according to which the matter formed in the heavy-ion collisions at ultra-relativistic energies is believed to pass through different phases depending on the temperature and baryon chemical potential (μ_B). Despite many advancements and extensive efforts, information and understanding of the transition from the hadronic phase to the QGP phase and the critical phenomena exhibited by matter formed in these collisions still remain limited both theoretically and experimentally.

One of the simplest observables to characterize the system formed in heavy-ion collisions is multiplicity, the number of particles produced in an event. Multiplicity distributions and fluctuations therein have the potential to reveal the mechanism of multiparticle production processes and other important thermodynamic parameters of the system formed in these collisions. Fluctuation studies of multiplicity distributions help to understand not only the processes that lead to particle production but also the phenomena like phase transition and critical point. Multiplicity fluctuations, representing deviations from the average number of particles produced, are intimately linked with dynamical correlations of the system of particles in integrated form. These correlations offer insight into the underlying mechanisms governing particle production processes. Local density fluctuations, manifested by uneven particle densities within the phase-space regions, are a consequence of these dynamical correlations. Thus, an effective approach to understand the dynamics of the system is to analyze these fluctuations. One of such studies is the factorial moment analysis, more commonly termed as intermittency analysis, that analyses patterns and particle configurations and unveils the correlations in multiparticle production, the final state of high energy heavy-ion collisions.

Large bin-to-bin fluctuations in the particle distributions or spatial patterns are believed to have connection with the phenomenon of phase transition. A fundamental characteristic of the critical behaviour of a system undergoing phase transition is that it exhibits fluctuations on all scales. Intermittency, characterized by an increase in the normalized factorial moments as a function of the resolution of the phase space, serves as a key indicator of scale invariant local density fluctuations. In intermittency analysis, one studies the scaling behaviour of the

normalized factorial moments (NFMs) of multiplicity fluctuations. Scale invariance is also characteristic feature of the self-similar systems. A scaling exponent (ν) derived from this analysis may provide information about the critical nature of the systems under study. For the second order phase transition in Ginzburg-Landau formalism and Ising model calculations, ν is predicted to have an average value of 1.304.

Intermittency analysis characterized by the power-law behaviour of NFMs, has been widely studied for various systems at low energies in the early 1990s. However, these studies were limited by low bin multiplicities at high spatial resolutions. The advantage of heavy-ion collisions at ultra-relativistic energies, such as at LHC, is the production of a large number of particles in every event that enables the study of event-by-event fluctuations. With an interest to comprehend multiparticle production processes, investigations using intermittency methodology which is yet not explored to the full potential, are performed.

The research work embodied in this thesis pertains to the study of scaling behaviour of multiplicity fluctuations of the charged particles produced in the Pb–Pb collisions at $\sqrt{s_{\rm NN}}$ = 2.76 TeV, recorded with the ALICE detector at LHC. An analysis of data from Pb–Pb collisions at LHC energies has the significance of bringing out hidden features in the data that may not be trivial and may otherwise be washed out with averaging up of the observable. The results of these first measurements from this study at LHC energies, is presented. Thesis is organized in seven chapters. A brief account of the chapters is given below:

- **Chapter 1** provides a quick and general overview of the standard model of particle physics focusing on the key concepts such as asymptotic freedom and confinement. Following that, there is a brief discussion about quark-gluon plasma (QGP), a few signatures of its formation such as direct photons, J/ψ suppression, jet quenching, strangeness enhancement, elliptic flow, and dileptons. Subsequently, fluctuations particularly multiplicity fluctuations and statement of physics problem investigated in this work is discussed.

- **Chapter 2** gives a brief introduction to the LHC and one of its experimental setup A Large Ion Collider Experiment (ALICE). It also outlines the specific

detectors of the ALICE experiment, the data recorded by which has been analysed in this work. An overview of the detectors viz., Inner Tracking System (ITS), Time Projection Chamber (TPC), and VZERO (V0) detector is given. Additionally, the chapter focuses on the ALICE analysis framework, including discussions on the online/offline computing system and the reconstruction software in the LHC GRID framework.

- **Chapter 3** aims to provide details on the methodology to calculate normalized factorial moments ($F_{\rm q}$). Discussion on two dimensional intermittency analysis technique that is used here to analyze data is given. The various scaling behaviours ($F_{\rm q}$ as function of M (M-scaling) and F_2 (F-scaling)), extraction of scaling exponent (ν) and fractal parameters ($D_{\rm q}$ and $\lambda_{\rm q}$) are deliberated including their predictions from theoretical and model studies.

- **Chapter 4** presents phenomenological study of Toy model events having uncorrelated particles, aimed to understand the baseline behaviour of the normalized factorial moments. Generation and analysis of Toy model events including sensitivity checks of the observables are discussed. Toy model events show absence of intermittency while normalized factorial moments are found to be sensitive to the fluctuations present in the data. Procedure to implement efficiency corrections is also deliberated.

- **Chapter 5** discusses the studies performed using the simulation data from Monte Carlo event generators. In the field of high energy physics, simulation studies are vital to understand and interpret experimental outcomes. Simulated events using the HIJING and the AMPT model for Pb–Pb collisions at $\sqrt{s_{\rm NN}}$ = 2.76 TeV have been analyzed. Observations and results from the intermittency analysis, closure tests using these events is given. The two-dimensional intermittency analysis of the events shows weak M- and F-scaling behaviour. Scaling exponent (ν) extracted from the models is found to be different from the theoretically predicted value.

- **Chapter 6** focuses on the results from the experimental data analysis. Local fluctuations in the spatial patterns of the charged particles, produced in the two-dimensional (η, φ) phase space during Pb-Pb collisions at $\sqrt{s_{\rm NN}}$ =2.76

TeV recorded by the ALICE experiment at LHC, are studied using normalized factorial moments ($F_{\rm q}$). Results from the analysis performed for the various transverse momentum ($p_{\rm T}$) intervals having $p_{\rm T} \leq 2.0$ GeV/c in the mid rapidity region ($|\eta| \leq 0.8$) with full azimuth are discussed. Scaling properties of the multiplicity fluctuations studied using NFM are presented. The factorial moments quantifying the fluctuations in the spatial patterns of the events show linear dependence on the phase space resolution. F-scaling in data is observed, scaling exponent (ν) is extracted and its dependence on the $p_{\rm T}$, $p_{\rm T}$-bin width and centrality is presented. Fractal parameters, $D_{\rm q}$ and $\lambda_{\rm q}$, are calculated that offer insight into the structure of self-similar multiparticle systems in the collisions. The results obtained are compared with that from the Toy model and Monte Carlo event generators.

- **Chapter 7** provides a summary of results obtained from this work that advances our understanding about multiparticle production in heavy-ion collisions. An overview of the follow-up work to further extend the analysis is also given.

Contents

Figures

Tables

Chapter 1

Introduction

In the early universe, a few microseconds after the Big Bang, it is believed that a state of matter called quark-gluon plasma (QGP) [1] existed, where quarks and gluons were free particles instead of being confined within hadrons. Currently, quarks are regarded as the fundamental building blocks of matter, while gluons are the force carriers that "glue"quarks together to form protons, neutrons, and other hadrons. Examining the ultra-relativistic heavy-ion collisions is akin to investigating the early universe [2–5]. Experiments namely ALICE (A Large Ion Collider Experiment) at LHC (Large Hadron Collider) and STAR at RHIC (Relativistic Heavy Ion Collider) aim to explore the properties of the QGP. The direct investigation of QGP is not feasible as it lasts for a few microseconds after its formation. Indirect measurements to investigate heavy-ion collisions are performed to characterize the properties of QGP, locate critical point in the nuclear matter phase diagram, determine the temperature and the order of the phase transitions, extract the transport coefficients etc., which are some of the important goals in the field of heavy-ion collisions [6, 7].

In addition to QGP the other nuclear properties that are of interest in heavy-ion collisions, are nuclear shadowing, anti-shadowing, gluon saturation, and hadronic reabsorption, etc. However, due to the dominance of the hot nuclear medium (QGP), it is challenging to isolate these effects. Nevertheless, they can be studied using hadron-nucleus collisions such as proton-lead (pPb) collisions. Since these effects occur at relatively low temperatures, they are referred to as cold nuclear matter effects (CNM) [8]. For the quantitative description of both cold and hot nuclear matter, measurements performed on hadron-hadron collisions such as proton-proton (pp) collisions serve as a baseline to these investigations, as

the nuclear effects are negligible there, and the expected initial energy densities are not enough to create the QGP.

Among the myriad of investigations proposed for characterizing the system formed during heavy-ion collisions, one notable approach involves the study of fluctuations of physical observables. An important global observable to characterize the evolving system is the multiplicity, the number of produced particles. An in-depth exploration of multiplicity distributions and associated fluctuations offer valuable insight into the mechanisms governing multiparticle production processes.

The Standard Model, a popular and successful model of particle physics, is briefly discussed in the next section before going on to the introduction to heavy-ion collision and physics analysis performed in this thesis.

1.1 The Standard Model

Particle physics aims to comprehend the universe by exploring its fundamental building blocks and their interactions at the sub-atomic level. Decades ago, atoms were considered to be the smallest element of matter that could not be split. However, after discovering the constituents of atoms, i.e., electrons and nucleons, the scientific community tried further to figure out the fundamental constituents of matter. Numerous particles were postulated and later found in experiments over time. Many theories and models have been introduced for a better understanding of these particles and interactions among them. The widely accepted and successful Standard Model (SM) of particle physics provides a comprehensive understanding of the fundamental particles. It was proposed by Abdus Salam, Sheldon Glashow, and Steven Weinberg. According to this model, at elementary level, matter consists of quarks and leptons, interacting through gauge bosons like photons and gluons. Among the four fundamental forces present in the universe: gravitational, electromagnetic, weak, and strong nuclear interactions, the Standard Model successfully describes three of these forces, excluding gravity [9–12]. It's theoretical framework, known as the electroweak theory, unified the electromagnetic and weak nuclear forces and successfully predicted the existence of the

$W^{\pm}$ and Z^0 bosons. Experimental validation of electroweak theory came with the discovery of these bosons at European Organization for Nuclear Research (CERN) in the 1980s, earning Salam, Glashow, and Weinberg the Nobel Prize in Physics in 1979 for their contributions to understanding elementary particles and their interactions. The electroweak interaction theory unifies electromagnetism and weak interactions, while the quantum chromodynamics (QCD) explains the strong interactions between quarks and gluons within a nucleon.

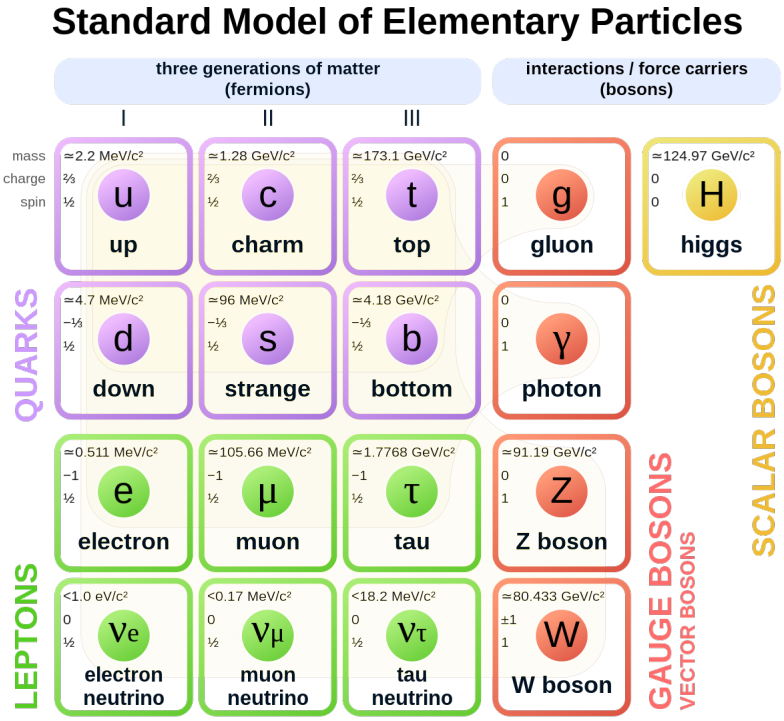

Figure 1.1. Elementary particles within the Standard Model [13].

All particles within the framework of the Standard Model are classified into two groups viz., quarks and leptons. Quarks and leptons are both fermions, possessing a spin of $\frac{1}{2}$ and obey Fermi-Dirac statistics. Leptons are further categorized into three generations based on their masses and properties. The first generation includes the electron (e) and the electron neutrino (ν_e), which are the lightest and the most stable known particles. The heavier and less stable matter is represented by the second and third generation of particles: muon (μ) and muon neutrino (ν_μ) which belong to the second generation, while the third generation comprises of tau (τ) and tau neutrino (ν_τ). These generations of leptons also include antiparticles of each particle. Leptons can participate in both electromagnetic and

weak interactions [14]. Mesons, that comprises of a quark and an antiquark, and baryons, consists of three quarks, serve as the fundamental constituents of hadrons. Together with leptons, hadrons constitute the building blocks of matter in the Standard Model, showcasing the intricate connection between fundamental particles and their interactions.

Regarding quarks, there are three generations: up (u) and down (d) quarks is the first generation, charm (c) and strange (s) quarks is the second generation, and top (t) and bottom (b) quarks constitute the third generation. Along with quarks each generation has anti-quark as well. The quark u, c, and t have an electric charge of $+\frac{2}{3}$, whereas d, s, and b quark have electric charge $-\frac{1}{3}$, respectively. Quarks possess colour charge, in addition to the electric charge. Each quark contains one of the three different colour charges: red, green, or blue. Anti-quarks, on the other hand, can have anti-red, anti-green, or anti-blue colour charges. Quarks can participate in all the three types of interactions: strong, electromagnetic, and weak.

In addition to fundamental matter particles, quarks and leptons, the Standard Model also includes field particles, or force carriers, known as gauge bosons. Photons (γ) are the exchange particles of electromagnetic interaction between electrically charged particles. The weak interaction occurring between various types of quarks and leptons is mediated by the $W^{\pm}$ and Z^0 bosons, while gluons (g) mediate the strong interaction between quarks. These field particles have integral spin and follow Bose-Einstein statistics. Gluons carry colour charge and interact with quarks to exchange this charge, effectively "gluing"them together. Furthermore, the Standard Model contains a scalar boson called the Higgs, named after Peter Higgs. In 1964, Higgs, along with five other physicists, proposed the Higgs mechanism. As per this mechanism, particles interact with the Higgs field and acquire mass [15, 16]. In 2012, ATLAS and CMS experiments at CERN announced the experimental discovery of the Higgs boson [17, 18]. With this important aspect of Standard Model has been proved experimentally.

Although the Standard Model provides the most accurate explanation of the subatomic world at the moment, it does not explain the complete picture of the

fundamental working principles of world around. The model only accounts for three of the four fundamental forces and leaves out gravity, another fundamental force of the nature. In addition to this there are many other open questions [19]. However, the Standard Model is still the most successful model explaining fundamentals of matter and interactions. Next a brief overview of the Quantum Chromodynamics (QCD), the theory of one of these fundamental interactions, the strong interactions, is given.

1.2 Quantum Chromodynamics

Quantum Chromodynamics (QCD) is a well established theory of strong forces that describes the interactions among quarks and gluons. According to QCD, quarks and gluons combine to form hadrons. Quarks and gluons are subject to strong interactions mediated by a quantum property known as colour exchange, akin to electric charge in quantum electrodynamics (QED). Quarks and antiquarks are analogous to electrons and positrons, while gluons, the mediating gauge bosons, are analogous to photons. However, unlike QED, which features a single type of charge, QCD introduces three distinct types of charges known as colour charges (red, green, and blue), each with a corresponding anti-charge or anticolour. Another significant distinction is that photons are electrically neutral whereas gluons carry a colour charge. Consequently, gluons can interact with each other, leading to unique properties of QCD [14]. Two key characteristics of QCD, asymptotic freedom and colour confinement, are discussed below:

1.2.1 Asymptotic freedom

The property of asymptotic freedom was first reported by Gross, Politzer, and Wilczek, for which they were awarded the Nobel Prize in Physics for the year 2004 [20–22]. Asymptotic freedom implies that the interaction strength between quarks decreases as the distance between them decreases. In QCD, the strong

coupling constant α_s is related to momentum transfer Q^2 [23], as

$$\alpha_s(Q^2) = \frac{4\pi}{\beta_0 \ln(Q^2/\Lambda^2_{\mathrm{QCD}})} \tag{1.1}$$

where $\beta_0 = 11 - \frac{2}{3}n_f$ is a constant determined by the number of active quark flavours (n_f), and Λ_{QCD} is a dimensional parameter representing the energy scale where α_s diverges to infinity. The behaviour of QCD coupling constant as a function of Q has been experimentally verified by a large variety of measurements of different processes [23], as summarized in Fig. 1.2. The figure clearly illustrates that towards low momentum transfer Q, indicating a larger probed length scale, the coupling strength increases. This behaviour is closely linked to the concept of confinement, which dictates that isolated colour charged objects are not observed in nature. Conversely, for large momentum transfers Q, corresponding to smaller probed length scales, the coupling decreases. In the limit where the coupling tends to zero, quarks and gluons exhibit free behaviour, a characteristic that results in where quarks can be considered as free a concept known as asymptotic freedom. The formation of the Quark-Gluon Plasma (QGP) is a direct consequence of this property of strong interaction.

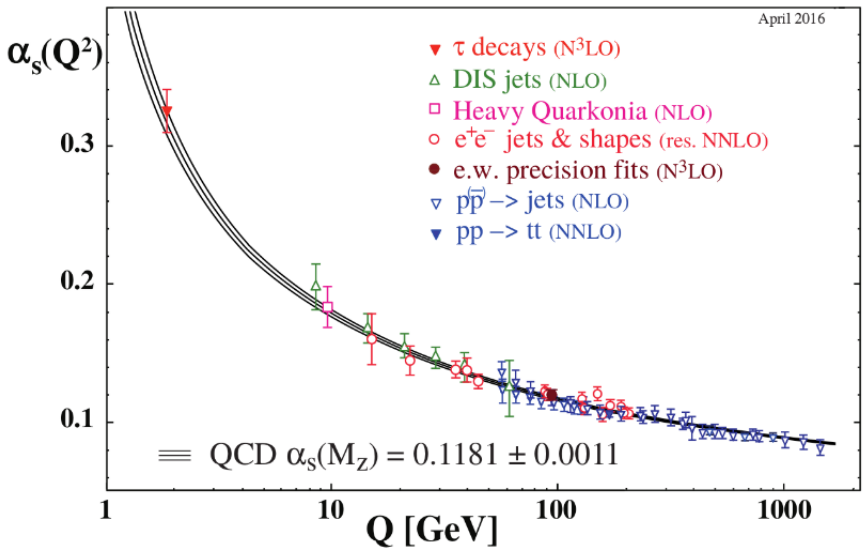

Figure 1.2. Variation of QCD coupling constant with momentum transfer [23].

1.2.2 Confinement

Another important feature of QCD is confinement, a feature that pervents the existence of free colour-charged particles like quarks and gluons. The confinement property of the quarks is explained by their strong interaction potential. The equation that provides the QCD potential for the strong force is;

$$V_s = -\frac{4}{3}\frac{\alpha_s}{r} + kr \tag{1.2}$$

where r is the distance between colour charges, k signifies the colour string tension between quarks, and α_s is the strong interaction coupling constant or running coupling constant. The term α_s/r emerges due to single gluon exchange and dominates at small r. It is comparable to the Coulomb potential between elementary charged particles. The confinement of quarks at large r is linked to the linear term (second term) in the equation (1.2).

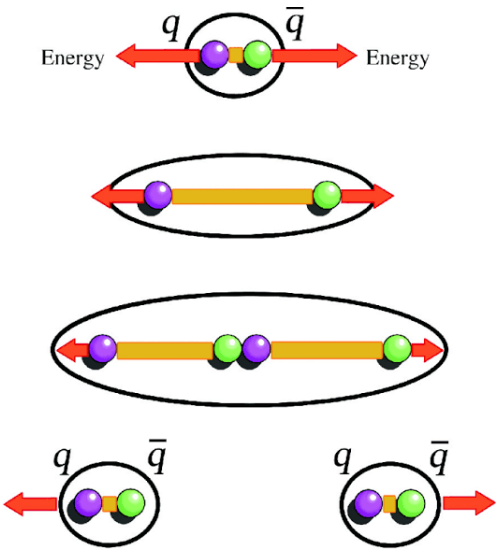

Figure 1.3. Schematic view depicting inseparability of quarks and anti-quarks inspite of applying more energy and hence depicting confinement properly [24].

Colour-charged quarks are confined in groups with other quarks, forming colour-neutral combinations and do not exist in isolation. If a quark in a given meson (a bound state of a quark and an antiquark pair) is pulled away from its antiquark, the colour force field stretches between the quark and its neighbour. Consequently, the colour force field gains energy and expands, leading to the for-

mation of a new quark-antiquark pair. In this process, energy remains conserved as the energy stored within the colour force field is utilized to produce the mass of newly generated quarks, enabling the colour force field to revert to its unstretched state. Consequently, the energy required to achieve significant separation far surpasses the pair production energy of a quark-antiquark pair. Instead of isolating a single quark, a pair of mesons is created since the produced quark-antiquark pair combines, as illustrated in Fig.1.3.

The nuclear matter phase diagram that is still not completely understood and is one of the widely studied area of research in the field of high energy physics is discussed.

1.3 Nuclear matter phase diagram

A conjectured phase diagram of strongly interacting matter is shown in Fig. 1.4. QCD matter comprises hadrons (quarks and gluons) that are confined together at low chemical potential (μ_B[1]) and temperature (T). At a high net baryon density, QGP matter is formed due to the compression of nuclear matter as is present inside the core of neutron stars. Lattice QCD calculations have predicted a first-order phase transition from hadron gas to QGP at higher chemical potential (μ_B) and lower temperature (T), which is a finite discontinuity in the first derivative of thermodynamic potential in the infinite volume limit. The critical point is thus the point at which the first order phase transition ends [26, 27]. However, at high temperatures and zero baryon chemical potential, the phase transition from hadron gas to the QGP phase is believed to be a cross-over [28]. This area of the phase diagram is currently under investigations both at LHC and RHIC. The major goal of the RHIC Beam Energy Scan (BES) [29] program is to determine the precise location of the critical point. At the time of writing this thesis, no evidence of critical point is reported by any experiment. The region of high baryon

[1]Chemical potential, also known as baryon chemical potential or net baryon density, is the amount of energy required to raise the total number of baryons and antibaryons in a system to a unit increase.

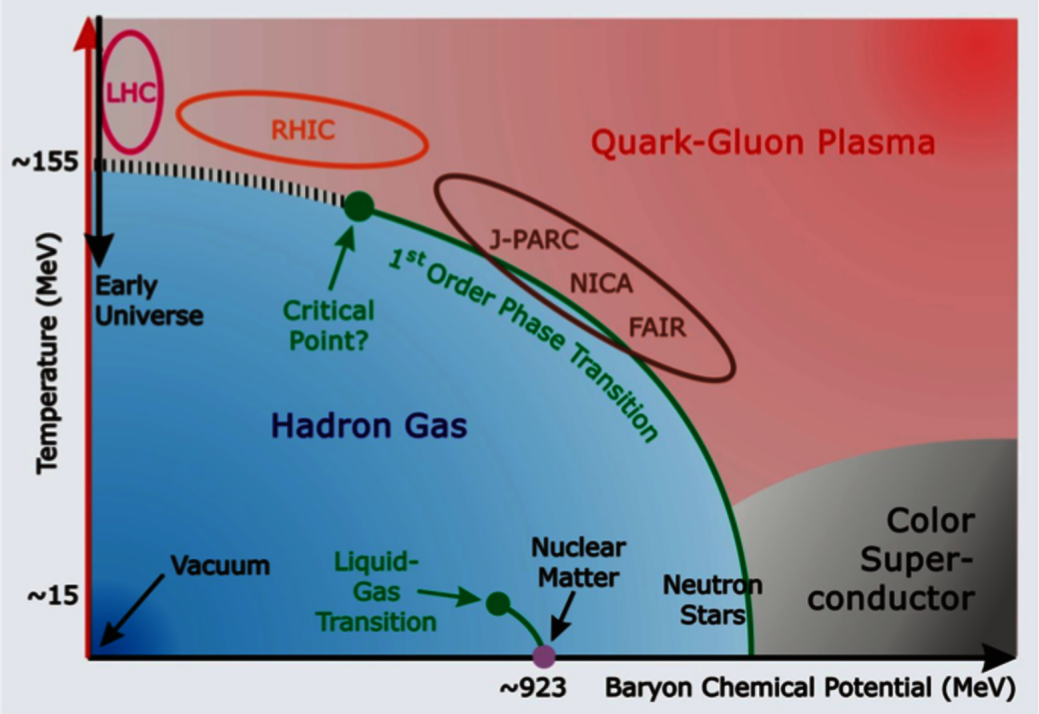

Figure 1.4. Conjectured phase diagram of the strongly interacting matter [25].

chemical potential of the phase diagram will be explored by the experiment at the Facility for Antiproton and Ion Research (FAIR) at the GSI [30, 31], Germany, and the Nuclotron-based Ion Collider Facility (NICA) [32] at Joint Institute for Nuclear Research (JINR), Russia [27]. A brief overview of heavy-ion collisions and signatures of QGP formation are discussed below.

1.4 Ultra-relativistic heavy-ion collisions

In quark-gluon plasma, the individual quarks are not bound in the colourless triplets (baryons) or doublets (mesons) but are "quasi-free"particles. The conditions of extreme energy and density leading to the formation of this state of matter can be reached in the laboratory by colliding heavy nuclei at ultra-relativistic high energies where it may be formed for a very small time and making it possible to experimentally study QGP medium in the laboratory. The first heavy-ion collision was performed with a collision energy of 1–2 A GeV/c in 1970 at Bevalac, Lawrence Berkeley National Laboratory(LBNL), USA. Following the Bevalac experiment's success, other heavy-ion collision experiments started to operate at various ac-

celerator facilities all over the world, such as Alternating Gradient Synchrotron (AGS) and RHIC [33] at Brookhaven National Laboratory (BNL), USA and Super Proton Synchrotron (SPS) and Large Hadron Collider (LHC) at CERN [34]. Major experimental facilities spread over the globe are listed in Table 1.1.

Table 1.1. A few heavy-ion collision facilities at various accelerator facilities.

Year(s) of operation	Facility Name	Type	Energy range
1987-1984	AGS (Alternating Gradient Synchrotron) at BNL (Brookhaven National Laboratory)	Fixed target	< 14.2 GeV
1994-now	SPS (Super Proton Synchrotron) at CERN (European Organization for Nuclear Research)	Fixed target	5.0-17.3 GeV
2002-2014	SIS18 (Schwer Ionen Synchrotron) at GSI Helmholtz Centre for Heavy Ion Research	Fixed target	< 2.4 GeV
2000-now	RHIC (Relativistic Heavy Ion Collider) at BNL	Collider	7.7-200 GeV
2009-now	LHC (Large Hadron Collider) at CERN	Collider	2.76, 5.02 and 5.44 TeV
2010-now	FAIR (Facility for Antiproton and Ion Research) at GSI Helmholtz Centre for Heavy Ion Research	Fixed target	Up to 29 GeV/nucleon
2015-now	NICA (Nuclotron-based Ion Collider fAcility) at JINR (Joint Institute for Nuclear Research)	Fixed target	Up to 4.5 GeV/nucleon

In a heavy-ion collision experiment, two nuclei are collided at high energies with speeds reaching the speed of light that leads to nuclei getting Lorentz contracted along the direction of motion and appear to be "disk-like" objects as shown in a cartoon in the Fig. 1.5. When the collision takes place, the part of the nuclei that participates in the collision is called the overlap region. This region depends on the impact parameter (b), that is the perpendicular distance between the centers of two colliding nuclei. The nucleons that participate in the collision and come into this overlap region are called *participants*, and those which do not participate are called *spectators*. The system so formed during the collisions expands and evolves in space and time and passes through various stages.

Space-time evolution of heavy-ion collision

The head-on collision of the two equal Lorentz-contracted nuclei travelling at near to the speed of light along the z-axis is shown in Fig. 1.6 which illustrates a

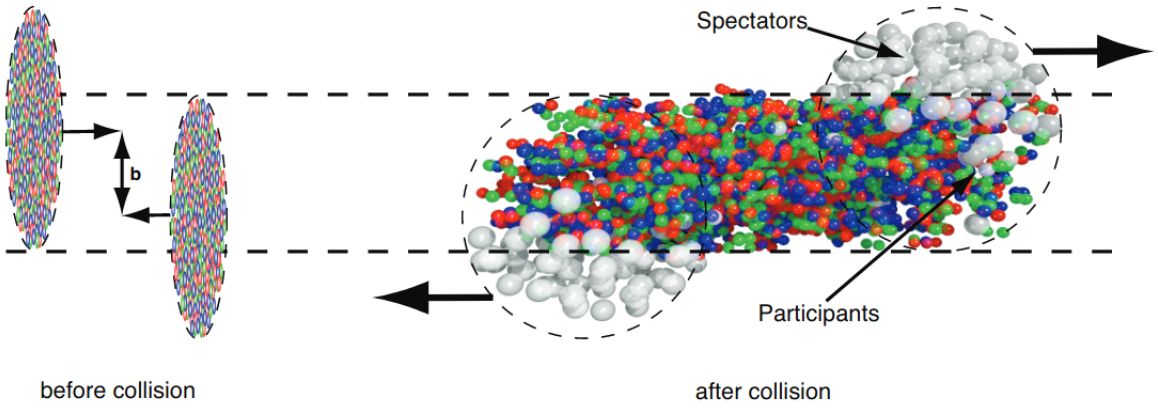

Figure 1.5. Schematic view of ultra-relativistic heavy-ion collisions of two Lorentz contracted nuclei [35].

schematic diagram of the space-time evolution of ultra-relativistic nucleus-nucleus collision with two possible scenario viz with and without QGP formation. The ordinate represents the time axis, while the abscissa represents the beam direction (z-direction). The two nuclei travel towards each other along the z-axis, and the coordinates are arranged such that they collide at the origin $(z, t) = (0, 0)$. The proper time (τ) of evolution is calculated from the space-time hyperbola as $\tau = \sqrt{t^2 - z^2}$. The evolution of hadronic collisions is supposed to proceed through several stages;

1. **Pre-equilibrium stage:** This phase appears to be present for an evolution time of $\tau \leq 1$ fm/c [37]. During this period, partons interact in an inelastic way to create a large number of deconfined quarks and gluons. Since it is an initial stage of the evolution of collision, the majority of the particles formed in it are produced by hard QCD processes and have large transverse momentum. Hard scattering between partons results in the production of jets and heavy quarks via perturbative QCD. At this point in time, the system is in a non-equilibrium state of partons.

2. **Quark-Gluon Plasma and its expansion:** In this scenario where QGP is formed in a collision, while the energy density of the system is high enough, the partons are formed in the pre-equilibrium phase and interact among themselves a multiple number of times. The system approaches a local thermal equilibrium with thermalization time ≈ 1 fm/c. These interactions

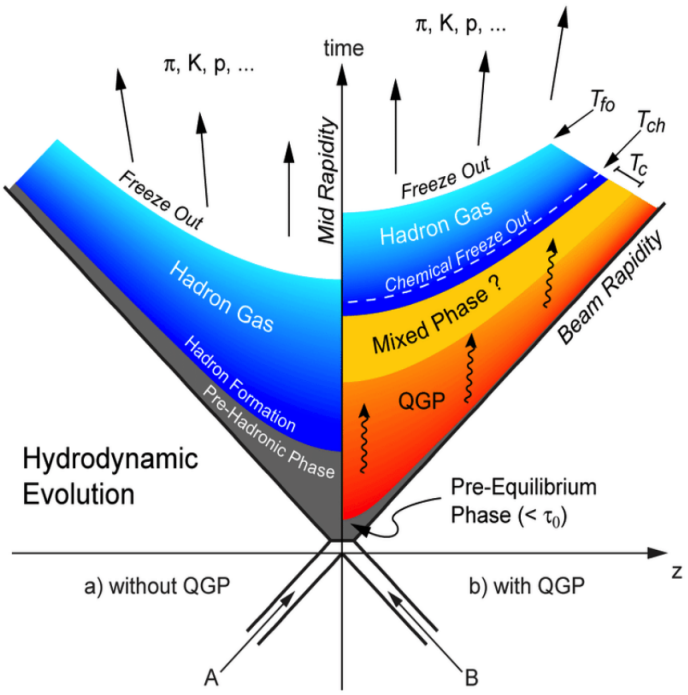

Figure 1.6. Schematics of space-time evolution in a relativistic heavy-ion collision. The RHS of the figure shows the evolution of the system with QGP formation, and the LHS illustrates the evolution of the system without QGP [36].

results in a hot, dense, and thermally equilibrated matter known as Quark-Gluon Plasma (QGP). A hydrodynamical description of the QGP suggests that the medium formed in heavy-ion collision behaves more like a strongly coupled liquid than a weakly interacting gas [38] and the same has been observed experimentally [39]. The system expands due to the pressure gradient of the collisions and subsequently cools down. Hadronization process, quarks and gluons confining to form hadrons, starts when the temperature drops below a specific critical temperature. This results in a mixed-phase system wherein both QGP and hadrons exist together.

3. **Chemical freeze-out:** After the mixed phase stage, the system continues to undergo inelastic hadronic interactions, which are expected to maintain a form of chemical equilibrium. When the temperature drops below chemical freeze-out temperature (T_{ch}), all inelastic processes cease, and the chemical composition of the system freezes, i.e., no new particles are produced. Hadrons now interact elastically and this transition from inelastic scatterings to elastic hadronic gas interactions is known as chemical freeze-out [40].

4. **Kinetic freeze-out:** After the chemical freeze-out, hadrons interact elastically until the temperature approaches T = T_{fo}. At this temperature, elastic collisions among hadrons stop, when the mean free path of hadrons is approximately equal to the size of the system. Beyond this point, the transverse momentum (p_{T}) distribution of the hadrons is fixed. When the mean free path becomes much greater than the system size, all the particles in the final state travel freely and are eventually detected in the detectors. This stage is called kinetic freeze-out.

The other possible scenario is the one where Quark-Gluon Plasma medium is not formed as the temperature and energy density of the system do not reach the threshold value (Fig. 1.6(a) (without QGP)). This leads to the formation of a pre-hadronic phase which is followed by nucleon recombination resulting in the formation of new hadrons. Subsequently, after the hadronic freeze-out, the produced hadrons are detected in the detectors. This space-time evolution scenario is commonly observed in hadronic collisions.

In experiments at LHC, the detection of final-state particles involve measuring their position and momentum or energy and time using detectors. This approach is crucial for gaining a more comprehensive understanding of the space-time dynamics in the relativistic collisions and studying broader observables related to the creation of the strongly interacting matter. To do this effectively, it is necessary to have an understanding of the kinematic variables relevant to ultra-relativistic collisions, a brief introduction of which is given in Appendix A whereas a detailed description of these is available in Ref. [41].

1.5 Signatures of QGP

The strongly interacting matter, QGP, that may get created in the heavy-ion collisions, is expected to have a lifetime of around 10^{-23} seconds, after which, as the system cools the transition from the QGP state to the hadronic state takes place. Due to extremely small lifetime, it is experimentally impossible to detect this state of matter directly. Hadrons in the final state of collision are detected

by detectors. In order to learn about this state of the matter, one relies on experimental measurements that can provide information about the properties of this medium. These measurements and observations so made give the evidence of QGP formation and hence are known as signatures of QGP formation [42]. Some of the main signatures are discussed below:

1.5.1 Direct photons

The strong interactions among quarks and gluons in the plasma state give rise to the production of direct photons [43]. Photons interact electromagnetically and their mean free path is large compared to the size of the system formed, so they escape from the strong interaction region without rescattering and carry information about the conditions and properties of the matter at the time of their production [44]. Moreover, as the emission rate of photons is a strongly increasing function of temperature, most of the direct photons are abundantly produced when the temperature and energy density have their largest values. Thus direct photons act as unique spectator of the exotic state of matter created in the heavy-ion collisions. Besides this, there are several other important photons contributing sources throughout the evolution process, such as, photons from hard scattering in the QGP phase, photons from partonic decay, etc. By isolating photons from these background processes, the measured direct photons accurately reflect the thermodynamic characteristics of quarks and gluons in the system prior to hadronization.

The first attempt at direct photon measurement was made by the WA98 collaboration in Pb−Pb collisions at 158 A GeV [46]. ALICE collaboration at CERN also studied the invariant yield of direct photons for 0-20%, 20-40%, and 40-50% centrality classes in p_{T} range $0.9 < p_{\mathrm{T}} < 14.0$ GeV/c. Fig. 1.7 shows the measurement of direct photons in Pb−Pb collisions at $\sqrt{s_{\mathrm{NN}}} = 2.76$ TeV for the three centralities. The behaviour as expected by the pQCD calculations for high $p_{\mathrm{T}} > 5.0$ GeV/c is seen. At high p_{T}, there is no evidence of medium influence on direct photon generation. In peripheral collisions in the low p_{T} region ($p_{\mathrm{T}} < 2$ GeV/c), no direct photon signal is seen; however, in the mid-central and

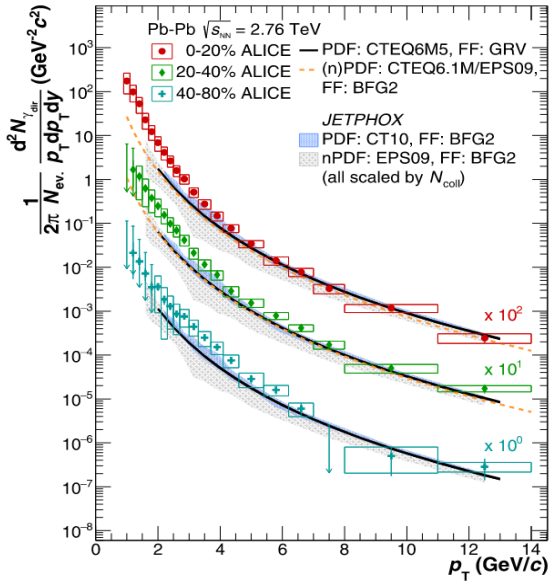

Figure 1.7. Direct photons spectra measured by ALICE in Pb−Pb collisions at $\sqrt{s_{\rm NN}}$ = 2.76 TeV in different centrality classes and compared to the pQCD predictions for the direct photon yield in pp collisions at the same energy [45].

central collisions, an excess over the prompt photon contributions is observed [45]. In this measurement, models that assume the formation of a QGP were found consistent within uncertainties.

1.5.2 J/ψ suppression

J/ψ is bound state of charm quark(c) and charm antiquark($\bar{\rm c}$). These particles are produced during the hard scattering processes in the initial stage of the collision and, therefore, serve as an excellent tool to understand the dynamics of the medium formed in the heavy-ion collisions. In QGP medium, the colour charge of a quark is subjected to Debye screening due to the presence of quarks, antiquarks and gluons. If a J/ψ is present in this medium, the interaction between c and $\bar{\rm c}$ may become weaker due to Debye screening. Also, because of the distribution of quarks and gluons around c$\bar{\rm c}$, the potential between c and $\bar{\rm c}$ may change considerably. The combined effect of these two situations may result in J/ψ dissociation into c and $\bar{\rm c}$ and hadronizing as D-mesons, which are made up of charm and a light antiquark. This reduced production of J/ψ is known as J/ψ suppression and serves as a signature of QGP [47]. The first report on this suppression was given

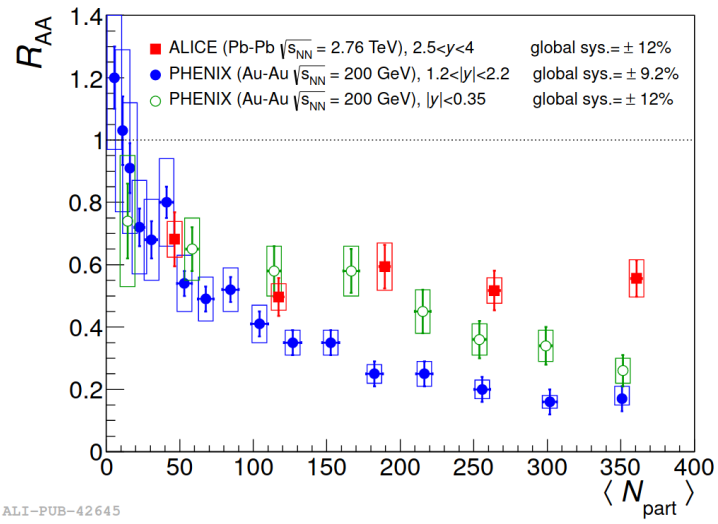

Figure 1.8. R_{AA} of J/ψ as a function of average number of participant nucleons in the Pb−Pb collisions at $\sqrt{s_{\mathrm{NN}}} = 2.76$ TeV and results from PHENIX collaboration for Au−Au collisions at $\sqrt{s_{\mathrm{NN}}} = 200$ GeV [51].

by the SPS experiment at the CERN [48]. Later, this suppression was further confirmed by experiments at RHIC [49] and at LHC [50]. Fig. 1.8 shows the nuclear modification factor (R_{AA}) of J/ψ as function of centrality (average number of participants, $\langle N_{part} \rangle$) at RHIC and LHC energies. Large $\langle N_{part} \rangle$ values correspond to central collisions, while small $\langle N_{part} \rangle$ values correspond to peripheral collisions. It is observed that the amount of suppression observed at the RHIC is greater than that at the LHC. These observations at LHC are associated with the formation of QGP medium, which suppresses the production of J/ψ, and the subsequent recombination process, in which some c$\bar{\mathrm{c}}$ pairs coalesce and increase the production of J/ψ.

1.5.3 Jet quenching

Two colliding nuclei at ultra-relativistic energies result in the production of large number of partons at very high transverse momentum. These partons disperse in all possible directions from the collision point and finally fragment into narrow cones of hadrons called jets [52]. These jets comprise of highly energetic secondary particles, including quarks, antiquarks, and gluons, which are often referred in theory as "jet partons". When these jet particles pass through the hot and dense

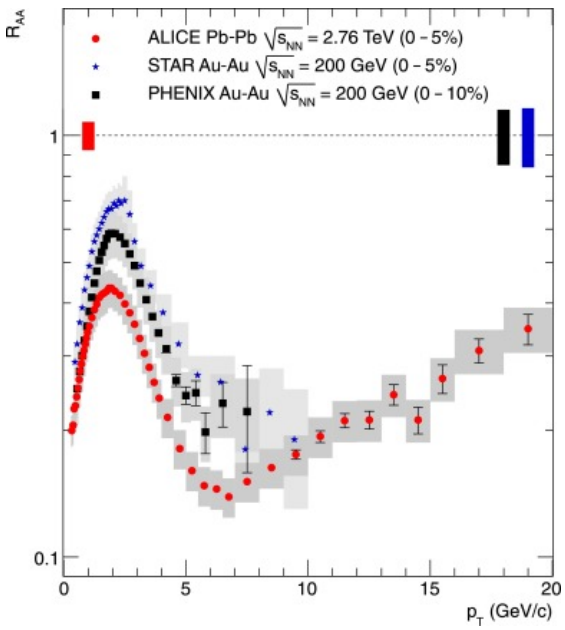

Figure 1.9. R_{AA} as a function of transverse momentum in the central Pb−Pb collisions at $\sqrt{s_{\mathrm{NN}}} = 2.76$ TeV measured by ALICE is compared with STAR and PHENIX experiments results [55].

medium namely QGP, they interact with the medium particles and lose the energy and momentum before hadronizing, and thus leading to suppression of the yield of the high p_{T} hadrons. This loss is observed through a mathematical ratio, the nuclear modification factor, R_{AA}, defined as

$$R_{AA}(p_T) = \frac{1}{\langle T_{AA} \rangle} \frac{yield_{AA}}{yield_{pp}} \tag{1.3}$$

This ratio, first suggested by Bjorken [53], shows the energy loss of any jet parton and is commonly termed as jet quenching. The numerator of the ratio shows the yield of charged particles in the heavy-ion collisions (denoted by the subscript "AA"), while the denominator shows the yield in proton-proton collisions (denoted by "pp"). If we suppose that AA collision is an incoherent superposition of pp collisions, then the R_{AA} must be unity for all jet momenta. Any value of R_{AA} below unity implies the presence of the effects caused by the medium. Fig. 1.9 shows the results of the nuclear modification factor for charged particles as measured by various experiments. A clear effect of jet quenching is observed both at RHIC and LHC energies [54].

1.5.4 Strangeness enhancement

The enhancement of strange particle production is considered as one of the important signals of QGP formation and was first proposed in [56]. The concept of strangeness enhancement is based on different mechanisms of strange particle production in the QGP phase and the hadronic phase. If the system created in a heavy-ion collision does not evolve through the QGP phase, the strange particles must be created by the rescattering of particles within the expanding hadronic gas system. Since strangeness is a conserved quantity, strange and anti-strange particle production rates should be equal. Therefore, the threshold energy required to generate strange hadrons is very high. Contrarily, in the QGP phase, quark masses are reduced to their bare minimum, which lowers the threshold energy for the formation of strange-antistrange pairs [57, 58] to just being the sum of the masses of the two strange quarks, or about 200 MeV. As a result, the production rates of strange particles increases significantly in case QGP phase is created.

In the QGP phase, strange quarks are produced mainly by gluon-gluon fusion and quark-antiquarks interactions. Strangeness enhancement is quantified through the enhancement factor (ϵ), which is defined as the yield per participant in the Pb−Pb (or pPb) collisions normalised to the yield per participant in the pp collisions and is expressed as,

$$\epsilon = \frac{2}{\langle N_{part} \rangle} \frac{Yield_{AA}}{Yield_{pp}} \tag{1.4}$$

where $\langle N_{part} \rangle$ is the average number of participants in the nuclear-nuclear collisions. If the value of ϵ is greater than one, then it can be attributed to an enhancement in the production of strangeness. Fig. 1.10 shows the strangeness enhancement factor (ϵ) as a function of $\langle N_{part} \rangle$ in Au−Au and Pb−Pb collisions [59]. This enhanced production of the strange particles in heavy-ion collisions relative to pp collisions indicates the formation of a hot and dense partonic medium. With the increase in center-of-mass energy, the enhancement factor is perceived to be decreasing, and this decrease is believed to occur due to the so-called canonical suppression mechanism [60], according to which the rate of such processes is suppressed because the energy levels and phase-space required for $s\bar{s}$ pair production

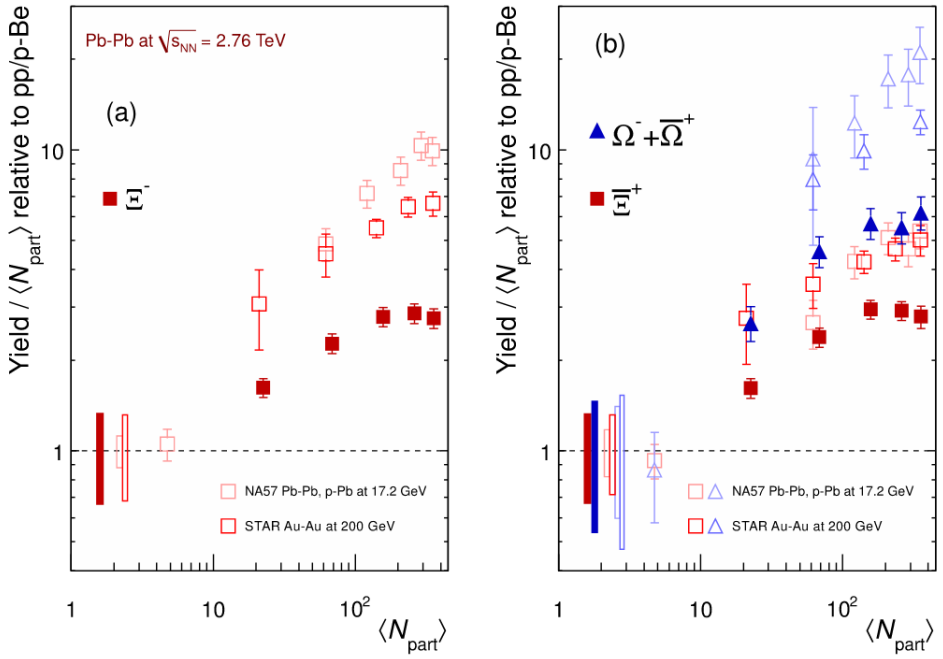

Figure 1.10. Strangeness enhancement factor of the different strange hadrons measured by the ALICE are compared with the results of the lower energies STAR and NA57 experiment [59, 61].

in a small system are not present. As a result, the denominator term of the enhancement factor decreases, increasing the value of strangeness enhancement for lower energies than LHC energies.

1.5.5 Elliptic flow

In heavy-ion collisions, one of the most important observables to understand the initial conditions and collectivity of the produced medium is the elliptic flow of the produced particles. The overlapping area between the two colliding nuclei in non-central heavy-ion collisions exhibits an almond-like shape. When constituents interact, a pressure gradient develops, transforming the initial spatial anisotropy into the momentum anisotropy. This momentum anisotropy is converted into an azimuthal anisotropy of the produced particles, resulting in asymmetrical particle emission in the perpendicular plane, which is expressed by the Fourier expansion of the azimuthal distribution of emitted particles

$$E\frac{dN}{d^3p} = \frac{1}{2\pi}\frac{dN}{p_{\mathrm{T}}dp_{\mathrm{T}}dy}\left[1 + \sum_{n=1}^{\infty} 2v_n cos(n(\varphi - \psi))\right] \tag{1.5}$$

where φ is the azimuthal angle of the produced particles and ψ is the reaction plane angle (angle made by the reaction plane with the x-axis). The coefficients of expansion are called flow parameters and are defined as $v_n = \langle cos(n(\varphi - \psi_n))\rangle$, where the average is taken over all the particles in all the events. The second coefficient, v_2 is known as *elliptic flow*.

Hydrodynamical models accurately predict and explain the majority of elliptic flow measurements for light hadrons at the low transverse momentum ($p_{\mathrm{T}} < 2 - 3$ GeV/c). The elliptic flow measurements provide evidence that the created matter equilibrates in an early stage of the collision and evolves according to the laws of hydrodynamics, behaving nearly like a perfect fluid[2] [1, 62].

Results for v_2 of π, K and p in Pb–Pb collisions at $\sqrt{s_{\mathrm{NN}}} = 2.76$ TeV [63] are shown in Fig. 1.11. This figure compares the results from ALICE with those from STAR [64] and PHENIX [65] experiments. The observed v_2 from ALICE and STAR behaves in a qualitatively similar manner at low transverse momentum values ($p_{\mathrm{T}} < 1.5$ GeV/c). On the other hand, for $p_{\mathrm{T}} > 1.5$ GeV/c, the v_2 measurements at the LHC are significantly higher than RHIC energies. This difference is commonly attributed to the larger radial flow present at LHC energies compared to those at RHIC.

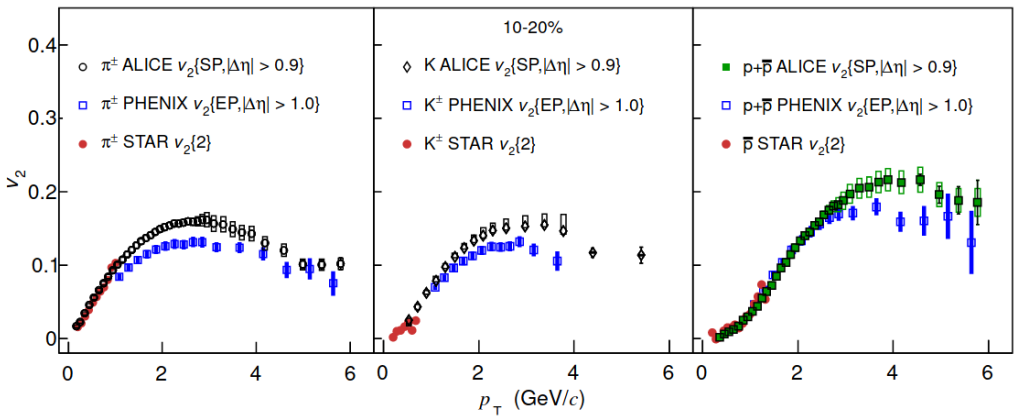

Figure 1.11. The comparison of the p_{T} differential v_2 for 10% to 20% centrality class of Pb−Pb and Au−Au collisions at the LHC and RHIC energies [63].

[2]Quark-Gluon Plasma (QGP) behaves as a nearly perfect fluid, characterized by minimal viscosity and strong collective behaviour, a property inferred from experimental observations and theoretical calculations.

1.5.6 Dileptons

Dileptons are produced in various ways during high-energy nuclear collisions and serve as signature of QGP formation. They can originate from quark-antiquark annihilation or from interactions within the hadronic medium, such as through the decay of particles like pions, rho mesons, omega mesons, or J/ψ particles. Among the most noticeable dileptons are those involving high-energy electron-positron pairs and muon-antimuon pairs. Another source of dilepton production is through Drell-Yan processes, where a quark annihilates with a sea antiquark from another nucleon to create a virtual photon, which then decays into a lepton pair. Leptons and their antileptons travel through the medium and interact electromagnetically, so they remain largely unaffected by the strong forces, providing valuable information about the thermodynamic properties of the QGP medium. The production rate and momentum distribution of generated lepton and anti-lepton pairs are influenced by the momentum distributions of quarks and antiquarks within the plasma, which are regulated by the thermodynamic properties of the plasma. Therefore, the lepton-antilepton pairs contain information regarding the thermodynamic state of the medium at the time of their production [66–68].

Dileptons face challenges similar to photons in terms of their production throughout the entire evolution of the QGP. However, when examining the distribution of dilepton spectra against the invariant mass of lepton pairs, signals from the QGP phase can be observed in the mass range of approximately 300–500 MeV.

1.6 Fluctuations

To have an insight into the mechanism of particle production and phase changes from hadrons to QGP and vice-versa study of fluctuations of observables from experiments has great significance [69]. Existence of the QCD phase transition would cause an increase and divergence of fluctuations [70]. In general, any change or variation in any quantity over space and time is referred to as fluctuation. Fluctuations are intimately linked to the phase transitions. For instance, the well-known phenomenon of critical opalescence arises from fluctuations at all length scales,

characteristic of a second-order phase transition. Conversely, first-order transitions manifest as bubble formation, representing extreme density fluctuations. This intrinsic relationship between fluctuations and phase transitions underscores their significance in understanding the dynamic behaviour of matter across different phases [71]. The heavy-ion collision facilities such as LHC and RHIC have provided us with the extensive data sets that is conducive to do fluctuations studies in understanding the intricate dynamics of QGP formation and phase transitions.

Fluctuations in observables can originate from various sources. There can be trivial fluctuations that arise due to the finite number of particles used to define a particular observable in a given event. These fluctuations, which are a consequence of finite multiplicity, are referred to as statistical fluctuations. All other fluctuations are classified as dynamical fluctuations. Dynamical fluctuations can further be broadly categorised as fluctuations that remain constant across events, and the fluctuations that vary on an event-by-event basis.

The most efficient method to study the dynamical (non-statistical) fluctuations in a physical system is through the study of event-by-event fluctuations, where a given quantity is studied on an event-by-event basis, as the averaging over the event space may smear out signatures of interest [69, 72]. Imagine putting a sheet of paper outside on a rainy day. If you leave it there for a long time, the paper will become uniformly wet, making it seem like a continuous mist of rain. However, if observed for just a few seconds, one would notice individual raindrops hitting the paper, revealing a distinct droplet pattern. This shows how examining each event separately can reveal unique details. The abundance of high multiplicity data from collider experiments at the LHC and RHIC, an event-by-event fluctuation study is feasible and promises to reveal the true nature of the system created in ultra-relativistic energies and high density [73].

The study of event-by-event fluctuations provides a test bench to characterize the thermodynamic properties of the system. For example, fluctuations of conserved quantities are predicted to signal the presence of the QGP and indicate a phase transition. The event-by-event fluctuation studies carried in the ALICE experiment encompass a wide range of investigations, including studies

on net-charge fluctuations [74], balance functions [75], mean p_{T} fluctuations [76], multiplicity fluctuations [77], particle ratio fluctuations [78], temperature fluctuations, etc. In this thesis, the focus is on the study of multiplicity fluctuations, which is briefly introduced next.

1.6.1 Multiplicity fluctuations

In heavy-ion collision experiments, multiplicity refers to the total number of particles produced and charged particle multiplicity is the number of charged particles produced in a collision event. This quantity is indicative of an overall activity and complexity of the collision process. Multiplicity is influenced by various factors such as the energy of the colliding particles, the collision geometry, collision system and the properties of the nuclear matter created in the collision, including its temperature and density. The charged particle multiplicity in heavy-ion collisions is function of the energy and temperature conditions of the collision [70]. Thus, multiplicity fluctuations is an important observable of these experiments, that promises to provide information on the characteristics of the state of the system created in the collisions and thus revealing the particle production mechanisms, correlations among various particles and the dynamics of the system.

Intermittency analysis is a method used in high-energy physics to study non-statistical density fluctuations in the particle production. It involves calculating normalized factorial moments, which quantify fluctuations across different size scales. Intermittency is defined as a power-law behaviour of the normalized factorial moments of the particle density fluctuations in spatial or momentum space, with increasing number of bins [79–81]. Presence of intermittency indicates a self-similar or scale-invariant structure of the system involved. This power-law behaviour is significant because it can be connected to phase transitions, such as the quark-hadron phase transition. In low-energy experiments, intermittency analysis has been applied to search for the formation of quark-gluon plasma and to understand the quark-hadron phase transition [70]. However, challenges like low bin multiplicities remained infeasible to draw definitive conclusions about the critical point, order of phase transition, or nature of multiplicity fluctuations or

to get the signal of QGP formation [81]. Despite these challenges, intermittency analysis remains a valuable tool for investigating the complex dynamics of nuclear matter under extreme conditions and has been extensively investigated for various systems and energies [70, 81]. The availability of data from recent colliders, featuring high charged particle density per bin, has sparked renewed interest in using this methodology to understand multi-particle production processes [82]. Investigations on these lines have been performed by the STAR experiment at RHIC that reports the first measurement of intermittency in Au−Au collisions across a range of collision energies from $\sqrt{s_{\rm NN}} = 7.7$ to 200 GeV [82]. A power-law behaviour in normalized factorial moments is observed, with a decreasing scaling exponent (ν) from peripheral to central collisions. The measured ν exhibits a non-monotonic energy dependence, reaching a minimum around $\sqrt{s_{\rm NN}} = 27$ GeV. This observation prompts questions regarding the QCD phase transition and the underlying dynamics of heavy-ion collisions and supports the case to explore ALICE data at LHC energies.

1.7 Organization of thesis

The thesis presents an event-by-event analysis of the charged particle multiplicity fluctuations in the data, recorded using ALICE detector at LHC, CERN during RUN 1. In *Chapter 2*, there is a brief introduction to the Large Hadron Collider (LHC), the ALICE experiment, and a few detectors used in the ALICE. *Chapter 3* focuses on the details of the analysis methodology for the study of multiplicity fluctuations using normalized factorial moments. Observations and results from the analysis performed using Toy model events are given in *Chapter 4* and that from Monte Carlo models like HIJING and AMPT are given in *Chapter 5*. *Chapter 6* focuses on the results and observations from the analysis of ALICE data. In *Chapter 7* summary of the work reported in this thesis is presented along with conclusions and outlook.

Chapter 2

The experimental setup

This chapter gives a brief overview of the Large Hadron Collider (LHC) and setup of the ALICE experiment. It also addresses main points of data acquisition system and online-offline computing for data processing using the AliROOT framework.

2.1 Introduction to the LHC

The Large Hadron Collider (LHC) at European organization for Nuclear Research (CERN), which started its operation in 2009, is today the largest and the most powerful particle accelerator in the world [34]. It is installed in 26.7 km tunnel that was previously built for the Large Electron Positron (LEP) collider [83]. It is situated beneath the Swiss-French border region at a depth fluctuating between 50 to 175 meters beneath the Earth's surface. Fig. 2.1 gives a schematic view of the CERN's accelerator complex, which consists of different accelerator systems. The LHC is designed to collide proton beams with a maximum energy of $\sqrt{s} = 14$ TeV and heavy ions (Pb-ions) with a maximum energy of $\sqrt{s_{\rm NN}} = 5.5$ TeV achieving luminosities of $10^{34}\,{\rm cm}^{-2}\,{\rm s}^{-1}$ and $10^{27}\,{\rm cm}^{-2}\,{\rm s}^{-1}$ for proton and Pb-ion beams, respectively [84]. Consequently during RUN 1 of LHC operations, it provides proton-proton (pp) collisions with energies of up to $\sqrt{s} = 8$ TeV and lead-lead (Pb–Pb) collisions with energies of up to $\sqrt{s_{\rm NN}} = 2.76$ TeV. In Run 2, the accelerator achieved collision energies of $\sqrt{s_{\rm NN}} = 5.02$ TeV for Pb−Pb collisions. In the RUN 3 operation during 2022-23, lead nuclei were accelerated and made to collide, achieving an unprecedented energy of 5.36 TeV for nucleon-nucleon collision.

The main objective of the LHC's proton-proton collisions is to create and learn more about the Higgs boson, which gives elementary particles their mass [17].

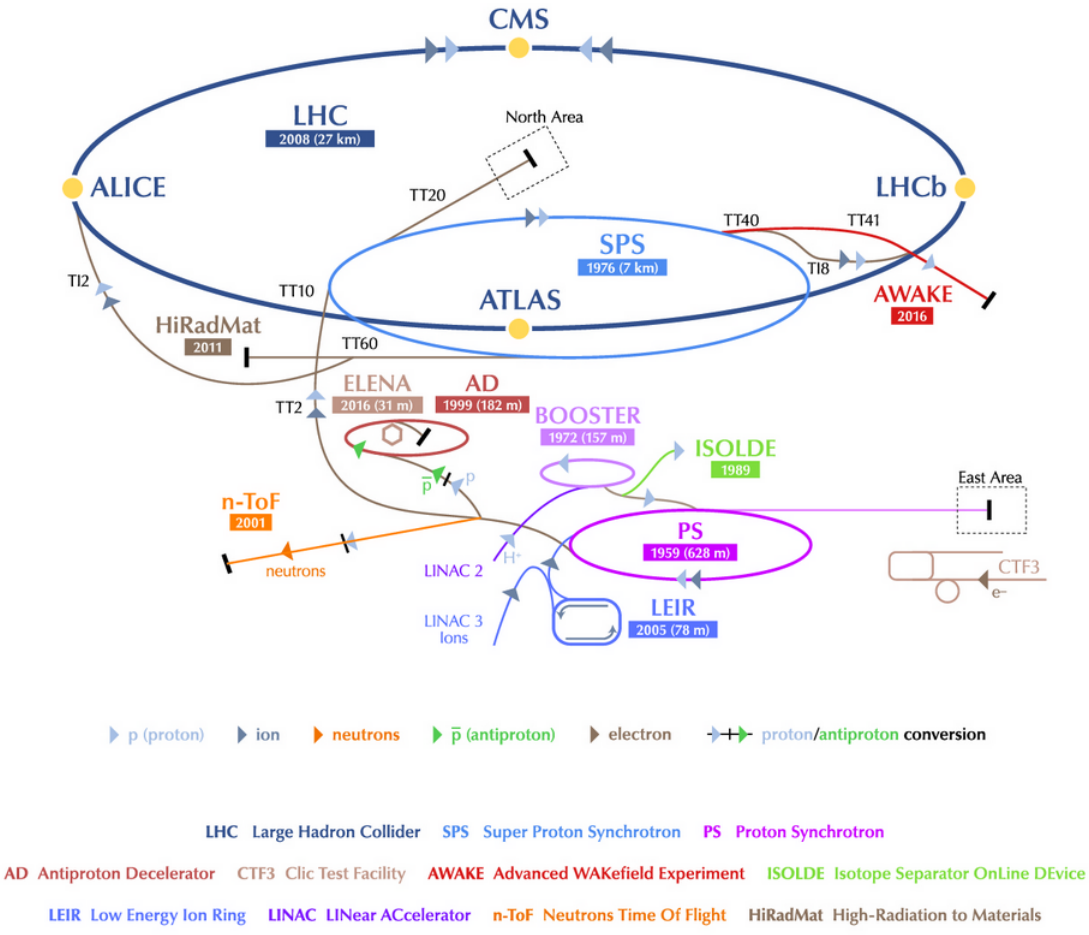

Figure 2.1. Schematic view of the CERN accelerator complex and the locations of the four major LHC experiments [85].

Furthermore, the LHC explores topics such as supersymmetry, dark matter, and dark energy. Additionally, through heavy-ion collisions, the LHC provides insights into the quark-gluon plasma, a state of matter that existed in the universe just a few microseconds after the Big-Bang. To achieve ultra-relativistic energies in the laboratory, particles undergo pre-acceleration through several accelerator systems before entering the LHC ring.

For pp collisions, the accelerating process begins with hydrogen gas as a proton source. To obtain protons, hydrogen atoms are stripped of their electron using an electric field. Protons are then accelerated up to 100 keV and transferred to a Radio Frequency Quadrupole (QRF) to speed up and focus the particle beam. The proton beam is further accelerated by the QRF up to 750 keV. Subsequently, the proton beam is directed into a linear accelerator known as LINAC 2 [86, 87], capable of accelerating protons to energies of up to 50 MeV. From LINAC 2, protons are transferred to the Proton Synchrotron (PS) Booster [86], followed by the Super Proton Synchrotron (SPS) [88] in subsequent stages, where their energy is increased to 450 GeV. After this process, the protons are directed into the main LHC ring in two different directions, where their energy is scaled up to the appropriate collision energy.

The lead (Pb) ion beam, on the other hand, begins with vapour of lead atoms that is produced while heating a 2 cm long, 500 mg pure lead sample to 500° C. A few electrons are removed from the Pb atom using an electric field. These recently formed Pb ions are initially accelerated by a LINAC 3 [87] up to the energy of 4.2 MeV per nucleon and further electrons are removed from the Pb ions. The ions are then accelerated in the Low Energy Ion Ring (LEIR) [89] to 72 MeV per nucleon. Pb ions are then further accelerated in the PS and SPS. The remaining electrons from the Pb ions are stripped away in the PS, and here the energy of Pb ions is increased to 5.9 GeV per nucleon. The Pb beam is accelerated in the SPS to a maximum of 177 GeV per nucleon before being eventually injected into the LHC in two different directions where the beams can achieve energy in TeV. A comprehensive heavy-ion program at the LHC is aimed at two main objectives: to collide the largest available nuclei at the highest achievable energy and systematically studying various collision systems (pp, p-A, A-A) at different

beam energies.

In Fig. 2.2, which provides a schematic layout of the LHC operation points, two injection points are shown through which particles are injected into the LHC ring in two opposing directions, originating at points 2 and 8. The beams move in opposing directions through two distinct ultra-high vacuum tubes referred to as beam pipes. The beams are accelerated up to their achievable energy, and once their energy stabilizes, they collide at the four interaction points, namely, 1, 2, 5, and 8. At these four interaction points, the LHC hosts four major experiments: ALICE [90], ATLAS [91], CMS [92], and LHCb [93], arranged around its circumference, as depicted in Fig. 2.2.

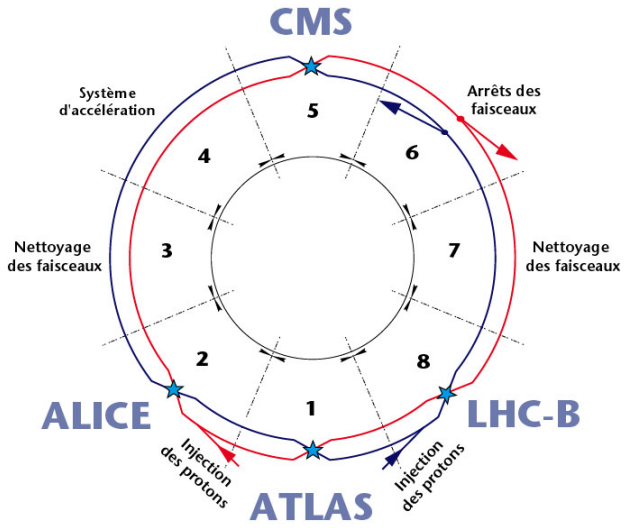

Figure 2.2. Schematic view of the main experiments along Large Hadron Collider beam ring [94].

The experimental setups at LHC at different interaction points are designed with the goal of exploring a wide range of physics topics. One of these setups, LHCb (Large Hadron Collider beauty), is situated at one of the four interaction points and is specifically dedicated to studying particles containing beauty (b) quarks, a field known as b-physics. The ATLAS (A Torroidal LHC Apparatus) and the CMS (Compact Muon Solenoid) are the bigger experimental setups at two interaction points of the LHC that are diametrically opposite to each other. These are general-purpose experiments to investigate a large range of physics topics, mainly focusing on the realm of particle physics. They look for new and heavier elementary particles. Even though, the scientific objectives of both of these

Table 2.1. An overview of data recorded at LHC during different periods.

	Collision System	Energy in centre of mass	Year of data taking
RUN 1	pp	900 GeV and 2.76 TeV	2010
	Pb–Pb	2.76 TeV	2010
	pp	7 TeV	2011
	Pb–Pb	2.76 TeV	2011
	pp	8 TeV	2012
	pPb	5.02 TeV	2013
RUN 2	pp	5.02 TeV and 13 TeV	2015
	Pb–Pb	5.02 TeV	2015
	pPb	5.02 and 8.16 TeV	2016
	Xe–Xe	5.44 TeV	2017
	Pb–Pb	5.02 TeV	2018

experiments are similar, there is a difference in the technological approaches and detector magnet system designs used to accomplish these objectives. In contrast to these, the major objective of the ALICE (A Large Ion Collider Experiment) detector system is to investigate the physics of strongly interacting matter at high energy densities and temperatures using both heavy and light ions (Pb–Pb, Xe–Xe, pPb, pp) collisions. A summary of data recorded for various colliding systems and energies by ALICE during first two runs of LHC operations is given the Table 2.1.

An overview of the ALICE experiment and its different sub-detectors is given in the following section.

2.2 A Large Ion Collider Experiment (ALICE)

A Large Ion Collider Experiment (ALICE) [90] is a heavy-ion detector specifically designed to explore the intriguing physics possibilities of nucleus-nucleus interactions at the LHC energies. The goal of the ALICE experiment is to learn about the physics of strongly interacting matter at very high energy densities, where the emergence of a new phase of matter, QGP is expected. The ALICE detector is located at the interaction point 2 (IP2) of the LHC ring. It is 26 m in length, 16 m in width, and 16 m in height and weighs around 10,000 tons. It has been optimized to detect particles in a setting with extremely high particle densities. It also provides excellent particle identification (PID) for the comprehensive study of hadrons, electrons, muons and photons produced during the collisions.

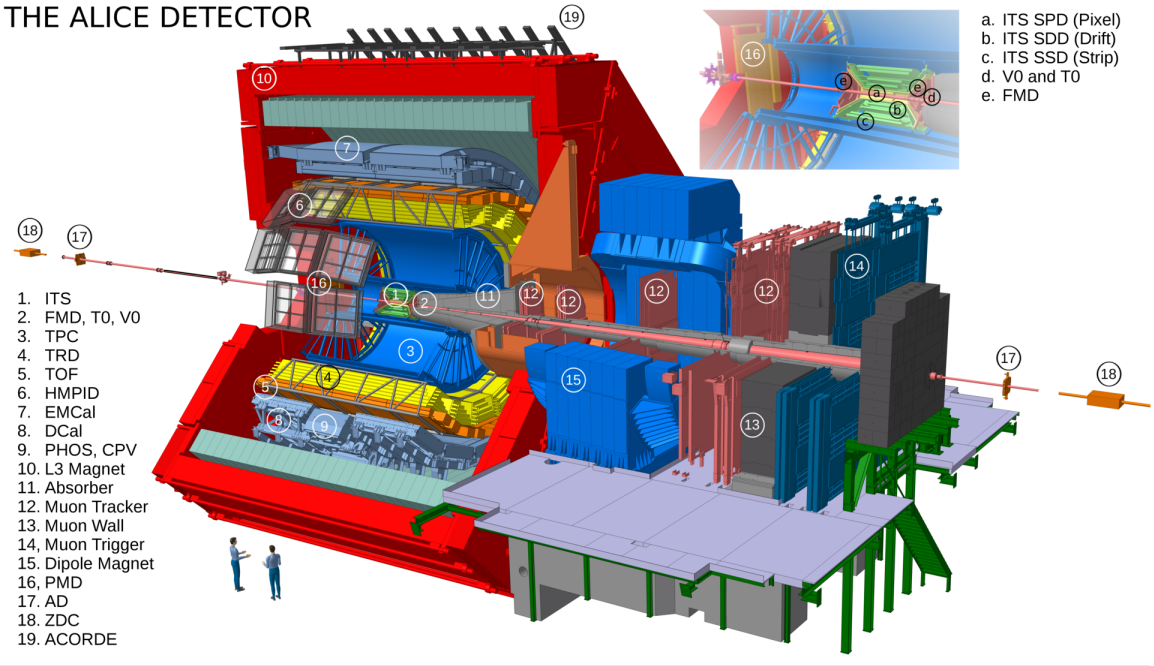

Figure 2.3. Schematic diagram for the ALICE experiment detector setup [95].

The schematic view of the ALICE detector during RUN 1 and RUN 2 is shown in Fig. 2.3. It is mainly composed of two parts: one is the central barrel region, and the other is forward region.

2.2.0.1 Central Barrel Detectors

The central barrel region, situated near the interaction point (IP), with several sub-detectors which cover a mid rapidity region ($|\eta| < 0.9$) and azimuthal range of 2π, is used for tracking, vertex reconstruction and particle identification. All the detectors in the central barrel region are housed within a massive solenoidal magnet, previously employed in the L3 experiment at LEP [83]. This magnet generates a maximum magnetic field of 0.5 T. The central barrel detector system comprises the following detectors, listed in order from the innermost to the outermost layers:

- Inner Tracking System (ITS) [96]
- Time-Projection Chamber (TPC) [97]
- Transition Radiation Detector (TRD) [98]
- Time-Of-Flight (TOF) [99]
- High-Momentum Particle Identification Detector (HMPID) [100]

- Electro-Magnetic calorimeters: Electromagnetic + Dijet Calorimeter (EMCAL + DCAL) [101] and Photon Spectrometer (PHOS) [102]
- ALICE COsmic Ray DEtector (ACORDE) [103]

2.2.0.2 The Forward Detectors

Forward detectors, situated in the high pseudorapidity region and consequently at a small angle relative to the beam pipe, play important roles in triggering events and measuring global event characteristics. The forward detectors, including the Muon spectrometer, are listed below :

- Muon Chamber (MCH) [104]
- Zero Degree Calorimeter (ZDC) [105]
- Photon Multiplicity Detector (PMD) [106]
- Forward Multiplicity Detector (FMD) [107]
- Time Zero Detector (T0) [107]
- VZERO Detector (V0) [107]

The data recorded by ITS, TPC, and V0 detectors is primarily used in the present analysis work and thus a brief overview of these detectors is given below:

2.2.1 The Inner Tracking System (ITS)

The Inner Tracking System (ITS) detector [108, 109] is the main detector in the central barrel system responsible for measuring the primary vertex of the collisions, as it is the closest detector to the beam pipe. It covers a pseudorapidity range of $|\eta| < 0.9$ and extends from an inner radius of 3.9 cm to an outer radius of 43 cm. The inner and outer radii of the detector are determined by the size of the beam pipe and the need for good track matching efficiency with the TPC. The primary functions of the ITS are:

- primary vertex reconstruction using the first two layers of ITS.
- to reconstruct the secondary vertices.
- particle identification of low momentum particles (< 1 GeV).

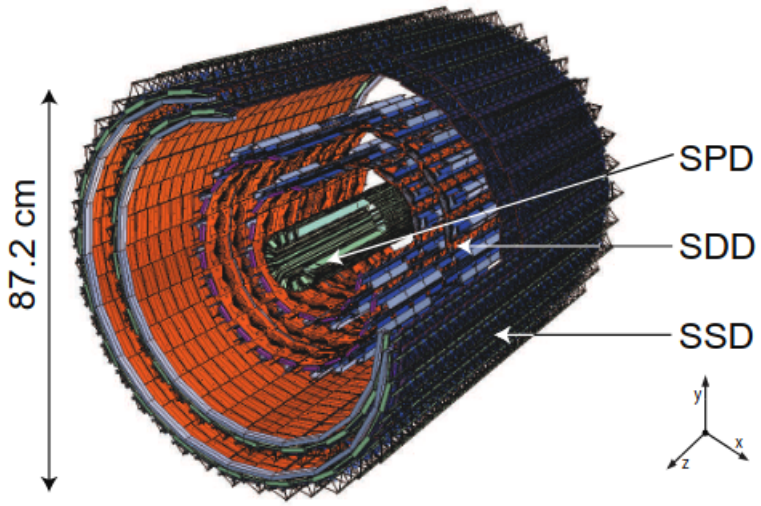

Figure 2.4. Layout of the Inner Tracking System (ITS) detector in ALICE during RUN 1 and RUN 2 [109].

- tracking and reconstruction of low p_T particles.

A geometrical layout of the ITS used in RUN 1 and RUN 2 of LHC is shown in Fig. 2.4. ITS comprises of six layers of silicon detectors based on three different technologies. These include two layers of Silicon Pixel Detectors (SPD) for high resolution tracking, two layers of Silicon Drift Detectors (SDD) for precise position measurements, and two layers of Silicon Strip Detectors (SSD) offering excellent spatial resolution. As the name suggests, these detectors are made of silicon semiconductors which implies that these detectors operate on the fundamental principles of silicon semiconductor technology. In general, a semiconductor detector works on the principle of utilizing semiconductor materials to detect charged particles. When a charged particle interacts with the semiconductor material, it transfers energy to the electrons within the material, causing them to move from the valence band to the conduction band. This creates electron-hole pairs, where the electrons become mobile and can be collected at an electrode. By applying a bias voltage across the semiconductor, these mobile charge carriers are directed towards the electrodes, generating a measurable electric current or voltage signal. This signal can then be processed and analyzed to determine properties of the incident particles, such as energy, trajectory, and their type. Different detector

designs were chosen in accordance with the particle density, which in case of LHC for Pb–Pb collisions is very high near to the collision point. As one moves away from the interaction point this density decreases.

SPD consists of two hybrid pixel detector layers, and it equips the innermost part of the ITS. Both layers are 14.1 cm long and are located at a radial distance $r = 3.9$ cm and $r = 7.6$ cm from the nominal beam line. The first layer of SPD has the pseudorapidity coverage of $|\eta| < 1.98$ and therefore, it provides a continuous measurement of the charged particle multiplicity density in combination with the FMD detector in an extended pseudorapidity range. There is no energy loss information available and the readout of the SPD is binary, and hence, it can also be used to trigger decisions. SPD's primary goals are to determine the position of the primary vertex and to calculate the impact parameter of secondary vertices originating from weak decays of strange, charm, and beauty particles [110].

SDD constitutes the two intermediate layers of the ITS situated at radial distances of $r = 15$ cm and $r = 23.9$ cm. It is based on modules having a sensitive area that is split into two drift regions where electrons move in opposite directions under a drift field of about 500 V/cm. This is used for particle identification using specific energy loss (dE/dx) and tracking of the tracks passing through it [111].

SSD composed of last two layers of ITS is also used for particle identification and tracking. It comprises two layers of double-sided silicon strip detectors positioned at radial distances of $r = 38$ cm and $r = 43$ cm. The SSD provides the dE/dx measurements and provides a two dimensional measurement of the track position crucial for the matching of tracks with the TPC [112].

The ITS used in RUN 1 and RUN 2 which consisted of a total six cylindrical layers is replaced by a new design in 2021. The new ITS for RUN 3 of LHC operations is now based on monolithic active pixel sensors (MAPS) with a granularity of 30×30 micrometer, implemented in CMOS imaging technology (similar to digital camera sensors). The new detector incorporates seven layers, enabling track reconstruction solely based on ITS information [108].

2.2.2 Time Projection Chamber (TPC)

The Time Projection Chamber (TPC) [97,113] is the primary tracking detector of the ALICE experiment that is used for tracking of charged particles and particle identification. The ALICE TPC is a cylindrical chamber of volume 90 cubic metre, placed coaxially with the beam axis. It has an active volume extending from an inner radius of approximately 85 cm to an outer radius of 250 cm, with a length of 500 cm, covering a pseudorapidity range $|\eta| < 0.9$. A schematic diagram of the TPC is shown in Fig. 2.5.

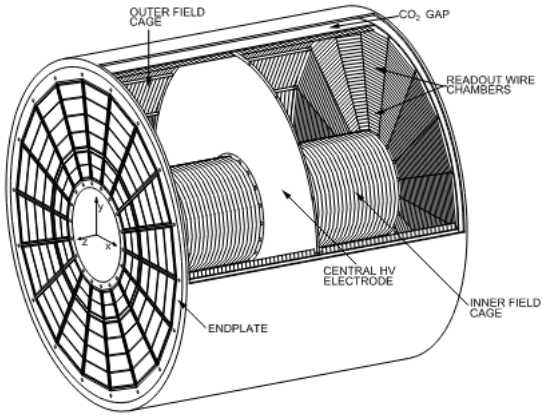

Figure 2.5. Schematic layout of a Time Projection Chamber (TPC) detector [113].

TPC in ALICE is a gaseous detector that operates in the proportional region filled with a gas of 90% Ne, 10% CO_2 and N_2 in RUN 1, Ar+CO_2 in RUN 2 and Ne+CO_2+N_2 in RUN 3. Choice of gas mixture is optimized to ensure good momentum resolution, high rate handling capacity, low space charge effect and low scattering. A high voltage electrode, acting as the cathode, divides the huge cylindrical field cage of the TPC into two sections. The charged particles going through the gas volume ionize the gas and liberate electrons which drift towards the readout plates with a drift velocity of approximately 2.7 cm/s and eventually hit the readout pads. The readout of the signal is done by the pads of Multiwire Proportional Chamber (MWPC) installed in 18 trapezoidal sectors at both ends of the TPC. The (x,y) position of the path of the particle is determined by the hit in MWPC at the end plates and z coordinate is measured from the arrival time of the signal relative to collision time of the beams. On applying uniform magnetic

field, particles follow a helical trajectory and this curvature is used to determine their momentum. The position resolution of the TPC ranges from 1100 - 800 µm in the r, φ plane and from 1100 - 1250 µm in the z direction. The specific energy loss (dE/dx) is determined by the charge collected from the readout pads. Knowing the particle momentum and <dE/dx>, the particle identity can be found from the Bethe-Bloch formula.

$$\frac{dE}{dx} = \frac{4\pi e^4}{m_0}\frac{z^2}{v^2}NZ\left\{ln\left(\frac{2m_0v^2\gamma^2}{I}\right) - \beta^2 - \delta^2 - \frac{2C}{Z}\right\}, \tag{2.1}$$

where, N and Z are number density and atomic number of absorber material respectively, z is the charge of primary particle, v is the velocity of the charged particle and m_0 is the rest mass of electron. I is the mean excitation potential, δ is the density correction factor and C is shell correction factor. TPC can separate the particles well upto $p_T = 1$ GeV/c using dE/dx measurement. The dE/dx distribution for various charged particles recorded in ALICE for Pb–Pb collisions at $\sqrt{s_{\rm NN}} = 2.76$ TeV is as shown in Fig. 2.6, where the solid line is the expectations from the Bethe-Bloch formula.

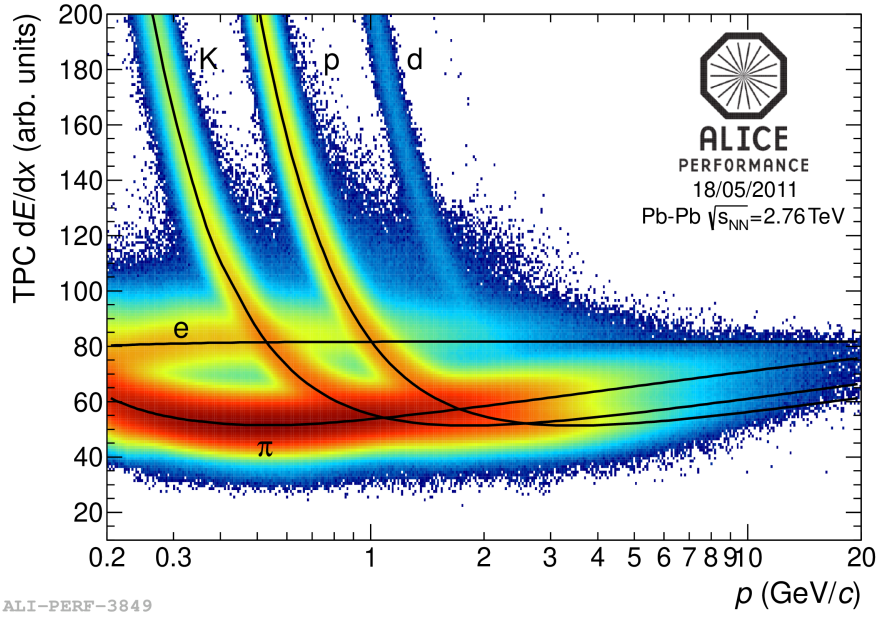

Figure 2.6. Energy deposited per unit length versus momentum measured with the ALICE TPC for Pb–Pb collisions at $\sqrt{s_{\rm NN}} = 2.76$ TeV during RUN 1 [114].

2.2.3 VZERO detector (V0)

The VZERO (V0) detector [115] is the main detector to estimate centrality of the collision. Centrality is obtained from the deposited energy in the V0 detectors. Since this deposited energy is directly proportional to the number of primary particles produced and hence to the centrality of the collision. It is a small angle detector that consists of two arrays of scintillator counters, called V0A and V0C, installed on either side of the ALICE interaction point. The position of V0A is 3.4 meters away from the vertex, on the side that faces the muon spectrometer, whereas V0C is positioned at the front face of the front absorber, 0.90 meters away from the vertex. The pseudorapidity coverages of V0A and V0C are $2.8 < \eta < 5.1$ and $-3.7 < \eta < -1.7$, respectively. Each array of the V0 detector comprises of four rings in the radial direction segmented into 32 individual counters, connected with 1 mm diameter Wave-Length Shifting (WLS) fibre, that guide the light to a photomultiplier tube (Fig. 2.7). The two V0 detectors are not placed symmetrically around the IP is attributed to the presence of the hadron absorber within the muon spectrometer.

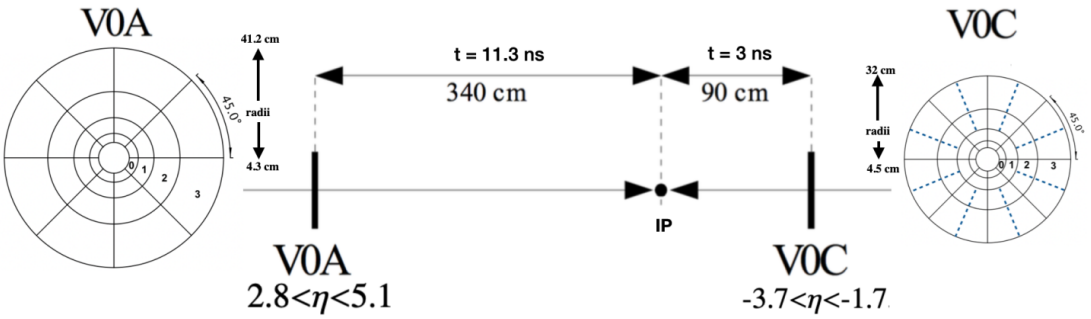

Figure 2.7. A schematic view of V0 detector geometry. Layout of V0A (left) and V0C (right) rings are shown [115].

Charged particles passing through the scintillator array of the V0 detector excites the material, which then emits photons during the de-excitation process. These photons are transmitted to a photo-multiplier tube (PMT) and are converted into an electrical signal. The fast response of the scintillator detector makes it suitable for use as trigger detectors. The V0 serves as an indicator of collision centrality by analyzing the recorded event multiplicity. This detector also participates in the measurement of luminosity in pp collisions with a good precision of

about 10 %.

The primary goal of the V0 detector in ALICE is to provide the minimum-bias trigger for the central barrel detectors in pp and Pb−Pb collisions. Minimum bias trigger requires the condition of at least one particle hit on V0A, V0C and both V0A and V0C. Trigger efficiency could be higher with either V0A or V0C alone. However, the background generated by the interaction of the beam with the residual gas in the beam pipe offsets this potential advantage. By measuring the V0 time information, it can also be used to eliminate background events, or events that are not caused by beam-beam collisions. There is approximately a 6 ns discrepancy between real events and events associated with beam gas interactions. The mean number of hits is 10-20 for the rings of V0C and slightly lower for V0A. To identify a beam-beam collision, the event should occur on both V0A and V0C at the expected time, i.e. the timing for detection after the collision is 11 ns for V0A and 3 ns for V0C.

More details on these detectors and other detectors of the ALICE experimental setup during RUN 1 of LHC are in Ref. [90]. In section below an overview of the software framework used for the data collection, recording and analysis is given.

2.3 ALICE online and offline system

A huge amount of data has been recorded by the various detector systems of the ALICE experiment. For better data management and efficient analysis of the data to extract physics, high quality robust software is required. ALICE collaboration has developed software for both online and offline processing of the data. An overview of the online software used in the first two runs of LHC operations is given below.

2.3.1 ALICE online system

The subdetectors in the ALICE experiment interact with numerous online systems during data collection. It comprises of Detector Control System (DCS),

Data Acquisition (DAQ), Trigger system (TRG), High-Level Trigger (HLT), and experiment Control System (ECS) [116].

The primary objective of the Detector Control System (DCS) is to facilitate the safe and straightforward operation of ALICE at the LHC. DCS controls hardware operations and is in charge of controlling all the detector services. DCS is responsible for managing and overseeing various essential services connected to the detectors, including high and low-voltage power supplies, gas systems, magnets, and cooling systems. Importantly, it remains operational continuously, even during shutdown periods. Meanwhile, the ALICE Experiment Control System (ECS) assumes the role of coordinating the activities of all online systems to ensure they work together effectively to achieve their shared objectives. ECS components receive status updates from online systems and issue commands through Finite-State Machine interfaces (FSM), while access control mechanisms govern permissions at ECS-online system interfaces. Online systems may either be managed by the ECS or operate autonomously, with the later providing status updates to the ECS without receiving directives.

The Trigger System (TRG) combines the information from all triggering detectors and for every bunch-crossing of the LHC, makes a decision within microseconds whether the resulting data is worth being recorded. It transmits a series of trigger signals to all detectors for each successful decision in order to synchronize their readings.

The ALICE detectors have two-level trigger systems, a low-level trigger and a high-level trigger. The low-level trigger is a hardware trigger and is known as the Central Trigger Processor (CTP). The high-level trigger (HLT), on the other hand, is a software trigger. The CTP integrates the trigger signals from the various sub-detectors to decide the acceptance of an event [117]. Depending upon the arrival times of the trigger inputs and the time synchronization of the detector, CTP further has three levels of triggers. The first level, known as Level-0 (L0), is delivered after 1.2 µs, the second, called Level-1 (L1), after 6.5 µs. After 100 µs, the last trigger, which is known as Level-2 (L2) trigger, is delivered. At the end of the final level trigger, the system chooses whether the selected event is to be

stored or not [116].

The ALICE High-Level Trigger (HLT) is a software trigger that consists of multiprocessor computers. It is being used to significantly reduce the size of the event by selecting the required portion of the data. The architecture of the HLT system is depicted in Fig. 2.8. The data collected by different sub-detectors of ALICE is received in layer 1 through the 454 Detector Data Links (DDL). The basic calibration of these data is carried out by the first layer, and the hits and clusters are subsequently extracted by the second layer. The reconstruction of the event for each detector is performed in the third layer. After that, the fourth layer combines the processed and calibrated information from all detectors to reconstruct the whole event. From these reconstructed events, layer five selects an event with physics interest. In the sixth layer, complex data compression algorithms are applied to the approved and selected data, reducing event size while preserving important physics information [118].

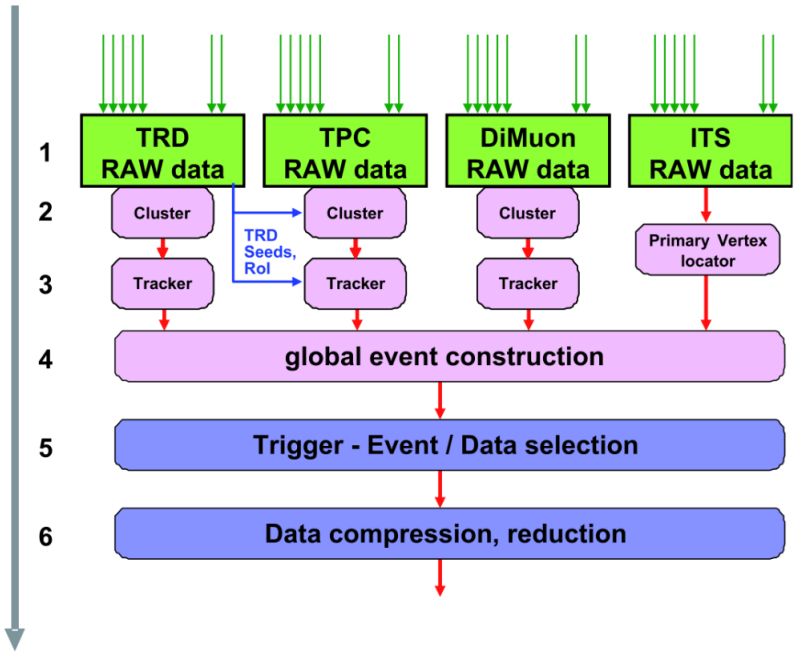

Figure 2.8. The six architectural layers of the High-Level Trigger [90].

Realizing the data flow from the detector to the data storage is the primary purpose of a data acquisition system (DAQ) [118]. The DAQ system also contains software tools for system performance monitoring and data quality checking. The main task of the ALICE DAQ system is event building and export of assembled

events from detector-related electronics to permanent storage. Event building is done in two steps. Detector Data Linkages (DDLs) on Local Data Concentrators (LDCs) receive data from the sub-detectors. The function of LDCs is to assemble the data into sub-events and this information is further moved to Global Data Collectors (GDCs). The GDCs archive the data to the Transient Data Storage (TDS) as data files with a fixed size through the storage network. During a run period, every GDC produces a sequence of these files and registers them in the ALICE Grid software (AliEn) [119]. An overview of the architecture of ALICE DAQ showing various sections and the dataflow is shown in Fig. 2.9.

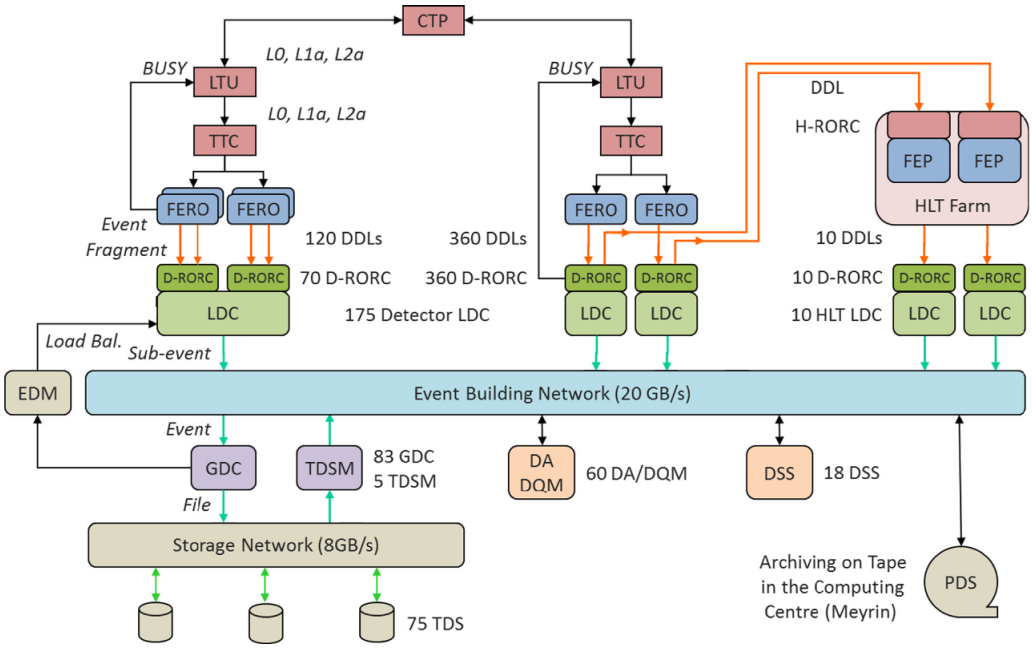

Figure 2.9. Overview of the hardware architecture of the ALICE DAQ system [116].

2.3.2 ALICE offline system

The raw data obtained from the detector systems is required to be processed before being ready in the form of events for further physics analysis. The goal of the ALICE offine project is to create a framework that will ensure proper data processing. This includes tasks such as simulation, reconstruction, calibration, alignment, visualization, and finally analyses of the collected data. There are different levels at which these functions are performed, as is briefed below.

2.3.2.1 ALICE grid system

Huge amount of data is recorded and collected by each of the experiments at the LHC. For this the distributed computing approach is adopted by the experiments. For example, for a central Pb–Pb collision, the TPC in ALICE experiment is read out by 557568 channels, producing event sizes up to 75 MB. The ALICE Grid concept was introduced in order to handle and process enormous amount of data. Data processing is spread among a number of computing facilities located all over the globe. This distributed computing infrastructure used in the LHC experimental program is managed under the Worldwide LHC Computing Grid (WLCG) project [120]. This Grid serves as a platform for running codes and generating output, which is then utilized to derive the results from the various physics analysis as one is presented in this thesis.

The purpose of the WLCG is to offer global computing resources for the storage, distribution, and analysis of LHC data. All actual data come from CERN, which has a very large data centre called Tier-0. The function of a secure data storage facility is shared with CERN by large regional computer facilities, called Tier- 1. Tier- 2 are the smaller centers that are logically clustered around Tier- 1. The primary responsibilities of Tier- 2 include user analysis tasks and Monte-Carlo simulations. As an example, the Variable Energy Cyclotron Centre (VECC) at Kolkata in India has a Tier- 2 centre.

2.3.2.2 Dataflow

The approach to data processing varies depending on the type of collision being analyzed. For proton-proton (pp) collisions, the data captured by the Data Acquisition System (DAQ) are initially stored in a disk buffer at the Tier-0 computing center located at CERN. Simultaneously, the RAW data are duplicated onto CASTOR (CERN Advanced STORage manager) tapes and distributed to Tier-1 centers, where a secondary copy is maintained. This redundancy is crucial for subsequent stages of data processing, including initial reconstruction, alignment and calibration constant processing, and scheduled analysis, all of which take place at the Tier-1 centers. Additionally, a rapid processing of specific data sets occurs at the CERN Analysis Facility (CAF). In case of nucleus-nucleus runs,

the processing of RAW data follows these steps:

- RAW data registration in CASTOR.
- Partial export of data to Tier-1 centers, allowing remote users to access it.
- Partial initial processing at the Tier-0 center to quickly assess the performance of the offline data processing chain.
- Swift processing and analysis conducted on the CERN Analysis Facility (CAF).

Reconstruction in heavy ion collisions involves identifying and tracking the paths of particles produced during the collisions. During the initial pass of reconstruction, a process that involves generating high-precision alignment and calibration data, as well as producing a preliminary set of Event Summary Data (ESD) and Analysis Object Data (AOD), is undertaken. Feedback obtained from this initial pass, which includes analysis activities, is utilized to fine-tune the code and parameters for the subsequent processing pass. A complete copy of the raw data is securely stored at CERN, while another copy is shared among the Tier-1 centers located outside CERN. The responsibility for the first pass of reconstruction lies with CERN itself. However, subsequent tasks such as data reduction, analysis, and Monte Carlo production are collaborative efforts involving all Tier levels. Tier-2 centers, in particular, play an active role in Monte Carlo simulations and end-user analysis.

2.3.2.3 AliEn Framework

ALICE uses the ALICE Environment (AliEn) system as an interface to connect to the Grid composed of ALICE-specific services that are part of the AliEn framework [119]. The AliEn framework is used for data reconstruction and analysis. It provides a universal file system for data storage and to execute jobs on the Grid. The analysis jobs are divided up into numerous identical sub-jobs that are executed simultaneously on various computer nodes of the Grid system. The progress of the jobs on the Grid can be monitored using the AliEn interface.

2.3.2.4 ALICE Analysis Framework: AliROOT

The data collected by several ALICE detectors is analysed in order to explore important details about the particle production mechanism and properties of the state of matter formed during collisions. The software framework used for the analysis of the data collected by ALICE is known as AliPhysics and its schematic steps of working is shown in Fig. 2.10. It is the ALICE offline framework based on

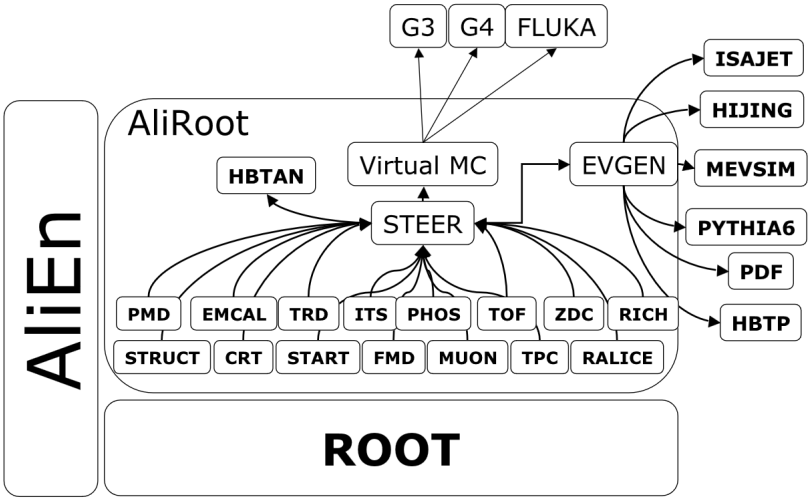

Figure 2.10. A schematic view of the AliPhysics framework of ALICE used for data analysis [90].

the Object-Oriented techniques for programming and, as a supporting framework, it has the ROOT [121]. The analysis codes for specific physics analysis are stored in AliPhysics. AliPhysics primarily uses C++ for its codes, while some AliRoot macros are indeed written in FORTRAN and are wrapped inside C++. The operations which can be performed are simulation, reconstruction, calibration, quality assurance, and analysis of both experimental and simulated data.

Simulation: The simulation of events in real experimental setup holds a crucial role in the analysis of high-energy collision experiments. Simulated samples are employed to adjust physics data for detector efficiency and limitations in data acceptance. These simulations are typically composed of two components: the event generator and the transport code. Event generators are focused on generating events and particles that mimic the average behaviour observed in the real data, drawing upon our theoretical understanding of collision dynamics. Various event

generators employ different theories and physical processes to generate events that closely resemble known real data. Monte Carlo techniques are employed in these simulations, and as a result, the simulated data produced by the event generators are commonly referred to as Monte Carlo samples. The most popular event generator that ALICE uses to simulate pp occurrences is PYTHIA [122, 123]. Other prominent event generators include EPOS [124], HIJING [125] and the AMPT [126].

Reconstruction: The process of reconstructing raw data for storage in ESD and AOD files begins with calibration, followed by separate clusterization for each detector. A cluster is a group of neighbouring hits or cells that have registered signals above a threshold, and these clusters serve as input for track/tracklet reconstruction in tracking detectors. Additionally, clusters obtained from calorimeter-based detectors are included in the ESD files. The position of the interaction vertex is determined using algorithms that exploit correlations between SPD tracklets [127]. Tracklets are created from adjacent clusters found in both layers of the SPD, aligning them with the reconstructed primary vertex within a narrow azimuthal window, typically on the order of 0.01 radians [128]. The initial estimation of the interaction vertex is determined as the spatial point where the maximum number of lines resulting from a linear extrapolation of the tracklets converge. The accuracy of this vertex determination relies on the multiplicity of tracklets [127].

In the central barrel of ALICE, track recognition and reconstruction are carried out using the Kalman filter method [129] in three iterations. The first iteration starts from the outer radius of the TPC (Time Projection Chamber). A track seed is constructed based on the primary vertex estimation derived from SPD (Silicon Pixel Detector) data and pairs of TPC clusters in adjacent pad rows. This track seed is then projected inward toward the inner radius of the TPC and is continually updated at each step by associating it with the nearest TPC cluster, provided it satisfies certain proximity criteria. At this stage, there is also a preliminary particle identification based on the measurement of energy loss ($\mathrm{d}E/\mathrm{d}x$). These tracks are referred to as TPC-only tracks. Subsequently, these tracks are propagated toward the ITS (Inner Tracking System) for further track finding within

the ITS and are further extrapolated to determine their point of closest approach to the preliminary interaction vertex. In the second iteration, the tracks obtained from the preliminary vertex estimation are traced backward to the outer radius of the TPC, utilizing the clusters identified in the previous iteration. Additionally, particle identification is updated by considering the specific energy loss measurements. These tracks are then extended towards various detectors such as TRD, TOF, HMPID, EMCAL, and PHOS for cluster matching. In the final iteration, the tracks are re-fitted inward, utilizing the clusters from the second iteration to determine their points of closest approach to the SPD vertex. These tracks are referred to as *global tracks*. The final interaction vertex is recalculated with higher precision using these global tracks, surpassing the accuracy of the preliminary interaction vertex estimation.

Analysis: The last action taken on the data is the analysis, which aims to identify and analyse its physics content. The analysis is done either on the data sets created after the reconstruction of real or simulated data (ESDs), or on the data sets known as Analysis-Object Data (AODs).

Chapter 3

Analysis methodology

In the field of heavy-ion collisions, fluctuation analysis of the observables is significant tool to understand the dynamics of the system created. Observation of unusually large particle density fluctuations [130] in the cosmic ray experiments prompted vigorous investigations of multiplicity fluctuations in the heavy-ion collision data and related phenomenological studies. These fluctuations being reminiscent to the intermittency spikes in spatio-temporal turbulence triggered studies of patterns in the distributions of particles in the decreasing domains of phase-space. Particle density fluctuations of the hadronic states that are produced in high-energy collisions in the restricted regions of the phase space allow a detailed analysis of the mechanism of particle production. The analysis methodology is termed as intermittency analysis.

Intermittency in physical systems is studied by examining scaling properties of moments of the distributions, of relevant variables over a range of scales. Intermittency if observed reveals the presence of large density fluctuations in the phase space volume of the system. Bialas and Peshanski [79, 131] first introduced the concept of intermittency to study dynamical fluctuations in particle density distributions obtained in the heavy-ion collisions. To explain unexpectedly large fluctuation in the high multiplicity event (Fig. 3.1), reported by JACEE Collaboration [130], they used scaled factorial moments of multiplicity distribution as a function of resolution, a concept borrowed from the theory of turbulence in liquids. This led to experimental and theoretical investigations by lot many groups in the community in search of intermittency. The evidence of intermittency, which defines the power-law behaviour of normalized factorial moments (NFM) in the decreasing bin size in the phase space, are reported in experimental data

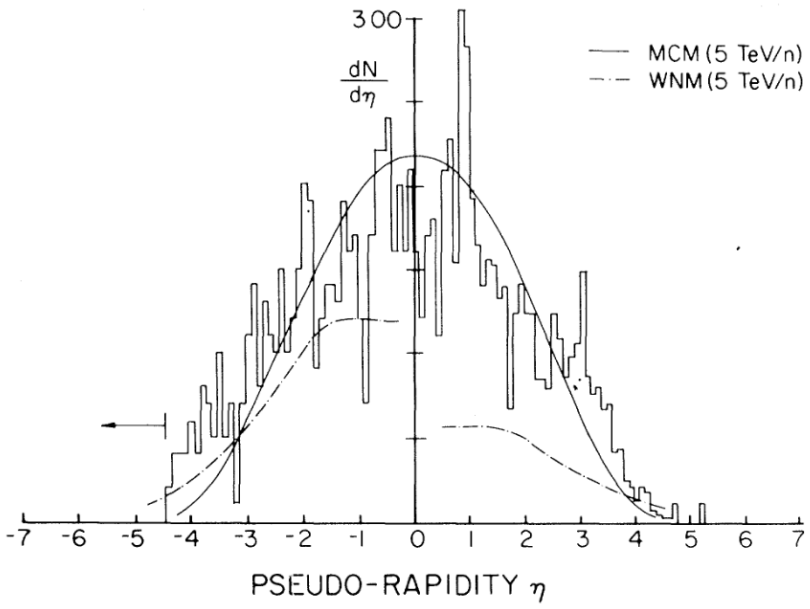

Figure 3.1. Pseudorapidity distribution of charged particles in the Si+AgBr event [130].

of e^+e^- annihilation [132–134], muon-hadron [135, 136], hadron-nucleon [137, 138] and nucleus-nucleus collisions [137–144].

In the vicinity of phase transitions, the emergence of clusters of all sizes, exhibit collective behaviour without a specific characteristic scale [145]. As such systems undergoing phase transition near critical point exhibit large density fluctuations. Scaled factorial moments, synonymously termed as normalized factorial moments are investigated to look for QGP-hadron transition and underlying physics of hadronization [72]. Scaled factorial moments have the property of filtering fluctuations due to statistical sources and to reveal any dynamics of the system packed in the particle density distributions.

Power-law behaviour is intimately connected to the fractal geometry of the system under study. Thus, a look into the intermittency in the multiparticle production in heavy-ion collisions also invigorates studies of fractal nature of the system. In this thesis a two dimensional analysis as proposed in Ref. [72, 146], to gauge bin-to-bin fluctuations in the event space of the ALICE data, Toy model and Monte-Carlo events generated using HIJING and the AMPT, has been performed. A mathematical formulation and other analysis details are given below.

3.1 Mathematical formulation

A two-dimensional intermittency analysis is performed in the angular (η, φ) phase space of the events to measure bin-to-bin particle density fluctuations. NFM for the particles produced are determined on event-by-event basis. These can be calculated as *vertically averaged horizontal moments* that involves first averaging over bins, followed by averaging over events. Conversely, for horizontally averaged vertical factorial moments, the process begins with averaging over events, followed by averaging over bins. For the calculation of NFM, the methodology proposed in Ref. [72] for the vertically averaged horizontal moments is followed. Here kinematically accepted (η, φ) region of the events is partitioned into M^2 bins with M bins along each dimension as graphically illustrated in Fig. 3.2 where the case for M = 3, 5 and 9 are shown. M, the number of bins, takes some minimum value of M_{min} to a maximum value M_{max} with positive integer values constrained by the detector resolution, charged particle density and acceptance region. Particles produced in an event in the kinematic acceptance are mapped onto this phase space partitioned into M^2 bins in the form of a matrix. The number of particles that go into each bin defines its bin multiplicity. In Fig. 3.3, this is depicted for a case where M = 5. Since each event is unique and different from the other, this mapping will lead to unique configurations for each M and each event.

For an i^{th} bin in an e^{th} event having bin multiplicity n_{ie}, the q^{th} order factorial moment is defined as

$$f_{\mathrm{q}}^{e}(n_{ie}) = n_{\mathrm{ie}}(n_{\mathrm{ie}}-1).....(n_{\mathrm{ie}}-q+1) \tag{3.1}$$

Then q^{th} order event factorial moment of the event for M^2 bins is

$$f_{\mathrm{q}}^{e}(M) = \frac{1}{M^2}\sum_{i=1}^{M^2} n_{\mathrm{ie}}(n_{\mathrm{ie}}-1)\ldots(n_{\mathrm{ie}}-q+1) \tag{3.2}$$

$$= \langle n_{\mathrm{ie}}(n_{\mathrm{ie}}-1).....(n_{\mathrm{ie}}-q+1)\rangle_{\mathrm{h}}, \tag{3.3}$$

where the order of the moment q takes positive integer values $\geq$2 and $\langle\ldots\rangle_h$ defines average over all bins and is referred to as the horizontal average over an

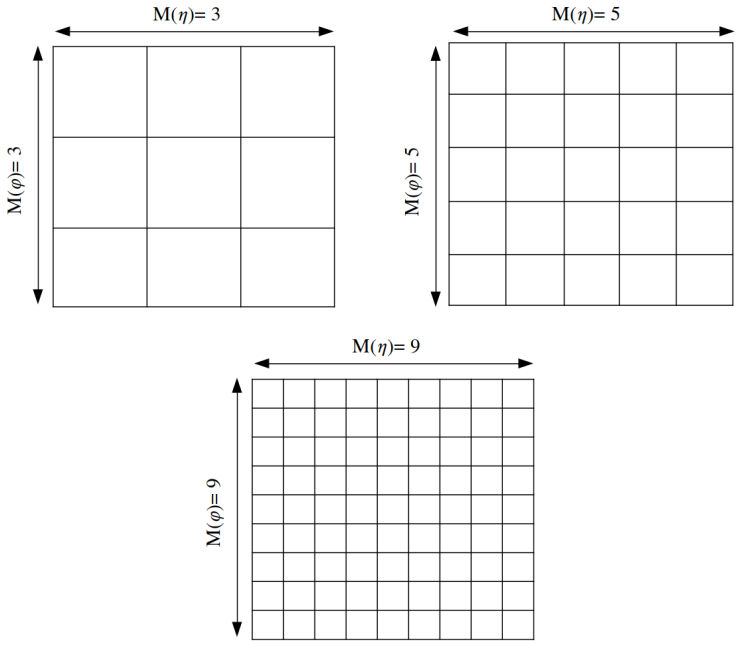

Figure 3.2. Pictorial representation of binning in the two-dimensional (η, φ) phase space. Different cases with number of bins M = 3, 5, 9 along each direction are shown to depict the increasing resolution of the phase space. As M increases, the size of bins decreases.

event, following the practice of treating different events as being vertically stacked. In general, for M^{d} bins in a d-dimensional phase space Eq. 3.2 can be written as

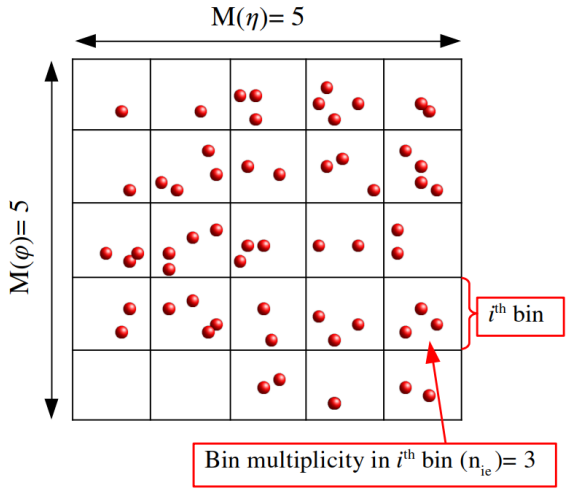

Figure 3.3. Pictorial representation of mapping of particles in an event onto the (η, φ) phase space partitioned into 25 bins (M = 5).

$$f_{\mathrm{q}}^{e}(M) = \frac{1}{M^{\mathrm{d}}} \sum_{i=1}^{M^{\mathrm{d}}} n_{\mathrm{ie}}(n_{\mathrm{ie}} - 1) \ldots (n_{\mathrm{ie}} - q + 1). \tag{3.4}$$

For an event, the normalized factorial moment, which is called normalized event factorial moment of order 'q' for M^d bins, is

$$F_{\mathrm{q}}^{e}(M) = \frac{f_{\mathrm{q}}^{e}(M)}{[f_{1}^{e}(M)]^{\mathrm{q}}}, \tag{3.5}$$

where,

$$f_{1}^{e}(M) = \frac{1}{M^{\mathrm{d}}} \sum_{i=1}^{M^{\mathrm{d}}} n_{\mathrm{ie}}. \tag{3.6}$$

Then, for a sample with total N events, the q^{th} order normalized factorial moments for M^{d} number of bins is defined as;

$$F_{\mathrm{q}}(M) = \frac{\frac{1}{N}\sum_{e=1}^{N}\frac{1}{M^{\mathrm{d}}}\sum_{i=1}^{M^{\mathrm{d}}} n_{ie}(n_{ie}-1)\ldots(n_{ie}-q+1)}{\left(\frac{1}{N}\sum_{e=1}^{N}\frac{1}{M^{\mathrm{d}}}\sum_{i=1}^{M^{\mathrm{d}}} n_{ie}\right)^{q}}. \tag{3.7}$$

For two-dimensional case (d = 2) above equation can be written as

$$F_{\mathrm{q}}(M) = \frac{\frac{1}{N}\sum_{e=1}^{N}\frac{1}{M^{2}}\sum_{i=1}^{M^{2}} n_{ie}(n_{ie}-1)\ldots(n_{ie}-q+1)}{\left(\frac{1}{N}\sum_{e=1}^{N}\frac{1}{M^{2}}\sum_{i=1}^{M^{2}} n_{ie}\right)^{q}} \tag{3.8}$$

In short this equation is

$$F_{\mathrm{q}}(M) = \frac{\langle f_{\mathrm{q}}^{e}(M)\rangle_{v}}{(\langle f_{1}^{e}(M)\rangle_{v})^{q}} \tag{3.9}$$

where $\langle\ldots\rangle_{v}$ is averaging over events. The factorial moments so defined are vertically averaged horizontal factorial moments and are termed here as normalized factorial moments (NFM).

Analysis using intermittency methodology proposed in Refs. [79, 131] led to revival of correlation studies in the high-energy physics field with aim to get signal of QGP. R.C. Hwa with C.B. Yang in Ref. [72] have proposed to look at particle density fluctuations in the LHC data, for it has high charged particle density per pseudorapidity bin [147], using event-by-event intermittency like analysis in the low p_{T} range. With model (Successive Contraction and Randomization (SCR)

model) based studies it is shown that the scaling behaviour of NFM are suitable measures to differentiate the fluctuations of different critical nature, (Appendix C).

3.2 Scaling behaviour

Scaling is a concept that allows for the simplification and understanding of complex systems by examining how physical quantities change with size or scale. Many natural phenomena exhibit scaling behaviours described by power laws, where the relationship between quantities follow a specific exponent. Scaling studies are important for understanding how systems behave across different sizes, from microscopic to macroscopic levels. Scale invariance is a property of scaling where a system or pattern remains unchanged even when its size is altered. A scale-invariant system means that, scaling it up or down does not change its fundamental characteristics or behaviour. For example, a fractal pattern looks similar whether you zoom in or out, demonstrating scale invariance as shown in Fig. 3.4. The scaling behaviours of the NFM studied in this work are discussed below.

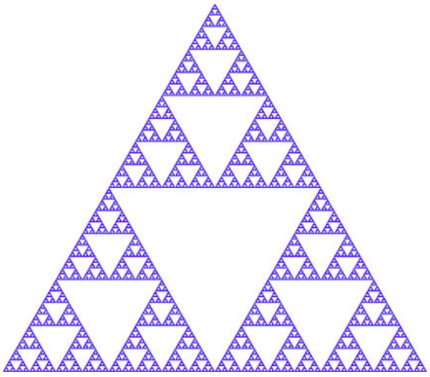

Figure 3.4. Pictorial representation of fractal patterns (Sierpinski triangle) [148].

3.2.1 M-scaling

Physical basis of studying fluctuations in the spatial patterns is that the critical systems exhibit patches of all sizes without a characteristic scale [145]. Factorial moments are calculated to look for scaling properties in the fluctuations of spatial

configurations. The behaviour of normalized factorial moments ($F_{\rm q}$) can be studied as a function of number of bins (M). Since the number of bins define the resolution of the phase space, this may be termed as resolution scaling behaviour. For δ being the size of a bin in the phase space, the power-law behaviour of q^{th} order scaled factorial moments with the resolution defined [79] as

$$F_{\rm q}(\delta) \propto (\delta^d)^{-\phi_{\rm q}}, \tag{3.10}$$

is termed as *resolution scaling*. In terms of number of bins, since $1/\delta^d \propto M^d$, Eq. 3.10 can be put as

$$F_{\rm q}(M) \propto (M^d)^{\phi_{\rm q}}. \tag{3.11}$$

As M denotes number of bins, this power-law behaviour of $F_{\rm q}$ with M may simply be termed as *M-scaling* and phenomenon is known as *intermittency* [72, 81]. The systems showing intermittency are known as intermittent systems. In case $F_{\rm q}$ is independent of M it signifies there are no bin-to-bin fluctuations. For presence of any dynamical behaviour over and above the smooth Poissonian behaviour $F_{\rm q} > 1$ and follows positive dependence on M as M $\to \infty$. ϕ_q in Eq. 3.11 are called intermittency indices and define the strength of an intermittent structure of the distributions. Modelling with large density fluctuations as in critical systems [72], $F_{\rm q}(M)$ moments show power-law behaviour with increasing M whereas in the other extreme case of non-critical modelling no power-law is observed. With this sensitivity of the observable the work here aims to study charged particle multiplicity fluctuations to understand the dynamics of multiparticle production at LHC energies.

3.2.2 F-scaling and the scaling exponent (ν)

In case there are no fluctuations in the number of particles from bin-to-bin, the NFM ($F_{\rm q}$) do not show any dependence on M i.e., M-scaling behaviour is said to be absent. However, it is still possible that $F_{\rm q}(M)$ for $q > 2$ have dependence on

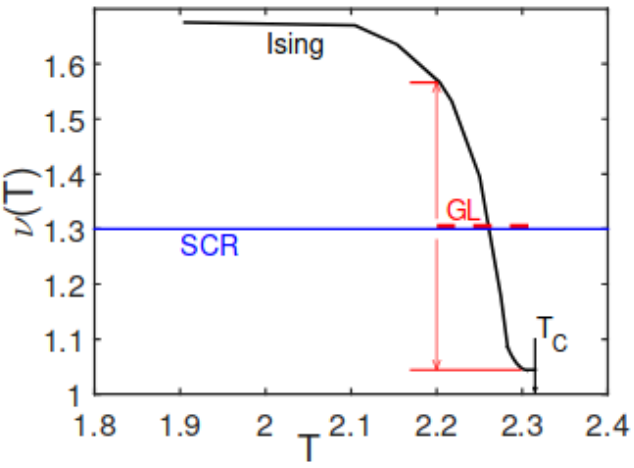

Figure 3.5. Values of $\nu(T)$ from three models: (a) Ising (solid/black), (b) Ginzburg–Landau (dashed/red), (c) SCR (horizontal/blue). In Ising model, the critical temperature is $T_c = 2.315$ in Ising units. The Ginzburg–Landau value is obtained by the average of the Ising values between $T = 2.2$ and T_c and given by dashed red line [146].

the second order factorial moment $F_2(M)$ as

$$F_{\mathrm{q}}(M) \propto F_2(M)^{\beta_{\mathrm{q}}}. \tag{3.12}$$

This *order scaling* termed as *F-scaling* was first reported by Hwa and Nazirov in [149] where β_{q}, the exponents are observed to be related to the order of the moment q through an exponent ν as [72, 146, 149, 150]

$$\beta_{\mathrm{q}} = (q-1)^{\nu}. \tag{3.13}$$

Exponent ν is a dimensionless exponent called as the *scaling exponent*. While the scaling properties of fluctuations in geometrical configurations of the produced particles is studied, ν is proposed as a specific measure to quantify the scaling properties [149]. Formalism for second-order phase transition in the Ginzburg-Landau (GL) theory supports F-scaling with an average value of the scaling exponent as 1.304 [151]. ν is a universal quantity and is independent of the underlying dimension or the parameters of the system.

Simulation of critical behaviour with second-order type phase transition in the two-dimensional Ising model, analysed using NFM, shows scaling behaviour

of $F_q(M)$ which is in agreement with Eq. 3.12 [152]. In the Ising model, where temperature is a parameter that can be controlled, ν is observed to have temperature dependence with an average value of 1.3 in line with the value from the GL formalism for the second order phase transition as is shown in Fig. 3.5 (from Ref. [146]). Possible characteristics responsible for the phase transition of the quark system into hadrons are implemented in the Successive Contraction and Randomization (SCR) model. This model has global effects of confinement forces with thermal randomization, opposing the ordered collective motion [72, 146, 153], so as to have time evolution of average density and fluctuations. The curve $\nu(T)$ (Fig 3.5) as function of temperature (T) provides an interpretation of the scaling exponent, where ν that gives an average value is close to the universal value of 1.304 from GL theory [149]. As quick summary, the values of scaling exponent (ν) obtained from some of the theoretical, experimental and model based studies are tabulated in Table 3.1. So far the universal value of $\nu = 1.304$ is experimentally established by the photon production at threshold of lasing which is describable as a second-order phase transition [154].

Table 3.1. Scaling exponents from various theoretical and model based studies.

Theory/Model	ν
Without Kinetic Term in GL potential [149]	1.304
With Kinetic Term in GL potential [151]	1.316 ± 0.012
SCR Model [146]	1.41
AMPT Model at $\sqrt{s_{\rm NN}} = 2.76$ TeV [155]	1.79 ± 0.10
EPOS3 Model at $\sqrt{s_{\rm NN}} = 2.76$ TeV [156]	1.80 ± 0.16
UrQMD model with pp collisions at $\sqrt{s_{\rm NN}} = 13$ TeV [157]	1.743 ± 0.016
AMPT model with Au-Au collisions at $\sqrt{s_{\rm NN}} = 200$ TeV [158]	1.86 ± 0.07
EMU01 and KLM Collaboration [137, 159]	1.55 ± 0.12
NA22 Collaboration for pp collisions at $\sqrt{s_{\rm NN}} = 13$ TeV [160]	1.49

3.3 Fractal parameters

Intermittency is a phenomenon exhibited by rare events with large multiplicity fluctuations in small bins. Observing intermittency or power law growth of $F_q(M)$ with M at high values of M (when the bin sizes become vanishingly small) im-

plies the presence of large density fluctuations that are independent of the scale and hence are self-similar. Fluctuations that exhibit self-similarity are fractal in nature [161]. On magnifying a small portion of a structure, if it shows the same complexity as that of the entire system, then it is called *fractal*. This property of fractal objects is called "scale symmetry"that is associated with systems which have characteristics of self-similarity.

When the underlying space is of two or higher dimension, based on the scales used, there are two kinds of fractals; *self-similar* and *self-affine*. For an object which is fractal there is a measure of the object which depends on the resolution of the measurement in a power-law fashion. On partitioning the phase space equally in all directions if power-law of observable holds then the fractal is called self-similar whereas in case power-law holds when different partitioning is done in different directions it is called self-affine fractal. Self-similar behaviour or fractal corresponds to isotropic multiplicity fluctuations while self-affine corresponds to the non-isotropic fluctuations. Fractals are complex structures and their presence in the particle distributions suggests underlying correlations and complex dynamics [162].

Concept of fractals is applied to understand the scaling laws and self-similarity in heavy-ion collisions. As fractal systems are structures or patterns that display self-similarity across different scales that means that the same pattern repeats itself at various levels of magnification. Fractals can be observed in nature, such as in the shapes of coastlines, mountains, clouds, and trees, as well as in mathematical constructs. Fractal system can also be classified as *monofractals* and *multifractals* [161, 163, 164]. A monofractal system is a type of fractal where a single scaling property is consistent throughout the entire structure. Monofractal systems are described by one fractal dimension, which is a measure of their complexity. In contrast, multifractal systems are more complex than monofractals. *In multifractal systems, different parts of the structure can follow different scaling properties.* This means that the degree of complexity can vary in different regions of the system. Multifractal systems require more than one fractal dimension to describe their scaling behaviour.

3.3.1 Fractal dimension (D_{q})

Intermittency is intimately related to the fractal geometry of the underlying distribution [81]. One of the basic properties of the fractals that describe the scaling behaviour is the generalized anomalous fractal dimension D_{q} introduced by Hentschel and Procaccia [165], which is used to describe the size of the fractal sets and is related to the intermittency index ϕ_{q} [166] as

$$D_{\mathrm{q}} = D_{\mathrm{T}} - d_{\mathrm{q}}, \quad d_{\mathrm{q}} = \frac{\phi_{\mathrm{q}}}{q-1}, \tag{3.14}$$

where q is the order of the fractal dimension, D_T is the topological dimension (its value is 1 for one dimensional analysis and 2 for two dimensional analysis). D_{q} and d_{q} are the generalized fractal (R'enyi)) dimensions and co-dimensions [167, 168]. The dependence of D_{q} on the moment order parameter q provides information about the nature of the particle production. D_{q} being independent of q suggests a *monofractal* system. On the other hand, a decrease of D_{q} with increasing q indicates a *multifractal* system, where fluctuations exhibit different scaling behaviours for different scales or regions.

In Ref. [166], to explore the impact of multiple fractal distributions on the intermittency signal, a simple multifractal one-parameter model is employed. This model allows for the simulation of random superpositions of fractal distributions within a single event. *The key observation from this study is the weakening of intermittency as the number of fractal sources within a single event increases.* In other words, the more fractal sources that are combined, the less pronounced the intermittency signal becomes as is shown in Fig. 3.6(left) [166]. The theoretical curve for the generalized dimensions D_i, with i being the order of fractal dimension is shown as a full line. This curve is compared with the measurements taken from 1000 simulated events, each having a total multiplicity of 9 particles. The intermittency signal and hence D_{q} dependence on q decreases when number of fractal sources combined into a single event increases from 2 to 10. Data from various experiments, like e^+e^- [133], two-jet events [169] for central collisions, show varying intermittency levels, with stronger signals in simpler events and weaker effects in more complex collisions. A consistent decrease in intermittency is also

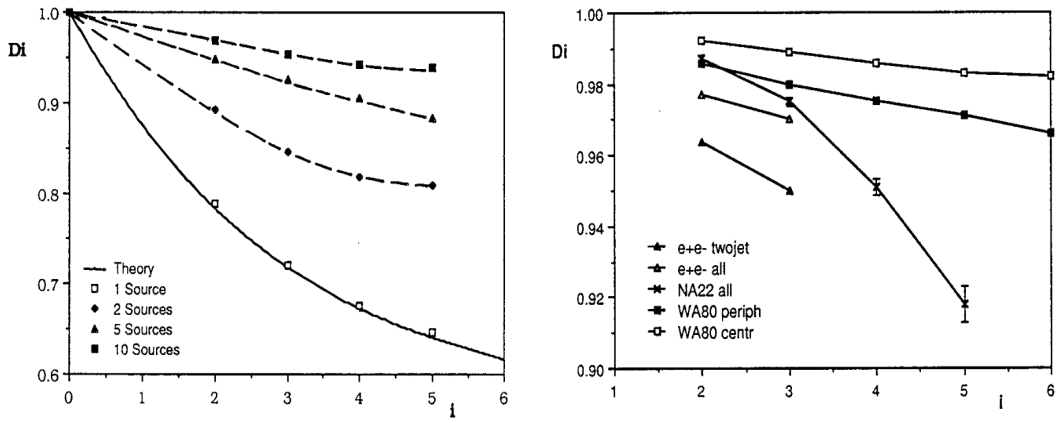

Figure 3.6. Generalized fractal dimension D_i as a function of i for (Left) different combination of fractal sources and (Right) various low energy experiments [166]. *Here i is the order of the moment.*

observed in reaction types where the occurrence of multiple subprocesses or less independent processes is anticipated (Fig. 3.6(right)). As reported in Ref. [166], within experiments, at a fixed energy, *intermittency strength is expected to decline with rising multiplicity*, reflecting the intricate dynamics of particle interactions.

3.3.2 Coefficient λ_{q}

Multifractals (MF) are the complex systems that exhibit different scaling behaviours at various length scales. The structure of different phases of self-similar multiparticle complex systems in particle collisions have been investigated using multifractal analysis [170, 171]. In simpler terms, this analysis technique helps in understanding patterns that repeat themselves in similar ways but with variations across different levels of magnification. MF help to characterize the distribution of particles across different spatial or temporal scales by a coefficient, λ_{q}, first proposed by Bialas and Zalewski [172]. It is suggested that the intermittent behaviour observed in the particles produced after ultra-relativistic collisions can be linked to a non-thermal phase transition. This transition might be an underlying cause for the occurrence of the anomalous events [173, 174]. The coefficient λ_{q} is related to intermittency index ϕ_{q} through a relationship:

$$\lambda_{\mathrm{q}} = \frac{\phi_{\mathrm{q}} + 1}{q}. \tag{3.15}$$

For a system undergoing a non-thermal phase transition, λ_q will have a minimum value at some critical value of $q = q_c$ [172] as is shown in Fig. 3.7(a). The value q_c need not be an integer, and its significance lies in demarcating different behaviours of the system. In the region where $q < q_c$, the system is characterized by numerous fluctuations with not more than q_c particles per bin. These fluctuations might have a smaller impact on the overall behaviour of the system. Conversely, in the region where $q > q_c$, rarely occurring large fluctuations may dominate. These large fluctuations can have significant consequences for the system, leading to the anomalous events. This scenario resembles a combination of a "liquid" composed of many relatively small fluctuations and a "dust" consisting of a few densely packed "grains". The coexistence of these phases is evident, where the dominating liquid phase is observed when probed by a moment of the order $q < q_c$, while the dust phase becomes apparent for $q > q_c$. Moments of higher order are insensitive to small fluctuations, hence highlighting the dust phase.

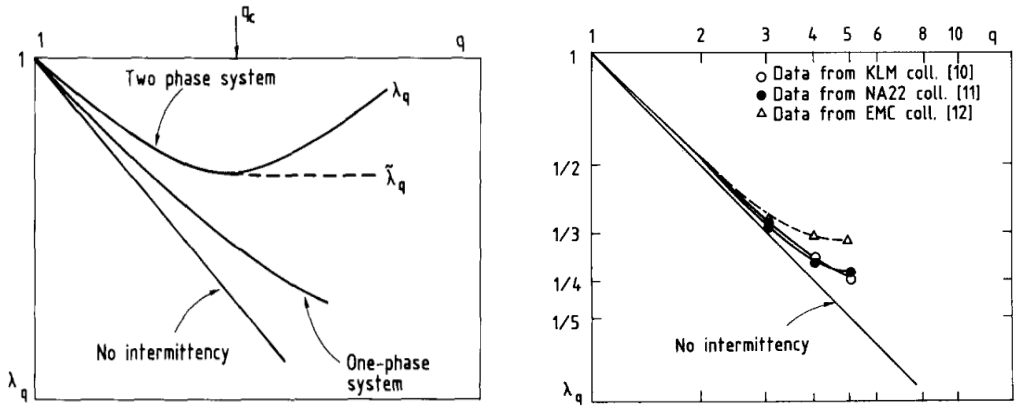

(a) (b)

Figure 3.7. (a) Dependence of coefficient λ_q on q for various conditions of the thermal systems (b) λ_q vs q from different experiments [172].

Figure 3.7(b) presents the behaviour of λ_q as a function of q for a few experimental studies performed at low energies as given in Ref. [172]. It can be observed that the data given in the figure are not yet sufficient to conclusively determine if λ_q indeed has a minimum at a certain q value. Further experimental validation and interpretation of these phases could provide valuable insights into the underlying theory of strong interactions at high energies such as at LHC.

3.4 Detector effect study

In case there is perfect reconstruction of tracks, with all required track cuts, etc., the tracking efficiency should be 1. However, in general the detectors used in the experiments have certain limitations. Various detector effects may distort the measured observables. Because of the stochastic nature of particle interactions with the detector medium, not all particles passing through the detector will leave signal. This affects detector efficiencies and hence measurements are not the true values which come from the collision. To measure detector efficiencies, Monte-Carlo simulation studies are performed. These efficiencies are then used to correct the observables. In Monte Carlo simulation, particles generated(true) using an event generator are passed through the detector geometry and electronic read-out. Track reconstruction routines same as that are used in the real data reconstruction are employed which replicates the response of the actual detector during the collisions. Next, the reconstructed events from the Monte Carlo are compared with the true Monte Carlo events that gives an ideal case where no detector response is present. By calculating the ratio of the reconstructed to the true Monte Carlo events, one can determine tracking efficiencies of the detector. Using tracking efficiencies, the true values of the observables can be obtained. The procedure to correct NFM for efficiencies is discussed below.

3.4.1 Tracking Efficiency Corrections

The tracking efficiency is defined as the ratio of the number of physical primary reconstructed tracks (tracks recorded by detector) to the physical primary generated tracks

$$\epsilon = \frac{No.\ of\ Reconstructed\ tracks}{No.\ of\ Generated\ tracks} \tag{3.16}$$

For a bin with bin multiplicity n_{ie} in the i^{th} bin and e^{th} event, the factorial moment of order q defined as in Eq. 3.1, the reconstructed and true values are related as

$$f_{\mathrm{q}}^{true}(n_{\mathrm{ie}}) = \frac{f_{\mathrm{q}}^{rec}(n_{\mathrm{ie}})}{\epsilon_{\mathrm{i}}^{q}} \tag{3.17}$$

where ϵ_i is the efficiency in the i^{th} bin. Then for an event, the corrected factorial moments for M^2 number of bins, for analysis in two dimensions is given as

$$f_{\rm q}^{e\_corr}(M) = \frac{1}{M^2}\sum_{i=1}^{M^2}\frac{f_{\rm q}^{e\_rec}(n_{\rm ie})}{(\epsilon_{\rm i})^q} = \left\langle \frac{f_{\rm q}^{e\_rec}(n_{\rm ie})}{(\epsilon_{\rm i})^q} \right\rangle_h \tag{3.18}$$

$\langle \ldots \rangle_h \implies$ represents averaging over total number of bins $M^2 = (M \times M)$ bins. As Eq. 3.6, for $q = 1$, this equation becomes

$$f_1^{e\_corr}(M) = \frac{1}{M^2}\sum_{i=1}^{M^2}\frac{f_1^{e\_rec}(n_{\rm ie})}{\epsilon_{\rm i}} = \frac{1}{M^2}\sum_{i=1}^{M^2}\frac{n_{ie}^{e\_rec}}{\epsilon_{\rm i}} = \left\langle \frac{n_{\rm ie}^{e\_rec}}{\epsilon_{\rm i}} \right\rangle_h \tag{3.19}$$

Thus from Eq. 3.8, the q^{th} order normalized factorial moments for N events and M^2 number of bins, corrected for efficiencies is defined as

$$F_{\rm q}^{corr}(M) = \frac{\frac{1}{N}\sum_{e=1}^{N}\left\langle \frac{f_{\rm q}^{e\_rec}(n_{\rm ie})}{(\epsilon_{\rm i})^q} \right\rangle_h}{\left(\frac{1}{N}\sum_{e=1}^{N}\left\langle \frac{n_{ie}^{e\_rec}}{\epsilon_{\rm i}} \right\rangle_h\right)^q} \tag{3.20}$$

For the model based studies if $F_{\rm q}^{rec}(M)$ and $F_{\rm q}^{gen}(M)$ represent the NFM for the reconstructed and generated events then for closure, it is required that $F_{\rm q}^{rec}(M) \approx F_{\rm q}^{gen}(M)$ or $F_{\rm q}^{true}(M)$. Generated events are also termed as true events. If this is not the case then this efficiency corrections procedure that is Eq. 3.20 should be used to achieve the best possible closure so that $F_{\rm q}^{corr}(M) \approx F_{\rm q}^{true}(M)$.

3.5 Statistical uncertainties

Statistical uncertainties observed in the measured results, arise due to the inherent stochastic nature of collisions at high energies, fluctuations within the measurement processes etc. It is common practice to calculate statistical uncertainties for fluctuation measures using either the error propagation technique or the sub-sampling method. In sub-sampling method, to determine statistical uncertainties, total events are divided into equal size N independent subsamples. Calculations are made for each subsample. The standard deviation of the observable obtained

for these N subsamples, then define statistical uncertainty

$$\sigma_{\langle F_q \rangle} = \frac{\sigma}{\sqrt{N}} \tag{3.21}$$

where

$$\langle F_q \rangle = \frac{1}{N} \sum (F_q)_N, \tag{3.22}$$

and

$$\sigma = \sqrt{\frac{\sum((F_q) - \langle F_q \rangle)^2}{N-1}} \tag{3.23}$$

The statistical uncertainties on the normalized factorial moments are estimated using sub-sampling method. Error propagation method, as described in [175], has been observed to give the same values of statistical uncertainties.

Observations and results from Monte Carlo model studies and experimental data are discussed in next chapters.

Chapter 4

Toy model study

Event generators are widely used in the field of heavy-ion collisions to simulate experimental conditions and to predict outcomes based on known physics. These models are also widely used by theoreticians to test and upgrade existing models and to develop new models. Since the mechanisms underlying multiparticle production in heavy-ion collisions is not yet completely understood, numerous approaches have been developed to know and to learn about these. Towards developing the knowledge about various characteristics of the system created in these collisions, information on the baseline behaviour is significant. For that, the normalized factorial moments, in the contours of intermittency methodology, have been investigated using Toy model events.

4.1 Toy model: Event generation

To understand the intricate processes of multiparticle production in heavy-ion collisions, the data recorded by the ALICE experimental setup at LHC is investigated in this thesis. The analysis proposed in Ref. [72] for LHC data, in line with intermittency analysis first proposed in [79], is performed as discussed in chapter 3. To get the baseline behaviour, toy model events are generated with constraints of charged particle experimental data. The ALICE experiment has central barrel detector system comprising of the Time Projection Chamber (TPC), Inner Tracking System (ITS), and Time-Of-Flight (TOF) detectors, which collectively measure charged particles within a common angular phase space defined by pseudorapidity of $|\eta| \leq 0.8$ and full azimuthal coverage $0 \leq \varphi \leq 2\pi$ [90, 176]. Toy model events are generated using the multiplicity constraints derived from ALICE data

for Pb−Pb collisions at $\sqrt{s_{\rm NN}} = 2.76$ TeV for the charged particles recorded using TPC and ITS detectors in ALICE. Event multiplicity for the toy model event is obtained taking Gaussian distribution function, with mean and standard deviation value from the experimental charged particle multiplicity distribution in the transverse momentum interval $0.4 \leq p_{\rm T} \leq 0.6$ GeV/c, in gRandom3() member function of the ROOT5 [121]. Tracks per event are generated using uniform distribution function, in the pseudorapidity window $|\eta| \leq 0.8$ and azimuthal angle $0 \leq \varphi \leq 2\pi$ with gRandom3() member function of ROOT5, taking system clock as seed. Three more samples with 500K events per sample are generated using experimental charged particle multiplicity distributions from $0.4 \leq p_{\rm T} \leq 1.0$ GeV/c, $0.4 \leq p_{\rm T} \leq 2.0$ GeV/c and $0.2 \leq p_{\rm T} \leq 5.0$ GeV/c transverse momentum bins. The multiplicity distributions for the four toy model event samples are given in Fig. 4.1 and their η and φ distributions are given in Fig. 4.2. Observations and results from the analysis of Toy model events, as described in chapter 3 with $\langle N \rangle = 952$ corresponding to $p_{\rm T}$ bin $0.4 \leq p_{\rm T} \leq 1.0$ GeV/c, are discussed in the following sections. However, in section 4.2.2 results on dependence of observable $F_{\rm q}(M)$ on average multiplicity are given for all four event samples.

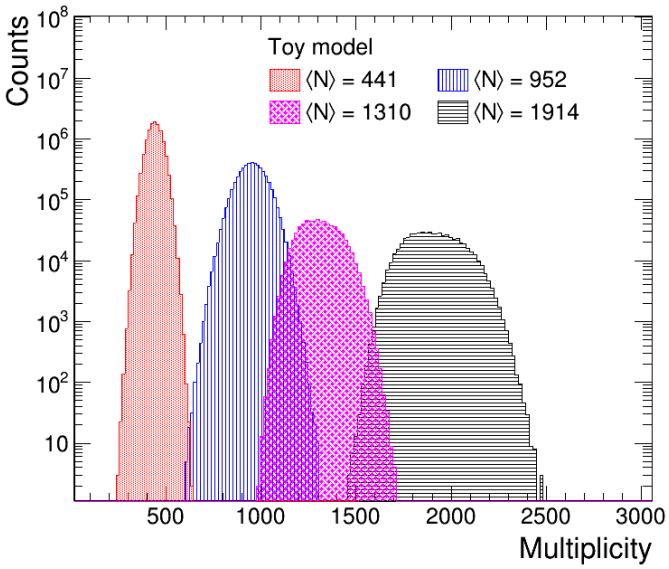

Figure 4.1. Multiplicity distributions for the four samples of Toy model events with average multiplicity and standard deviation corresponding to different ALICE data $p_{\rm T}$ bins.

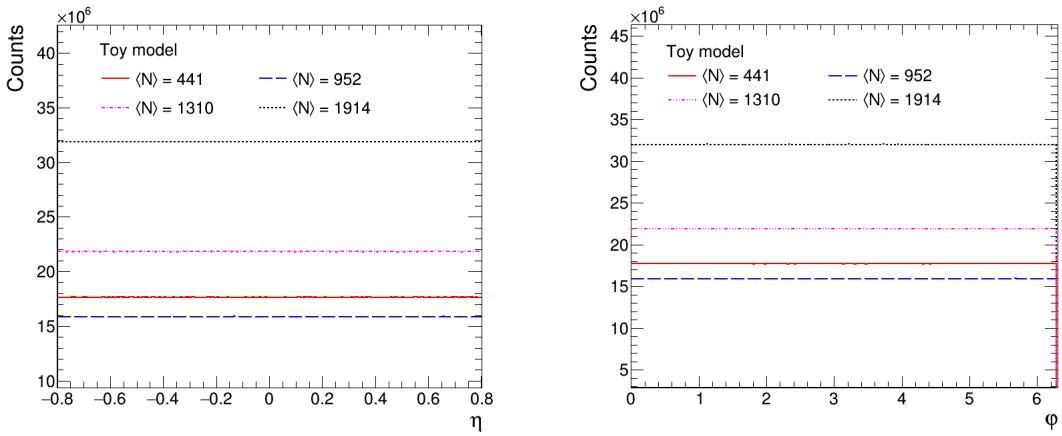

Figure 4.2. Pseudorapidity and azimuthal angle distributions for the four samples of Toy model events. Uniform distribution function is used to generate tracks with $|\eta| \leq 0.8$ and $0 \leq \varphi \leq 2\pi$.

4.2 Observations

Two-dimensional intermittency analysis as detailed in chapter 3, is performed on the Toy model events. The (η, φ) phase space of each event is partitioned into an M×M grid, resulting into a total of M^2 bins. The number of bins along each axis range from a minimum value of 6 to a maximum of 105, in the intervals of 3. For each M, normalized factorial moments (NFM) for q = 2 to 5 are determined as defined in Eq. 3.8.

4.2.1 M-scaling

The NFM ($F_q(M)$) determined from Toy model events are studied for their dependence on the resolution, that is on number of bins, M^2, termed as M-scaling. The log-log plot of F_q versus M^2 is shown in Fig. 4.3 for the event sample with $\langle N \rangle = 952$. For all q values i.e., 2, 3, 4, and 5, F_q do not show power-law increase with M^2. Absence of a notable increase in $\ln F_q$ with $\ln M^2$ in the Toy model events suggests that the particle generation is not self-similar. However, $F_5 > F_4 > F_3 > F_2$ for all values of M. With no density fluctuations, a negligible dependence of $F_q(M)$ on the number of bins M^2 in the Toy model events is observed at very high M and high q. These events simulated with uniform distribution function give baseline behaviour of the NFM and show absence of

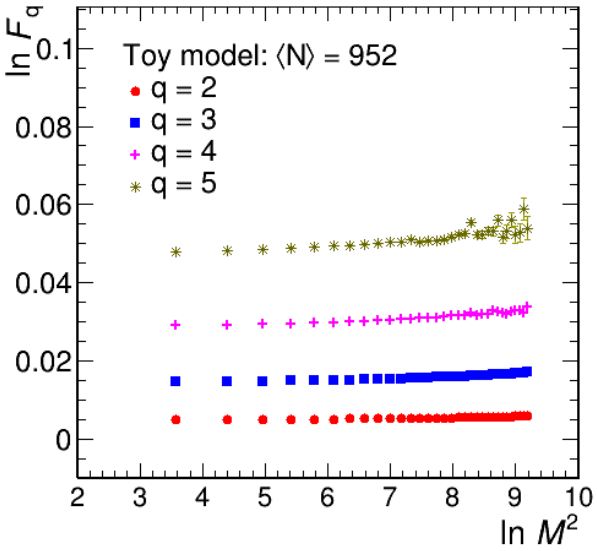

Figure 4.3. log-log plot of $F_{\rm q}(M)$ vs M^2 for q = 2, 3, 4 and 5.

intermittency. To evaluate the sensitivity of these moments to the fluctuations in the spatial configurations, an exercise as described below is performed.

Fluctuations are added with hand in each event by populating a few bins of the phase space, partitioned in M^2 bins, with more tracks so as to introduce density fluctuations. The event sample so obtained is termed as *modified Toy model events*. Fluctuations are added into each toy event by following two different methods. In the first method, referred to as Method 1, the multiplicity of the toy event remains unchanged when tracks are added. For each track added in a bin, a track is removed from some other bin, so that the total event multiplicity is unaffected. In this way, number of tracks, around five percent of the event multiplicity, are added to each event and the same number of tracks are removed. In the second method, termed here as Method 2, tracks are added to the event without removing any track, and hence there is an increase in the event multiplicity. With both these methods, tracks are included in certain regions of the phase space, where track density in certain bins increases compared to the neighbouring bins. This introduces density fluctuations in the phase space. As an example Fig.4.4 shows the (η, φ) lego plot of a Toy model event in the left panel, where the phase-space is divided into 40×40 bins. The right panel shows the same event after fluctuations are added with hand using Method 1. These figures give visualization of how bin multiplicity in (η, φ) phase space of an event varies after adding fluctuations with

hand.

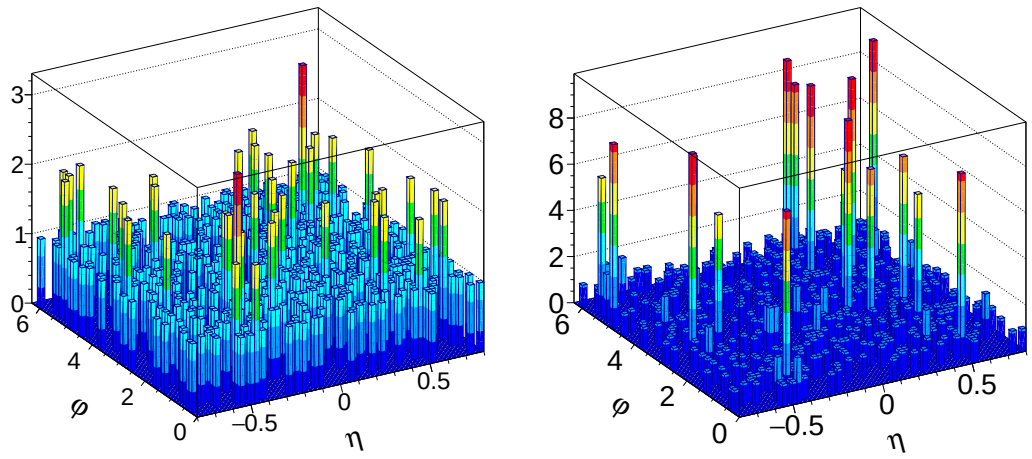

Figure 4.4. Lego plot of particles distributed in the (η, φ) phase space of a Toy event(left) and same event with added fluctuations using Method 1(right).

Normalized factorial moments are determined for the modified toy model events obtained using Method 1 and Method 2, for q = 2, 3, 4 and 5. The ln $F_q(M)$ vs ln M^2 plot is shown in Fig. 4.5. It is observed that $F_q(M)$ shows a strong power law growth with M^2 and thus M-scaling is observed for all q with $F_{q+1} > F_q$. Infact multiple linear regions are also observed. Comparative plots of $F_q(M)$ vs M^2 with and without added fluctuations in the toy events, for all orders of q are given in Fig. 4.6. NFM values from the modified Toy model events are higher than that from Toy model events. There is qualitative and quantitaive differences between the two which increases as M increases. NFM from Method 1 and Method 2 show a small quantitative difference in the $F_{\rm q}(M)$ values but have similar qualitative behaviour. These results demonstrate that NFMs are highly responsive to bin-to-bin multiplicity fluctuations, and thus are a sensitive and suitable measure for quantifying such fluctuations. Further this study shows that dynamics which results into density fluctuations in the phase space will lead to the power-law scaling behaviour.

4.2.2 F-scaling and scaling exponent (ν)

In the above section it is observed that $F_q(M) \neq 1$, that is ln $F_q(M)$ values are > 0 and $F_{q+1} > F_q$. At high q, a very weak dependence of F_q from toy events

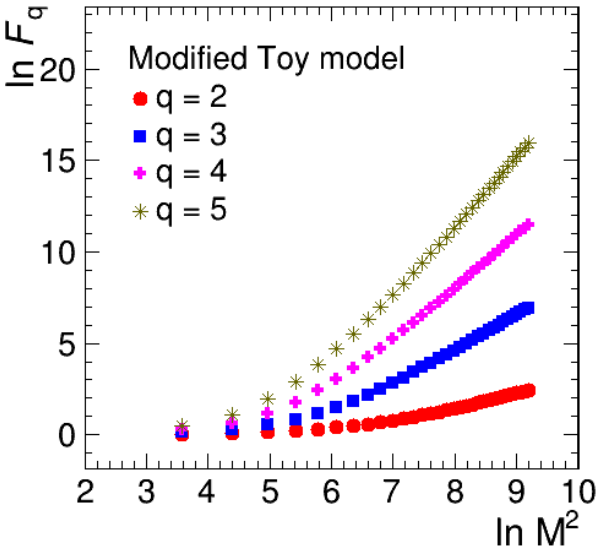

Figure 4.5. log-log plot of $F_{\rm q}(M)$ vs M^2 (M-scaling) for q = 2, 3, 4 and 5 of a modified Toy model event sample with $\langle N \rangle = 952$ (Method 1).

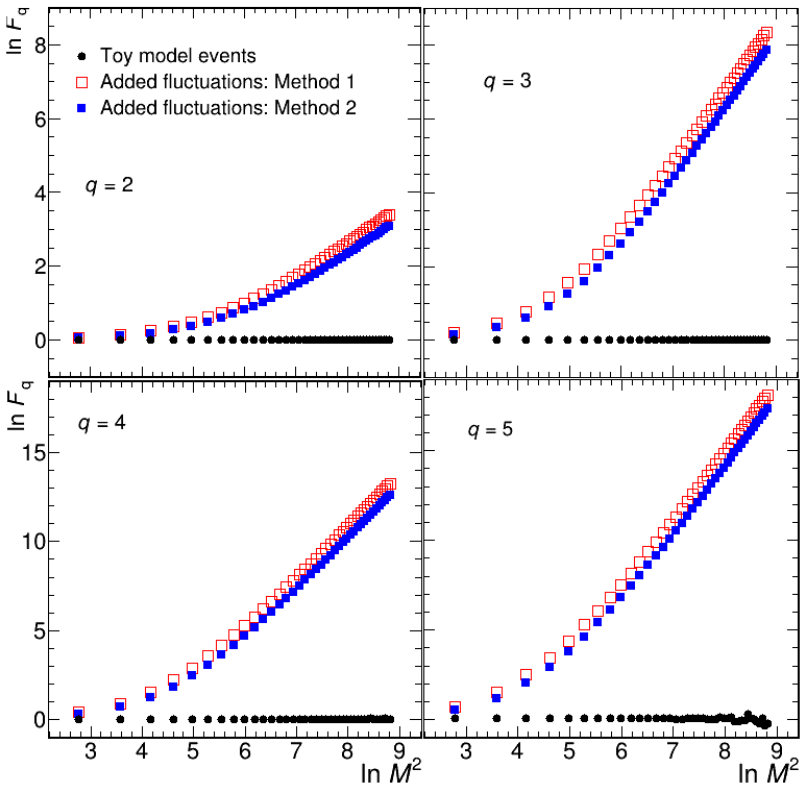

Figure 4.6. ln $F_{\rm q}(M)$ versus ln M^2 for Toy model events, and modified toy model events.

on the resolution i.e., number of bins, is observed (Fig. 4.3). As discussed in chapter 3, the other scaling which is of interest is the F-scaling or order scaling that is independent of the M-scaling. If for higher order $q(q > 2)$ $F_q(M)$ shows

any dependence on $F_2(M)$ it features F-scaling. For toy model events, ln $F_q(M)$ vs ln $F_2(M)$ is shown in Fig. 4.7(a). A weak F-scaling behaviour in toy model events is observed. However, in the modified toy model events with added fluctuations (Fig. 4.7(b)), a good F-scaling is observed, indicating a robust linear relationship of $F_{\rm q}$ with F_2. Fig. 4.7(b) shows data points corresponding to high M region with high resolution only.

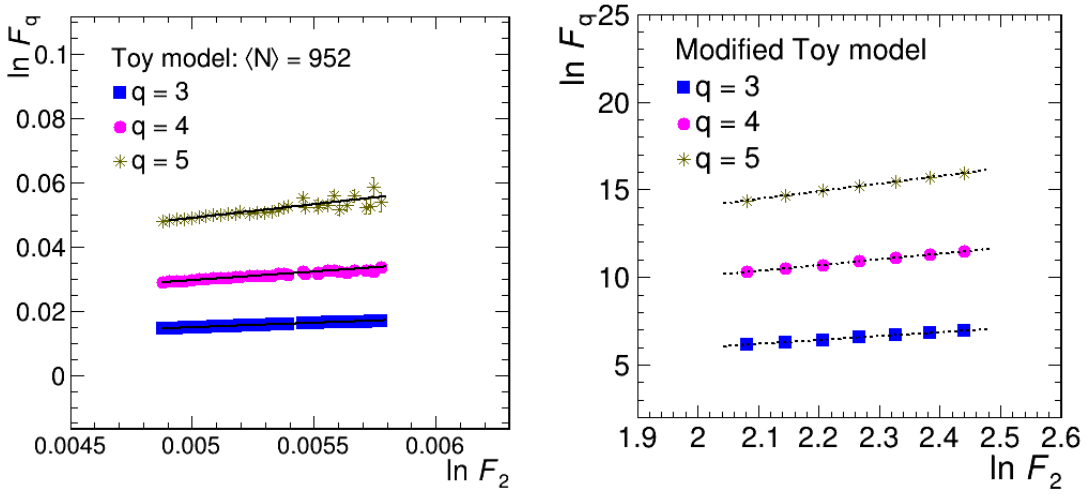

(a) (b)

Figure 4.7. log-log plot of $F_{\rm q}(M)$ vs F_2 (F–scaling) for q = 3, 4 and 5 from (a) Toy model events with $\langle N \rangle$ = 952 and (b) modified toy model events (Method 1).

Performing line fits to the F-scaling plots, β_q values are obtained. A dimensionless scaling exponent (ν) as defined in the relation (3.13) is obtained which is independent of the system parameters and signifies the dynamics of the system. By performing line fitting on $ln\beta_{\rm q}$ versus $ln(q-1)$ plot (Fig. 4.8), the scaling exponent for the Toy model events at higher M region is found to be 1.603 ± 0.016 . For the modified Toy model events, where the fluctuations are added with hand, the value of ν for high M region is obtained to be 0.998 ± 0.004 (Fig. 4.8). *A significant decrease in the scaling exponent is seen from the baseline value when fluctuations are introduced in the spatial configurations.*

Multiplicity dependence of scaling exponent

In high-energy physics experiments, multiplicity increases with an increase in the collision energy. It is thus interesting to explore the dependence of scaling ex-

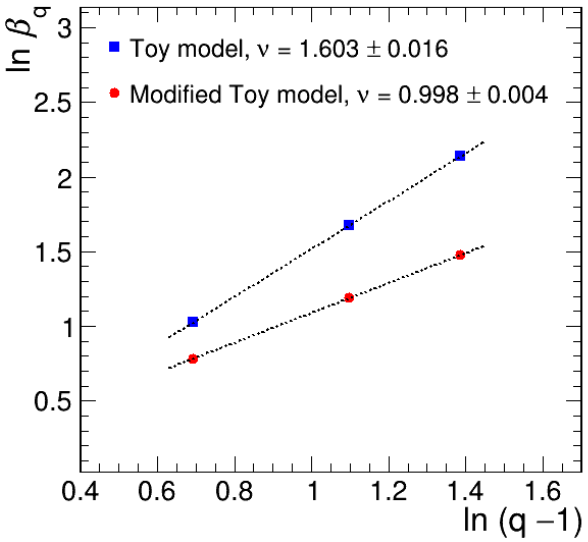

Figure 4.8. Scaling exponent (ν) obtained from linear fit to $ln\beta_{\mathrm{q}}$ vs $ln(q-1)$ plot for the Toy model events and modified Toy model events.

ponent on multiplicity, and thus collision energy. This is investigated with event samples having multiplicity distributions with mean value ranging from 441 to 1914 corresponding to the increase in the width of p_{T} (transverse momentum) region. Scaling behaviour as shown in Fig. 4.3 is observed for all the four event samples. For q = 2, $\ln F_{\mathrm{q}}(M)$ vs $\ln M^2$ plot from these four event samples is given in Fig. 4.9(a). Scaling exponent (ν) is determined for all the four event samples which show no dependence on the average multiplicity of the event samples (Fig. 4.9(b)). Values predicted from the SCR model and the Ginzburg-Landau theory for second order phase transition [149] are also given. The scaling exponent, is a parameter that can characterize the systems with different degrees of fluctuations. These four toy model event samples have event tracks generated from the same uniform distribution function with no difference except that of multiplicity distributions. Thus it may be concluded that with similar dynamics of track generation, ν has no dependence on multiplicity.

4.2.3 Fractal dimension (D_q)

The fractal parameter D_{q} measures the fractal nature of particle production. This parameter is calculated using Eq. 3.14 which is related to the intermittency index

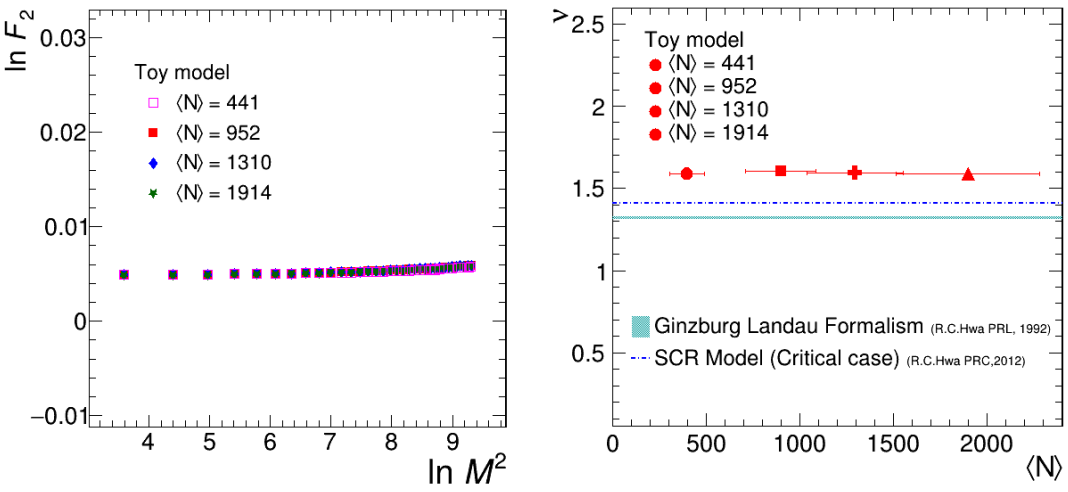

(a) (b)

Figure 4.9. (a) log-log plot of $F_{\mathrm{q}}(M)$ for q = 2 vs M^2 for the four Toy model event samples with mean multiplicities $\langle N \rangle$ = 441, 952, 1310 and 1914 and (b) Scaling exponent as function of average multiplicity of the event samples.

ϕ_q. Fig. 4.10 shows the plot of D_{q} versus q for the toy model events. When a

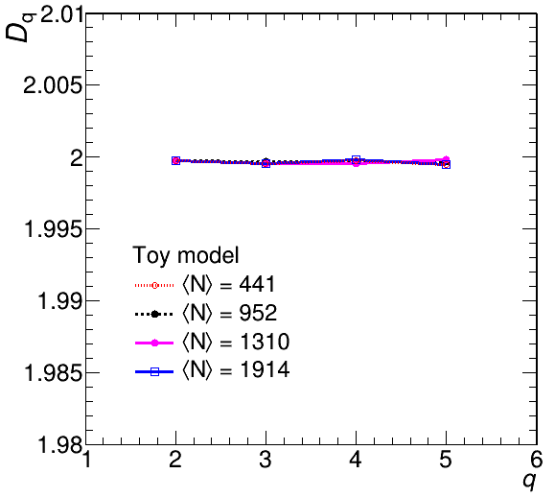

Figure 4.10. (a)Dependence of D_{q} on q for toy model events. Lines connecting data points are to guide the eye.

decreasing trend is observed in D_{q} as a function of q, it signifies the presence of multifractal behaviour in the particle production. Here absence of D_{q}'s dependence on q indicates monofractal structure in the particle generation with the Toy model.

4.3 Resilience of NFM to efficiency corrections

In real detector setups, efficiencies of the measurements may remain consistent or vary within the acceptance region, depending on the design and phase space. That is, constrained by different sets of conditions, detector efficiencies within the acceptance region can either follow a binomial or non-binomial distribution. The efficiency correction procedure for uniform (binomial) and non-uniform (non-binomial) efficiencies has been tested for its efficacy using the toy model events.

Considering detector efficiency to be 80%, an event sample is created with uniform efficiency by removing 20% of the tracks uniformly from each toy model event. Then modified events, termed as *reconstructed-uniform (recU)* events, retain 80% of the original tracks present in the Toy model events. These events are then analyzed to calculate the NFM, F_q^{recU}(M), using equation (Eq. 3.8). Two-dimensional efficiency maps are obtained for each value of M for the *reconstructed-uniform events* such that for each bin in the phase space, there is an efficiency value. An example of such a map for one M value is shown in Fig. 4.11. Subsequently, the efficiency-corrected normalized factorial moments (F_q^{corrU}(M)) are computed for these recU events, using equation (Eq. 3.20). log-log plots of NFM as function of number of bins for q = 2 are shown in Fig. 4.12. It is observed that F_{q}(M), F_q^{recU}(M), and F_q^{corrU}(M) are approximately equal where F_{q} is NFM for Toy model events. The ratio plots in the lower panel show that NFM have the same value, as the ratio values are close to 1. Thus, for binomial type detector efficiencies, the NFM are not affected. In other words, normalized factorial moments are resilient to binomial (uniform) efficiencies.

The other possible case is that of the non-binomial efficiencies of the detector. To generate events with 80% non-uniform efficiencies, 20% of the tracks are removed from the (η, φ) phase space, region of each Toy model event randomly. This process produces events with non-binomial efficiencies and the sample created is referred to as *reconstructed non-uniform (recNU)* events. Analysis is performed on recNU events, and normalized factorial moments (F_q^{recNU}(M)) are computed using Eq. 3.8. It is observed that $F_q(M) \neq F_q^{recNU}$(M), indicating that if the efficiency values are non-binomial, the NFM values differs from that of true sam-

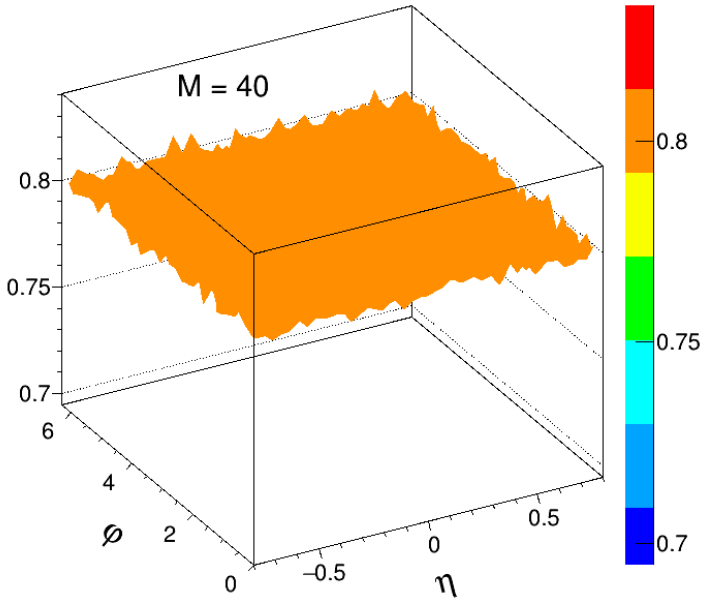

Figure 4.11. Efficiency map in (η, φ) space for $M = 40$ with uniform removal of tracks from Toy model events.

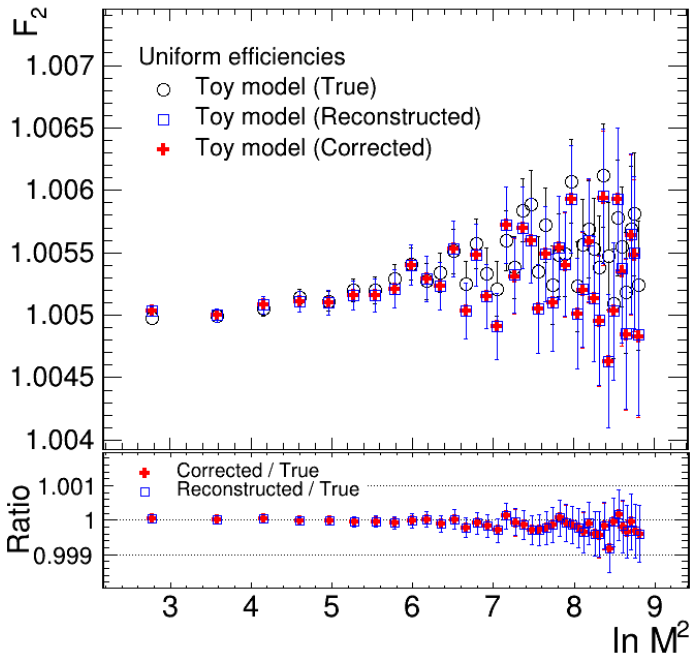

Figure 4.12. $F_{q=2}$ vs $\ln M^2$ plot in case of binomial efficiencies. The lower panel shows the ratio plots of reconstructed and corrected with respect to true/generated Toy model samples.

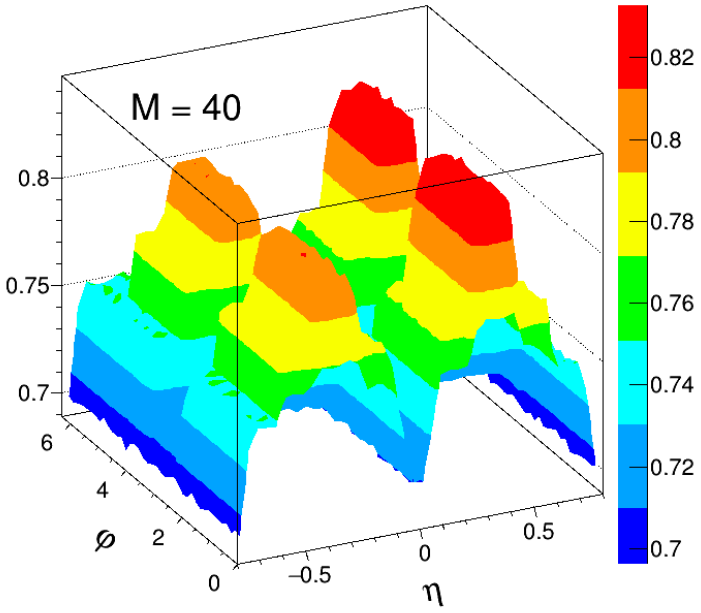

Figure 4.13. Efficiency map in (η, φ) space for $M = 40$ with non-uniform removal of tracks from Toy model events.

ple of events. Efficiency maps are obtained for these recNU events for each M value. Efficiency map for one M value in this case is shown in Fig. 4.13. Applying efficiency correction formula (Eq. 3.20), to calculate NFM, the corrected NFM, F_q^{corrNU}(M) are obtained. It is observed that $F_q(M) = F_q^{corrNU}$(M) (Fig. 4.14), and hence the efficiency correction procedure gives the true values of NFM. Normalized factorial moments are thus observed to be robust against uniform detector efficiencies, but for non-uniform detector efficiencies, an efficiency correction formula for NFM (Eq. 3.20) must be used to get true normalized factorial moments and hence to do further analysis and calculations.

From this analysis of toy model events, a baseline behaviour of NFM is obtained. In summary, this study shows that in the absence of fluctuations in the spatial patterns, $F_q(M)$ moments are negligibly dependent on the binning resolution and no effective intermittency type of behaviour is observed. The scaling exponent value is much greater than 1.304, a value predicted for formalism with second order phase transition as per Ginzburg-Landau theory. For the experimental data analysis using intermittency technique, to take care of detector effects, the

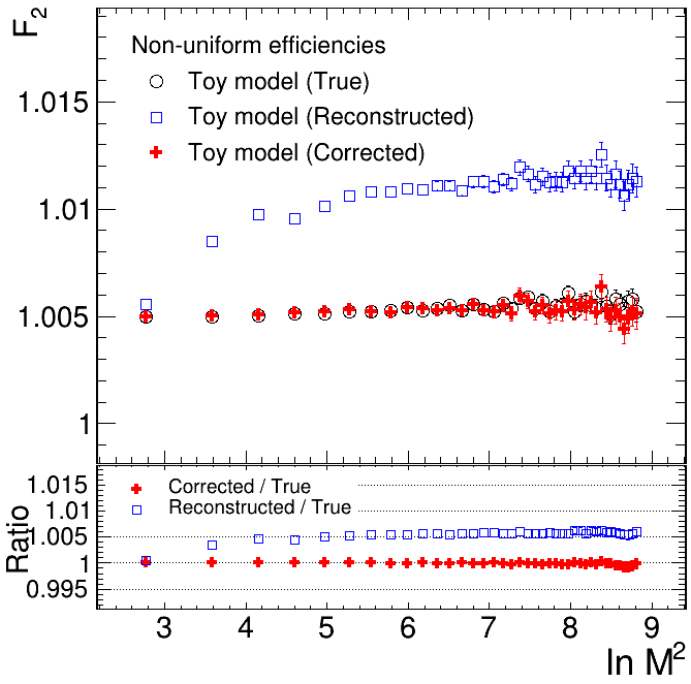

Figure 4.14. $F_{q=2}$ as function of $\ln M^2$ for Toy model events, reconstructed-non Uniform (recNU) and efficiency corrected recNU events. The lower panel shows the ratio plots of reconstructed and corrected with respect to true/generated Toy model sample.

efficiency corrections must be applied in case there are non-binomial efficiencies. The methodology of analysis as detailed in chapter 3 is found to be sensitive and robust one to gauge presence of any dynamical fluctuations in the data.

Chapter 5

Simulation studies

5.1 Introduction

Simulation studies play a pivotal role in extracting physics information from the heavy-ion collision experiments. These studies, based on the known physics, utilize advanced computational techniques to replicate the complex dynamics of colliding heavy ions, such as xenon, copper, gold, lead etc, at ultra-relativistic speeds. Monte Carlo (MC) event generators which serve as virtual laboratories for particle physicists [177], simulate the intricate collisions of particles within accelerators, offering valuable insights into fundamental physics phenomena. Experimentalists utilize these tools to cross-reference their data against theoretical predictions, ensuring consistency and accuracy. Meanwhile, theorists rely on MC event generators to anticipate experimental outcomes and devise innovative experimental techniques. In detector simulation, sophisticated software models are employed to replicate the behaviour of particle interactions within the real detector setups.

In the present work, simulated events generated using Monte Carlo event generators. HIJING (Heavy Ion Jet INteraction Generator) [125] and the AMPT (A Multi-Phase Transport Model) [126] are the widely used MC event generators, used in heavy-ion collision simulations and offer insight into the formation of dense nuclear matter and subsequent space-time evolution. Simulated events from HIJING and the AMPT using detector geometry simulation tool GEANT3 for the ALICE experiment, are analyzed. These simulated event samples are termed as the Monte Carlo (MC) productions. The events in the MC productions are anchored to the experimental runs for Pb−Pb collisions at $\sqrt{s_{\rm NN}}$ = 2.76 TeV recorded with the ALICE experimental setup at LHC in the year 2010. These

achored MC production runs (Appendix D) have the similar conditions set as are there in the experiment. A fast simulation, is event generation using MC event generator but not passed through detector geometry. Three sets of fast simulation using the AMPT are also analyzed.

5.2 Monte Carlo event generators

The HIJING model is a Monte Carlo event generator designed to simulate high energy heavy-ion collisions. It provides a framework for studying the initial stages of these collisions, focusing on the interactions between the colliding nuclei and particle production after collision. HIJING generates initial conditions for heavy-ion collisions based on the Glauber model, which describes the spatial and momentum distributions of particles produced by the colliding nuclei. It incorporates parton distribution functions to model the internal structure of nucleons and nuclei. One of the key features of the HIJING is its ability to model both soft and hard processes occurring during the collision. Soft processes involve low-energy interactions such as multiple parton scattering and gluon radiation, while hard processes involve high-energy interactions such as the production of jets and heavy quarks. By simulating jet production and possible interactions within the QGP, HIJING significantly enhances our understanding of the fundamental properties of nuclear matter under extreme conditions. HIJING event generator is an important tool to offer insights into the initial stages of the collisions and helping to interpret the experimental data from particle colliders. Further information about this model is available in [125, 178, 179].

The AMPT model is a Monte Carlo transport model for heavy-ion collisions at relativistic energies. It comprises of four key components: initial conditions, partonic interactions, the conversion from partonic to hadronic matter, and hadronic interactions. Initial conditions, including the distributions of minijet partons and soft string excitations, are derived from the HIJING model. Parton scatterings are simulated using Zhang's parton cascade (ZPC) [180], focusing on two-body interactions with cross sections derived from perturbative quantum chromodynamics (pQCD). The transition from partonic to hadronic matter is an

important phase in the collision evolution. The AMPT works on two modes of operation: Default and String Melting. In the default AMPT mode, partons recombine with their parent strings and are converted to hadrons using the Lund string fragmentation model [181]. In AMPT with string melting mode, a quark coalescence model is used for hadron formation. Subsequent evolution in both modes involve a hadronic cascade, based on the ART (A Relativistic Transport) model. This cascade describes the sequential interactions of hadrons as they propagate through the collision medium. The AMPT model provides a framework for studying heavy-ion collisions, from initial conditions to the evolution of hadronic matter, making it an important tool for understanding particle physics. More details on the model can be found in [126, 182–184].

5.3 Monte Carlo event samples

To simulate events for Pb−Pb collisions at $\sqrt{s_{\rm NN}} = 2.76\,\text{TeV}$, ALICE employs event generators. These simulations mimic experimental conditions to generate Monte Carlo productions. GEANT3 is employed to implement ALICE detector geometry, ensuring an accurate representation of experimental setups. In ALICE, data files are stored in two formats namely ESD (Event Summary Data) and AOD (Analysis Object Data). After processing of raw data the first level of data files that contain events with information from all subdetectors are ESD files, while the AOD files contain a subset of ESD information selected for specific analysis. The MC production events from the HIJING and the AMPT event generator are used for the simulation studies in the present work. The HIJING-generated general-purpose Monte Carlo productions for Pb–Pb collisions at $\sqrt{s_{NN}} = 2.76\,\text{TeV}$ is LHC11a10a_bis. This production is anchored with the experimental data from production LHC10h pass2. The production LHC11a10a_bis serves as a general-purpose dataset with a minimum bias setting.

The production LHC12a11a is from the AMPT production for 0−5% central events and anchored to LHC10h whereas, LHC13f3a(String melting ON, rescattering OFF), LHC13f3b(String melting OFF, rescattering ON), LHC13f3c(String melting ON, rescattering ON) are the AMPT-generated Monte Carlo productions

Table 5.1. Monte-Carlo production cycles analyzed in this work.

Event Generator	Production name	No. of events	ESD/AOD
HIJING	LHC11a10a_bis	3 M	AOD 162
AMPT	LHC12a11a	0.09 M	AOD 081
AMPT	LHC13f3a	39 M	
(Fast Simulation)	LHC13f3b	53 M	ESD
	LHC13f3c	38 M	

without GEANT simulation for detector geometry. Table 5.1 enlists the information on the MC event samples analyzed.
For the analysis, various cuts applied for selection of events and tracks are discussed below.

5.3.1 Vertex and Trigger cut

A trigger can be used to filter and select relevant events based on specific criteria or requirements of the analysis. The key focus of the trigger system is to select events that result from the beam collisions and reject events that are caused by interactions between the beam and residual gas present in the beam pipe. In this analysis, kMB trigger is used which is a minimum bias trigger that requires a hit in both the V0A and V0C detectors. A minimum bias trigger is a type of trigger that is used to select inelastic events with as little bias as possible.

Once an event is selected, the next level of event selection which is typically applied to further refine the event sample, is to make a primary vertex selection. This involves selecting events that have a well-defined primary interaction vertex. The interaction point is typically set up at the center of the detector (x = 0, y = 0, z = 0) and it is the point where the two beams are supposed to collide. The actual point of collision between the two beams is called the vertex of the event. Primary vertices are often reconstructed using the information from SPD tracklets. After the reconstruction, events whose primary vertex lies within ± 10 cm range along the z-axis, from the interaction point are considered in the present analysis. The z vertex cut is used to eliminate events that have a primary vertex far away from the center of the detector along the z-axis [185]. A variation in the V_z value is

considered in the estimation of systematic uncertainties.

5.3.2 Centrality estimation

The measurement of the overlap region between colliding nuclei, defined in terms of centrality of the collision, holds significant importance to characterize the QCD matter. Accurate determination of centrality aids in comparing ALICE measurements not only with other experiments but also with theoretical calculations [186]. Typically, centrality percentile is derived by integrating the impact parameter distribution. In ALICE, centrality is defined as the percentile of the hadronic cross-section corresponding to multiplicity above a threshold value (N_{ch}) or energy deposited in ZDC below some given value (E_{ZDC})

In heavy-ion collisions, the strong electromagnetic field contaminates the hadronic cross-section in the most peripheral collisions. Centrality determination is thus restricted to the extent where this contamination effect is negligible.Centrality estimation in heavy-ion collisions utilizes the V0 detector, which measures the sum of V0A and V0C amplitudes. These amplitudes correspond to the ionization energy deposited in the detectors and are expressed as percentiles of selected events. Centrality classes are defined based on these percentiles, providing a quantitative measure of the collision centrality in experiments [187]. Fig. 5.1 illustrates the distribution of V0M amplitude alongside the Glauber Monte Carlo fit for Pb–Pb collisions at $\sqrt{s_{\mathrm{NN}}} = 2.76\,\mathrm{TeV}$ [186]. Centrality classes are a way to quantify the degree of centrality in the heavy-ion collisions for example, the 0-5% range is related to the upper 5% of the distribution. This is considered as the most central or highest amplitude class, as it represents the events with the highest sum of amplitudes. Similarly, the other classes such as 5-10%, 10-20%, 20-30%, etc. represent decreasing degrees of centrality or lower sum of amplitudes.

Once the right type of events specific to the analysis are chosen, selection of the tracks within the event, needs to be selected. The cuts considered for track selection in this analysis, called track selection cuts, are discussed below.

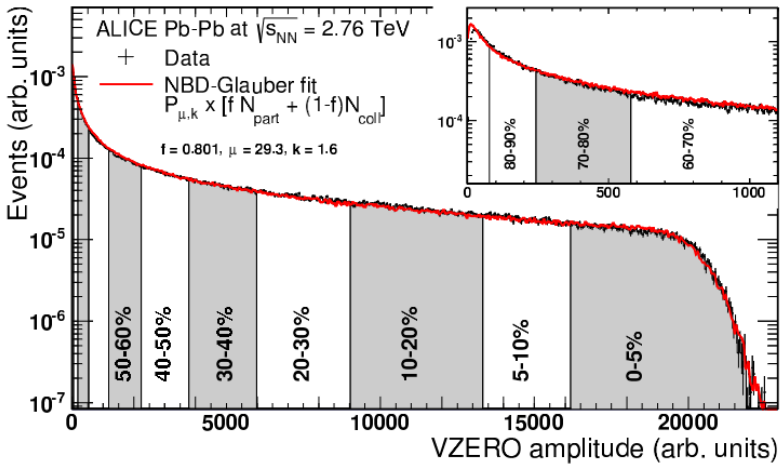

Figure 5.1. Centrality in Pb–Pb collisions at $\sqrt{s_{\rm NN}}$ = 2.76 TeV is determined by selecting events based on the V0M amplitude distribution. A Glauber model fit is represented by the red line, with the inset plot offering a magnified view of peripheral collisions (source [186]).

5.3.3 Track selection

In ALICE, the main detector used to track charged particles is the Time Projection Chamber (TPC). Track selection criteria is used to minimize the contamination from the secondary particles and to enhance the tracking efficiency. Primary tracks are required to satisfy certain quality criteria in order to be selected for the physics analysis. This criteria includes, having a signal in at least one of the layers of SPD, a maximum chi-square per cluster value of 36 from the fit of ITS clusters, and meeting the selection criteria on the distance of closest approach (DCA) of the primary track to the primary vertex. Primary tracks are chosen within kinematic acceptance such that transverse momentum $p_{\rm T} > 0.2$ GeV/c is taken to ensure good momentum resolution and uniform track reconstruction efficiency, and $|\eta| \leq 0.8$ to avoid edge effects in the TPC acceptance [185].

In this thesis work, the tracks termed as hybrid tracks are used, which refer to tracks that are reconstructed using a combination of ITS and TPC detector systems. Hybrid track-cuts are a combination of three types of global tracks comprising of global tracks with SPD hit(s) and an ITS refit, global tracks without SPD hit(s) but with an ITS refit constrained to the primary vertex, and global tracks without an ITS refit but constrained to the primary vertex. In the track selection criteria for hybrid tracks, a minimum of 70 clusters are required in the

TPC, with a maximum chi-square per cluster value for TPC set at 4. Furthermore, constraints on the maximum distance of closest approach (DCA) to the vertex set at 2.4 in the XY plane and 3.2 along the Z direction. These are termed as FilterBit 768 (FB 768) tracks, based on the nomenclature used in ALICE, to select tracks after applying various cuts to filter tracks for analysis from the raw tracks.

5.3.4 Kinematic cuts

The analysis focuses on the charged particles generated in the mid-rapidity region ($|\eta| \leq 0.8$) with full azimuth ($0 \leq \varphi \leq 2\pi$) in low transverse momentum region with $p_{\mathrm{T}} < 2.0$ GeV/c. To study the dependence of observables on transverse momentum and on p_{T} bin width, the intervals for which analysis is performed are tabulated in the Table 5.2.

Table 5.2. Kinematic cuts used for the track selection.

Pseudorapidity range	$-0.8 \leq \eta \leq 0.8$
Azimuthal coverage	$0 \leq \varphi \leq 2\pi$
Transverse momentum range (Wide) ($\delta p_T \geq 0.6$)	$0.4 \leq p_T \leq 1.0$ GeV/c $0.4 \leq p_T \leq 1.5$ GeV/c $0.4 \leq p_T \leq 2.0$ GeV/c $0.6 \leq p_T \leq 1.0$ GeV/c
Transverse momentum range (Narrow) ($\delta p_T = 0.2$)	$0.4 \leq p_T \leq 0.6$ GeV/c $0.6 \leq p_T \leq 0.8$ GeV/c $0.9 \leq p_T \leq 1.1$ GeV/c

5.4 HIJING: Observations and results

For the Monte Carlo studies performed here, the observable, the normalized factorial moments is obtained as discussed in Chapter 3. The quality assurance plots for the HIJING events analyzed here, are given below, followed by other observations and results.

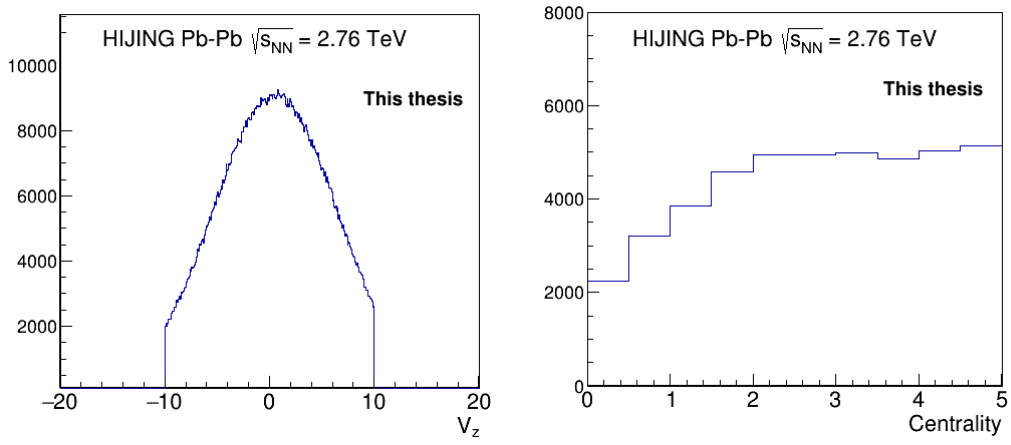

(a) (b)

Figure 5.2. Quality Assurance (QA) plots: (a) V_z distribution and (b) Centrality distribution for Pb−Pb HIJING data at $\sqrt{s_{\rm NN}}$ = 2.76 TeV.

5.4.1 QA plots: Event and track selection

The V_z distribution of the HIJING events, after applying the vertex cut ($|V_z| \leq 10cm$) is given in Fig.5.2(a). A total of 154 K minimum bias HIJING events are taken. After vertex cut, in 0−5% centrality bin (Fig. 5.2(b)), 87 K events are left. Multiplicity distributions for the generated and reconstructed tracks for these events are shown in Fig. 5.3(a) for the $0.4 \leq p_{\rm T} \leq 1.0\,{\rm GeV/c}$ transverse momentum bin. The transverse momentum distribution, pseudorapidity and azimuthal distributions for the tracks in this bin are given in Fig. 5.3(b), 5.3(c) and 5.3(d) respectively. The observed difference between reconstructed and generated events pertain to the detector efficiency not equal to 100%. Fig. 5.4 shows the multiplicity distributions of reconstructed HIJING events in $p_{\rm T}$ bins given in Table 5.2 from 0−5% central Pb−Pb collisions at $\sqrt{s_{\rm NN}}$ = 2.76 TeV.

5.4.2 Closure studies

The Monte Carlo closure study using HIJING events is performed as is described in section 3.4.1 of Chapter 3. The tracking efficiencies in $p_{\rm T}$, η and φ space for 0−5% central events in low $p_{\rm T}$ bins are given in Fig. 5.5 and 5.6 respectively. For the intermittency analysis in (η, φ) phase space, efficiencies are determined on bin-by-bin basis for each M value, as is described in section 3.4.1. As an example,

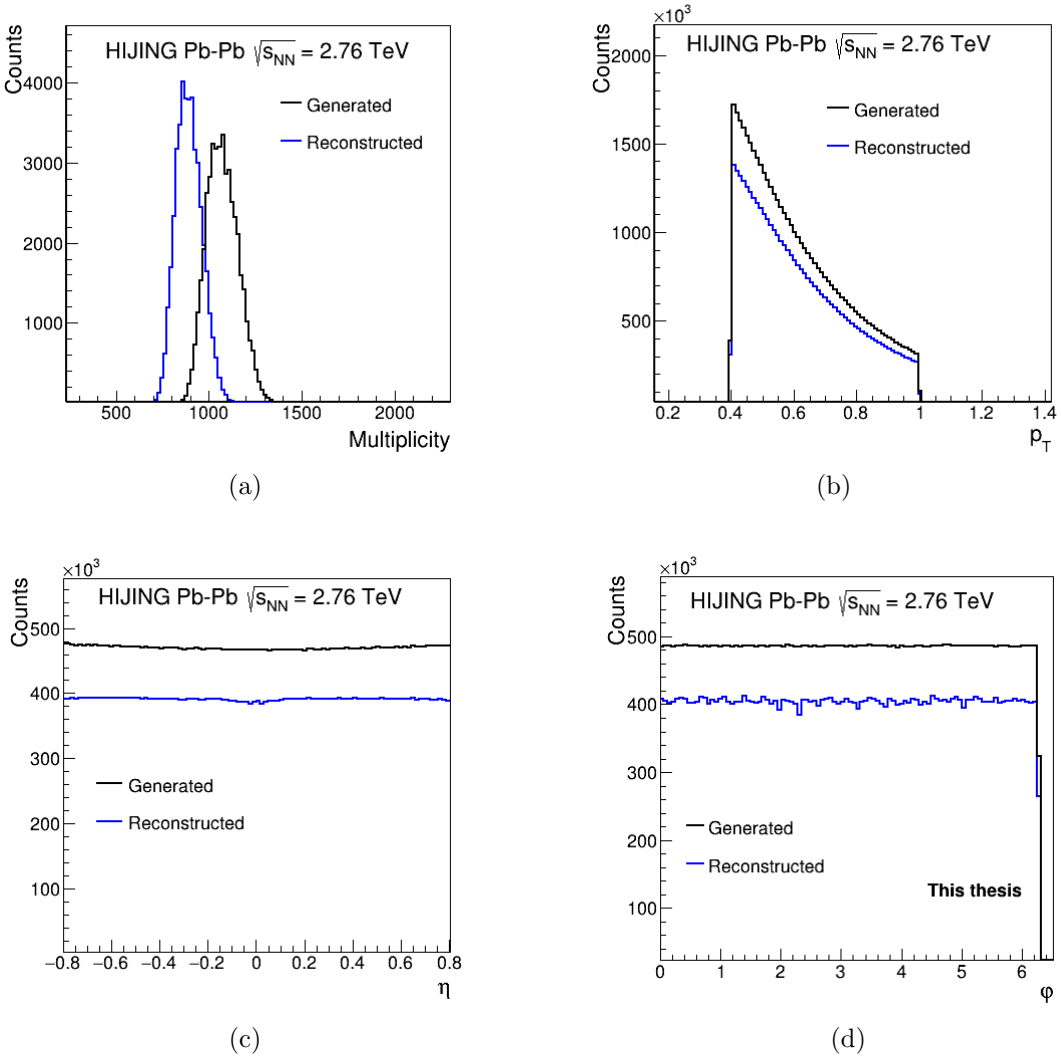

Figure 5.3. Quality Assurance (QA) plots: (a) Multiplicity distributions (b) p_{T} distribution (c) η distribution (d) φ distribution from the reconstructed and generated tracks for Pb−Pb collisions using HIJING, at $\sqrt{s_{\mathrm{NN}}} = 2.76$ TeV in the transverse momentum bin $0.4 \leq p_{\mathrm{T}} \leq 1.0$ GeV/c. These figures show the difference in the generated and reconstructed events from HIJING production in ALICE at LHC.

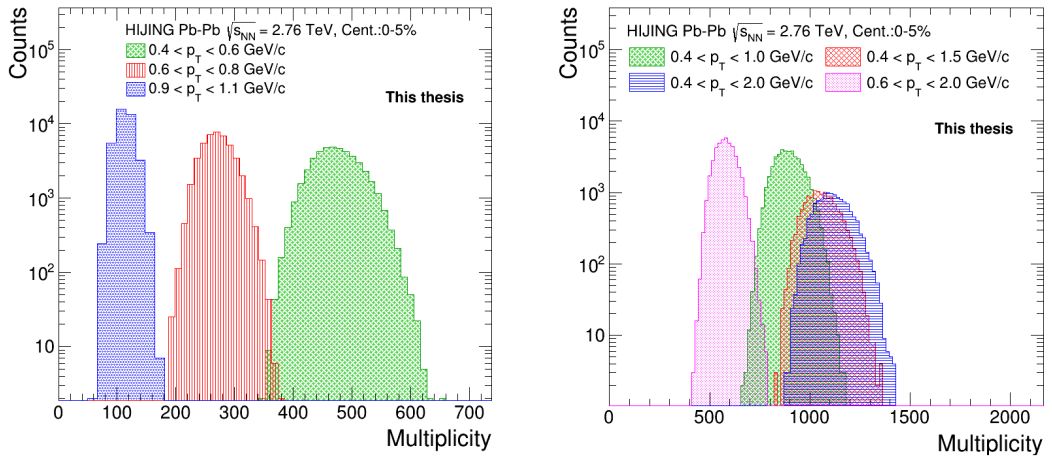

(a) (b)

Figure 5.4. HIJING(Reconstructed): Multiplicity distributions in (a) narrow p_{T} bins and (b) in wide p_{T} bins, for Pb−Pb collision events at $\sqrt{s_{\mathrm{NN}}}$ = 2.76 TeV for 0−5% centrality and $|V_z| \leq 10$ cm.

two-dimensional efficiency maps in (η, φ) phase space for $M = 20$ are shown in Fig. 5.7(a) and 5.7(b) for $0.4 \leq p_{\mathrm{T}} \leq 0.6\,\mathrm{GeV/c}$ and $0.6 \leq p_{\mathrm{T}} \leq 0.8\,\mathrm{GeV/c}$ bin respectively. A Monte Carlo closure test for NFM has been performed for these two narrow p_{T} bins.

The normalized factorial moments obtained from the reconstructed HIJING tracks are subjected to weighting with correction factors to give F_{q}^{corr} using Eq. 3.20 and compared with the normalized factorial moments (F_{q}^{gen}) derived from the generated HIJING tracks. It is observed that for q = 2, $F_{\mathrm{q}}^{corr} \sim F_{\mathrm{q}}^{rec}$, that is the application of efficiency corrections do not make a change in the NFM values. For $p_{\mathrm{T}} > 0.4$ GeV/c, efficiencies are binomial in nature, as is observed in Fig. 5.5 and 5.6, which cancel out in the Eq. 3.20. Ratio of the two, F_{q}^{rec} and F_{q}^{corr} is thus equal to 1 (given in lower panel of Fig. 5.8). From the observations made for the various p_{T} intervals, it is found that $F_{\mathrm{q}}^{rec}(M)/F_{\mathrm{q}}^{gen}(M) \approx 1$. A deviation of this ratio around 2% is observed as M goes beyond 60 with $\ln M^2 > 7.0$ (Fig.5.9).

From above discussion it is again shown with HIJING events that normalized factorial moments are robust against uniform efficiencies (also reported in Ref. [188]). The reconstructed HIJING tracks in the transverse momentum region $\leq$ 2.0 GeV/c, where the efficiencies are binomial in nature, are not required to be

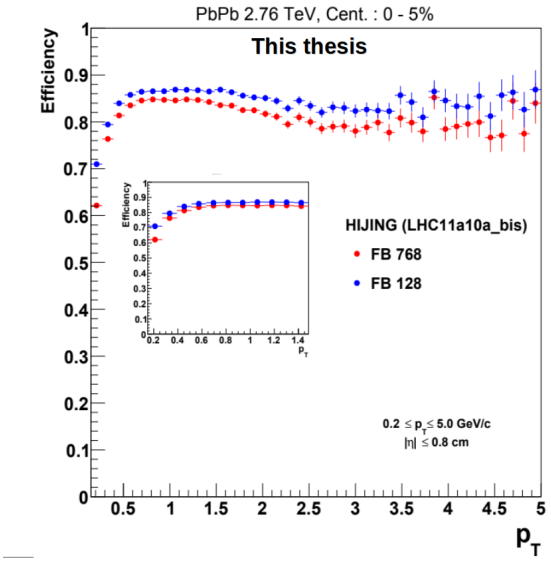

Figure 5.5. HIJING: Tracking efficiency of charged particles selected using FilterBit 768 and FilterBit 128 (TPC only track filterbit) as a function of transverse momentum.

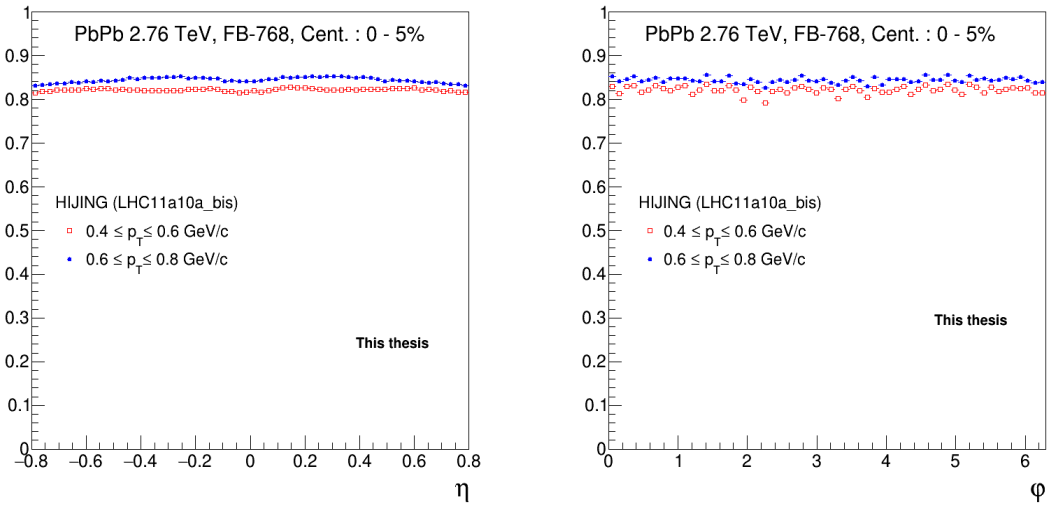

(a) (b)

Figure 5.6. HIJING: Tracking efficiency (a) in η phase space (b) in φ phase space for $M=$ 60 in the two p_{T} bins with 0–5% central events from Pb–Pb collisions at $\sqrt{s_{\mathrm{NN}}} = 2.76$ TeV.

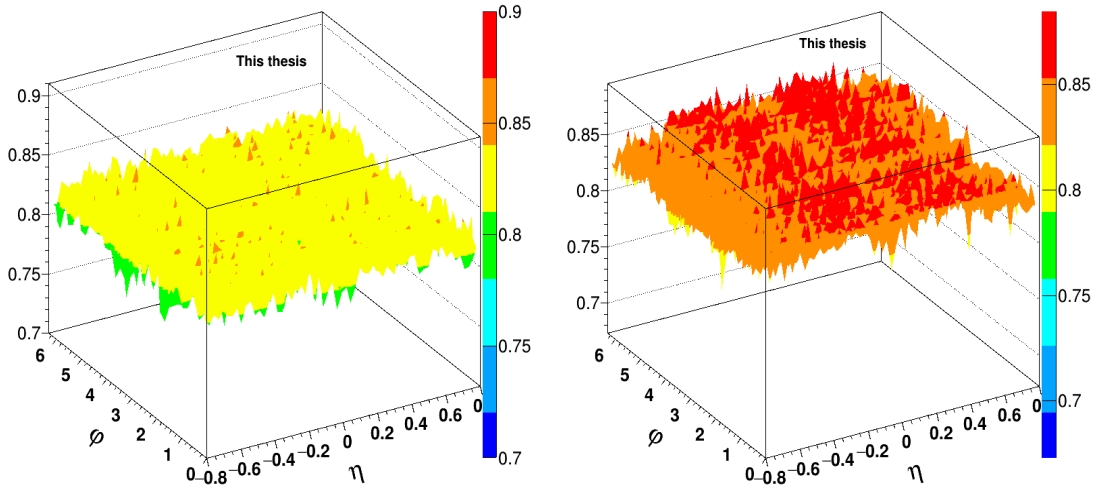

(a) (b)

Figure 5.7. HIJING: Two dimensional tracking efficiency maps in (η, ϕ) phase space for$M=$ 20 in a) $0.4 \leq p_{\mathrm{T}} \leq 0.6\,\mathrm{GeV/c}$ bin and b) $0.6 \leq p_{\mathrm{T}} \leq 0.8\,\mathrm{GeV/c}$ bin, for 0−5% central Pb–Pb collision events at $\sqrt{s_{\mathrm{NN}}} = 2.76$ TeV using HIJING.

corrected for efficiencies. For the p_{T} bins, the M value upto which Monte Carlo closure is 98% or above is taken as M_{max} and subsequently the scaling exponent is determined. In Fig. 5.9, the ratio plot of the $F_{\mathrm{q}}^{rec}(M)$ and $F_{\mathrm{q}}^{gen}(M)$ are shown for the p_{T} bins analysed, with red dashed line showing the region of 98% closure. The closure analysis for different transverse momentum (p_{T}) bins (Table 5.2) gives values for M_{max}. For the bins $0.4 \leq p_{\mathrm{T}} \leq 0.6\,\mathrm{GeV/c}$ and $0.6 \leq p_{\mathrm{T}} \leq 0.8\,\mathrm{GeV/c}$, M_{max} is set at 82. However, for the $0.9 \leq p_{\mathrm{T}} \leq 1.1\,\mathrm{GeV/c}$ bin, M_{max} is found to be 70, as shown in Fig. 5.9(a). When considering wider p_{T} bins, the values of M_{max} increase. For the $0.4 \leq p_{\mathrm{T}} \leq 1.0\,\mathrm{GeV/c}$, M_{max} is 105, and for $0.4 \leq p_{\mathrm{T}} \leq 1.5\,\mathrm{GeV/c}$, it goes up to 111. In other bins with wider ranges, such as shown in Fig. 5.9(b), M_{max} is taken as 120 that is M ranges from 6 to 120.

5.4.3 Scaling behaviour

Normalized factorial moments are calculated in the two-dimensional (η, ϕ) phase space in the midrapidity region ($|\eta| \leq 0.8$) within $0.4 \leq p_{\mathrm{T}} \leq 1.0\,\mathrm{GeV/c}$ and M takes value from 6 to 123. Fig. 5.10 and 5.11 show the f_{q}^{e} distributions as defined in Eq. 3.1, for q = 2, 3, 4 and 5 for case of M = 30 and M = 60. There are long tails of

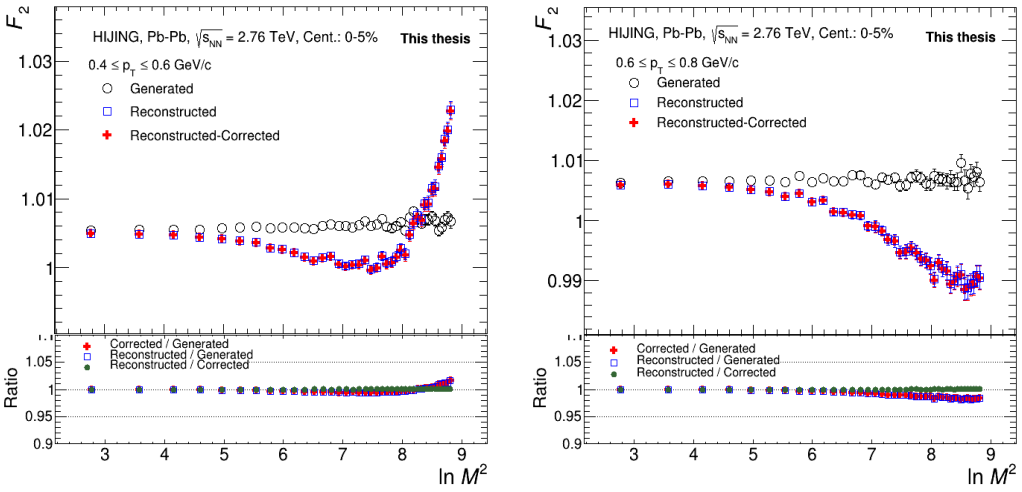

Figure 5.8. HIJING: F_{q} vs $\ln M^2$ plot for generated, reconstructed, and reconstructed-corrected factorial moments in (left) $0.4 \leq p_{\mathrm{T}} \leq 0.6$ GeV/c and (right) $0.6 \leq p_{\mathrm{T}} \leq 0.8$ GeV/c bin. Bottom panels show the ratio of reconstructed/generated, reconstructed/corrected and reconstructed-corrected/generated showing a closure around 98% for all M.

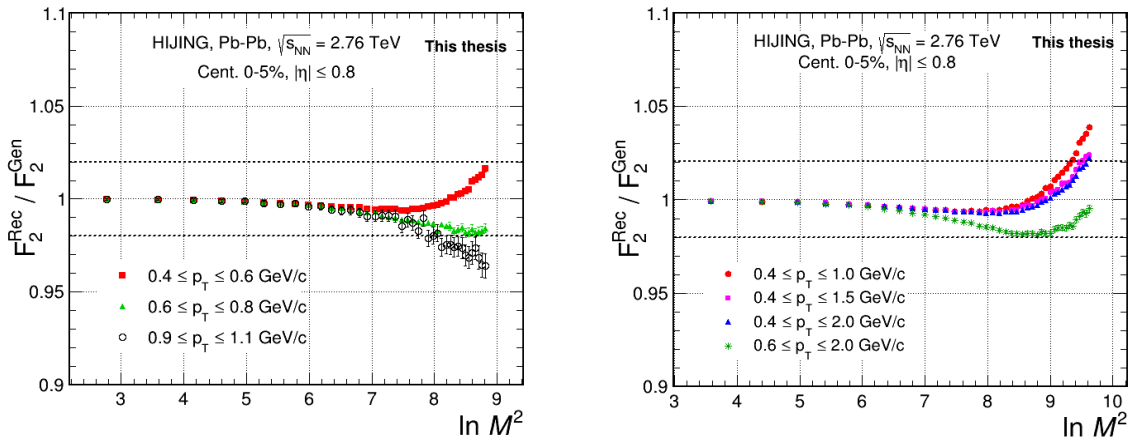

(a) (b)

Figure 5.9. HIJING Closure: Ratio plots of $F_{\mathrm{q}}^{rec}/F_{\mathrm{q}}^{gen}$ in (a) narrow p_{T} bins and (b) wide p_{T} bins.

the distributions as q and M increases. The normalized factorial moments are then obtained using Eq. 3.8 and studied as function of M, for the M-scaling behaviour. This is shown for HIJING (reconstructed) events in Fig. 5.12(a). A minimal dependence of $\ln F_{\mathrm{q}}(M)$ on $\ln M^2$ is observed, with considerable fluctuations in F_{q} values at higher M for q = 4 and 5. Statistical uncertainties are pronounced possibly for the reason that there are not many bins which have bin multiplicity greater than or equal to 4. Similar investigations are performed with generated tracks, and the results are given in Fig. 5.12(b). No apparent dependence of F_{q} on M is seen in generated tracks which have large statistical uncertainties at high M. In case of generated events, $\ln F_{\mathrm{q}} > 0$ with $F_{\mathrm{q+1}}(M) > F_{\mathrm{q}}(M)$. However, $\ln F_{\mathrm{q}}$ shows very weak dependence on M with large fluctuations in $F_{\mathrm{q}}(M)$ for q = 5 at high M. M-scaling or intermittency is thus observed to be absent and hence no self-similar spatial fluctuations are there in the HIJING event generation. Because of these uncertainties precise values of intermittency indices (ϕ_q) from linear fits cannot be determined.

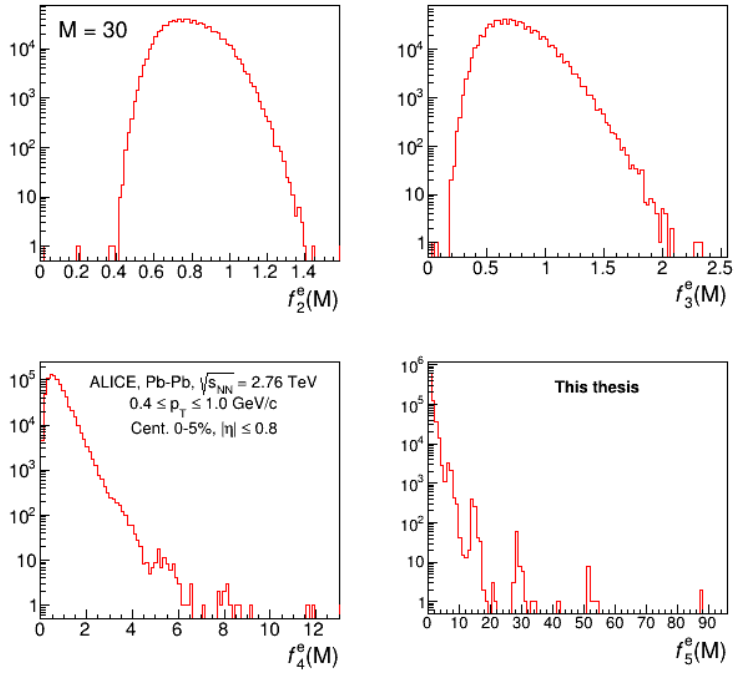

Figure 5.10. HIJING(Reconstructed): f_{q} distributions for q = 2, 3, 4 and 5 for M = 30 in $0.4 \leq p_{\mathrm{T}} \leq 1.0$ GeV/c bin for central Pb−Pb collision events.

The variation of $F_{\mathrm{q}}(M)$ for $q > 2$ with $F_2(M)$, termed as F-scaling is plotted in Fig. 5.13(a). Due to absence of robust linear dependence of $\ln F_{\mathrm{q}}$ on $\ln M^2$ for

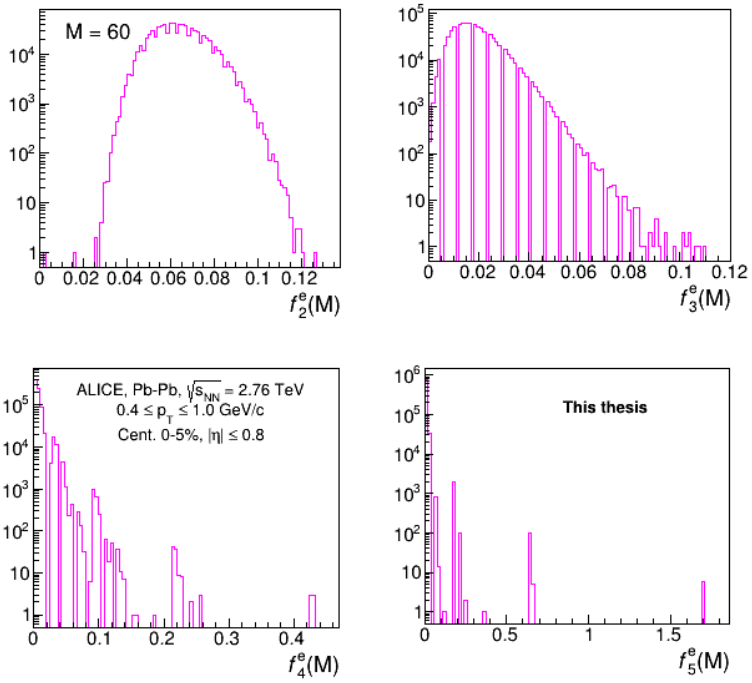

Figure 5.11. HIJING(Reconstructed): f_{q} distributions for q = 2, 3, 4 and 5 for M = 60 in $0.4 \leq p_{\mathrm{T}} \leq 1.0\,\mathrm{GeV/c}$ bin for central Pb−Pb collision events.

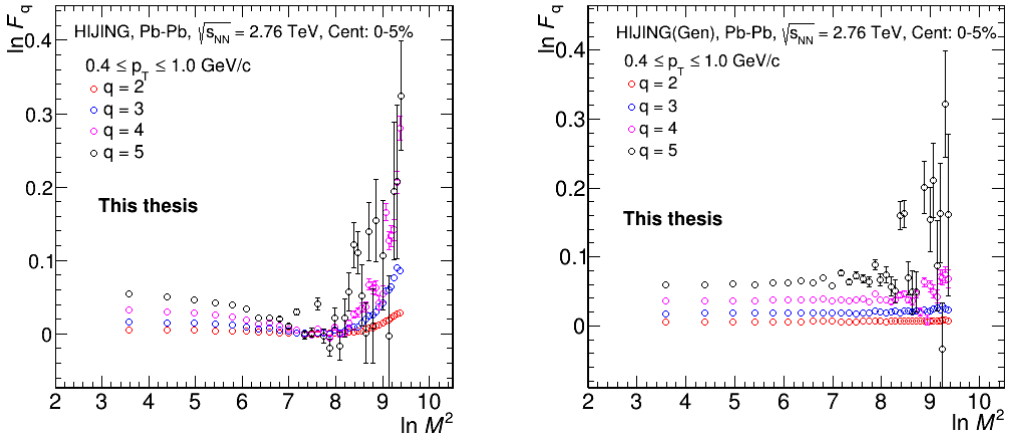

(a) (b)

Figure 5.12. HIJING: $\ln F_{\mathrm{q}}(M)$ vs $\ln M^2$ plot (M-scaling) for q = 2, 3, 4 and 5 in $0.4 \leq p_{\mathrm{T}} \leq 1.0\,\mathrm{GeV/c}$ for (a) reconstructed and (b) generated tracks.

all M values, F-scaling at lower M values is absent. In higher M region a weak power-law dependence of F_q on F_2 is observed. However, no robust dependence of F_q on F_2 is seen for all M and q. Line fits to these points are however done to obtain β_q for the calculation of scaling exponent, for HIJING (reconstructed). The $\ln \beta_q$ vs $\ln (q-1)$ is shown in Fig. 5.14(a) that gives a scaling exponent ν = 1.68±0.03 for $0.4 \leq p_T \leq 1.0$ GeV/c. The fitting is performed for low M region that has 99% closure with the generated tracks. In Fig. 5.13(b), $\ln F_q$ vs $\ln F_2$ plots for q = 3, 4 and 5 are given for the same p_T bin in case of HIJING generated events (true). $F_3(M)$ shows a little linear dependence on $F_2(M)$. For higher order (q = 4 and 5) there are large fluctuations and statistical errors. However, a value of scaling exponent is obtained in this case of HIJING generated which is 1.75±0.20 (Fig. 5.14(b)).

HIJING data does not show intermittency but weak F-scaling is observed with scaling exponent $\nu >> 1.304$ value, predicted for second order phase transition as per Ginzburg-Landau formalism. It is known that HIJING does not have physics of phase transition implemented and the same is confirmed through this study. Further absence of self-similar nature of particle generation is seen in the HIJING as no power law behaviour of F_q with resolution (M) is observed.

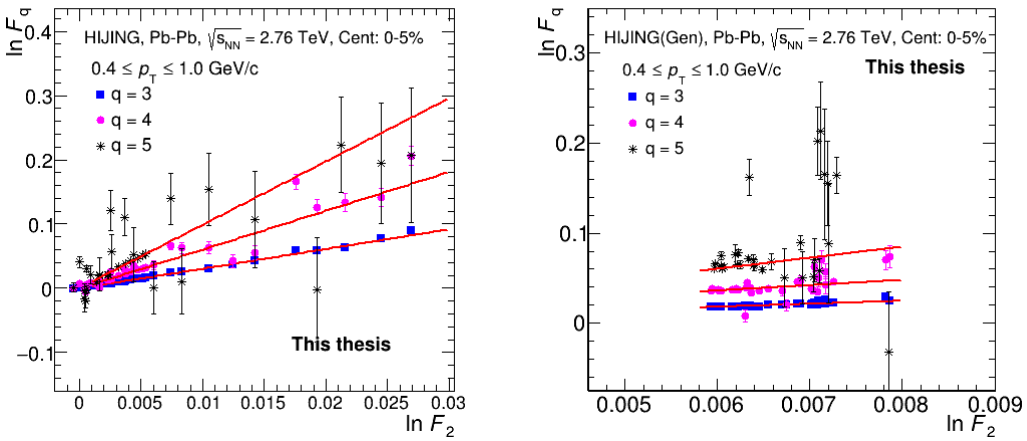

(a) (b)

Figure 5.13. HIJING: $\ln F_q(M)$ versus $\ln F_2(M)$ with linear fits in the higher M region in $0.4 \leq p_T \leq 1.0$ GeV/c for (a) reconstructed and (b) generated tracks.

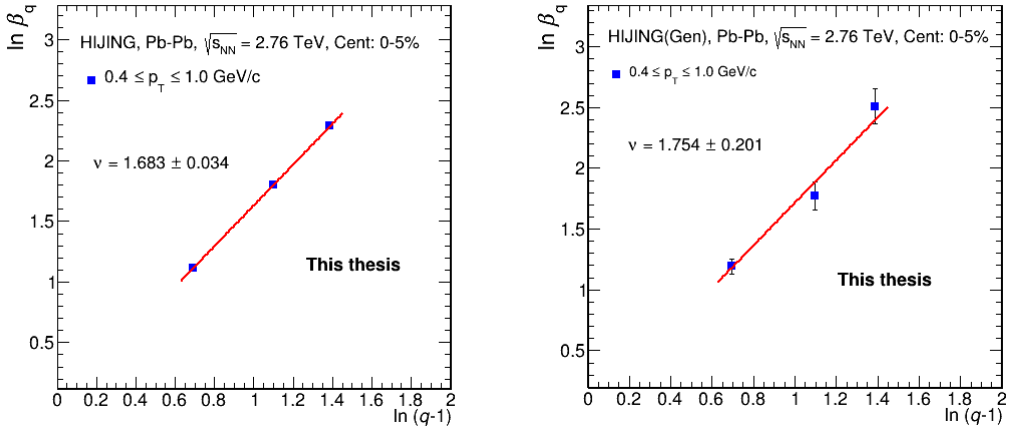

(a) (b)

Figure 5.14. HIJING: Scaling exponent (ν) from the $\ln \beta_q$ vs $\ln (q-1)$ plot in $0.4 \leq p_T \leq 1.0$ GeV/c for (a) reconstructed and (b) generated tracks.

5.5 AMPT: Observations and results

Monte Carlo studies using the AMPT model, similar to the one for HIJING, as discussed in previous section, are performed. AMPT events with string melting mode from ALICE production (LHC12a11a) with full simulation including detector having 0.09 million events and the ones from fast simulation are analyzed. The QA plots and observations are discussed below.

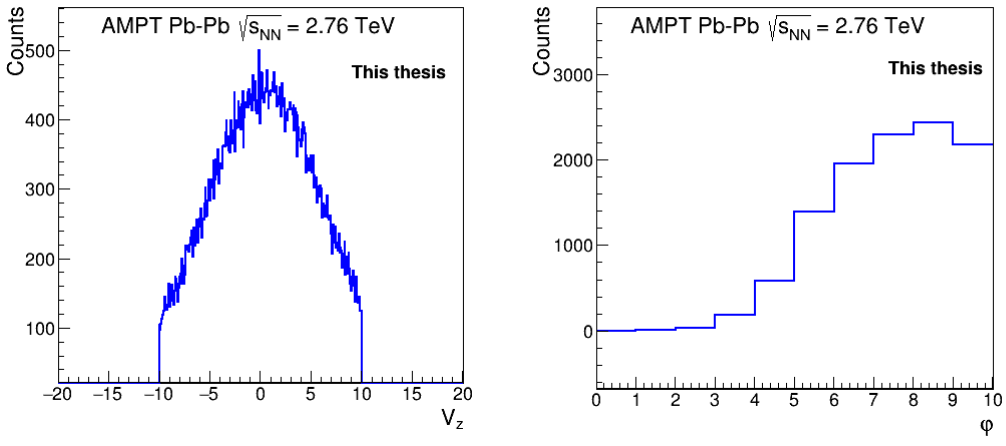

(a) (b)

Figure 5.15. (a) The V_z distribution and (b) the centrality distribution for Pb−Pb collisions using AMPT at $\sqrt{s_{\rm NN}} = 2.76$ TeV (LHC12a11a).

5.5.1 Quality Assurance (QA) plots

The Quality Assurance plots from the AMPT (LHC12a11a) for event selection are given in Fig. 5.15. Tracks selected using the cuts mentioned in section 5.3 are shown in Fig. 5.16 which shows the multiplicity, p_{T}, η and φ distributions for both reconstructed and generated tracks where $|\eta| \leq 0.8$ and $0 \leq \varphi \leq 2\pi$ in $0.4 \leq p_{\mathrm{T}} \leq 0.6\,\mathrm{GeV/c}$ bin.

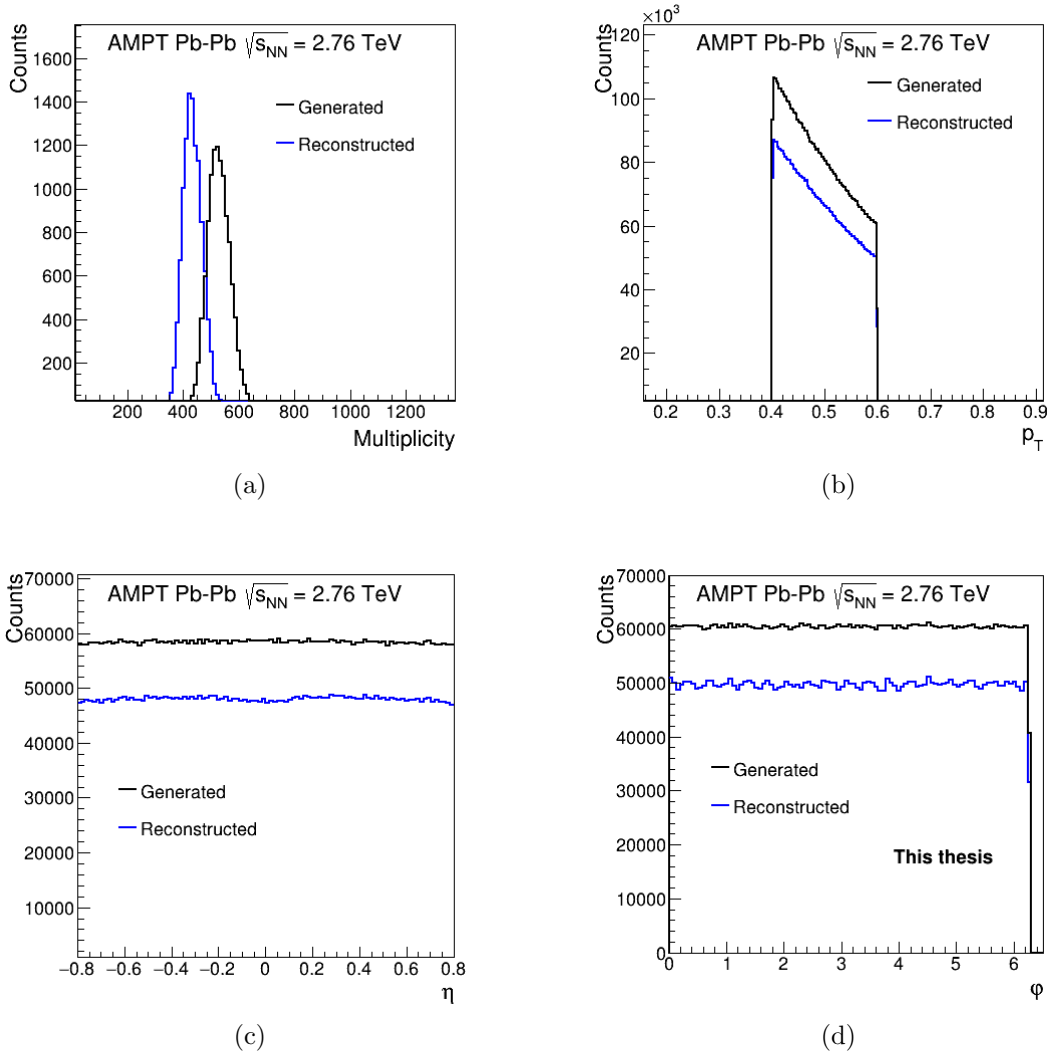

Figure 5.16. Quality Assurance (QA) plots: (a) Multiplicity distributions (b) p_{T} distribution (c) η distribution (d) φ distribution of the reconstructed and generated tracks for Pb−Pb collisions at $\sqrt{s_{\mathrm{NN}}}$ = 2.76 TeV (LHC12a11a) using the AMPT model.

QA plots of the AMPT fast simulation events (LHC13f3c) are given in Fig. 5.17. The multiplicity, p_{T}, η and φ distributions are given in Fig. 5.17

for the charged particle tracks in $0.4 \leq p_{\mathrm{T}} \leq 1.0\,\mathrm{GeV/c}$. Similar QA plots are obtained for other two fast generations using the AMPT.

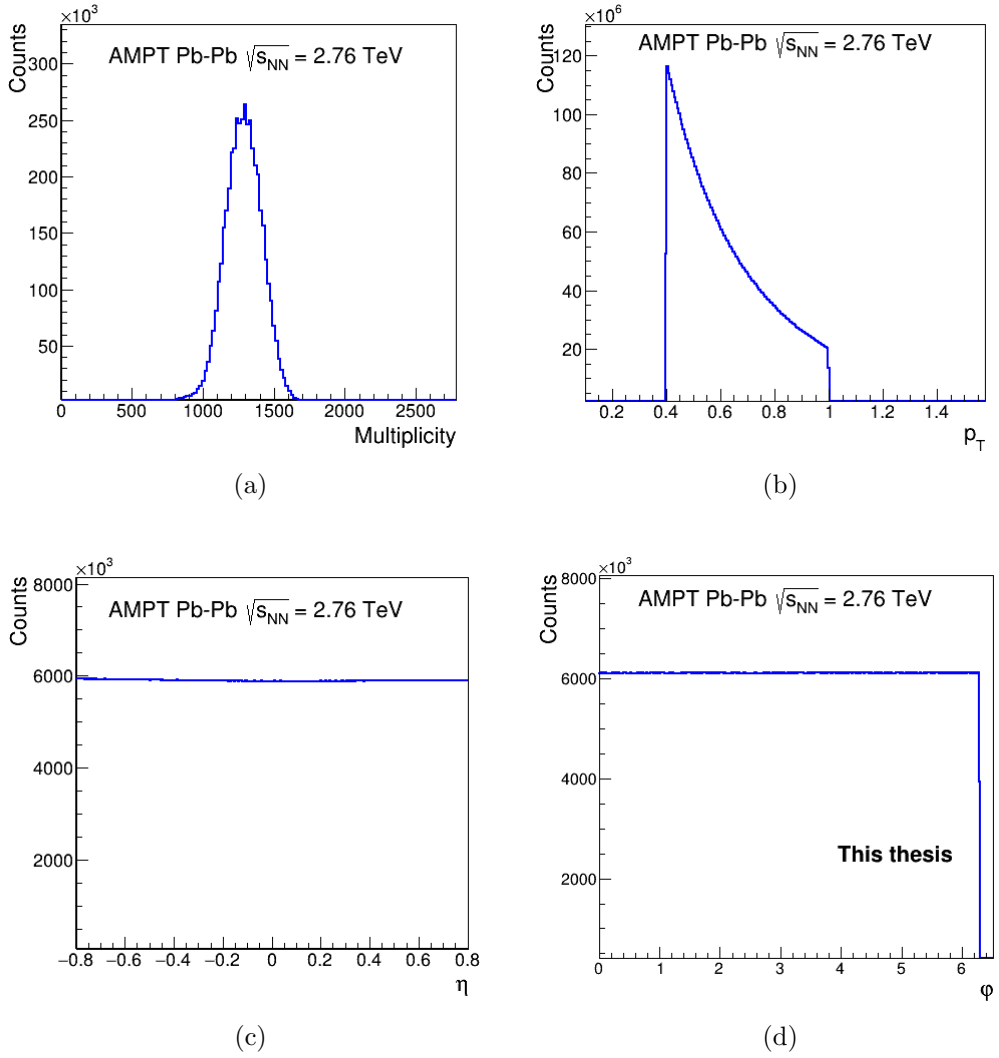

Figure 5.17. Quality Assurance (QA) plots: (a) Multiplicity distribution (b) p_T distribution (c) η distribution (d) φ distribution from AMPT fast simulation for Pb−Pb collisions at $\sqrt{s_{\mathrm{NN}}}$ = 2.76 TeV (LHC13f3c).

5.5.2 Closure studies

Efficiency maps in the angular (η, φ) phase space of the AMPT events are observed to be binomial in nature in the kinematic acceptance of the analysis. As an example Fig. 5.18 shows the efficiency maps for $0.4 \leq p_{\mathrm{T}} \leq 0.6\,\mathrm{GeV/c}$ and $0.6 \leq p_{\mathrm{T}} \leq 0.8\,\mathrm{GeV/c}$ bin in case of M = 60 along each dimension. From LHC12a11a, NFM for q = 2 to 5 are determined for reconstructed AMPT, generated and

reconstructed-corrected AMPT events. A closure of around 99-100% with and without corrections is obtained, for ln M^2 upto 8.7 as is shown in Fig. 5.19.

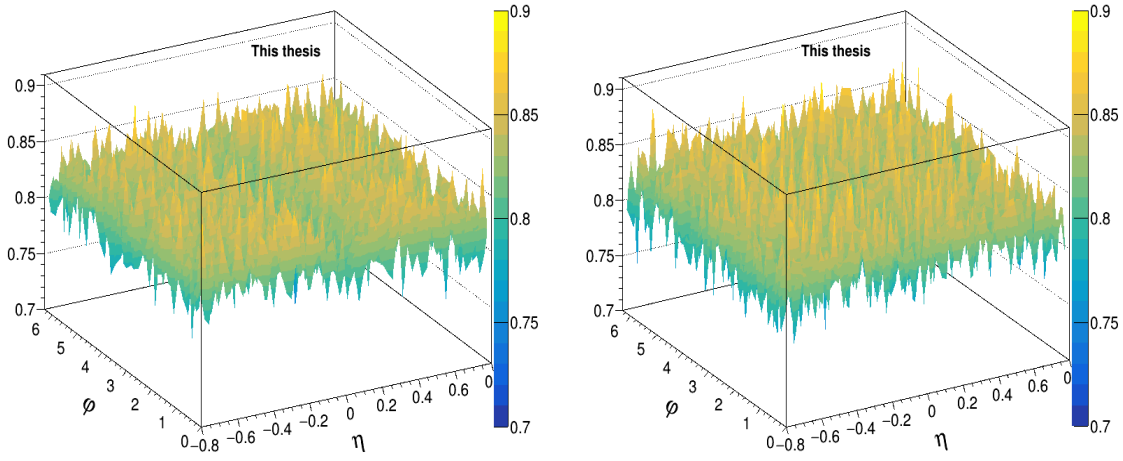

(a) (b)

Figure 5.18. AMPT (LHC12a11a): Two dimensional tracking efficiency maps in (η, ϕ) phase space partitioned with $M=$ 60 for tracks in a) $0.4 \leq p_{\mathrm{T}} \leq 0.6$ GeV/c bin and b) $0.6 \leq p_{\mathrm{T}} \leq 0.8$ GeV/c bin.

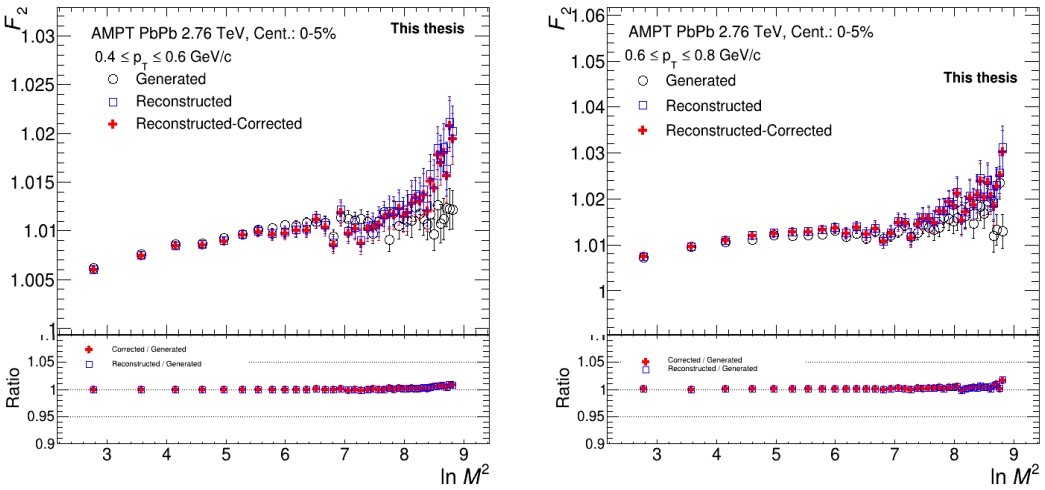

(a) (b)

Figure 5.19. AMPT (LHC12a11a): F_{q} vs ln M^2 plot for generated, reconstructed, and reconstructed-corrected factorial moments in (a) $0.4 \leq p_{\mathrm{T}} \leq 0.6$ GeV/c bin (b) $0.6 \leq p_{\mathrm{T}} \leq 0.8$ GeV/c bin for 0-5% central events with Pb–Pb collisions at $\sqrt{s_{\mathrm{NN}}} = 2.76$ TeV. Bottom panels show the ratio reconstructed/generated and reconstructed-corrected/generated showing the robustness of the NFM against uniform efficiencies.

5.5.3 Scaling behaviour

From the analysis of AMPT events, NFM are determined. Fig. 5.20 shows $\ln F_{\mathrm{q}}(M)$ dependence on $\ln M^2$ for q = 2, 3, 4 and 5. There are large error bars at high M and high q. Size of event sample in LHC12a11a production, for 0−5% central events is very small that results into large fluctuations as resolution of phase space that is (M) and order of the moments q increases.

To investigate this scaling behaviour in case of the AMPT model, three event samples with high statistics, generated using AMPT in three different modes without detector geometry, are analyzed. The size of these event samples from fast simulation using the AMPT are tabulated in Table 5.3.

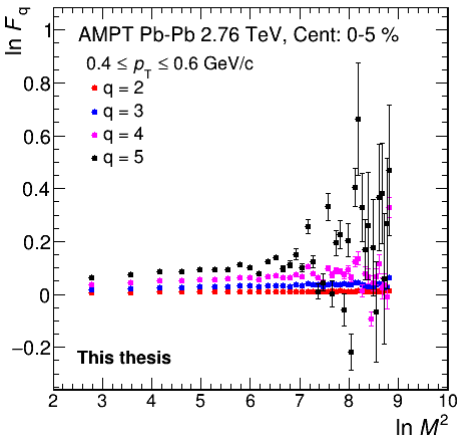

Figure 5.20. AMPT (LHC12a11a): $\ln F_{\mathrm{q}}(M)$ vs $\ln M^2$ plot (M-scaling) for q = 2, 3, 4 and 5 for charged particles generated with $0.4 \leq p_{\mathrm{T}} \leq 0.6$ GeV/c.

Table 5.3. AMPT fast simulation events.

Production name	Mode	No. of events
LHC13f3a	String melting ON, rescattering OFF	39 M
LHC13f3b	String melting OFF, rescattering ON	53 M
LHC13f3c	String melting ON, rescattering ON	39 M

For the String Melting ON and Rescattering ON mode of the AMPT events that is events from productions LHC13f3c, plots for $\ln F_{\mathrm{q}}(M)$ as function of $\ln M^2$ and $\ln F_2$ are shown in Fig. 5.21. For all values of M and q, $\ln F_{\mathrm{q}} \geq 0$ but with no power-law indicating no correlations in particle generation. $F_{\mathrm{q}}(M)$ is independent

of M with $F_{q+1} > F_q$ that gives F-scaling behaviour as in Fig. 5.21(b). Similar scaling behaviours of NFMs are observed in case of LHC13f3a and LHC13f3b.

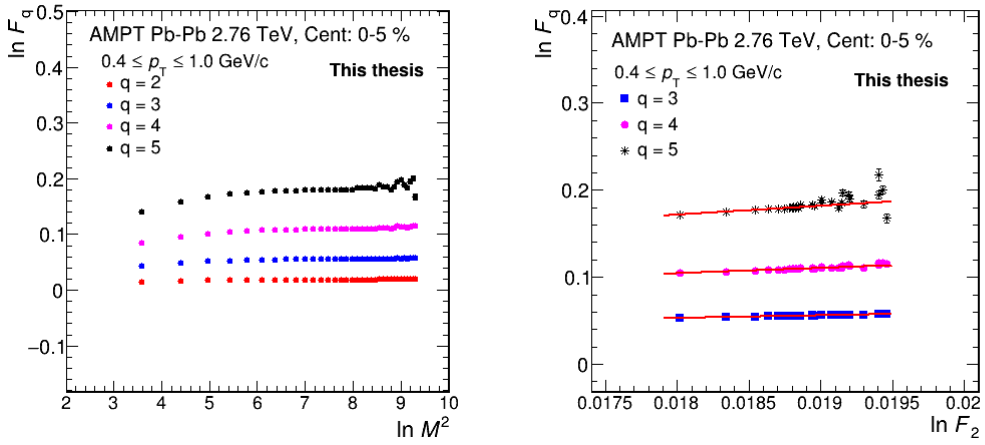

(a) (b)

Figure 5.21. AMPT (LHC13f3c): (a) ln $F_q(M)$ vs ln M^2 plot (M-scaling) for q = 2, 3, 4 and 5 (b) ln F_q versus ln F_2 with linear fits in the higher M^2 region to get scaling exponent.

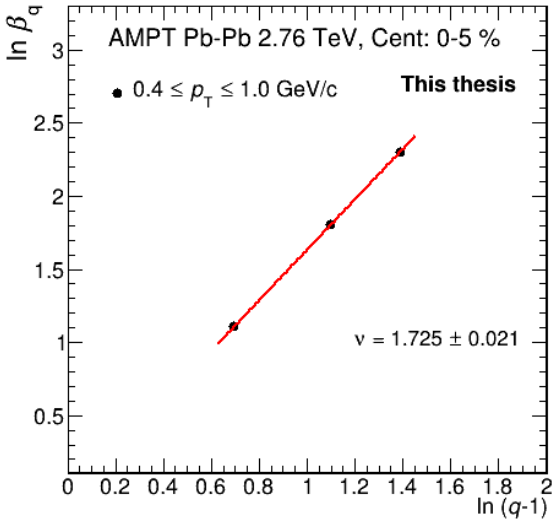

Figure 5.22. AMPT (LHC13f3c): Scaling exponent ν from the ln β_q vs ln $(q-1)$ plot for $0.4 \leq p_T \leq 1.0$ GeV/c p_T bin.

From the linear fits performed in F-scaling plot, scaling exponent (ν) is found to be 1.72±0.02 for the $0.4 \leq p_T \leq 1.0$ GeV/c bin (Fig.5.22). Similarly, investigations are carried for other p_T intervals and event samples with other AMPT modes. The scaling exponent (ν) values obtained from the analysis performed for various

p_{T} bins with different modes are tabulated in the Table 5.4. It is observed that for all cases $\nu > 1.63$ which is a value $>>$ 1.304, a universal value of scaling exponent with formalism for second order phase transition using Ginzburg-Landau theory. This is no surprise as the AMPT event generator does not have physics of phase transition. However, results obtained here give the baseline to understand results from experimental data.

Table 5.4. Scaling exponent (ν) from the AMPT fast simulation.

p_{T} **bin (GeV/**c**)**	**Scaling Exponents(**ν**)**		
	String melting ON, rescattering OFF (LHC13f3a)	String melting OFF, rescattering ON (LHC13f3b)	String melting ON, rescattering ON (LHC13f3c)
$0.4 \leq p_{\mathrm{T}} \leq 0.6$	1.68±0.01	1.67±0.01	1.67±0.01
$0.6 \leq p_{\mathrm{T}} \leq 0.8$	1.68±0.01	1.69±0.01	1.68±0.01
$0.9 \leq p_{\mathrm{T}} \leq 1.1$	1.63±0.02	1.66±0.01	1.64±0.02
$0.4 \leq p_{\mathrm{T}} \leq 1.0$	1.73±0.02	1.67±0.01	1.73±0.01
$0.4 \leq p_{\mathrm{T}} \leq 1.5$	1.68±0.01	1.70±0.01	1.72±0.01
$0.4 \leq p_{\mathrm{T}} \leq 2.0$	1.71±0.01	1.71±0.02	1.72±0.01
$0.6 \leq p_{\mathrm{T}} \leq 2.0$	1.68±0.02	1.68±0.02	1.66±0.02

5.5.4 Fractal parameters

The intermittency index ϕ_q, is the slope of line fits on $\ln F_{\mathrm{q}}(M)$ vs $\ln M^2$ plots. For the dataset LHC13f3c, Fig. 5.23 shows the $\ln F_{\mathrm{q}}(M)$ vs $\ln M^2$ plots for high M-region where the fits are performed. The fractal parameters, D_{q} and λ_{q}, are calculated from intermittency index (ϕ_q) using equations 3.14 and 3.15 respectively. Fig. 5.24(a) gives the plot of D_{q} as a function of q, showing a constant trend with increasing q. This suggests the monofractal nature of the particle generation in AMPT. Fig. 5.24(b) shows the variation of λ_{q} with q. λ_{q} exhibits a decreasing trend with increasing q, without any discernible minima and thus the system formed is characterized as a single-phase system.

The model based analysis using intermittency analysis, as discussed in chapter 3, for the HIJING and the AMPT model available from the ALICE production,

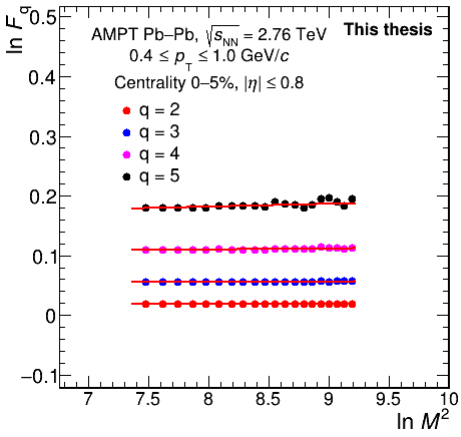

Figure 5.23. AMPT (LHC13f3c): ln $F_{\mathrm{q}}(M)$ vs ln M^2 plot (M-scaling) for q = 2, 3, 4 and 5 with line fits at higher M^2 for $0.4 \leq p_{\mathrm{T}} \leq 1.0$ GeV/c p_{T} bin.

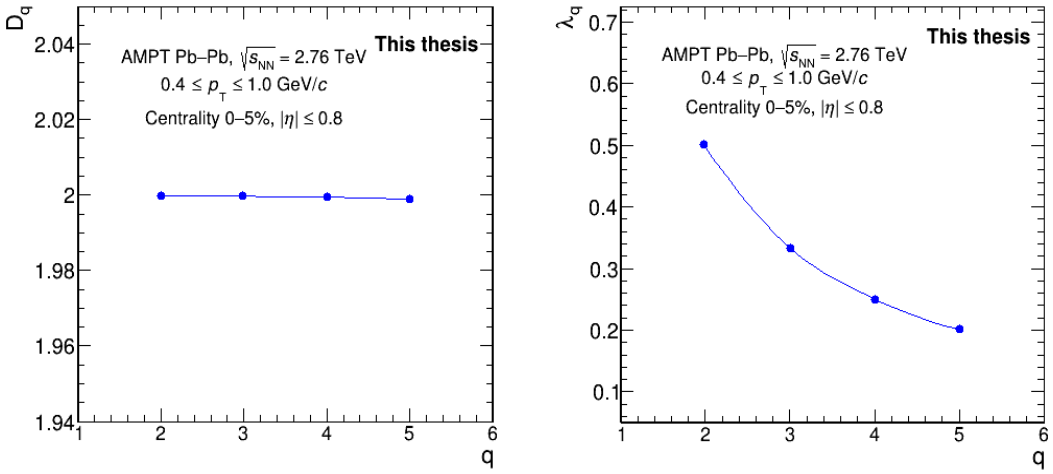

(a) (b)

Figure 5.24. AMPT (LHC13f3c): (a)D_{q} and (b) λ_{q} as a function of q in $0.4 \leq p_{\mathrm{T}} \leq 1.0$ GeV/c bin in 0-5% central events.

is presented in this chapter. To summarize, the closure study is performed for the charged particles generated with $|\eta| \leq 0.8$ and the different p_{T} bins (< 1.0 GeV/c). that gives 99 to 100% closure for the second order NFM (F_2) for all M values studied. While no scaling is seen in HIJING, the AMPT shows a very weak power-law at high M region where resolution of the phase space is very high. No robust self-similar behaviour in particle generation is observed for these models. The scaling exponent ν obtained for all transverse momentum bins studied in the soft p_{T} region are independent of p_{T} value with $\nu > 1.6$. In the absence of any phase transition physics implemented in these models, the observations made are in line with the expectations. These Monte Carlo studies provide a fundamental framework for interpreting ALICE data analysis discussed in next chapter.

Chapter 6

ALICE data analysis

To improve upon our knowledge about the multiparticle dynamics, one of the basic techniques is to investigate multiparticle correlations. The introduction of intermittency technique, that uses factorial moments, in the field of heavy-ion collisions has made possible the study of correlations in the data which otherwise seemed to be interactable. Observations and results from the factorial moment analysis, specifically normalized factorial moment analysis [72], of charged particles produced in Pb−Pb collisions at $\sqrt{s_{\rm NN}}$ = 2.76 TeV measured using ALICE [90] detector at LHC [34] are presented in this chapter.

6.1 Quality Assurance Plots

The ALICE data analyzed here was recorded in 2010 during RUN 1 of the LHC operations. The run production name of the data set is LHC10h. The various run numbers are given in Appendix D. Analysis is performed over 83 million events.

6.1.1 Event selection

For event selection, the trigger selection criteria used is same as discussed in section 5.3.1. The Pb−Pb collision data is collected using Minimum Bias (kMB) trigger, which requires at least one hit in V0A or V0C or Silicon Pixel Detectors (SPD). Events for which the primary vertex lies within 10 cm ($|V_z| \leq 10$ cm) are selected. The V_z distribution of the selected events is shown in Fig. 6.1(a). Limiting the primary V_z range to ± 10 cm ensures high acceptance and efficiency for particle detection and tracking as discussed in section 5.3.1. Further the most central

events with 0−5% centrality are mainly studied to look for fluctuations in the spatial patterns. Fig.6.1(b) shows the centrality distribution of these events (0.8 M).

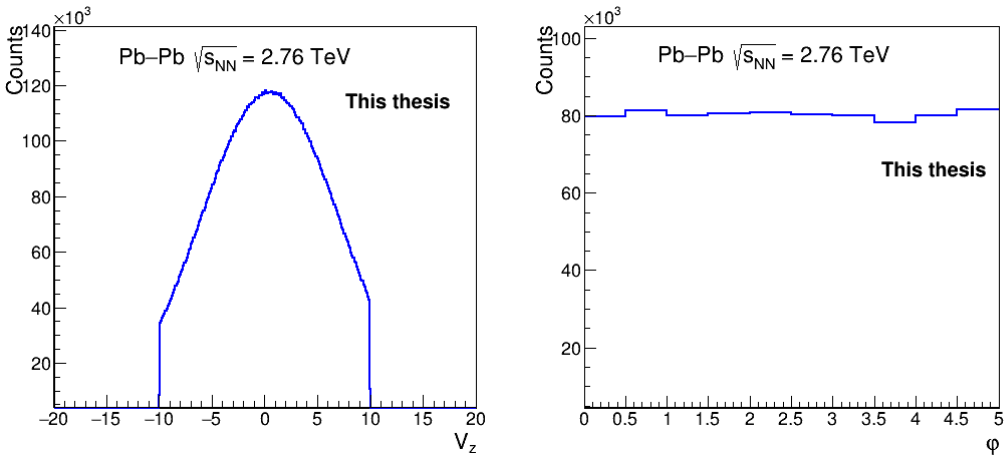

(a) (b)

Figure 6.1. (a) V_z distribution (b) Centrality distribution of 0−5% central Pb−Pb collisions at $\sqrt{s_{\rm NN}}$ = 2.76 TeV recorded using the ALICE at LHC.

6.1.2 Track selection

The track selection cuts that are used for HIJING events analysis (section 5.3.3), same track selection cuts are used for the experimental data analysis. Kinematic cuts applied are given in Table 5.2. Analysis has been performed for the charged particles in the various transverse momentum intervals for the tracks with $p_{\rm T} \leq 2.0$ GeV/c. The multiplicity distributions for the charged particle tracks in these bins are given in Fig. 6.2(a) and 6.2(b) for narrow non-overlapping ($\delta p_{\rm T}$ = 0.2) $p_{\rm T}$ bins and wide overlapping $p_{\rm T}$ bins. η and φ distributions for the full data set of these tracks produced in these $p_{\rm T}$ intervals are shown in Figs. 6.3 and 6.4. Trivial trends for experimental multiplicity, η and φ distributions are observed with no major dips or peaks. Soft charged particles with $p_{\rm T} \geq 0.4$ GeV/c have been considered for the reason that $p_{\rm T}$ (transverse momentum) efficiency for charged particles in $0.4 \leq\ p_{\rm T} \leq 5.0$ GeV/c range is uniform/binomial (as shown in Fig. 5.5).

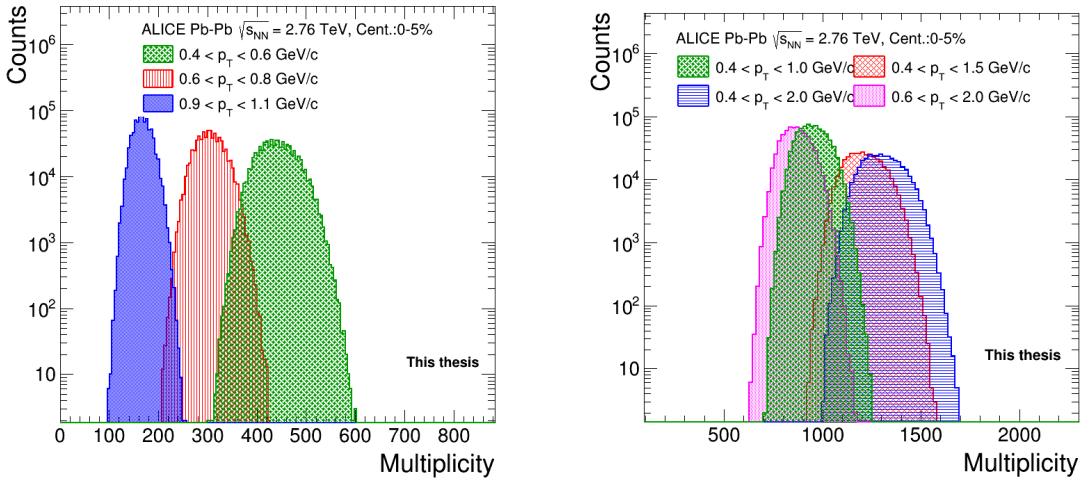

(a) (b)

Figure 6.2. Multiplicity distributions of the charged particles produced in (a) small non-overlapping p_{T} bins: $0.4 \leq\ p_{\mathrm{T}} \leq 0.6$ GeV/c, $0.6 \leq\ p_{\mathrm{T}} \leq 0.8$ GeV/c and $0.9 \leq\ p_{\mathrm{T}} \leq 1.1$ GeV/c and (b) wide overlapping p_{T} bins: $0.4 \leq\ p_{\mathrm{T}} \leq 1.0$ GeV/c, $0.4 \leq\ p_{\mathrm{T}} \leq 1.5$ GeV/c, $0.4 \leq\ p_{\mathrm{T}} \leq 2.0$ GeV/c and $0.6 \leq\ p_{\mathrm{T}} \leq 2.0$ GeV/c.

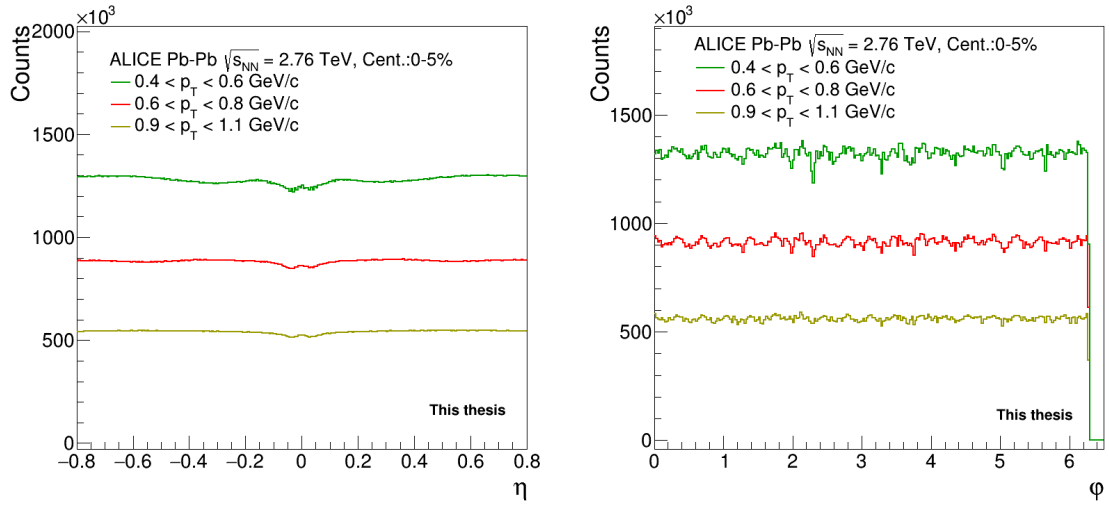

(a) (b)

Figure 6.3. (a) η distributions (b) φ distributions, of the charged particles produced in the small non-overlapping ($\delta p_{\mathrm{T}} = 0.2$) transverse momentum bins: $0.4 \leq\ p_{\mathrm{T}} \leq 0.6$ GeV/c, $0.6 \leq\ p_{\mathrm{T}} \leq 0.8$ GeV/c and $0.9 \leq\ p_{\mathrm{T}} \leq 1.1$ GeV/c.

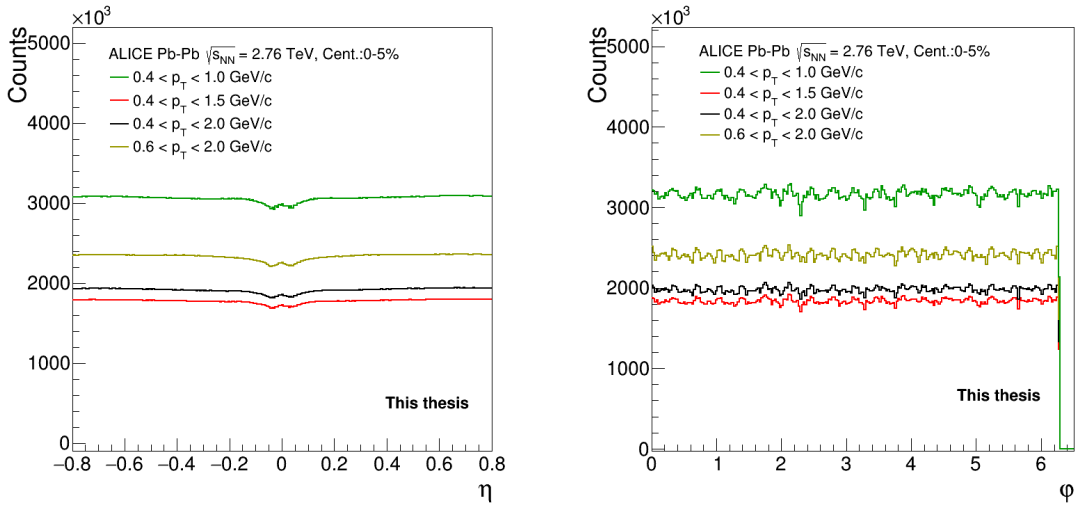

(a) (b)

Figure 6.4. (a) η distributions (b) φ distributions, of charged particles in overlapping transverse momentum bins: $0.4 \leq p_{\mathrm{T}} \leq 1.0\,\mathrm{GeV/c}$, $0.4 \leq p_{\mathrm{T}} \leq 1.5\,\mathrm{GeV/c}$, $0.4 \leq p_{\mathrm{T}} \leq 2.0\,\mathrm{GeV/c}$ and $0.4 \leq p_{\mathrm{T}} \leq 1.0\,\mathrm{GeV/c}$.

6.2 Observations and results

The analysis methodology given in chapter 3 is performed for the ALICE data on event-by-event basis. Charged particles in an event, in the selected kinematically accepted region are mapped onto the two dimensional (η, φ) phase space, partitioned into M^2 bins. The number of particles going in each bin defines the bin multiplicity (n_{ie}) that varies from bin to bin and is function of the dynamics of the system. In this analysis the number of bins into which the phase space is divided to form a matrix of cells, the minimum value of M is taken as 6 and maximum value of M varies depending on the MC closure (disussed in section 5.4.2).

6.2.1 Average bin content

For the normalized factorial moments (NFM), as defined in Eq. 3.8, the normalization factor is the average bin content. Fig. 6.5 shows the average bin content as function of $\ln M^2$ for the p_{T} bins analyzed here. A trivial decreasing behaviour of the average bin content is observed with increase in M value. This implies that mean particle density per bin decreases with increase in M value.

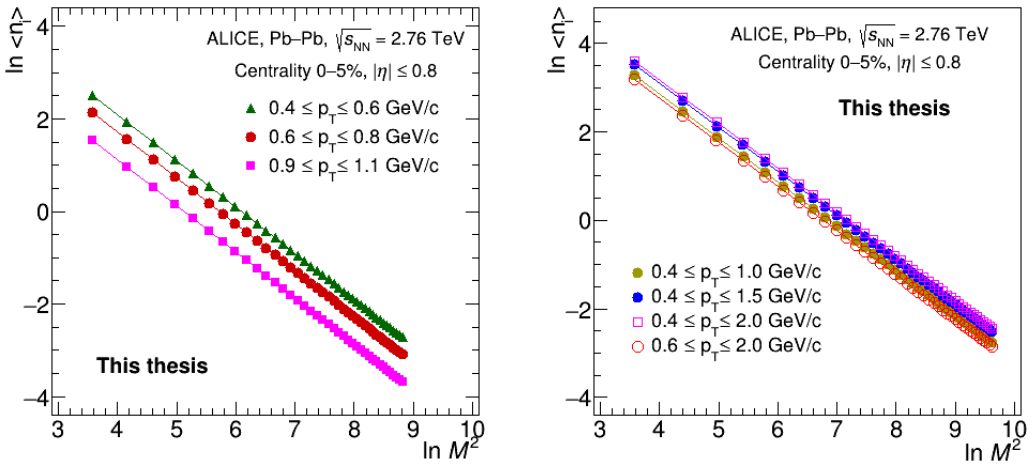

Figure 6.5. log-log plot of average bin content of charged particles in two dimensional (η, φ) phase space as a function of M^2 in various p_{T} ranges with $|\eta| \leq 0.8$ and $0 \leq \varphi \leq 2\pi$ are shown. Left plot shows the average bin content in narrow non-overlapping p_{T} intervals, while the right one shows the same for wide overlapping p_{T} intervals in the central Pb−Pb collision events at $\sqrt{s_{\mathrm{NN}}} = 2.76$ TeV. M_{max} is different in each case depending on closure.

6.2.2 f_q^e distributions

To determine normalized factorial moments $(F_{\mathrm{q}}(M))$ for $q = 2$, 3, 4 and 5, the phase space cells that are considered are the ones for which the the bin content $(n_{ie}) \geq$ q. As defined in Eq. 3.3, for each event first the factorial moments f_{q} are determined for all q and M values. f_{q} values define bin-to-bin fluctuations in the particle density in the (η, φ) phase space. As an example, for the transverse momentum bin $0.4 \leq p_{\mathrm{T}} \leq 1.0\,\mathrm{GeV/c}$, the f_{q} distributions for $q = 2$, 3, 4 and 5, when M = 30 and 60, are shown in Figs. 6.6(a) and 6.6(b). It is observed that as order of the moments increase, the width of distributions increase. That means fluctuations in the spatial configurations increase from event-to-event as q increases. Similar trends are observed for all M values and in all p_{T} bins.

6.2.3 Scaling behaviour

The event factorial moment distributions are used to determine the normalized factorial moments (NFM), $F_{\mathrm{q}}(M)$ of the charged particle data from Pb−Pb collisions, as defined in the Eq. 3.8. $F_{\mathrm{q}}(M)$ moments are determined for $q = 2$, 3, 4

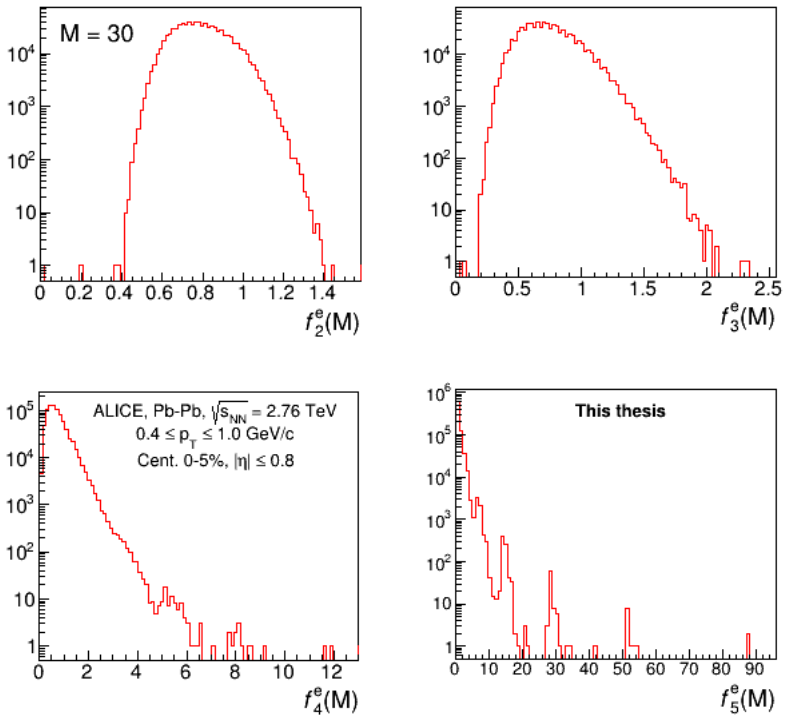

(a)

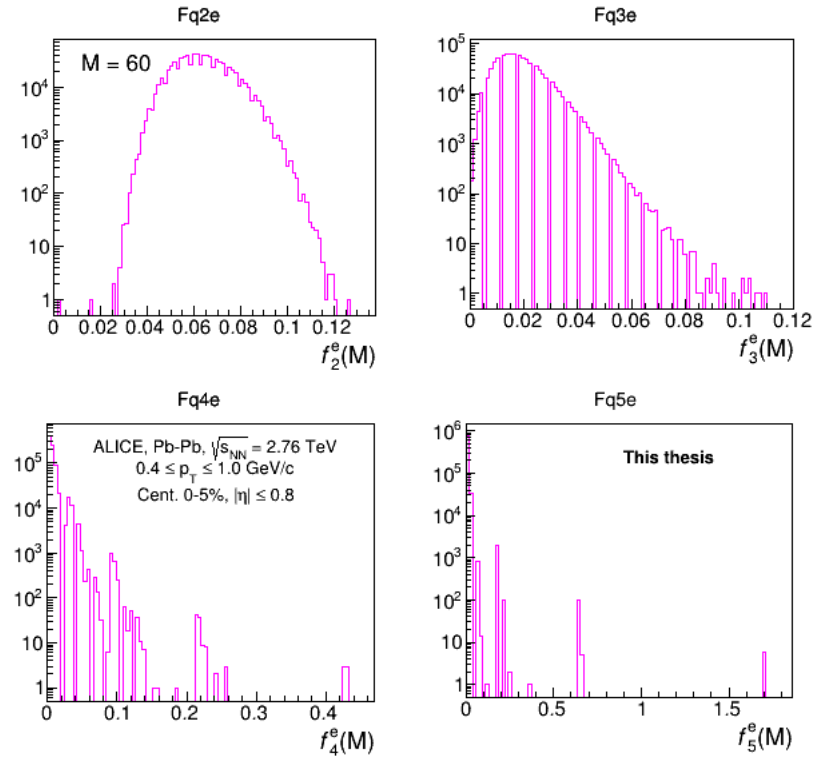

(b)

Figure 6.6. f_{q}^{e} distributions for q = 2, 3, 4 and 5 in case of (a) M = 30 and (b) M = 60, for charged particles produced in $0.4 \leq p_{\mathrm{T}} \leq 1.0\,\mathrm{GeV/c}$ bin during Pb−Pb central collision at $\sqrt{s_{\mathrm{NN}}}$ = 2.76 TeV recorded using ALICE at CERN.

and 5 and M = 6 to 123 in the intervals of 3. The observations on the two scaling behaviours of $F_q(M)$ moments are given below.

6.2.3.1 M-scaling

Dependence of NFM (F_q) on M is studied for the data using log-log plots of F_q versus M^2. The resolution scaling behaviour of the normalized factorial moments ($F_q(M)$) in the (η, φ) phase space within the $0.4 \leq p_T \leq 1.0$ GeV/c range and $|\eta| \leq 0.8$ is given in Fig. 6.7(a) for q = 2, 3, 4, and 5. It is observed that as the M value increases, $F_q(M)$ increases, showing a consistent monotonic variation of lnF_q with respect to lnM^2 across all q values. Further, $\ln F_q > 0$ and multiple linear regions are observed. This shows intermittency in ALICE data, where *intermittency* is defined as the scaling of NFM of multiplicity fluctuations over wide range of bin sizes especially in the region of high resolution (high M). At high M values, observation of intermittency signal, i.e., a linear relationship between $lnF_q(M)$ and lnM^2 (Fig. 6.7(b)) indicates presence of a scale-invariant patterns in the distribution of particles. This is one of the important observations of this work. From first analysis based on this methodology at LHC energies, a robust power-law behaviour of F_q with M^2 is observed. No saturation or oscillatory behaviour of $F_q(M)$ with M^2 is seen as was a case in HIJING and Toy model events. A straight line fit to the plots at high M values, as depicted in the Fig. 6.8(a), yields the intermittency indices, denoted by ϕ_q.

6.2.3.2 F-scaling

Like observation of M-scaling in the ALICE data for charged particles, F-scaling is also observed where a linear dependence of $F_q(M)$ for q = 3, 4 and 5 on $F_2(M)$ is seen in Fig. 6.9(a). Since $F_{q+1}(M) > F_q(M)$ observation of F-scaling is obvious. The order-scaling which in short is known as F-scaling is observed for the first time for the charged particles produced in Pb−Pb collisions recorded with TPC and ITS in ALICE. Fig. 6.9(a) shows F-scaling for the charged particle tracks in $0.4 \leq p_T \leq 1.0$ GeV/c bin for all M values. Whereas Fig. 6.9(b) shows the $\ln F_q$ on $\ln F_2$ for high M values with $81 \leq M \leq 105$. In this M region, $F_q(M)$ has linear

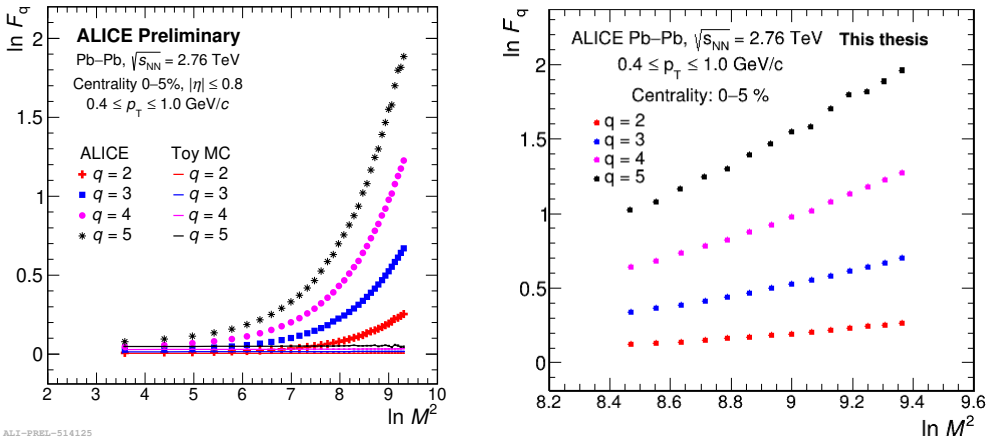

(a) (b)

Figure 6.7. $lnF_{\mathrm{q}}(M)$ vs lnM^2 plot (M-scaling) for q = 2, 3, 4 and 5 (a) for all M (b) for the high M values. A power law growth of $F_{\mathrm{q}}(M)$ with M is observed for the charged particles produced in $0.4 \leq p_{\mathrm{T}} \leq 1.0\,\mathrm{GeV/c}$ bin. Statistical uncertainties calculated using sub-sampling method, as discussed in section 3.5, are smeared into the markers.

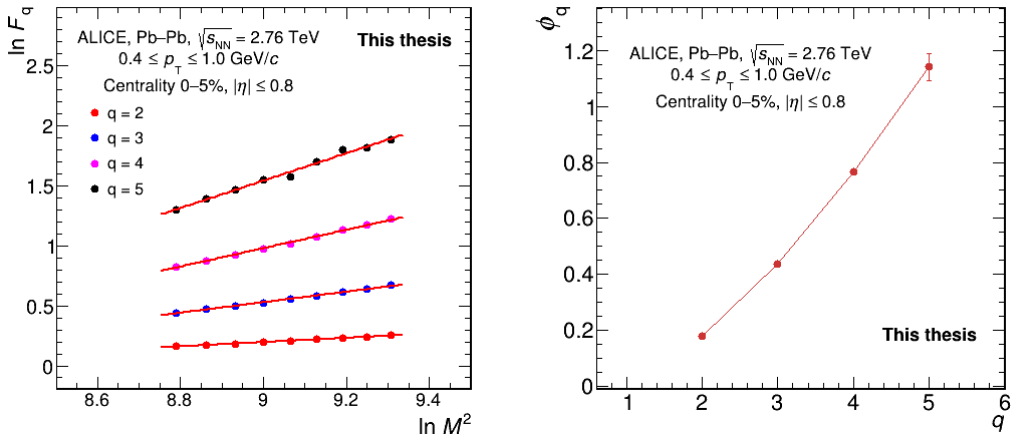

(a) (b)

Figure 6.8. ALICE: a) M-scaling with linear fits in the higher M region with 98% Monte Carlo closure. Lines joining data points are line fits. b) Dependence of ϕ_{q} on q for Pb−Pb collisions at $\sqrt{s_{\mathrm{NN}}}$ = 2.76 TeV. Line joining data points is to guide the eye.

dependence on M and there is 98 - 100% Monte Carlo closure.

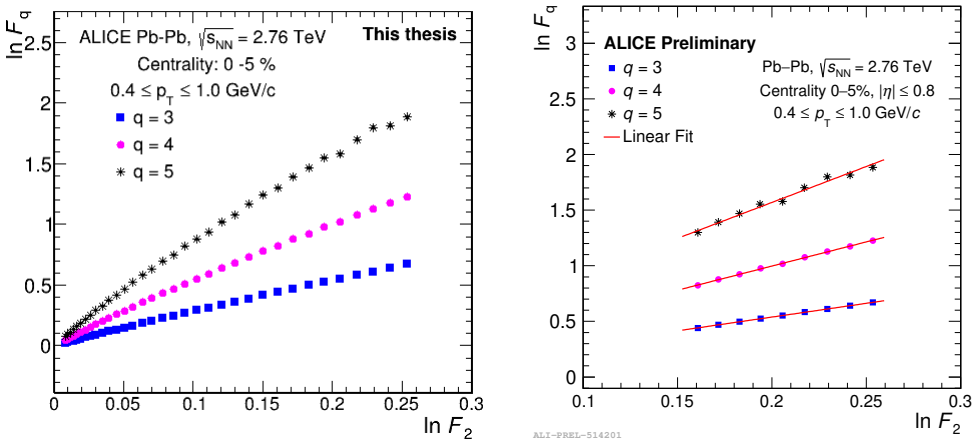

(a) (b)

Figure 6.9. Dependence of $\ln F_{\mathrm{q}}$ on $\ln F_2$ for q = 3, 4 and 5 (a) for all M (b) in the higher M region for p_{T} bin $0.4 \leq p_{\mathrm{T}} \leq 1.0\,\mathrm{GeV/c}$. Line fits on data points corresponding to high M values are performed to get slopes, β_q. Lines connecting data points in (b) show the line fitting. Statistical uncertainties are smeared into the markers.

6.2.3.3 Scaling exponent (ν)

Line fits to the F-scaling graphs (Fig. 6.9(b)) give slopes β_q. Further performing line fit to the log-log plot between β_q and (q−1) as shown in Fig. 6.10 gives slope, termed as scaling exponent, denoted by ν, which is dimensionless, scaling exponent that quantitatively summarizes the critical nature of system under study. It has been predicted to give a value of 1.304 in case there is transition taking place in line with formalism for second order phase transition as per Ginzburg-Landau theory [151]. The scaling exponent for data is found to be **1.39 ± 0.01**. For the critical fluctuations in SCR model [72], the scaling exponent value for two dimensional intermittency analysis is obtained as 1.41 which is very close to the ν value obtained in this work. This result hints that the system created in ALICE in RUN 1 is either close to critical point or has remnants of dynamical fluctuations after having passed through the critical point. These observations made here need further investigations to understand the results in light of critical fluctuations, self-similarity and cross-over type of phase transition physics predicted to be there at LHC.

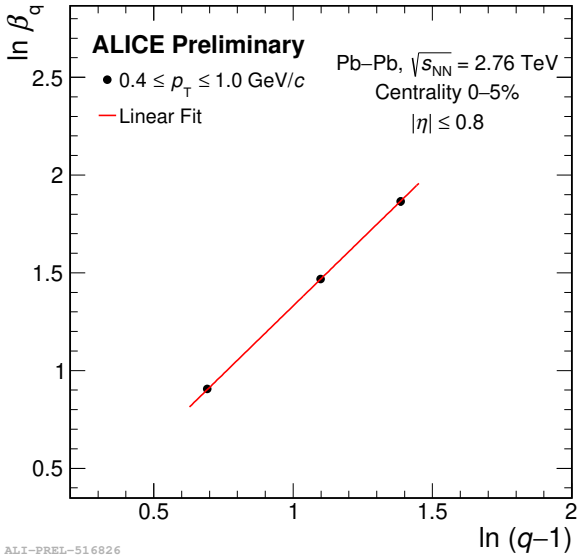

Figure 6.10. Scaling exponent ν from the ln β_q vs ln $(q-1)$ plot is 1.39 $\pm$ 0.01. Line joining data points is the line fit and small errors due to line fit to get slopes, β_q, are overlapped by the markers.

6.2.4 Fractal parameters

Observation of intermittency opens up further scope to investigate the fractal parameters, which provide insight into the multifractal nature of particle production in heavy-ion collisions. Fractal dimension D_q (Eq. 3.14) and coefficient λ_q (Eq. 3.15) are related to the intermittency indices ϕ_q. These indices are the slope values from the line fit to the high M region of ln F_q vs ln M^2 plot. For the $0.4 \leq p_T \leq 1.0$ GeV/c bin, Fig. 6.8(a) shows the ln F_q vs ln M^2 plot with linear fits, specifically in the higher M region, the slopes from which give the value of intermittency indices (ϕ_q), plotted against q (Fig. 6.8(b)). Intermittency indices are calculated for all the p_T bins under study and their values (ϕ_q) are tabulated in Table 6.1. It can be seen that in general ϕ_q increases with q and decreases with increasing p_T.

6.2.4.1 Fractal dimension D_q

The fractal dimension (D_q) for $q = 2$ to 5 is calculated from ϕ_q using Eq. 3.14. For the present analysis, in $0.4 \leq p_T \leq 1.0$ GeV/c bin, D_q as a function of q is shown in Fig. 6.11. It is noteworthy that the fractal parameter D_q decreases as

Table 6.1. Intermittency indices for q = 2, 3, 4 and 5 in various p_{T} bins for charged particles produced in 0−5% central Pb−Pb collisions at $\sqrt{s_{\mathrm{NN}}}$ = 2.76 TeV.

p_{T} bins (GeV/c)	Intermittency indices(ϕ_q)			
	$q = 2$	$q = 3$	$q = 4$	$q = 5$
$0.4 \leq p_{\mathrm{T}} \leq 0.6$	0.1881±0.0003	0.4537±0.0016	0.7786±0.0095	0.5194±0.0553
$0.6 \leq p_{\mathrm{T}} \leq 0.8$	0.1084±0.0006	0.2809±0.0038	0.5172±0.0248	0.7936±0.1659
$0.9 \leq p_{\mathrm{T}} \leq 1.1$	0.0583±0.0004	0.1568±0.0035	0.2125±0.0281	-
$0.4 \leq p_{\mathrm{T}} \leq 1.0$	0.1776±0.0001	0.4373±0.0007	0.7650±0.0039	1.1396±0.0211
$0.4 \leq p_{\mathrm{T}} \leq 1.5$	0.1363±0.0001	0.3501±0.0005	0.4926±0.0027	0.4675±0.0142
$0.4 \leq p_{\mathrm{T}} \leq 2.0$	0.1386±0.0001	0.3536±0.0005	0.6281±0.0028	0.9467±0.0152
$0.6 \leq p_{\mathrm{T}} \leq 2.0$	0.1247±0.0002	0.3190±0.0014	0.5725±0.0091	0.9165±0.0618

q increases indicating multifractal nature of the multiplicity fluctuations in the central ALICE data of charged particles recorded using TPC and ITS. This is contrary to what is observed for AMPT and Toy model events (Chapter 4 and Chapter 5).

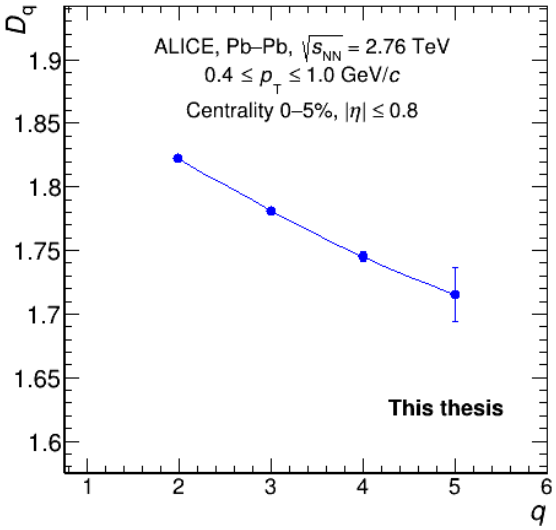

Figure 6.11. Variation of D_{q} with q for charged particles produced in central Pb−Pb collision events in $0.4 \leq p_{\mathrm{T}} \leq 1.0$ GeV/c bin. Line joining data points is to guide the eye.

6.2.4.2 Coefficient λ_{q}

The structure of different phases in self-similar multiparticle complex system created in particle collisions has been investigated using a coefficient (λ_{q}) [172]. The coefficient (λ_{q}) is anticipated to exhibit a minimum value at a specific $q = q_c$ if

there is non-thermal phase transition. Using Eq. 3.15, (λ_q) for q = 2 to 7 are determined from the ϕ_q values. To check whether λ_q has any minima, calculations are done for q = 2 to 7. For ALICE data, Fig. 6.12 shows the variation of λ_q with q for the charged particles in p_T bin $0.4 \leq p_T \leq 1.0$ GeV/c from 0−5% central Pb−Pb collision events. ϕ_q gives large fitting error for q = 6 and 7 and no definitive conclusions can be drawn. λ_q consistently decreases with increasing q and does not indicate any minima up to q = 7. Analysis at higher energies, where particle densities will be higher, may give some more insight on this.

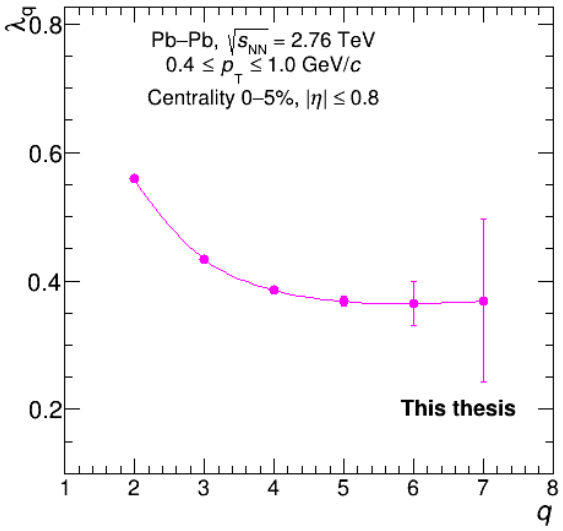

Figure 6.12. λ_q as a function of q for q = 2 to 7 for charged particles produced in $0.4 \leq p_T \leq 1.0$ GeV/c bin. Line joining data points is to guide the eye.

The observations and results presented here were for the charged particles produced in the $0.4 \leq p_T \leq 1.0$ GeV/c transverse momentum bin. Dependence of the observables on the p_T bin and p_T bin width is discussed below.

6.3 Dependence of M-scaling on p_T

To further investigate the scaling behaviour of normalized factorial moments, a dependence of $F_q(M)$ moments on the transverse momentum bins is carried. Analysis is performed for all the p_T bins (Table 5.2). The M-scaling graphs for the narrow p_T bins with width δp_T = 0.2 GeV/c are shown in Fig. 6.13 and the wide p_T

bins with $\delta p_{\mathrm{T}} > 0.2$ GeV/c are shown in Fig. 6.14. A power-law growth of $F_{\mathrm{q}}(M)$ moments with M is seen for all q and p_{T} bins. A similar scaling behaviour is seen in all the p_{T} bins with quantitative difference which grows with M, indicating increase in fluctuations in the charged particle density in the (η, φ) phase space as resolution of bins increases. However, at higher p_{T} that is in $0.9 \leq p_{\mathrm{T}} \leq 1.1$ GeV/c transverse momentum bin, there are large fluctuations and a smooth growth of F_{q} with M is not observed for $q > 3$. The reason can be that for $\delta p_{\mathrm{T}} = 0.2$ GeV/c, at higher p_{T}, the average bin content is less. In addition, as resolution increases with increase in M, if there are not many bins with bin multiplicity greater than q these fluctuations are expected.

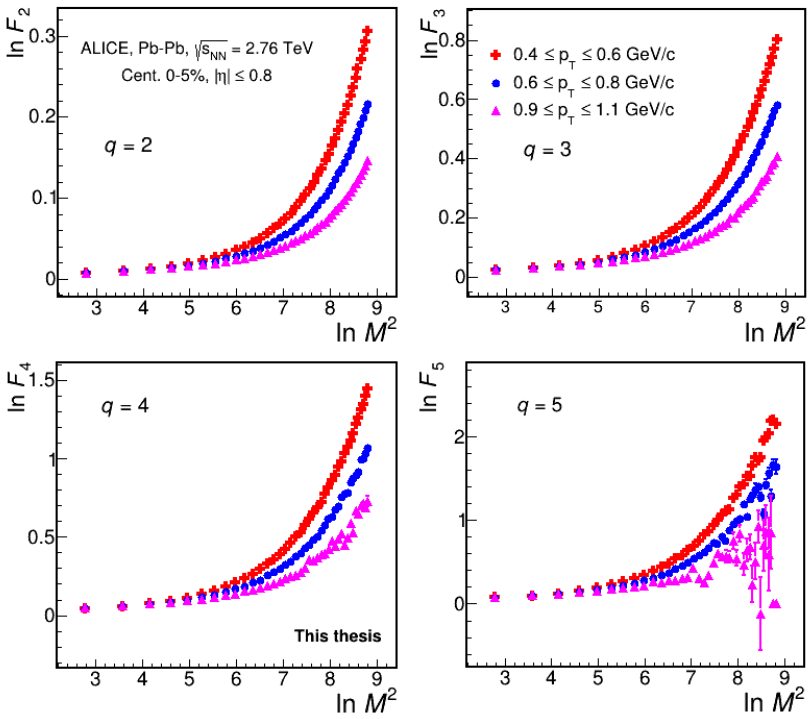

Figure 6.13. $lnF_{\mathrm{q}}(M)$ vs lnM^2 plots (M-scaling) for q = 2, 3, 4 and 5 for charged particle produced in narrow/non-overlapping p_{T} bins in the mid-rapidity region of the most central events recorded using ALICE.

Increasing the width of p_{T} bin gives the same qualitative behaviour of the M-scaling (Fig. 6.14). With increase in the width of the p_{T} bin from $0.4 \leq p_{\mathrm{T}} \leq 1.0$ GeV/c to $0.4 \leq p_{\mathrm{T}} \leq 1.5$ GeV/c and to $0.4 \leq p_{\mathrm{T}} \leq 2.0$ GeV/c in the (η, φ) phase space having $|\eta| \leq 0.8$ and $0 \leq \varphi \leq 2\pi$, there is increase in the number of particles in the phase space. This increase in the width of p_{T} reduces the $F_{\mathrm{q}}(M)$ values however, the scaling behaviour remains same that is there is

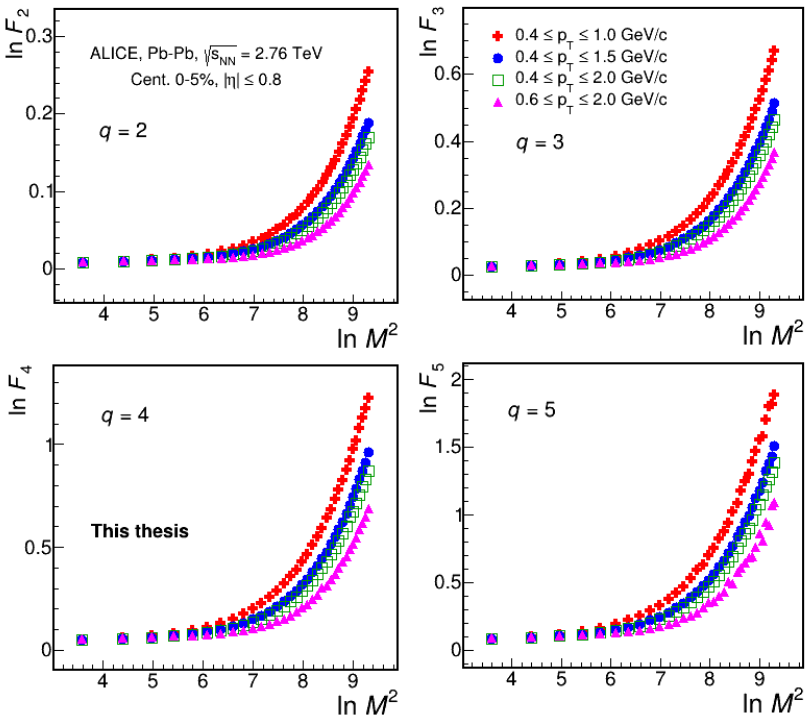

Figure 6.14. $lnF_{\mathrm{q}}(M)$ vs lnM^2 plots (M-scaling) for q = 2, 3, 4 and 5 for charged particle produced in wide/overlapping p_{T} bins in the mid-rapidity region of the most central events recorded using ALICE.

power-law growth of $F_{\mathrm{q}}(M)$ with M having multiple linear regions. Further it is observed that with increase in transverse momentum there is a continuous decrease in the $F_{\mathrm{q}}(M)$ values. A wider p_{T} bin at higher p_{T}, $0.6 \leq p_{\mathrm{T}} \leq 2.0\,\mathrm{GeV/c}$, also shows the same scaling behaviour but with quantitatively low values of F_{q}. This bin has low multiplicity in comparison to $0.4 \leq p_{\mathrm{T}} \leq 1.5\,\mathrm{GeV/c}$ bin but F_{q} values are smaller with large fluctuations in case of $q = 5$.

6.4 Dependence of ν on p_{T}

The plots of $\ln F_{\mathrm{q}}$ versus $\ln F_2$ and $\ln \beta_{\mathrm{q}}$ versus $\ln(\mathrm{q}-1)$ for the p_{T} bins with $\delta p_{\mathrm{T}} = 0.2$ GeV/c are given in Fig. 6.15. Similar plots for the wide p_{T} bins are shown in Fig. 6.16. Scaling exponent (ν) is determined in case of each p_{T} interval, as done for $0.4 \leq p_{\mathrm{T}} \leq 1.0$ GeV/c and discussed in section 6.2.3.3. Since different transverse momentum bins give MC closure of 98-100% at different M values thus for these bins M_{max} is different in each interval (in Table 6.2). Table 6.2 tabulates the scaling exponent values from these p_{T} bins and the same is shown in the

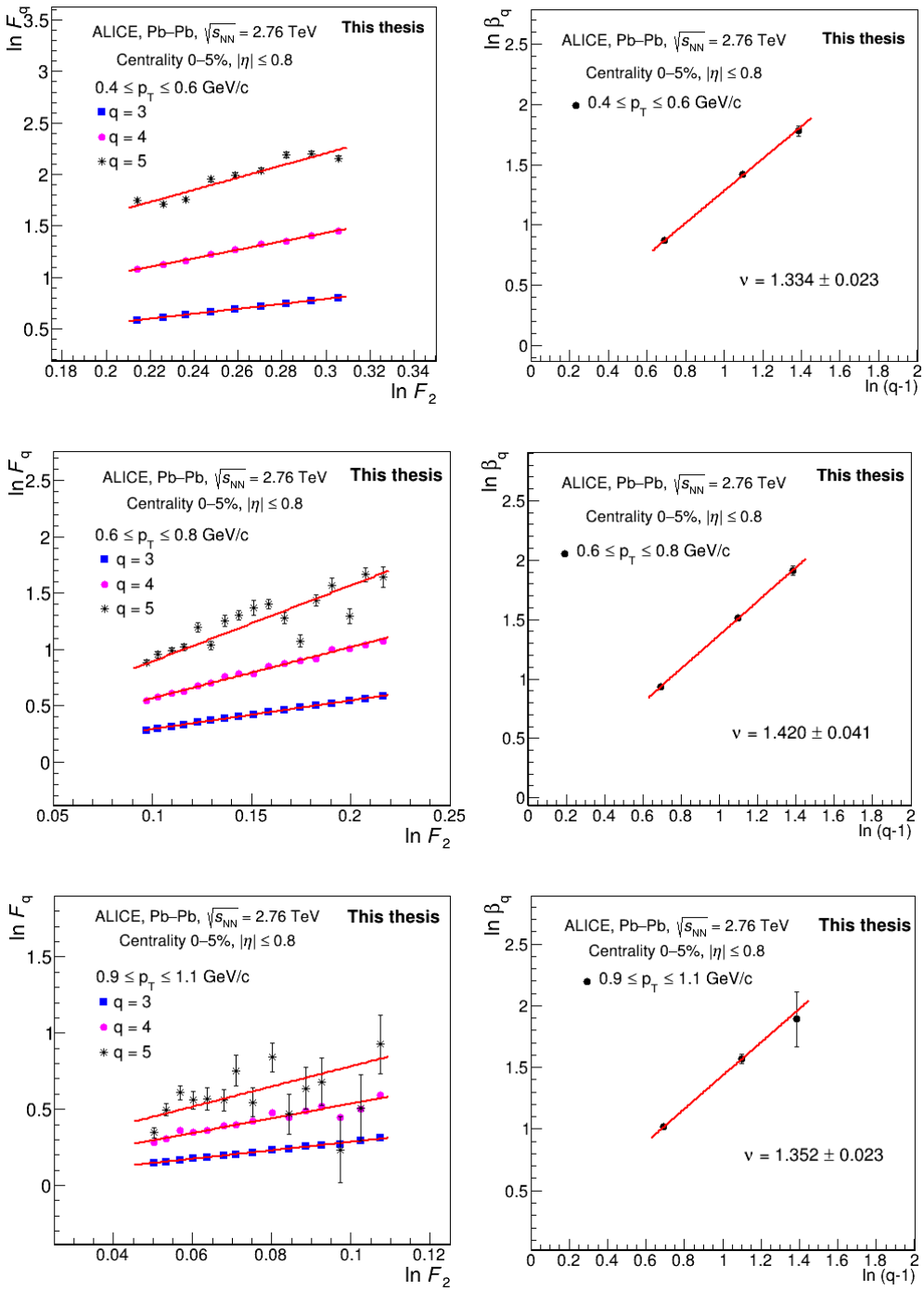

Figure 6.15. Small non-overlapping p_{T} bins: (Left)Dependence of ln F_{q} on ln F_2 with linear fits in the higher M region to extract β_q and (Right) the slope of linear fit to ln β_q vs ln $(q-1)$ gives scaling exponent (ν). Lines connecting data points show the line fitting.

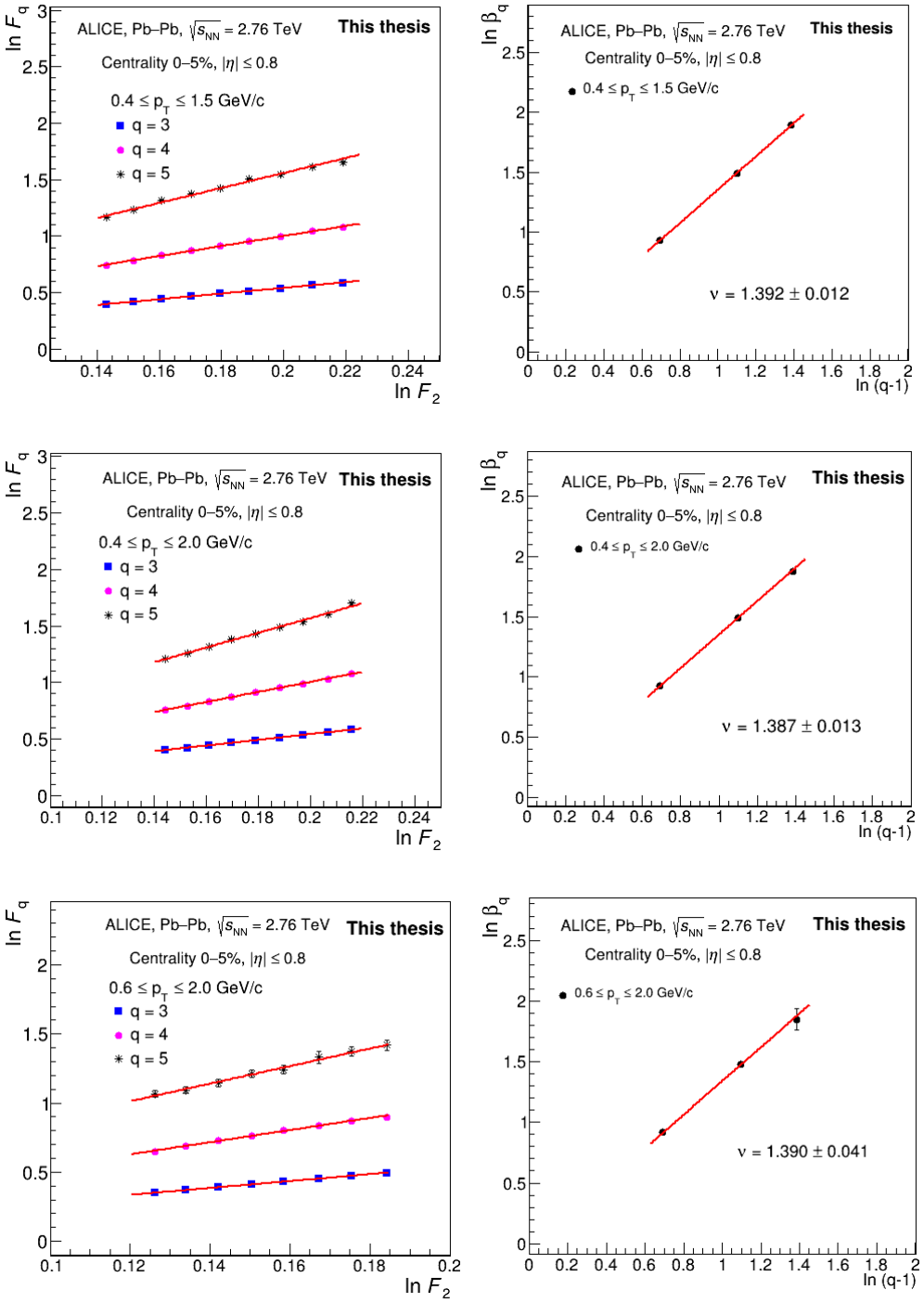

Figure 6.16. Wide overlapping p_{T} bins: (Left)Dependence of $\ln F_{\mathrm{q}}$ on $\ln F_2$ with linear fits in the higher M region to extract β_q and (Right) the slope of linear fit in $\ln \beta_q$ vs $\ln (q-1)$ gives scaling exponent (ν). Lines connecting data points show the line fitting.

Table 6.2. Scaling exponent values obtained from narrow and wide transverse momentum bins.

p_{T} bins (GeV/c)	$M_{\max}$	Scaling Exponent(ν)
$0.4 \leq p_{\mathrm{T}} \leq 0.6$	82	1.33±0.02
$0.6 \leq p_{\mathrm{T}} \leq 0.8$	82	1.42±0.02
$0.9 \leq p_{\mathrm{T}} \leq 1.1$	70	1.35±0.09
$0.4 \leq p_{\mathrm{T}} \leq 1.0$	105	1.39±0.01
$0.4 \leq p_{\mathrm{T}} \leq 1.5$	111	1.39±0.01
$0.4 \leq p_{\mathrm{T}} \leq 2.0$	120	1.39±0.01
$0.6 \leq p_{\mathrm{T}} \leq 2.0$	120	1.39±0.04

Fig. 6.17. In the Fig. 6.17(a), scaling exponent ν for p_{T} bin with $\delta p_{\mathrm{T}} = 0.2$ GeV/c

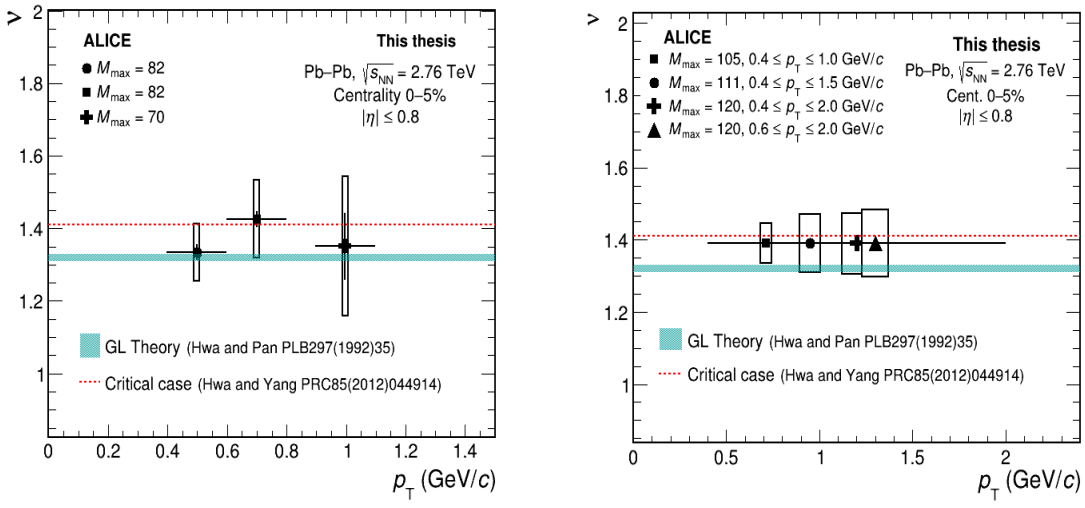

Figure 6.17. Scaling exponent as a function of p_{T} in (a) narrow non-overlapping p_{T} bins and (b) wide overlapping p_{T} bins. Horizontal bars show the width of the p_{T} bin with marker at the centre of the bin. Vertical error bars show the fitting error whereas box show the systematic uncertainties.

are given whereas Fig. 6.17(b) shows the ν as a function of various p_{T} bin widths. For the p_{T} bin opening around same p_{T} value the scaling exponent (ν) has same value. For the wide p_{T} bins with large multiplicities, both statistical and systematic uncertainties are small. The error bars on these markers are the fitting errors and the box are the uncertainties from systematics. From the plots, it is observed that within uncertainties, ν is independent of p_{T} bin width. Scaling exponent, ν from theory and the SCR model [72] with critical fluctuations are also shown in figures. ALICE data values of ν closely align with these predictions.

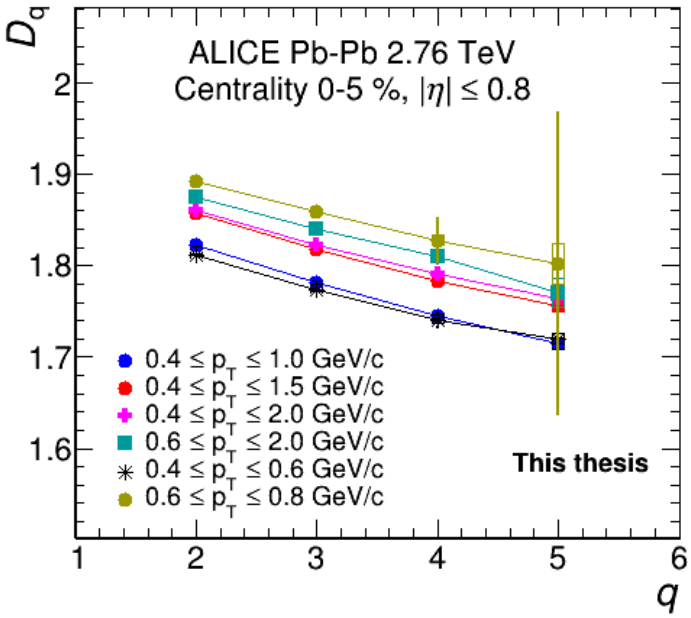

Figure 6.18. D_{q} as a function of order of moments q for different p_{T} bins. Vertical error bars show the fitting error whereas box show the systematic uncertainties. Lines connecting data points are to guide the eye.

6.5 Dependence of fractal parameters on p_{T}

Fractal parameter D_{q} for its dependence on p_{T} and p_{T} bin width is shown in Fig. 6.18. Lines joining the data points are to guide the eye. A consistent decreasing trend of D_{q} with increasing q is observed in case of all bins that indicates multifractal nature [168] of soft charged particle production in Pb−Pb collisions at $\sqrt{s_{\mathrm{NN}}} = 2.76$ TeV. λ_{q} with q = 2, 3, 4 and 5 as a function of q for different transverse momentum (p_{T}) bins is given in Fig. 6.19. Same qualitative trend is observed across all bins. Calculation for λ_{q} for q greater than 5 are not shown in the figure as there are large uncertainties at those points for all p_{T} intervals under study. These results of D_{q} and λ_{q} behaviour as function of q in various transverse momentum bins, depict that the mechanism of soft charged particle production in these bins is same having multifractal nature at LHC energies.

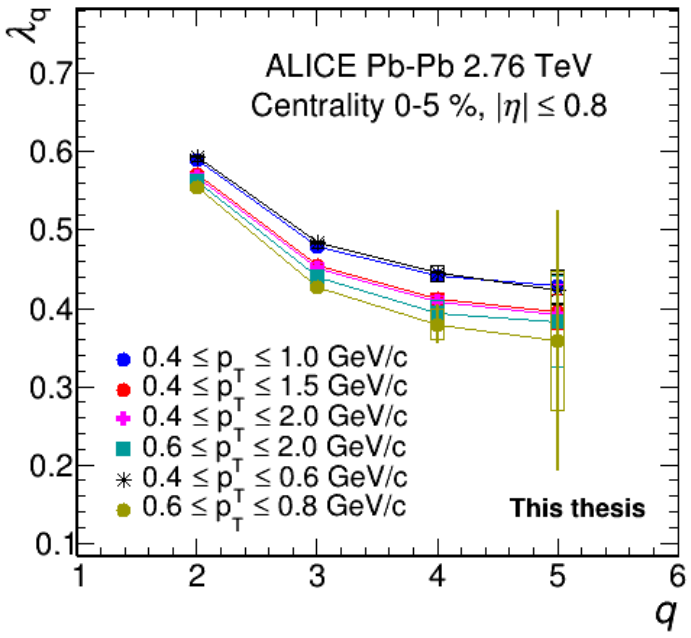

Figure 6.19. Dependence of λ_q on q for various p_T bins. Vertical error bars show the fitting error whereas box show the systematic uncertainties. Lines connecting data points are to guide the eye.

6.6 Centrality dependence of scaling and ν

To look for how scaling of $F_q(M)$ with M, depends on centrality the charged particles in the kinematic acceptance region where $|\eta| \leq 0.8$ and full azimuth with p_T bin $0.4 \leq p_T \leq 1.0$ GeV/c are analyzed for the centrality bins 0−5%, 5−10%, 10−20%, 20−40%, and 40−60%. The scaling behaviours, viz M- and F-scaling, for the charged particle data from the different centrality events are given in Fig. 6.20. It is observed from the Fig. 6.7(a) that strong power law behaviour is there in the central events 0−5% for all q and M values. However, with decrease in centrality, the multiplicity decreases. This decreases average bin content. It is observed that the quantitative difference among NFM for various orders of the moments (q) increases as centrality decreases. M-scaling with multiple linear regions is still observed for all centralities ((Fig. 6.20(Left panels))) with good F-scaling (Fig. 6.20(Right panels)). For semi-central and peripheral collisions, at high M for $q = 4$ and 5 there are large fluctuations due to less statistics and low event multiplicity.

Monte Carlo closure test is performed for each centrality to obtain the

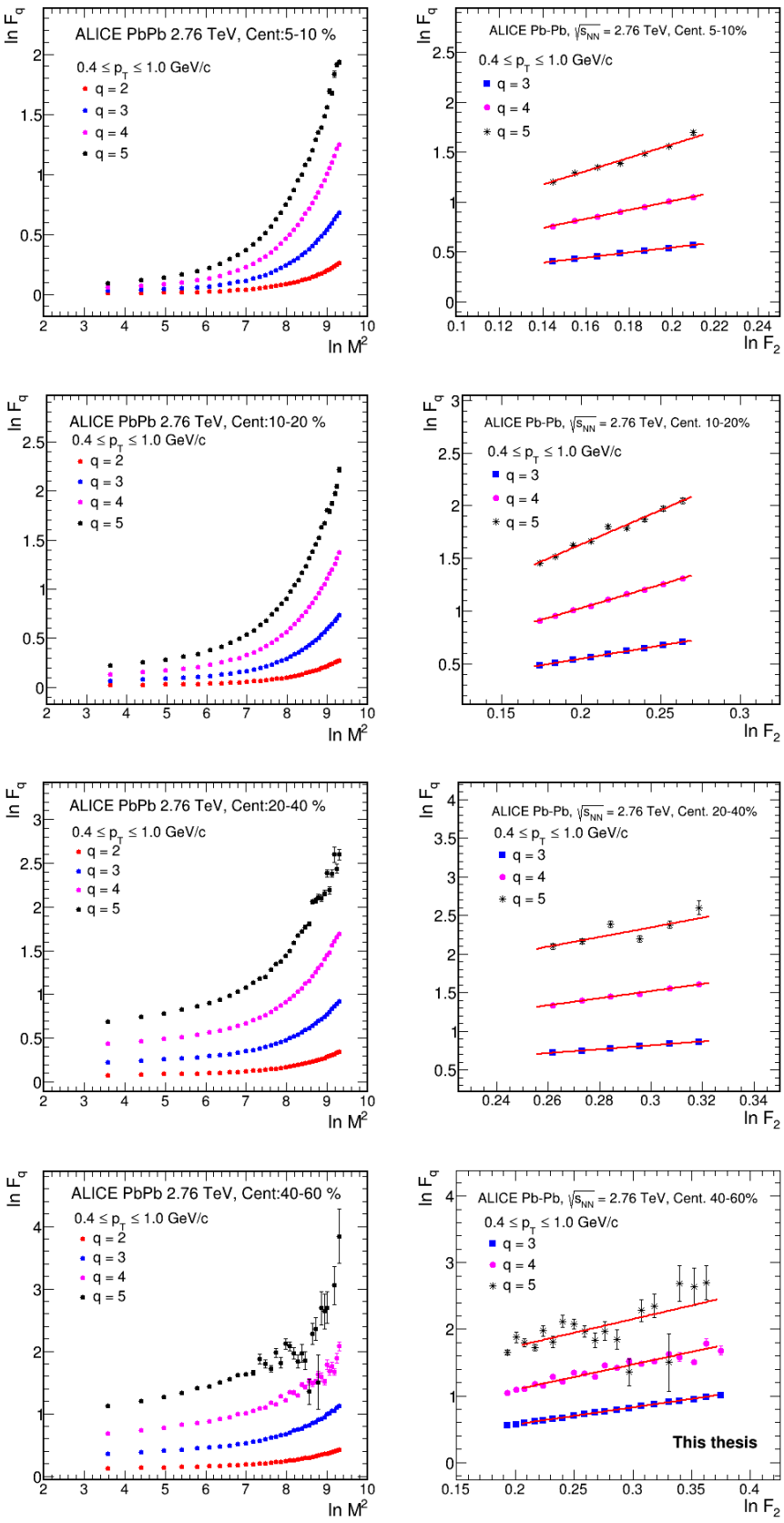

Figure 6.20. M-scaling and F-scaling for charged particles produced in the p_{T} window $0.4 \leq p_{\mathrm{T}} \leq 1.0$ GeV/c for events in 5-10%, 10-20%, 20-40% and 40-60% centrality bins.

$M_{\rm max}$ where minimum 98% of closure is achieved. Figures showing the F-scaling plots (Fig. 6.20(Right panels)) drawn for $F_{\rm q}$ upto M_{max} (Table 6.3). The lines on the data points are the polynomial 1 fits (line fits) that give β_3, β_4 and β_5 for q = 3, 4 and 5 respectively. The scaling exponents for the data from different centralities are obtained as discussed in section 3.2.2 by performing line fits on $\ln \beta_{\rm q}$ vs $\ln$ (q−1) plots. Systematic uncertainties are determined for variations in the cuts as discussed in next section. Fig. 6.21 shows the dependence of scaling exponent ν on centrality and values of ν are given in Table 6.3. Figure also includes values predicted by models and theoretical calculations. It is observed that within uncertainties ν is independent of centrality of Pb-Pb collisions. It is noted however, that uncertainties are significantly large in semi-central and peripheral events.

Table 6.3. Scaling exponent values for different centrality bins in transverse momentum interval $0.4 \leq p_{\rm T} \leq 1.0$ GeV/c.

Centrality	$M_{\rm max}$	**Scaling Exponent**(ν)
0−5%	105	1.39±0.01
5−10%	105	1.43±0.02
10−20%	100	1.42±0.02
20−40%	90	1.48±0.06
40−60%	90	1.36±0.13

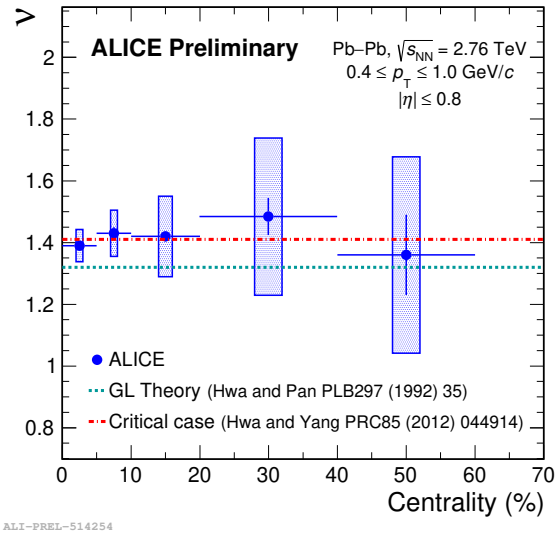

Figure 6.21. Dependence of scaling exponent ν on centrality. Values are compared with theoretical predictions from second-order phase transition formalism in Ginzburg-Landau theory and SCR model for the system having critical fluctuations. Systematic uncertainties are large in semi-central and peripheral events. Horizontal bars on markers are to show the width of centrality bin.

6.7 Systematic uncertainties

Systematic uncertainties refer to the potential differences in measurements that arise from factors other than random fluctuations. Unlike statistical uncertainties, which arise from the finite number of measurements and, can be reduced by increasing the sample size, systematic uncertainties are inherent to the experimental setup, procedures, or analysis methods. In high energy physics, experimental setup introduces certain limitations and minor differences among results are there because of different track-cuts, vertex-cuts, etc. It is important to estimate these differences as these lead to the origin of systematic uncertainties in the analysis.

Table 6.4. Cuts varied for systematic uncertainty estimation.

Source	Default	Variation
$\|V_z\|$	$\leq$ 10 cm	$\leq$ 7 cm
Magnetic Field Polarity	Average of + and -	+, -
Centrality Estimator	V0M	TRK
No. of TPC clusters	70	80
No. of TPC crossed rows	80	100

Systematic uncertainties are estimated using the standard technique of varying the default analysis cuts. These are derived from several key sources such as the $|V_z|$ position of the primary vertex of the event, the total number of TPC clusters, the total number of TPC crossed rows, and the magnetic polarity for Pb–Pb collisions. Centrality estimator is also varied for the source of systematic uncertainty. These sources and their respective variations that are considered are tabulated in Table 6.4. Specifically, for each systematic source, deviations in the values with respect to the default value is recorded. The maximum deviation observed is considered as the systematic uncertainty for that particular case. To calculate the total systematic uncertainty, contributions from various sources are combined in quadrature.

The total systematic uncertainty associated to D_{q}, λ_{q} and ν is obtained by taking the quadrature sum of all the sources listed in Table 6.4. Fig. 6.22 shows the relative uncertainty on D_{q} and λ_{q} as a function of q. The major source of uncertainty for D_{q} and λ_{q} is the polarity of the magnet. Fig. 6.23 shows the

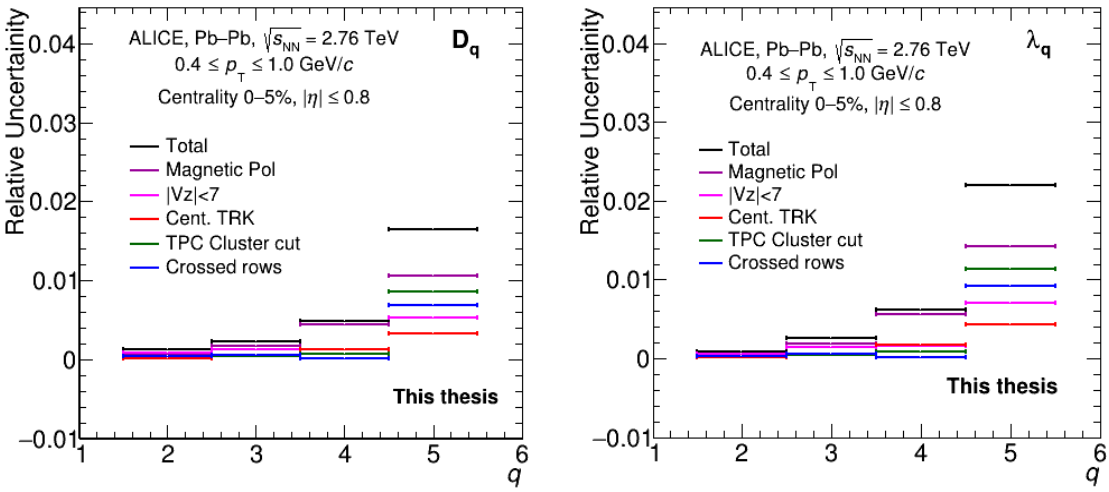

(a) (b)

Figure 6.22. Relative uncertainties from various sources and total systematic uncertainty on (a) D_q and (b) λ_q, as a function of q for central (0−5%) data in $0.4 \leq p_T \leq 1.0$ GeV/c bin.

relative uncertainty of scaling exponent ν as a function of p_T, in case of narrow p_T bins. The main source contributing to the systematics is magnetic polarity in $0.4 \leq p_T \leq 0.6\,\mathrm{GeV/c}$ p_T bin and TPC cluster cut for transverse momentum bins $0.6 \leq p_T \leq 0.8\,\mathrm{GeV/c}$ and $0.9 \leq p_T \leq 1.1\,\mathrm{GeV/c}$. Relative uncertainties on ν

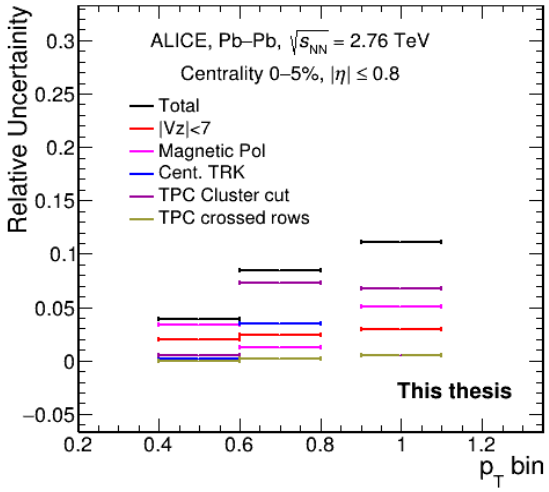

Figure 6.23. Relative uncertainties on scaling exponent ν from various sources and total systematic uncertainty as a function of p_T in small p_T bins.

for wide p_T bins is given in Fig. 6.24. Fig. 6.25 shows the relative uncertainty of scaling exponent ν as a function of centrality.

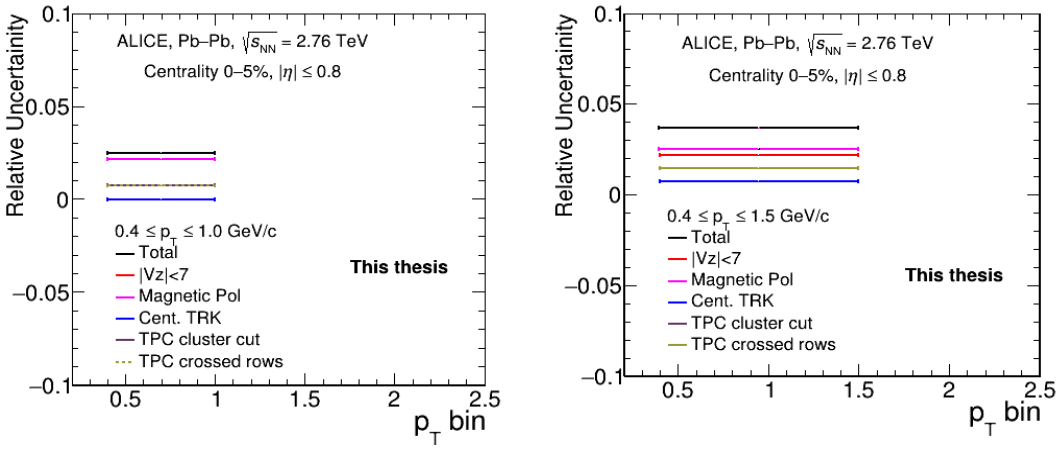

Figure 6.24. Relative uncertainties on scaling exponent ν from various sources and total systematic uncertainty as a function of p_{T} in (a) $0.4 \leq p_{\mathrm{T}} \leq 1.0$ GeV/c (b) $0.4 \leq p_{\mathrm{T}} \leq 1.5$ GeV/c (c) $0.4 \leq p_{\mathrm{T}} \leq 2.0$ GeV/c and (d) $0.6 \leq p_{\mathrm{T}} \leq 2.0$ GeV/c.

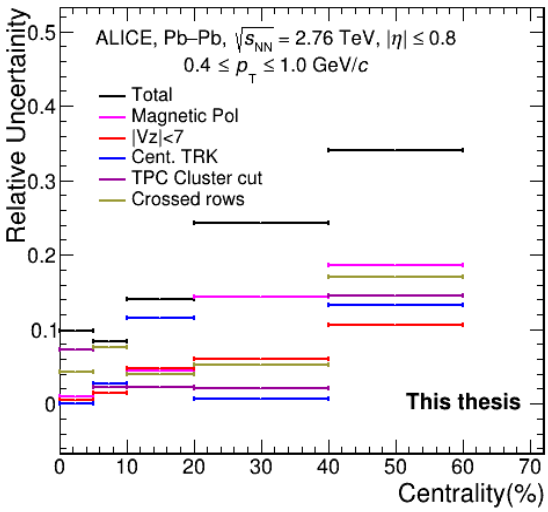

Figure 6.25. Relative uncertainties on scaling exponent ν from various sources and total systematic uncertainty as a function of centrality bin in Pb–Pb collisions at 2.76 TeV.

6.8 Comparison of results

6.8.1 With monte carlo event generators

M-scaling: M-scaling (F_q dependence on M) has been studied for both ALICE data and Monte-Carlo (MC) event generators. It is important to compare the results from experimental data with event generators to understand the underlying physics in heavy-ion collisions. For the $0.4 \leq p_T \leq 1.0\,\mathrm{GeV/c}$ p_T window, results from ALICE, Toy model, HIJING and the AMPT model event generators are shown in Fig. 6.26. From the figure it is observed that HIJING, AMPT and Toy model underestimate the data. There is qualitative and quantitative difference between data and models at high M, the region of interest. The power law behaviour of $F_q(M)$ with decreasing bin sizes in two dimensional (η, φ) phase space for ALICE is not explainable by any of these models. The NFM values for the data deviate from the models as M increases indicating large bin-to-bin scale-invariant fluctuations in the charged particle production in comparison to the models. The physics of self-similar particle production as revealed by power-law growth of F_q with M is not present in any of the model studied here.

Scaling exponent (ν): A comparison of scaling exponents from data and that

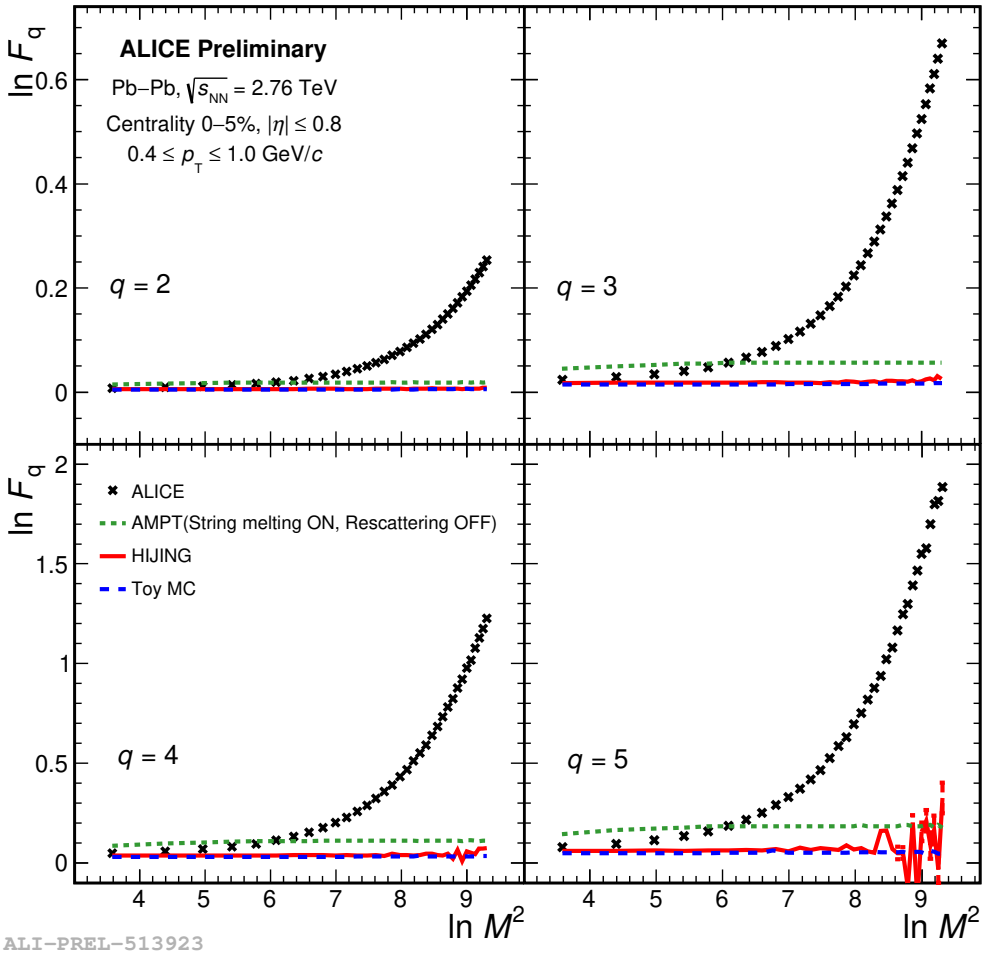

Figure 6.26. Dependence of ln F_{q} on ln M^2 for $q = 2$, 3, 4 and 5 in the central Pb$-$Pb collisions at $\sqrt{s_{\mathrm{NN}}} = 2.76$ TeV. Quantitative and qualitative difference is observed between data and models as the number of bins increase.

from the model (the AMPT model) shows difference between the two in case of all p_{T} intervals analyzed. Within systematic uncertainties scaling exponent from data is independent of p_{T} bin (Fig. 6.27) and p_{T} bin width (Fig. 6.28). In case of the AMPT models, event samples with different modes, same behaviour of ν is observed. However, the value of ν from data is different from the model. It is the quantitative value of ν which has significance of characterizing the system. From both the figures, it is observed that AMPT values are ≈1.7, greater than the scaling exponent value from ALICE data (1.33 - 1.42) at $\sqrt{s_{\mathrm{NN}}}$ = 2.76 TeV for Pb− collisions..

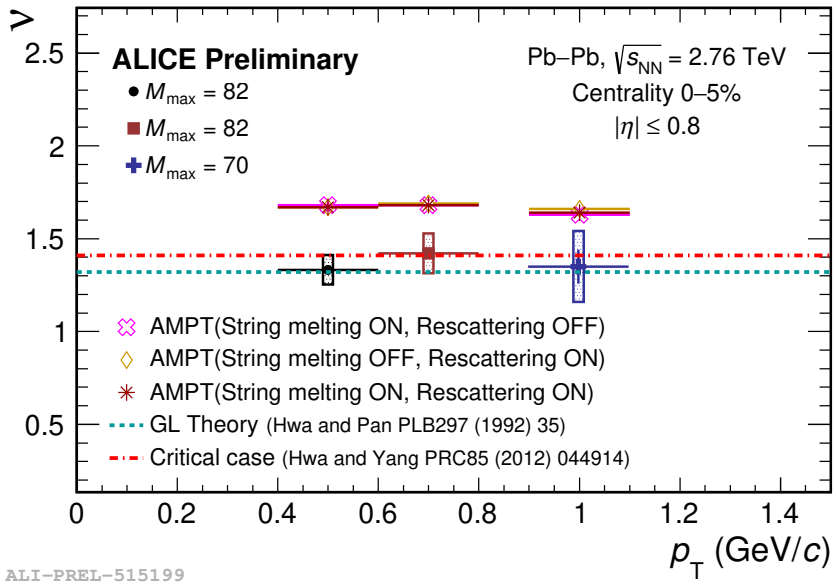

Figure 6.27. Scaling exponent as a function of p_{T} in narrow non-overlapping p_{T} bins in case of central Pb–Pb collisions at 2.76 TeV for the charged particles within $|\eta| \leq$0.8 and full azimuth.

Fractal dimension (D_{q}): The next parameter compared with Monte Carlo models is D_{q}. Fig. 6.29 shows D_{q} from ALICE data for the $0.4 \leq p_{\mathrm{T}} \leq 1.0$ GeV/c bin, compared with D_{q} from the AMPT and the Toy model. Notably, both AMPT and Toy model exhibit no discernible dependence of D_{q} on q, indicating a monofractal nature in particle generation whereas, ALICE data shows a decreasing trend of D_{q} with respect to q, suggesting a multifractal nature in particle production. The contrasting behaviour among the Monte Carlo generators and experimental data underscore the intricate nature of particle production in the data that needs to be

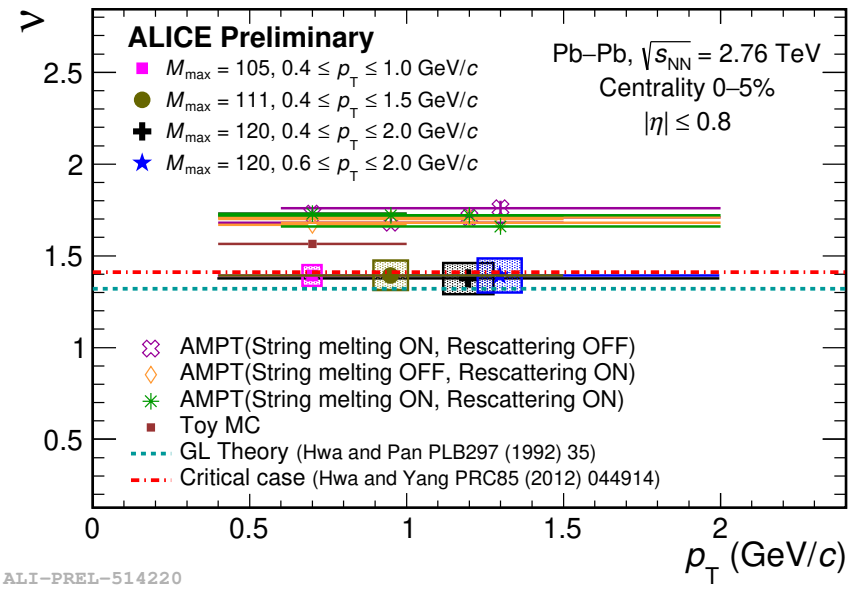

Figure 6.28. Scaling exponent as a function of p_{T} in wide overlapping p_{T} bins in case of central Pb–Pb collisions at 2.76 TeV for the charged particles within $|\eta| \leq$0.8 and full azimuth.

understood.

Coefficient (λ_q): A comparison of λ_q from ALICE with that from Monte Carlo event generators and low-energy experimental results is presented in Fig. 6.30. An absence of minima in λ_q as a function of q indicates absence of two-phase system. Calculations of λ_q for $q > 5$, are required, that are subject to large statistical fluctuations at present energies due to limited statistics. Consequently, drawing definitive conclusions from the λ_q coefficient is not possible. Further experiments such as RUN 3 ALICE data is suggested to be analysed to probe λ_q behaviour with q beyond $q = 5$.

6.8.2 With mixed events

In high energy collisions, various particles are produced with complex dynamics. Mixed events is a technique used in data analysis to understand and separate the signal (interesting events or particles of interest) from the background (random or uninteresting events). Mixed events are the events generated from the real events by taking tracks from different events of the data to build a mixed event, so as to

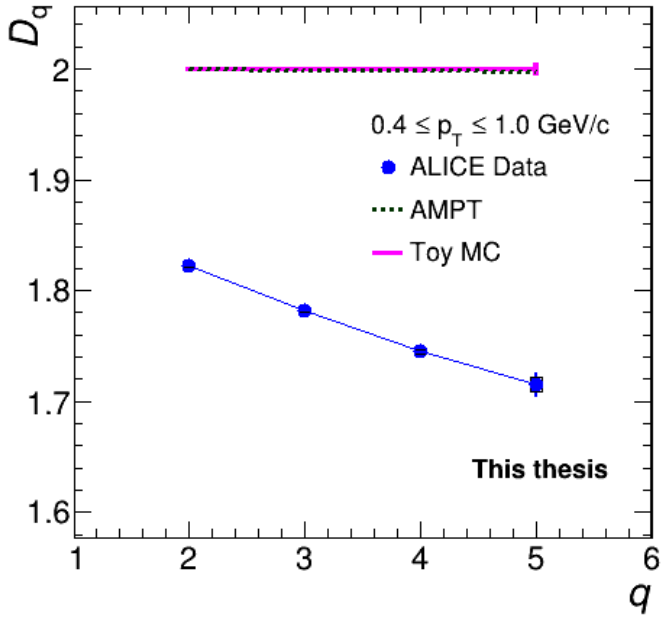

Figure 6.29. Dependence of D_{q} on q for charged particles produced in central Pb−Pb collisions at $\sqrt{s_{\mathrm{NN}}} = 2.76$ TeV in $0.4 \leq p_{\mathrm{T}} \leq 1.0$ GeV/c. Values from ALICE compared with that in AMPT and Toy MC events. Lines connecting the data points are to guide the eye.

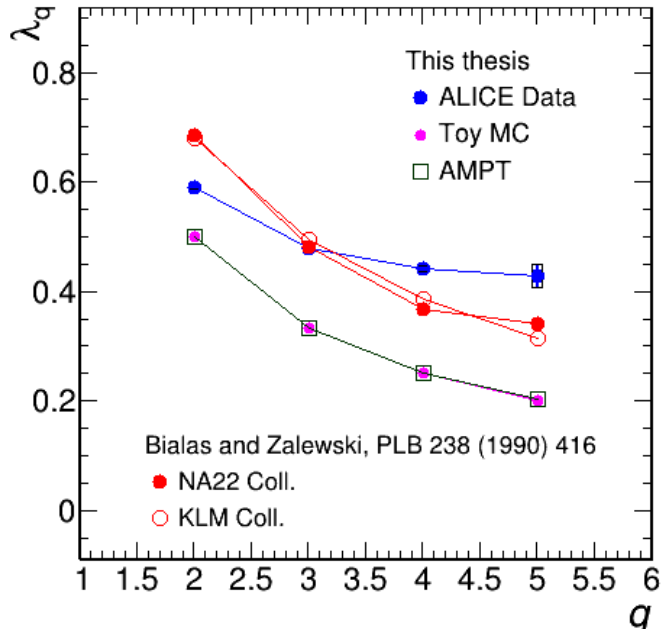

Figure 6.30. Dependence of λ_{q} on q for charged particles produced in central Pb−Pb collisions at $\sqrt{s_{\mathrm{NN}}} = 2.76$ TeV from ALICE for the $0.4 \leq p_{\mathrm{T}} \leq 1.0$ GeV/c. Values from ALICE are compared with that from the AMPT and Toy MC events and results from low energy experiments [172].

have correlation free tracks per mixed event. Various mixed event techniques are being used in the community that depends on the physics question involved.

In the event mixing method used here, mixed events are generated from the real events which qualify the event selection criteria of 0−5% centrality and $|V_z| \leq 10$ cm. From this pool of events, mixed events are build, with the tracks available from event pool, using the multiplicity constraints of the real experimental data. The event pool is made up of events that have similar characteristics, such as centrality and the primary vertex position along the z-axis ($V_{\rm Z}$). For this analysis, the mixed event pool is divided into six centrality bins and six $V_{\rm Z}$ bins as follows,

Centrality bins: (0,0.5), (0.5,1), (1,2), (2,3), (3,4), (4,5)

$V_{\rm Z}$ (cm) bins: (-10,-5), (-5,-1.8), (-1.8,0), (0,1.8), (1.8,5), (5,10)

Only events within the same centrality and $V_{\rm Z}$ bins are used to create the mixed event distribution. To ensure enough particles for the distribution, there must be at least five events in each bin. To build up a mixed event, tracks with $|\eta| \leq 0.8$ and $0 \leq \varphi \leq 2\pi$ are selected in such way that no two tracks come from the same event in the event pool. To further reduce the correlations inherent in the production of particles in the experimental data, an additional constraint is included, that the η and φ for a track in a mixed event are not picked from the same track of a real event. With these conditions a sample of mixed events is generated from the experimental data, in which there are negligible correlations of the data. This event sample generates background sample or can be used to remove background.

For the mixed event sample created from the charged particles recorded by ALICE in $0.4 \leq p_{\rm T} \leq 1.0\,{\rm GeV/c}$ bin, the NFM ($F_{\rm q}(M)^{mix}$) are calculated for $q = 2$ to 5 and M = 6 to 123. Fig. 6.31 shows the $\ln F_{\rm q}$ versus $\ln M^2$ graphs for the ALICE data (filled markers) and mixed event data (solid lines). It is observed that $F_{\rm q}(M)^{mix} < F_{\rm q}(M)^{data}$. However, the qualitative behaviour of the resolution scaling for the mixed event sample is same as that of the experimental data. This is probably because of some experimental data correlations still contributing to the mixed event data.

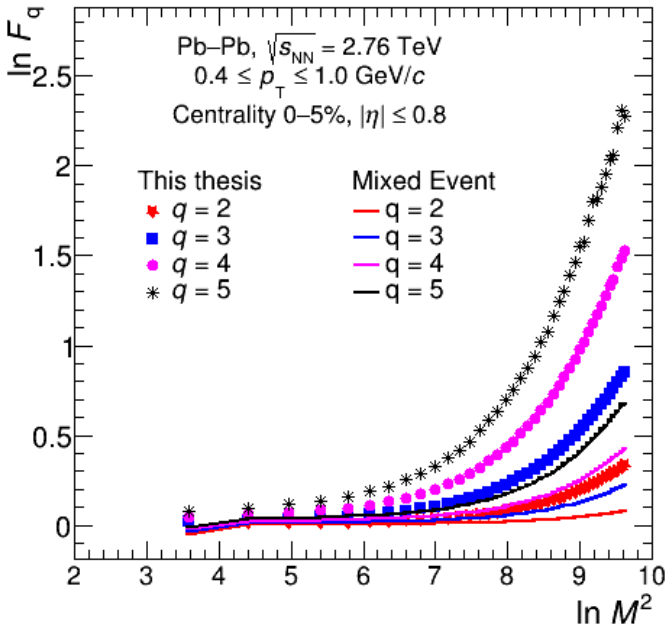

Figure 6.31. Dependence of ln F_q on ln M^2 for q = 2, 3, 4 and 5 for Mixed Events and ALICE experimental data.

6.8.3 With other experiments

Intermittency analysis is performed by the STAR [82] experiment for Au−Au collisions at BES energies and by NA61 collaboration [189] at SPS energies, where instead of determining NFM ($F_q(M)$), $\Delta F_q(M)$ is calculated as

$$\Delta F_q(M) = F_q(M)^{data} - F_q(M)^{mix}, \tag{6.1}$$

where $F_q(M)^{data}$ is NFM from data and $F_q(M)^{mix}$ is NFM from mixed events. STAR and NA61 study $\Delta F_q(M)$'s scaling behaviour as function of number of bins (M^2) and $\Delta F_2(M)$. To have a comparative analysis of work done in this thesis with the STAR and the NA61, the $\Delta F_q(M)$ for the charged particles produced in $0.4 \leq p_T \leq 1.0$ GeV/c p_T bin and midrapidity region with full azimuth are determined for ALICE data. As studied by STAR, the $\Delta F_q(M)$ vs $ln\, M^2$ for q = 2 to 5 results from this analysis are given in Fig. 6.32(a) which show strict linear dependence of $\Delta F_q(M)$ on M^2 as M increases. Similar linear behaviour is reported in Ref. [82] by the STAR experiment at RHIC which has performed this analysis for protons in the two dimensional momentum space for central Au−Au

collisions at centre of mass energies ranging from 7.7 to 200 GeV.

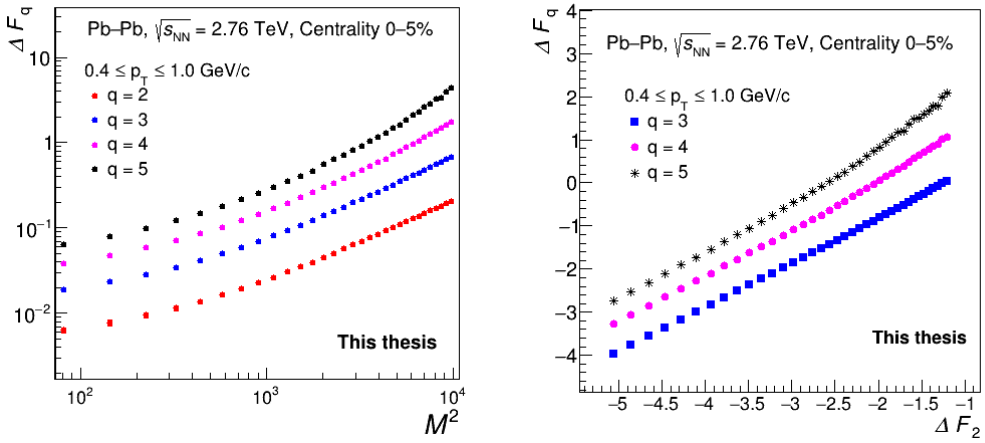

(a) (b)

Figure 6.32. ALICE data: (a) Dependence of $\Delta F_{\rm q} = F_{\rm q}(M)^{\rm data} - F_{\rm q}(M)^{\rm mix}$ on M^2 for q = 2, 3, 4 and 5 (b) Dependence of $\Delta F_{\rm q}$ on ΔF_2 for q = 3, 4 and 5 .

Scaling exponent (ν) is obtained from the order scaling study using $\Delta F_{\rm q}(M)$ moments. F-scaling, that is $\Delta F_{\rm q}(M)$ vs $\Delta F_2(M)$ behaviour for the ALICE data is given in Fig. 6.32(b). $\Delta F_{\rm q}$ (q = 3, 4 and 5) is plotted as function of $\Delta F_2(M)$ and $\beta_{\rm q}$ values are obtained from the line fits in the high M region. The value of scaling exponent (ν) for the ALICE data from line fit to ln $\beta_{\rm q}$ versus ln (q-1) (Fig. 6.33(b)) is 0.42±0.01. The ALICE data points relative to the STAR data points are shown in Fig. 6.34 for the 0−5% central events for two $p_{\rm T}$ bins. A non-monotonic trend in the values of ν is observed for the STAR data with minima at 27 GeV. Scaling exponent values from ALICE are comparable to this energy. ν is known to be a parameters independent of the phase space. ALICE data points from higher energies may give a vivid picture about relation of ν and the energy of the collisions.

In this chapter observations and results from the local multiplicity fluctuation analysis of experimental data (ALICE) and its comparison with the models and similar studies from the experiments is given. Normalized factorial moments of the soft charged particles produced in the midrapidity region $|\eta| \leq 0.8$ and full azimuth are calculated. NFM moments are observed to show power law behaviour with M as M $\rightarrow \infty$. This is indicative of self-similar scale invariant fluctuations (intermittency). Data is observed to show multifractal nature whereas both in-

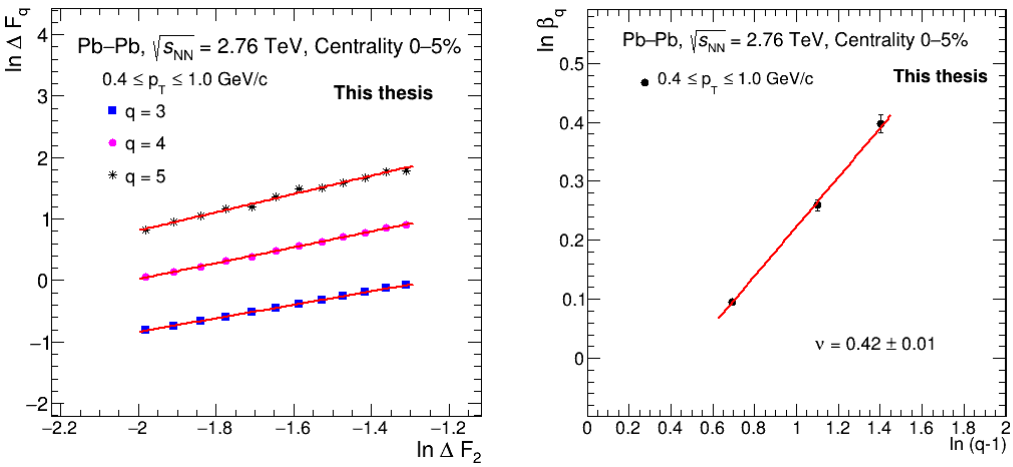

(a) (b)

Figure 6.33. ALICE data: (a) Linear fit in the high M region of ln ΔF_{q} vs ln ΔF_2 graph. Line fit to these data points give slope β_q.(b) Scaling exponent (ν) from $ln\beta_q$ vs ln (q-1) is 0.42±0.01.

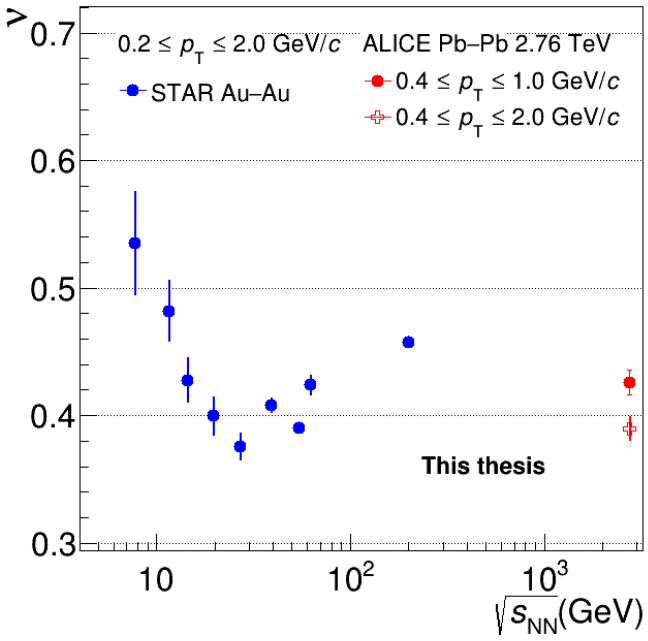

Figure 6.34. Scaling exponent ν obtained from this work and from STAR experiment [82] for Au−Au collisions at 200 GeV centre of mass energy from proton intermittency analysis in the momentum space.

termittency and multifractal nature of particle generation is found to be absent in HIJING and the AMPT. A comparison of data with baseline study from Toy model shows large deviations at high M. Data shows the presence of bin-to-bin dynamical fluctuations in spatial patterns. The value of scaling exponent (ν), which quantitatively characterizes the dynamics of fluctuations and hence the critical nature of the system, is very close to the values predicted by the Ginzburg-Landau theory. Results are motivating and promise to reveal important aspects of particle production in heavy-ion collisions. For the conclusive comments on the centrality dependence of scaling exponent ν or λ_{q} on q, more studies on similar lines at higher energies are proposed. A similarity of scaling exponent from ALICE and STAR, using mixed event removal technique, is interesting and inspires to investigate identified particles using intermittency analysis, that may provide more insights into the behaviour of particle production mechanism at extreme energy densities.

Chapter 7

Summary and conclusions

During ultra-relativistic heavy-ion collisions at extreme energy densities a primordial state of matter, known as quark-gluon plasma (QGP) is formed. These collisions create system with possibilities to unveil properties and dynamics of QGP. While the system so formed expands and cools down transitioning from the deconfined QGP phase to the hadronic state there may be large fluctuations leading to variations in the observables over space and time to offer insights into particle production mechanisms and phase change processes. As per lattice QCD, fluctuations become large near the critical point. Critical phenomena have features that are universal such as scale invariance where clusters of all sizes appear without a characteristic scale. This thesis focuses on multiplicity fluctuations, variations in the number of particles produced, that serve as important indicator of the various attributes of the system, especially shedding light on particle production mechanism and characteristics that reveal inherent correlations. A study of scaling properties of local multiplicity fluctuations in the charged particle production in Pb−Pb collisions at a center-of-mass energy of $\sqrt{s_{\mathrm{NN}}} = 2.76\,\mathrm{TeV}$, recorded using the ALICE detector at LHC, CERN, Geneva, is presented. Baseline behaviour of the observable, the normalized factorial moments (NFM), has also been studied using the Toy model, HIJING and the AMPT model.

A two-dimensional intermittency analysis in the angular (η, φ) phase space is performed on the data to measure charged particle density fluctuations. Intermittency analysis is a powerful tool for studying multiplicity fluctuations, an important feature of the systems near critical point where scale invariance and fractal structures are prevalent. Factorial moments of the produced particles are calculated on event-by-event basis. The midrapidity region ($|\eta| \leq 0.8$) with full

azimuth is divided into M^2 bins, where M ranges from $M_{min} = 6$ to $M_{max} = 123$, in the intervals of 3. Scaling behaviour of the NFM across various transverse momentum (p_{T}) intervals, with $p_{\mathrm{T}} \leq 2.0\,\mathrm{GeV/c}$, are studied. The variation of NFMs ($F_{\mathrm{q}}(\mathrm{M})$) is studied as a function of the number of bins (M^2), known as resolution scaling (M-scaling). For data a consistent monotonic variation of $\ln F_{\mathrm{q}}$ with respect to $\ln M^2$ is observed in all transverse momentum bins indicating intermittency and self-similar nature of the charged particle production. Presence of intermittency in the data suggests non-trivial dynamics in the particle production which has not been observed in HIJING, AMPT and the Toy model. Comparison of results from experimental data with Monte Carlo events shows deviations at high resolution. This highlights that these models do not fully capture the correlations in particle production, which are there in the experimental data. Interesting underlying physics in the data needs to be understood and implemented in the models.

For F-scaling, which is the scaling of F_{q} moments with second order factorial moments F_2, a linear relationship is observed between $\ln F_{\mathrm{q}}$ and $\ln F_2$, serving as the basis for determining the scaling exponent (ν). The scaling exponent is a dimensionless quantity and it characterizes the critical nature of the system under study. Scaling exponent from data is found to be independent of p_{T} and p_{T} bin width in the low p_{T} regions. From comparison of experimental results and models/theoretical predictions, it is observed that experimental values of ν align with that from the formalism for second order phase transition under Ginzburg-Landau theory ($\nu = 1.304$) and that from the SCR model with critical fluctuations ($\nu = 1.41$). The scaling exponent values derived from the AMPT model deviate significantly from 1.304. Centrality dependence study of the scaling exponent from data shows that within uncertainties ν is independent of various centrality ranges. Large systematic uncertainties that are observed in semi-central and peripheral events are primarily attributed to the low event multiplicities at these centralities.

Investigations into fractal parameters, generalized fractal dimension D_{q} and coefficient λ_{q}, provide information on the structure of self-similar multiparticle systems in heavy-ion collisions. For ALICE data, the parameter D_{q}, reflecting

particle production dynamics, shows a decreasing trend with q, indicating multifractal behaviour of the system created, while the AMPT and the Toy model exhibit a consistent monofractal nature. Further investigations at higher energies would be interesting. The investigation of λ_{q} with q which may reveal distinct behaviours of self-similar multiparticle systems, does not exhibit any minima up to $q = 5$. Absence of minima prompts for further investigations, particularly at higher energies, to determine the potential existence of a minimum in λ_{q} at certain q value and thus to confirm or rule out one phase system.

In summary, the first analysis of ALICE data using normalized factorial moments in the contours of intermittency gives a perspective on the hadronization processes and the system created at the LHC energies. This work gives important inputs for the heavy-ion collision event generation models and serves to unfold some important characteristics of the system at extreme energy and temperature. Intermittency is observed in the ALICE data with hybrid tracks (TPC and ITS tracks) having scaling exponents $\nu \simeq 1.30-1.45$. Intermittency is indicative of scale invariant spatial fluctuations and self-similarity with multifractal nature of the system created in the collisions. Scaling exponent (ν), quantifying spatial variations, shows the presence of dynamical fluctuations that are expected to be there in a system at critical point or having passed through it.

Results from the intermittency analysis of the ALICE data presented here may be refined further by applying track selection cuts taking care of track splitting and merging effects etc., so as to improve on the closure at high resolution. Further detailed study on the centrality dependence, volume fluctuation effects and identified particle analysis in the restricted phase space is what one can look next to learn more about the nature of matter at high energy densities using this analysis methodology. Moments of factorial moments can be calculated using erraticity analysis technique which may further unfold the characteristics of event-by-event fluctuations of the spatial fluctuations, giving in-depth insight into the dynamics of heavy-ion collisions.

Bibliography

[1] **STAR** Collaboration, J. Adamsz *et al.*, "Experimental and theoretical challenges in the search for the quark gluon plasma: The STAR Collaboration's critical assessment of the evidence from RHIC collisions," *Nucl. Phys. A* **757** (2005) 102–183, arXiv:nucl-ex/0501009.

[2] **ALICE** Collaboration, S. Acharya *et al.*, "Measurement of electrons from semileptonic heavy-flavour hadron decays at midrapidity in pp and Pb-Pb collisions at $\sqrt{s_{\rm NN}} = 5.02$ TeV," *Phys. Lett. B* **804** (2020) 135377, arXiv:1910.09110 [nucl-ex].

[3] **CMS** Collaboration, A. M. Sirunyan *et al.*, "Nuclear modification factor of $\rm D^0$ mesons in PbPb collisions at $\sqrt{s_{\rm NN}} = 5.02$ TeV," *Phys. Lett. B* **782** (2018) 474–496, arXiv:1708.04962 [nucl-ex].

[4] **LHCb** Collaboration, R. Aaij *et al.*, "Measurements of prompt charm production cross-sections in *pp* collisions at $\sqrt{s} = 13$ TeV," *JHEP* **03** (2016) 159, arXiv:1510.01707 [hep-ex]. [Erratum: JHEP 09, 013 (2016), Erratum: JHEP 05, 074 (2017)].

[5] **ALICE** Collaboration, S. Acharya *et al.*, "Measurement of inclusive charged-particle b-jet production in pp and p-Pb collisions at $\sqrt{s_{\rm NN}} = 5.02$ TeV," *JHEP* **01** (2022) 178, arXiv:2110.06104 [nucl-ex].

[6] **ALICE** Collaboration, K. Aamodt *et al.*, "Elliptic flow of charged particles in Pb-Pb collisions at 2.76 TeV," *Phys. Rev. Lett.* **105** (2010) 252302, arXiv:1011.3914 [nucl-ex].

[7] M. Gyulassy and L. McLerran, "New forms of QCD matter discovered at RHIC," *Nucl. Phys. A* **750** (2005) 30–63, arXiv:nucl-th/0405013.

[8] P. Giménez Molinelli, J. Nichols, J. López, and C. Dorso, "Simulations of cold nuclear matter at sub-saturation densities," *Nuclear Physics A* **923** (2014) 31–50. https://www.sciencedirect.com/science/article/pii/S0375947414000049.

[9] S. F. Novaes, "Standard model: An Introduction," in *10th Jorge Andre Swieca Summer School: Particle and Fields*, pp. 5–102. 1, 1999. arXiv:hep-ph/0001283.

[10] S. L. Glashow, "Partial Symmetries of Weak Interactions," *Nucl. Phys.* **22** (1961) 579–588.

[11] A. Salam and J. C. Ward, "Electromagnetic and weak interactions," *Phys. Lett.* **13** (1964) 168–171.

[12] S. Weinberg, "A Model of Leptons," *Phys. Rev. Lett.* **19** (1967) 1264–1266.

[13] https://www.quantumdiaries.org/2014/03/14/the-standard-model-a-beautiful-but-flawed-theory/, last accessed on 15/02/2024.

[14] D. J. Griffiths, *Introduction to elementary particles; 2nd rev. version*. Physics textbook. Wiley, New York, NY, 2008. https://cds.cern.ch/record/111880.

[15] P. W. Higgs, "Broken Symmetries and the Masses of Gauge Bosons," *Phys. Rev. Lett.* **13** (1964) 508–509.

[16] F. Englert and R. Brout, "Broken Symmetry and the Mass of Gauge Vector Mesons," *Phys. Rev. Lett.* **13** (1964) 321–323.

[17] **ATLAS** Collaboration, G. Aad *et al.*, "Observation of a new particle in the search for the Standard Model Higgs boson with the ATLAS detector at the LHC," *Phys. Lett. B* **716** (2012) 1–29, arXiv:1207.7214 [hep-ex].

[18] **CMS** Collaboration, S. Chatrchyan *et al.*, "Observation of a New Boson at a Mass of 125 GeV with the CMS Experiment at the LHC," *Phys. Lett. B* **716** (2012) 30–61, arXiv:1207.7235 [hep-ex].

[19] J. Ellis, "Physics Beyond the Standard Model," *Nucl. Phys. A* **827** (2009) 187C–198C, arXiv:0902.0357 [hep-ph].

[20] H. D. Politzer, "Reliable Perturbative Results for Strong Interactions?," *Phys. Rev. Lett.* **30** (1973) 1346–1349.

[21] D. J. Gross and F. Wilczek, "Asymptotically Free Gauge Theories - I," *Phys. Rev. D* **8** (1973) 3633–3652.

[22] D. J. Gross and F. Wilczek, "Ultraviolet Behavior of Nonabelian Gauge Theories," *Phys. Rev. Lett.* **30** (1973) 1343–1346.

[23] **Particle Data Group** Collaboration, C. Patrignani *et al.*, "Review of Particle Physics," *Chin. Phys. C* **40** no. 10, (2016) 100001.

[24] https://cds.cern.ch/record/2044439/plots, last accessed on 15/02/2024.

[25] https://www.gsi.de/work/forschung/theorie/theory-new/hot-and-dense-qcd, last accessed on 15/03/2024.

[26] F. Karsch, "Lattice QCD at high temperature and density," *Lect. Notes Phys.* **583** (2002) 209–249, arXiv:hep-lat/0106019.

[27] U. W. Heinz, "The Little bang: Searching for quark gluon matter in relativistic heavy ion collisions," *Nucl. Phys. A* **685** (2001) 414–431, arXiv:hep-ph/0009170.

[28] A. Bazavov *et al.*, "The chiral and deconfinement aspects of the QCD transition," *Phys. Rev. D* **85** (2012) 054503, arXiv:1111.1710 [hep-lat].

[29] **STAR** Collaboration, G. Odyniec, "Beam Energy Scan Program at RHIC (BES I and BES II) – Probing QCD Phase Diagram with Heavy-Ion Collisions," *PoS* **CORFU2018** (2019) 151.

[30] W. F. Henning, "FAIR: Recent developments and status," *Nucl. Phys. A* **805** (2008) 502–510.

[31] C. Sturm and H. Stocker, "The facility for antiproton and ion research FAIR," *Phys. Part. Nucl. Lett.* **8** (2011) 865–868.

[32] **NICA** Collaboration, A. N. Sissakian and A. S. Sorin, "The nuclotron-based ion collider facility (NICA) at JINR: New prospects for heavy ion collisions and spin physics," *J. Phys. G* **36** (2009) 064069.

[33] E. D. Courant and H. S. Snyder, "Theory of the alternating gradient synchrotron," *Annals Phys.* **3** (1958) 1–48.

[34] "LHC Machine," *JINST* **3** (2008) S08001.

[35] R. Snellings, "Collective Expansion at the LHC: selected ALICE anisotropic flow measurements," *J. Phys. G* **41** no. 12, (2014) 124007, arXiv:1408.2532 [nucl-ex].

[36] B. Betz, "Jet Propagation and Mach-Cone Formation in (3+1)-dimensional Ideal Hydrodynamics," other thesis, 10, 2009.

[37] A. Jaiswal and V. Roy, "Relativistic hydrodynamics in heavy-ion collisions: general aspects and recent developments," *Adv. High Energy Phys.* **2016** (2016) 9623034, arXiv:1605.08694 [nucl-th].

[38] W. A. Zajc, "The Fluid Nature of Quark-Gluon Plasma," *Nucl. Phys. A* **805** (2008) 283–294, arXiv:0802.3552 [nucl-ex].

[39] **BRAHMS** Collaboration, I. Arsene *et al.*, "Quark gluon plasma and color glass condensate at RHIC? The Perspective from the BRAHMS experiment," *Nucl. Phys. A* **757** (2005) 1–27, arXiv:nucl-ex/0410020.

[40] J. Xu and C. M. Ko, "Chemical freeze-out in relativistic heavy-ion collisions," *Phys. Lett. B* **772** (2017) 290–293, arXiv:1704.04934 [nucl-th].

[41] D. H. Perkins, *Introduction to High Energy Physics*. Cambridge University Press, 4 ed., 2000.

[42] S. A. Bass, M. Gyulassy, H. Stoecker, and W. Greiner, "Signatures of quark gluon plasma formation in high-energy heavy ion collisions: A Critical review," *J. Phys. G* **25** (1999) R1–R57, arXiv:hep-ph/9810281.

[43] G. David, "Direct real photons in relativistic heavy ion collisions," *Rept. Prog. Phys.* **83** no. 4, (2020) 046301, arXiv:1907.08893 [nucl-ex].

[44] J. Alam, B. Sinha, and S. Raha, "Electromagnetic probes of quark gluon plasma," *Phys. Rept.* **273** (1996) 243–362.

[45] **ALICE** Collaboration, J. Adam *et al.*, "Direct photon production in Pb-Pb collisions at $\sqrt{s_{NN}} = 2.76$ TeV," *Phys. Lett. B* **754** (2016) 235–248, arXiv:1509.07324 [nucl-ex].

[46] **WA98** Collaboration, T. Peitzmann, "Direct Photon Production in 158 AGeV Pb+Pb Collisions," *Nucl. Phys. A* **685** (2001) 399–406, arXiv:nucl-ex/0009014.

[47] T. Matsui and H. Satz, "J/ψ Suppression by Quark-Gluon Plasma Formation," *Phys. Lett. B* **178** (1986) 416–422.

[48] **NA50** Collaboration, M. C. Abreu *et al.*, "J / psi and Drell-Yan cross-sections in Pb Pb interactions at 158 GeV/c per nucleon," *Phys. Lett. B* **410** (1997) 327–336.

[49] **PHENIX** Collaboration, A. Adare *et al.*, "J/ψ Production vs Centrality, Transverse Momentum, and Rapidity in Au+Au Collisions at $\sqrt{s_{NN}} = 200$ GeV," *Phys. Rev. Lett.* **98** (2007) 232301, arXiv:nucl-ex/0611020.

[50] **ALICE** Collaboration, B. Abelev *et al.*, "J/ψ suppression at forward rapidity in Pb-Pb collisions at $\sqrt{s_{NN}} = 2.76$ TeV," *Phys. Rev. Lett.* **109** (2012) 072301, arXiv:1202.1383 [hep-ex].

[51] **ALICE** Collaboration, B. B. v. Abelev *et al.*, "Centrality, rapidity and transverse momentum dependence of J/ψ suppression in Pb-Pb collisions at $\sqrt{s_{\rm NN}}$=2.76 TeV," *Phys. Lett. B* **734** (2014) 314–327, arXiv:1311.0214 [nucl-ex].

[52] A. Ali and G. Kramer, "Jets and QCD: A Historical Review of the Discovery of the Quark and Gluon Jets and its Impact on QCD," *Eur. Phys. J. H* **36** (2011) 245–326, arXiv:1012.2288 [hep-ph].

[53] J. D. Bjorken, "Energy Loss of Energetic Partons in Quark - Gluon Plasma: Possible Extinction of High p(t) Jets in Hadron - Hadron Collisions,".

[54] S. Cao and X.-N. Wang, "Jet quenching and medium response in high-energy heavy-ion collisions: a review," *Rept. Prog. Phys.* **84** no. 2, (2021) 024301, arXiv:2002.04028 [hep-ph].

[55] **ALICE** Collaboration, K. Aamodt *et al.*, "Suppression of Charged Particle Production at Large Transverse Momentum in Central Pb-Pb Collisions at $\sqrt{s_{NN}} = 2.76$ TeV," *Phys. Lett. B* **696** (2011) 30–39, arXiv:1012.1004 [nucl-ex].

[56] J. Rafelski and R. Hagedorn, "From Hadron Gas to Quark Matter. 2.," in *International Symposium on Statistical Mechanics of Quarks and Hadrons*. 10, 1980.

[57] J. Rafelski and B. Muller, "Strangeness Production in the Quark - Gluon Plasma," *Phys. Rev. Lett.* **48** (1982) 1066. [Erratum: Phys.Rev.Lett. 56, 2334 (1986)].

[58] P. Koch, B. Muller, and J. Rafelski, "Strangeness in Relativistic Heavy Ion Collisions," *Phys. Rept.* **142** (1986) 167–262.

[59] **ALICE** Collaboration, B. B. Abelev *et al.*, "Multi-strange baryon production at mid-rapidity in Pb-Pb collisions at $\sqrt{s_{NN}} = 2.76$ TeV," *Phys. Lett. B* **728** (2014) 216–227, arXiv:1307.5543 [nucl-ex]. [Erratum: Phys.Lett.B 734, 409–410 (2014)].

[60] A. Tounsi, A. Mischke, and K. Redlich, "Canonical aspects of strangeness enhancement," *Nucl. Phys. A* **715** (2003) 565c–568c, arXiv:hep-ph/0209284.

[61] **STAR** Collaboration, B. I. Abelev *et al.*, "Energy and system size dependence of phi meson production in Cu+Cu and Au+Au collisions," *Phys. Lett. B* **673** (2009) 183–191, arXiv:0810.4979 [nucl-ex].

[62] **PHENIX** Collaboration, K. Adcox *et al.*, "Formation of dense partonic matter in relativistic nucleus-nucleus collisions at RHIC: Experimental evaluation by the PHENIX collaboration," *Nucl. Phys. A* **757** (2005) 184–283, arXiv:nucl-ex/0410003.

[63] **ALICE** Collaboration, B. B. Abelev *et al.*, "Elliptic flow of identified hadrons in Pb-Pb collisions at $\sqrt{s_{\rm NN}} = 2.76$ TeV," *JHEP* **06** (2015) 190, arXiv:1405.4632 [nucl-ex].

[64] **STAR** Collaboration, J. Adams *et al.*, "Azimuthal anisotropy in Au+Au collisions at s(NN)**(1/2) = 200-GeV," *Phys. Rev. C* **72** (2005) 014904, arXiv:nucl-ex/0409033.

[65] **PHENIX** Collaboration, S. S. Adler *et al.*, "Elliptic flow of identified hadrons in Au+Au collisions at s(NN)**(1/2) = 200-GeV," *Phys. Rev. Lett.* **91** (2003) 182301, arXiv:nucl-ex/0305013.

[66] E. V. Shuryak, "Quark-Gluon Plasma and Hadronic Production of Leptons, Photons and Psions," *Phys. Lett. B* **78** (1978) 150.

[67] K. Kajantie, J. I. Kapusta, L. D. McLerran, and A. Mekjian, "Dilepton Emission and the QCD Phase Transition in Ultrarelativistic Nuclear Collisions," *Phys. Rev. D* **34** (1986) 2746.

[68] **ALICE** Collaboration, S. Acharya *et al.*, "Measurement of dielectron production in central Pb-Pb collisions at $\sqrt{s_{\rm NN}} = 2.76$ TeV," *Phys. Rev. C* **99** no. 2, (2019) 024002, arXiv:1807.00923 [nucl-ex].

[69] M. A. Stephanov, K. Rajagopal, and E. V. Shuryak, "Event-by-event fluctuations in heavy ion collisions and the QCD critical point," *Phys. Rev. D* **60** (1999) 114028, arXiv:hep-ph/9903292.

[70] W. Kittel and E. A. De Wolf, *Soft multihadron dynamics*. World Scientific, 2005.

[71] V. Koch, "Fluctuations and correlations in heavy ion collisions," *J. Phys. Conf. Ser.* **50** (2006) 95–102.

[72] R. C. Hwa and C. B. Yang, "Local Multiplicity Fluctuations as a Signature of Critical Hadronization at LHC," *Phys. Rev. C* **85** (2012) 044914, arXiv:1111.6651 [nucl-th].

[73] H. Heiselberg, "Event-by-event physics in relativistic heavy ion collisions," *Phys. Rept.* **351** (2001) 161–194, arXiv:nucl-th/0003046.

[74] **ALICE** Collaboration, B. Abelev *et al.*, "Net-Charge Fluctuations in Pb-Pb collisions at $\sqrt{s_{NN}} = 2.76$ TeV," *Phys. Rev. Lett.* **110** no. 15, (2013) 152301, arXiv:1207.6068 [nucl-ex].

[75] **ALICE** Collaboration, B. Abelev *et al.*, "Charge correlations using the balance function in Pb-Pb collisions at $\sqrt{s_{NN}} = 2.76$ TeV," *Phys. Lett. B* **723** (2013) 267–279, arXiv:1301.3756 [nucl-ex].

[76] **ALICE** Collaboration, B. B. Abelev *et al.*, "Event-by-event mean $p_{\mathbf{T}}$ fluctuations in pp and Pb-Pb collisions at the LHC," *Eur. Phys. J. C* **74** no. 10, (2014) 3077, arXiv:1407.5530 [nucl-ex].

[77] **ALICE** Collaboration, S. Acharya *et al.*, "Charged-particle multiplicity fluctuations in Pb–Pb collisions at $\sqrt{s_{\rm NN}} = 2.76$ TeV," *Eur. Phys. J. C* **81** no. 11, (2021) 1012, arXiv:2105.05745 [nucl-ex].

[78] **ALICE** Collaboration, M. Arslandok, "Event-by-Event Identified Particle Ratio Fluctuations in Pb–Pb Collisions with ALICE using the Identity Method," *Nucl. Phys. A* **956** (2016) 870–873, arXiv:1512.03372 [hep-ex].

[79] A. Bialas and R. B. Peschanski, "Moments of Rapidity Distributions as a Measure of Short Range Fluctuations in High-Energy Collisions," *Nucl. Phys. B* **273** (1986) 703–718.

[80] A. Bialas, "Intermittency '90," *Nucl. Phys. A* **525** (1991) 345–360.

[81] E. A. De Wolf, I. M. Dremin, and W. Kittel, "Scaling laws for density correlations and fluctuations in multiparticle dynamics," *Phys. Rept.* **270** (1996) 1–141, arXiv:hep-ph/9508325.

[82] **STAR** Collaboration, M. Abdulhamid *et al.*, "Energy dependence of intermittency for charged hadrons in Au+Au collisions at RHIC," *Phys. Lett. B* **845** (2023) 138165, arXiv:2301.11062 [nucl-ex].

[83] T. Taylor and D. Treille, "The Large Electron Positron Collider (LEP): Probing the Standard Model," *Adv. Ser. Direct. High Energy Phys.* **27** (2017) 217–261.

[84] **ALICE** Collaboration, B. Abelev *et al.*, "Upgrade of the ALICE Experiment: Letter Of Intent," *J. Phys. G* **41** (2014) 087001.

[85] E. A. Mobs, "The CERN accelerator complex. Complexe des accélérateurs du CERN,". https://cds.cern.ch/record/2225847. General Photo.

[86] S. Gilardoni and D. Manglunki, eds., *Fifty years of the CERN Proton Synchrotron: Volume 1*. CERN Yellow Reports: Monographs. 2011.

[87] J.-P. Burnet *et al.*, "Fifty years of the CERN Proton Synchrotron : Volume 2," arXiv:1309.6923 [physics.acc-ph].

[88] N. Doble, L. Gatignon, K. Hübner, and E. Wilson, "The Super Proton Synchrotron (SPS): A Tale of Two Lives," *Adv. Ser. Direct. High Energy Phys.* **27** (2017) 135–177.

[89] M. Chanel, "LEIR: The low energy ion ring at CERN," *Nucl. Instrum. Meth. A* **532** (2004) 137–143.

[90] **ALICE** Collaboration, K. Aamodt *et al.*, "The ALICE experiment at the CERN LHC," *JINST* **3** (2008) S08002.

[91] **ATLAS** Collaboration, G. Aad *et al.*, "The ATLAS Experiment at the CERN Large Hadron Collider," *JINST* **3** (2008) S08003.

[92] **CMS** Collaboration, S. Chatrchyan *et al.*, "The CMS Experiment at the CERN LHC," *JINST* **3** (2008) S08004.

[93] **LHCb** Collaboration, A. A. Alves, Jr. *et al.*, "The LHCb Detector at the LHC," *JINST* **3** (2008) S08005.

[94] V. Frigo, "LHC structure.. Structure LHC.." AC Collection. Legacy of AC. Pictures from 1992 to 2002., 1997.

[95] https://alice-figure.web.cern.ch/node/11218, last accessed on 15/02/2024.

[96] **ALICE** Collaboration, *ALICE Inner Tracking System (ITS): Technical Design Report*. Technical design report. ALICE. CERN, Geneva, 1999. https://cds.cern.ch/record/391175.

[97] **ALICE** Collaboration, G. Dellacasa *et al.*, *ALICE time projection chamber: Technical Design Report*. Technical design report. ALICE. CERN, Geneva, 2000. http://cds.cern.ch/record/451098.

[98] **ALICE** Collaboration, P. Cortese, *ALICE transition-radiation detector: Technical Design Report*. Technical design report. ALICE. CERN, Geneva, 2001. http://cds.cern.ch/record/519145.

[99] **ALICE** Collaboration, G. Dellacasa *et al.*, *ALICE Time-Of-Flight system (TOF): Technical Design Report*. Technical design report. ALICE. CERN, Geneva, 2000. http://cds.cern.ch/record/430132.

[100] **ALICE** Collaboration, F. Piuz, W. Klempt, L. Leistam, J. De Groot, and J. Schükraft, *ALICE high-momentum particle identification: Technical Design Report*. Technical design report. ALICE. CERN, Geneva, 1998. http://cds.cern.ch/record/381431.

[101] **ALICE** Collaboration, V. I. Man'ko, W. Klempt, L. Leistam, J. De Groot, and J. Schükraft, *ALICE Photon Spectrometer (PHOS): Technical Design Report*. Technical design report. ALICE. CERN, Geneva, 1999. http://cds.cern.ch/record/381432.

[102] **ALICE** Collaboration, P. Cortese *et al.*, "ALICE electromagnetic calorimeter technical design report," tech. rep., 9, 2008. http://cds.cern.ch/record/1121574.

[103] **ACORDE** Collaboration, A. Fernández *et al.*, "ACORDE a Cosmic Ray Detector for ALICE," *Nucl. Instrum. Meth. A* **572** (2007) 102–103, arXiv:physics/0606051.

[104] **ALICE** Collaboration, *ALICE dimuon forward spectrometer: addendum to the Technical Design Report*. Technical design report. ALICE. CERN, Geneva, 2000. http://cds.cern.ch/record/494265.

[105] **ALICE** Collaboration, M. Gallio, W. Klempt, L. Leistam, J. De Groot, and J. Schükraft, *ALICE Zero-Degree Calorimeter (ZDC): Technical Design Report*. Technical design report. ALICE. CERN, Geneva, 1999. http://cds.cern.ch/record/381433.

[106] **ALICE** Collaboration, C. W. Fabjan, Y. P. Viyogi, and H. de Groot, *ALICE Photon Multiplicity Detector (PMD): addendum to the Technical Design Report*. Technical design report. ALICE. CERN, Geneva, 2003. http://cds.cern.ch/record/642177. Submitted on 19 Sep 2003.

[107] **ALICE** Collaboration, P. Cortese *et al.*, *ALICE forward detectors: FMD, TO and VO: Technical Design Report*. Technical design report. ALICE. CERN, Geneva, 2004. http://cds.cern.ch/record/781854. Submitted on 10 Sep 2004.

[108] **ALICE** Collaboration, B. Abelev *et al.*, "Technical Design Report for the Upgrade of the ALICE Inner Tracking System," *J. Phys. G* **41** (2014) 087002.

[109] **ALICE** Collaboration, K. Aamodt *et al.*, "Alignment of the ALICE Inner Tracking System with cosmic-ray tracks," *JINST* **5** (2010) P03003, arXiv:1001.0502 [physics.ins-det].

[110] A. Kluge *et al.*, "The ALICE silicon pixel detector," *Nucl. Instrum. Meth. A* **582** (2007) 728–732.

[111] **ALICE** Collaboration, D. Nouais *et al.*, "The Alice silicon drift detector system," *Nucl. Instrum. Meth. A* **501** (2001) 119–125.

[112] P. Kuijer, "The ALICE silicon strip detector system," *Nucl. Instrum. Methods Phys. Res., A* **447** no. 1-2, (2000) 251–256. https://cds.cern.ch/record/783069.

[113] J. Alme *et al.*, "The ALICE TPC, a large 3-dimensional tracking device with fast readout for ultra-high multiplicity events," *Nucl. Instrum. Meth. A* **622** (2010) 316–367, arXiv:1001.1950 [physics.ins-det].

[114] https://alice-figure.web.cern.ch/node/783, last accessed on 15/02/2024.

[115] **ALICE** Collaboration, E. Abbas *et al.*, "Performance of the ALICE VZERO system," *JINST* **8** (2013) P10016, arXiv:1306.3130 [nucl-ex].

[116] **ALICE** Collaboration, F. Carena *et al.*, "The ALICE data acquisition system," *Nucl. Instrum. Meth. A* **741** (2014) 130–162.

[117] **ALICE** Collaboration, M. Krivda, D. Alexandre, L. S. Barnby, D. Evans, P. G. Jones, A. Jusko, R. Lietava, J. Pospíšil, and O. V. Baillie, "The ALICE Central Trigger Processor (CTP) upgrade," *JINST* **11** no. 03, (2016) C03051.

[118] **ALICE** Collaboration, C. W. Fabjan, L. Jirdén, V. Lindestruth, L. Riccati, D. Rorich, P. Van de Vyvre, O. Villalobos Baillie, and H. de Groot, *ALICE trigger data-acquisition high-level trigger and control system: Technical Design Report*. Technical design report. ALICE. CERN, Geneva, 2004. https://cds.cern.ch/record/684651.

[119] **ALICE** Collaboration, P. Saiz, L. Aphecetche, P. Buncic, R. Piskac, J. E. Revsbech, and V. Sego, "AliEn - ALICE environment on the GRID," *Nucl. Instrum. Meth. A* **502** (2003) 437–440.

[120] J. Shiers, "The Worldwide LHC Computing Grid (worldwide LCG)," *Comput. Phys. Commun.* **177** (2007) 219–223.

[121] R. Brun and F. Rademakers, "ROOT: An object oriented data analysis framework," *Nucl. Instrum. Meth. A* **389** (1997) 81–86.

[122] T. Sjostrand, S. Mrenna, and P. Z. Skands, "PYTHIA 6.4 Physics and Manual," *JHEP* **05** (2006) 026, arXiv:hep-ph/0603175.

[123] T. Sjöstrand, S. Ask, J. R. Christiansen, R. Corke, N. Desai, P. Ilten, S. Mrenna, S. Prestel, C. O. Rasmussen, and P. Z. Skands, "An introduction to PYTHIA 8.2," *Comput. Phys. Commun.* **191** (2015) 159–177, arXiv:1410.3012 [hep-ph].

[124] T. Pierog and K. Werner, "EPOS Model and Ultra High Energy Cosmic Rays," *Nucl. Phys. B Proc. Suppl.* **196** (2009) 102–105, arXiv:0905.1198 [hep-ph].

[125] M. Gyulassy and X.-N. Wang, "HIJING 1.0: A Monte Carlo program for parton and particle production in high-energy hadronic and nuclear collisions," *Comput. Phys. Commun.* **83** (1994) 307, arXiv:nucl-th/9502021.

[126] Z.-W. Lin, C. M. Ko, B.-A. Li, B. Zhang, and S. Pal, "A Multi-phase transport model for relativistic heavy ion collisions," *Phys. Rev. C* **72** (2005) 064901, arXiv:nucl-th/0411110.

[127] E. Bruna, A. Dainese, M. Masera, and F. Prino, "Vertex reconstruction for proton-proton collisions in ALICE,". https://cds.cern.ch/record/1225497.

[128] D. Elia, J. Grosse-Oetringhaus, M. Nicassio, and T. Virgili, "The pixel detector based tracklet reconstruction algorithm in ALICE," tech. rep., CERN, Geneva, 2009. http://cds.cern.ch/record/1225500.

[129] R. Fruhwirth, "Application of Kalman filtering to track and vertex fitting," *Nucl. Instrum. Meth. A* **262** (1987) 444–450.

[130] T. H. Burnett *et al.*, "Extremely High Multiplicities in High-Energy Nucleus Nucleus Collisions," *Phys. Rev. Lett.* **50** (1983) 2062–2065.

[131] A. Bialas and R. B. Peschanski, "Intermittency in Multiparticle Production at High-Energy," *Nucl. Phys. B* **308** (1988) 857–867.

[132] **DELPHI** Collaboration, P. Abreu *et al.*, "A Study of intermittency in hadronic Z0 decays," *Phys. Lett. B* **247** (1990) 137–147.

[133] B. Buschbeck, P. Lipa, and R. B. Peschanski, "Signal for Intermittency in e^+e^- Reactions Obtained From Negative Binomial Fits," *Phys. Lett. B* **215** (1988) 788–791.

[134] **TASSO** Collaboration, W. Braunschweig *et al.*, "Study of Intermittency in Electron - Positron Annihilation Into Hadrons," *Phys. Lett. B* **231** (1989) 548–556.

[135] I. Derado, G. Jancso, N. Schmitz, and P. Stopa, "Investigation of Intermittency in Muon - Proton Scattering at 280-GeV," *Z. Phys. C* **47** (1990) 23–30.

[136] S.-S. Wang, J. Zhang, Y.-X. Ye, C.-G. Xiao, and Y. Zhong, "Intermittency exponents in p-p collisions at 400-GeV/c," *Phys. Rev. D* **49** (1994) 5785–5788.

[137] R. Holynski *et al.*, "Evidence for Intermittent Patterns of Fluctuations in Particle Production in High-Energy Interactions in Nuclear Emulsion," *Phys. Rev. Lett.* **62** (1989) 733–736.

[138] R. Holynski *et al.*, "One-dimensional and Two-dimensional Analysis of the Factorial Moments in 200-GeV/nucleon P, ^{16}O and ^{32}S Interactions With Ag / Br Nuclei," *Phys. Rev. C* **40** (1989) R2449–R2453.

[139] **HELIOS Emulsion** Collaboration, T. Akesson *et al.*, "A Search for multiplicity fluctuations in high-energy nucleus-nucleus collisions," *Phys. Lett. B* **252** (1990) 303–310.

[140] D. Ghosh, P. Ghosh, and A. Ghosh, "Intermittency and correlations in O-16 + Ag / Br interactions at 2.1-GeV/nucleon," *Phys. Rev. C* **49** (1994) 3219–3223.

[141] D. Ghosh, M. Lahiri, S. Das, K. Purkait, B. Biswas, J. Roychoudhury, R. Chatterjee, A. K. Jafry, and A. Deb, "Fluctuation study of pionisation

in ultrarelativistic nucleus nucleus interaction," *Z. Phys. C* **71** (1996) 243–249.

[142] D. Ghosh, A. Deb, R. Chattopadhyay, S. Sarkar, A. K. Jafry, M. Lahiri, S. Das, K. Purkait, B. Biswas, and J. Roychoudhury, "Evidence of multifractal nature of target-evaporated slow particles produced in ultrarelativistic heavy ion interactions," *Phys. Rev. C* **58** (1998) 3553–3559.

[143] D. Ghosh, A. Deb, S. Bhattacharyya, J. Ghosh, R. Das, and S. Mukherjee, "Evidence of intermittent type fluctuation of target residue in relativistic nuclear collisions at a few GeV/n," *Int. J. Mod. Phys. E* **12** (2003) 407–419.

[144] D. Ghosh, A. Deb, S. Bhattacharyya, J. Ghosh, and R. Sarkar, "Evidence of self-affine target fragmentation process in relativistic nuclear collision at a few GeV/n," *J. Phys. G* **29** (2003) 983–992.

[145] J. J. Binney, N. J. Dowrick, A. J. Fisher, and M. E. J. Newman, *The Theory of critical phenomena: An Introduction to the renormalization group*. Clarendon Press, 1992.

[146] R. C. Hwa and C. B. Yang, "Observable Properties of Quark-Hadron Phase Transition at the Large Hadron Collider," *Acta Phys. Polon. B* **48** (2017) 23, arXiv:1601.04671 [nucl-th].

[147] **ALICE** Collaboration, K. Aamodt *et al.*, "Charged-particle multiplicity density at mid-rapidity in central Pb-Pb collisions at $\sqrt{s_{NN}} = 2.76$ TeV," *Phys. Rev. Lett.* **105** (2010) 252301, arXiv:1011.3916 [nucl-ex].

[148] https://www.exploratorium.edu/snacks/fractal-patterns, last accessed on 10/06/2024.

[149] R. C. Hwa and M. T. Nazirov, "Intermittency in second order phase transition," *Phys. Rev. Lett.* **69** (1992) 741–744.

[150] R. C. Hwa, "Scaling exponent of multiplicity fluctuation in phase transition," *Phys. Rev. D* **47** (1993) 2773–2781.

[151] R. C. Hwa and J. Pan, "Intermittency in the Ginzburg-Landau theory," *Phys. Lett. B* **297** (1992) 35–38.

[152] Z. Cao, Y. Gao, and R. C. Hwa, "Scaling properties of hadron production in the Ising model for quark - hadron phase transition," *Z. Phys. C* **72** (1996) 661–670, arXiv:nucl-th/9601011.

[153] R. C. Hwa, "Recognizing Critical Behavior amidst Minijets at the Large Hadron Collider," *Adv. High Energy Phys.* **2015** (2015) 526908, arXiv:1411.6083 [nucl-ex].

[154] M. Young, Y. Qu, S. Singh, and R. C. Hwa, "Scaling behavior of photon number fluctuations at laser threshold," *Optics Communications* **105** no. 5, (1994) 325–329. https://www.sciencedirect.com/science/article/pii/0030401894904049.

[155] R. Sharma and R. Gupta, "Scaling Properties of Multiplicity Fluctuations in the AMPT Model," *Adv. High Energy Phys.* **2018** (2018) 6283801, arXiv:1806.10854 [hep-ph].

[156] R. Gupta and S. K. Malik, "Intermittency study of charged particles generated in Pb-Pb collisions at $\sqrt{s_{\rm NN}}$= 2.76 TeV using EPOS3," *Adv. High Energy Phys.* **2020** (2020) 5073042, arXiv:1911.13111 [hep-ex]. [Erratum: Adv.High Energy Phys. 2020, 7319894 (2020)].

[157] S. Bhattacharyya, "A Search for the Quark-Hadron Phase Transition in pp collisions at $\sqrt{s}$ = 13 TeV using UrQMD model," arXiv:2005.04488 [nucl-ex].

[158] Y.-L. Xie, G. Chen, J.-L. Wang, Z.-H. Liu, and M.-J. Wang, "Scaling properties of multiplicity fluctuations in heavy ion collisions simulated by AMPT model," *Nucl. Phys. A* **920** (2013) 33–44, arXiv:1303.2183 [nucl-th].

[159] M. I. Adamovich *et al.*, "Scaled factorial moment analysis of 200-A/GeV sulfur + gold interactions," *Phys. Rev. Lett.* **65** (1990) 412–415.

[160] R. C. Hwa, W. Ochs, and N. Schmitz, *Fluctuations and Fractal Structure*. World Scientific, 1992. https://www.worldscientific.com/doi/abs/10.1142/1525.

[161] B. Mandelbrot, *The Fractal Geometry of Nature*. Einaudi paperbacks. Henry Holt and Company, 1983. https://books.google.co.in/books?id=0R2LkE3N7-oC.

[162] R. C. Hwa, "Fractal Measures in Multiparticle Production," *Phys. Rev. D* **41** (1990) 1456.

[163] S. Ahmad and M. A. Ahmad, "A comparative study of multifractal moments in relativistic heavy-ion collisions," *J. Phys. G* **32** (2006) 1279–1293.

[164] G. Bhoumik, A. Deb, S. Bhattacharyya, and D. Ghosh, "Comparative Multifractal Detrended Fluctuation Analysis of Heavy Ion Interactions at a Few GeV to a Few Hundred GeV," *Adv. High Energy Phys.* **2016** (2016) 7287803.

[165] H. G. E. Hentschel and I. Procaccia, "The infinite number of generalized dimensions of fractals and strange attractors," *Physica* **8** (1983) 435–444.

[166] P. Lipa and B. Buschbeck, "From strong to weak intermittency," *Phys. Lett. B* **223** (1989) 465–469.

[167] E. K. Sarkisian, L. K. Gelovani, and G. G. Taran, "Fractality in central collisions of C-12 nuclei with Ne and Cu nuclei at 4.5-A/GeV/c," *Phys. Atom. Nucl.* **56** (1993) 832–840.

[168] E. K. Sarkisian, L. K. Gelovani, and G. G. Taran, "Fractality and fluctuations in charged particle pseudorapidity distributions in central C (Ne, Cu) collisions at 4.5-A/GeV/c," *Phys. Lett. B* **302** (1993) 331–335.

[169] W. Ochs and J. Wosiek, "Intermittency and Jets," *Phys. Lett. B* **214** (1988) 617–620.

[170] T. C. Halsey, M. H. Jensen, L. P. Kadanoff, I. Procaccia, and B. I. Shraiman, "Fractal measures and their singularities: The characterization of strange sets," *Phys. Rev. A* **33** (1986) 1141–1151. [Erratum: Phys.Rev.A 34, 1601 (1986)].

[171] G. Paladin and A. Vulpiani, "Anomalous scaling laws in multifractal objects," **156** no. 4, (1987) 147–225.

[172] A. Bialas and K. Zalewski, "Phase Structure of Selfsimilar Multiparticle Systems and Experimental Determination of Intermittency Parameters," *Phys. Lett. B* **238** (1990) 413–416.

[173] R. B. Peschanski, "On the Existence of a Nonthermal Phase Transition in Multiparticle Production," *Nucl. Phys. B* **327** (1989) 144–156.

[174] R. B. Peschanski, "Intermittency in particle collisions," *Int. J. Mod. Phys. A* **6** (1991) 3681–3722.

[175] W. J. Metzger, "Estimating the uncertainties of factorial moments," No. HEN-455(preprint). 2004. https://api.semanticscholar.org/CorpusID:97340706.

[176] **ALICE** Collaboration, J. Adam *et al.*, "Pseudorapidity dependence of the anisotropic flow of charged particles in Pb-Pb collisions at $\sqrt{s_{\mathrm{NN}}} = 2.76$ TeV," *Phys. Lett. B* **762** (2016) 376–388, arXiv:1605.02035 [nucl-ex].

[177] M. H. Seymour and M. Marx, "Monte Carlo Event Generators," in *69th Scottish Universities Summer School in Physics: LHC Physics*, pp. 287–319. 4, 2013. arXiv:1304.6677 [hep-ph].

[178] X.-N. Wang and M. Gyulassy, "HIJING: A Monte Carlo model for multiple jet production in p p, p A and A A collisions," *Phys. Rev. D* **44** (1991) 3501–3516.

[179] W.-T. Deng, X.-N. Wang, and R. Xu, "Hadron production in p+p, p+Pb, and Pb+Pb collisions with the HIJING 2.0 model at energies available at the CERN Large Hadron Collider," *Phys. Rev. C* **83** (2011) 014915, arXiv:1008.1841 [hep-ph].

[180] B. Zhang, "ZPC 1.0.1: A Parton cascade for ultrarelativistic heavy ion collisions," *Comput. Phys. Commun.* **109** (1998) 193–206, arXiv:nucl-th/9709009.

[181] B. Andersson, G. Gustafson, and B. Soderberg, "A General Model for Jet Fragmentation," *Z. Phys. C* **20** (1983) 317.

[182] B. Zhang, C. M. Ko, B.-A. Li, and Z.-w. Lin, "A multiphase transport model for nuclear collisions at RHIC," *Phys. Rev. C* **61** (2000) 067901, arXiv:nucl-th/9907017.

[183] J. Xu and C. M. Ko, "Pb-Pb collisions at $\sqrt{s_{NN}} = 2.76$ TeV in a multiphase transport model," *Phys. Rev. C* **83** (2011) 034904, arXiv:1101.2231 [nucl-th].

[184] Z.-W. Lin and L. Zheng, "Further developments of a multi-phase transport model for relativistic nuclear collisions," *Nucl. Sci. Tech.* **32** no. 10, (2021) 113, arXiv:2110.02989 [nucl-th].

[185] **ALICE** Collaboration, B. B. Abelev *et al.*, "Performance of the ALICE Experiment at the CERN LHC," *Int. J. Mod. Phys. A* **29** (2014) 1430044, arXiv:1402.4476 [nucl-ex].

[186] **ALICE** Collaboration, B. Abelev *et al.*, "Centrality determination of Pb-Pb collisions at $\sqrt{s_{NN}} = 2.76$ TeV with ALICE," *Phys. Rev. C* **88** no. 4, (2013) 044909, arXiv:1301.4361 [nucl-ex].

[187] **ALICE** Collaboration, J. Adam *et al.*, "Centrality Dependence of the Charged-Particle Multiplicity Density at Midrapidity in Pb-Pb Collisions at $\sqrt{s_{\rm NN}} = 5.02$ TeV," *Phys. Rev. Lett.* **116** no. 22, (2016) 222302, arXiv:1512.06104 [nucl-ex].

[188] C. Pruneau, S. Gavin, and S. Voloshin, "Methods for the study of particle production fluctuations," *Phys. Rev. C* **66** (2002) 044904, arXiv:nucl-ex/0204011.

[189] **NA61/SHINE** Collaboration, N. Davis, N. Antoniou, and F. K. Diakonos, "Recent Results from Proton Intermittency Analysis in

Nucleus–Nucleus Collisions from NA61 at CERN SPS," *Acta Phys. Polon. B* **50** (2019) 1029–1040.

[190] L. Mandel, "Fluctuations of photon beams and their correlations," *Proceedings of the Physical Society* **72** no. 6, (1958) 1037. https://dx.doi.org/10.1088/0370-1328/72/6/312.

[191] L. Mandel, "Fluctuations of photon beams: The distribution of the photo-electrons," *Proceedings of the Physical Society* **74** no. 3, (1959) 233. https://dx.doi.org/10.1088/0370-1328/74/3/301.

[192] E. Wolf and C. L. Mehta, "Determination of the statistical properties of light from photoelectric measurements," *Phys. Rev. Lett.* **13** (1964) 705–707. https://link.aps.org/doi/10.1103/PhysRevLett.13.705.

Appendix A

Kinematics in heavy-ion experiments

In heavy-ion experiments, kinematics play a crucial role in understanding the behaviour and interactions of the particles involved. Kinematics deals with the motion of objects without considering the forces causing the motion. In the context of heavy-ion collisions, kinematics helps describe the trajectories, momenta, and energies of the particles produced in the collision process. In the ALICE experiment at the LHC, the coordinate system is set up such that the z-direction aligns with the direction of the beams. The positive z-direction points from the starting point towards the V0A detector. The center of the Time Projection Chamber (TPC) detector, where the beams collide, is designated as the origin (0,0,0) of the coordinate system.

Transverse momentum

When analyzing the momentum of particles produced in collisions, it is useful to break down their momentum into two components. One component is the momentum along the direction of the beams (p_{z}), and the other is the momentum in the plane perpendicular to the beams (p_{T}), known as transverse momentum. The transverse momentum (p_{T}) is calculated as the square root of the sum of the squares of the momentum components along the x and y-axes as given below:

$$p_{\mathrm{T}} = \sqrt{p_x^2 + p_y^2} \tag{1.1}$$

The p_{T} is invariant under Lorentz transformation.

Rapidity variable

Rapidity (y) is a measure used to describe the relativistic velocity of a produced particle in heavy-ion collisions. It is advantageous because it remains additive under Lorentz transformations, unlike velocity in the relativistic limit. Rapidity is calculated using the energy (E) and longitudinal momentum (p_z) of the particle as

$$y = \frac{1}{2} \ln \frac{E + p_z}{E - p_z} \tag{1.2}$$

where E represents the energy of the particle, and y is equivalent to the velocity of the particle in the non-relativistic limit where the momentum (p_z) of a particle is comparable or smaller than its mass (m_0).

Pseudorapidity

To determine energy of particle, we require knowledge of its mass, which, in turn, necessitates identifying the particle. Pseudorapidity (η) is an approximation to rapidity used when it is challenging to identify particles. It is defined in terms of the angle (θ) between the momentum of the produced particle and the beam direction.

$$\eta = -\ln\left(\tan\left(\frac{\theta}{2}\right)\right) \tag{1.3}$$

Pseudorapidity can also be expressed in terms of momentum as

$$\eta = \frac{1}{2} \ln \left(\frac{|p| + p_z}{|p| - p_z}\right) \tag{1.4}$$

At large momemtum values pseudorapidity variable coincides with the rapidity variable. When particles discovered cannot be identified and their masses remain unknown, pseudorapidity emerges as a more practical experimental measure. In contrast, rapidity finds greater utility in phenomenological calculations, particularly when the mass of the desired particle is known.

Appendix B

Poisson-noise filtration

The investigation of dynamical fluctuations in high-energy collision scenarios necessitates a strategy to mitigate statistical noise arising from the finite number of particles within counting cells. A fundamental approach to address this is through the examination of factorial moments and their multivariate equivalents. This foundational technique, initially known in optics but later rediscovered in multi-hadron physics (referenced in [79, 131]), operates on the conjecture involving the multi-cell multiplicity distribution

$$P_M(n_1,\ldots,n_M) = \int d\rho_1 \ldots \int d\rho_M \, P_\rho(\rho_1,\ldots,\rho_M) \prod_{m=1}^{M} \frac{(\rho_m\delta)^{n_m}}{n_m!} exp(-\rho_m\delta) \quad (2.1)$$

This equation establishes a relationship between the distribution and the densities ρ_m, indicating Poissonian fluctuations around the average densities $\langle n_m \rangle$ within intervals. A complementary expression, further elaborates on $P_M(n_1,\ldots,n_M)$, as given below

$$P_M(n_1,\ldots,n_M) = \langle \prod_{m=1}^{M} \frac{(\rho_m\delta)^{n_m}}{n_m!} exp(-\langle n_m \rangle \rho_m) \rangle_\rho \quad (2.2)$$

This expression highlighting the averaging process over probability distributions of densities ρ_m, which solely encounter dynamical fluctuations, implying that in the absence of these fluctuations, $P_\rho(\rho_1,\ldots,\rho_M)$ becomes a product of delta functions.

The equations 2.1 and 2.2 resemble the multi-interval photo-electron counting probability distribution in quantum optics, associated with the Mandel formula [190, 191]. In optics, ρ_m represents space or time integrated field intensity,

calculated using the field density matrix for statistical analysis. These equations express $P_M(n_1, \ldots, n_M)$ as a linear transformation of $P_\rho(\rho_1, \ldots, \rho_M)$ with a "Poisson kernel," referred to as the "Poisson Transform" [192].

The Poisson-transform of a function $f(x)$ is denoted as $f(n)$ and is defined by the linear transformation

$$f(n) = \int_0^\infty dx\ f(x)\frac{x^n}{n!}e^{-x} \tag{2.3}$$

For example, the Bose-Einstein distribution $f(n)$ arises from this transform. The inverse Poisson-transform, closely associated with the Laplace-transform of $f(x)$, facilitates the derivation of $f(x)$ from its Poisson-transform counterpart.

The basic Poisson transform equation 2.2 yields the factorial moment generating function

$$G(z_1, \ldots, z_M) = \prod_{j=1}^{M} \exp(z_j \rho_j \delta)_\rho, \tag{2.4}$$

where statistical averaging takes place over the ensemble of densities $\rho_1, \ldots, \rho_M$. Comparing this with the (ordinary) moment generating function

$$Q(z_1, \ldots, z_M) = \int P_\rho(\rho_1, \ldots, \rho_M) \exp(\sum_{j=1}^{M} \rho_j z_j)\, d\rho_1 \ldots d\rho_M, \tag{2.5}$$

it follows that

$$G(z_1, \ldots, z_M) = Q(\delta\rho_1 z_1, \ldots, \rho_M z_M \delta) \tag{2.6}$$

This relationship implies that the normalized multivariate factorial moments are equivalent to the normalized multivariate moments of the relative density fluctuation $\rho_m/\langle\rho_m\rangle$, known as the "noise-suppression" theorem [79, 131]. This theorem, assuming Poissonian noise and unrestricted total multiplicity counts, underscores the utility of factorial moments in studying statistical properties of electromagnetic fields from photon-counting distributions, particularly in quantum optics.

Appendix C

Recent model predictions for LHC energies

Subject of intermittency and multifractal study in high energy physics of heavy ions was a subject of great interest as a signature of QGP and a way to understand density fluctuations and nature of the system created in heavy-ion collisions. In his work on the subject, R.C. Hwa and colleagues have developed and analysed models to understand the underlying mechanism of particle production. The Successive Contraction and Randomization (SCR) model was introduced in 2012 [72] and has been used to understand multiplicity fluctuations which notably inspires our current investigation utilizing the ALICE data. The subsequent section will provide a concise discussion of the findings presented in this paper.

The aim of work in [72] is to develop a method to simulate configurations across a spectrum of characteristics, spanning from critical to non-critical cases, without being biased by theoretical assumptions. The focus initially lies on devising a straightforward procedure to generate configurations that represent critical behaviour. To achieve this, the study reviews previous investigations concerning multiplicity fluctuations in systems undergoing second-order phase transitions described by the Ginzburg-Landau (GL) theory. These studies are connected to a cluster production formation, requiring only one parameter to describe clustering, facilitating the simulation of initial configurations before hadronization. For non-critical cases, the adjustment of this parameter aims to shift towards random distributions.

A spectrum of scenarios, spanning robust criticality to mundane randomness is simulated within the transition from quark to hadron phases. Emphasizing the

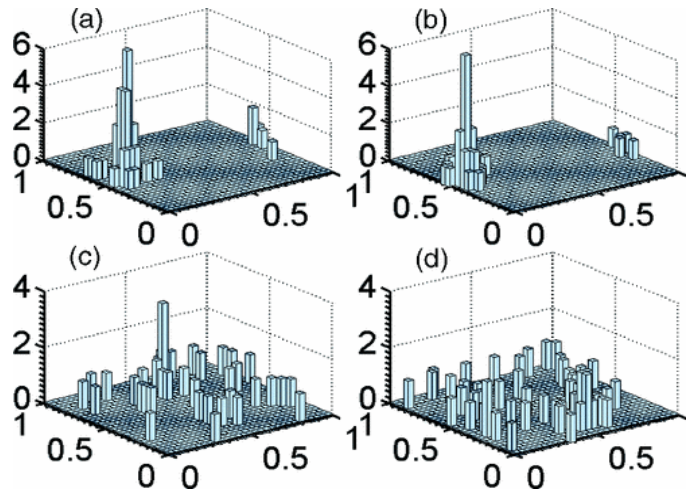

Figure C.1. Examples of bin multiplicity fluctuations in (η, φ) for the four cases arranged in the matrix form, i.e., (a) critical, (b) quasi-critical, (c) pseudo-critical, (d) non-critical. [72].

importance of uncovering unconventional signals, particularly in examining fluctuations in particle production during distinct types of hadronization, the study focuses on motivating experimental endeavours. It seeks to capture the dynamics between the conclusion of the quark phase and the initiation of the hadron phase, presuming low-density conditions where interactions among quarks and antiquarks lead to their rearrangement. The simulation confines its analysis to the central rapidity region, mapping the plasma cylinder's surface to a unit square S for a stepwise hadronization process. Employing an algorithm involving multiple time steps, it simulates the adjustments of quark and antiquark positions, reflecting confinement and pion emission dynamics. The study examines whether local fluctuations persist through the hadronization process and remain identifiable, acknowledging the challenges of precision within Quantum Chromodynamics (QCD) in the soft regime. Four different scenario are studied from the critical hadronization followed by discussions on less critical cases, aiming to explore and differentiate various characteristics of the hadronization process.

The described simulation aims to model different scenarios of hadronization dynamics from critical to non-critical cases as shown in Fig. C.1. In the first scenario, clustering of $q\bar{q}$ pairs occurs in the unit square, followed by a contraction process mimicking confinement forces, leading to pionization within a specified distance. This represents a critical transition. The quasi-critical scenario lacks

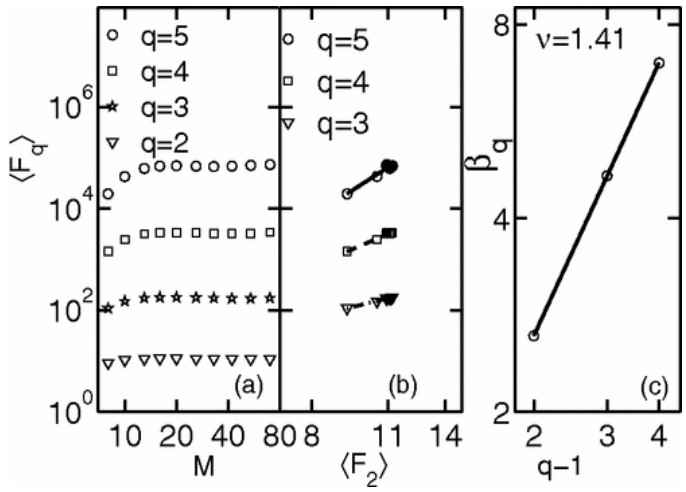

Figure C.2. Intermittency analysis for the critical case. [72].

clustering and resembles a cross-over phase diagram without achieving critical conditions. The pseudo-critical case involves clustering without contraction, simulating critical conditions but without the associated contraction. The non-critical scenario involves random configurations without organized dynamics, expected to lack significant content for analysis. These scenarios simulate different aspects of hadronization dynamics for comparison and understanding.

To analyze the scaling behaviour, log-log plots of ln $F_q(M)$ versus M were generated for q=2 to 5 witin a narrow interval of around 1 GeV/c. In Fig C.2, for the critical case, there is an initial increase with M before convergence around M>20, displaying scaling behaviour for different q values. The F-scaling behaviour (Fig C.2) shows a linear relationship when $F_q(M)$ is plotted against $F_2(M)$, leading to a value of ν_{crit}=1.41 (Fig C.2c). Similar scaling properties with ν_{quasi}=1.33 are observed in the quasi-critical case. In contrast, the pseudo-critical cases (Fig C.3) exhibit robust scaling behaviour (Fig C.3a) and linear relationships in the F-scaling plots (Fig C.3b) with ν_{pseudo}=1.26 (Fig C.3c). However, in the non-critical case (Fig C.4), $F_q(M)$ decreases with increasing M (Fig C.4a), suggesting that bin multiplicities do not deviate significantly from the average, leading to Poissonian-like fluctuations at smaller bin sizes. While there is some regularity in the $F_q(M)$ plotted against $F_2(M)$ (Fig C.4b), it contrasts the behaviour observed in critical and other cases. Consequently, no sensible value of ν can be calculated in this non-critical case.

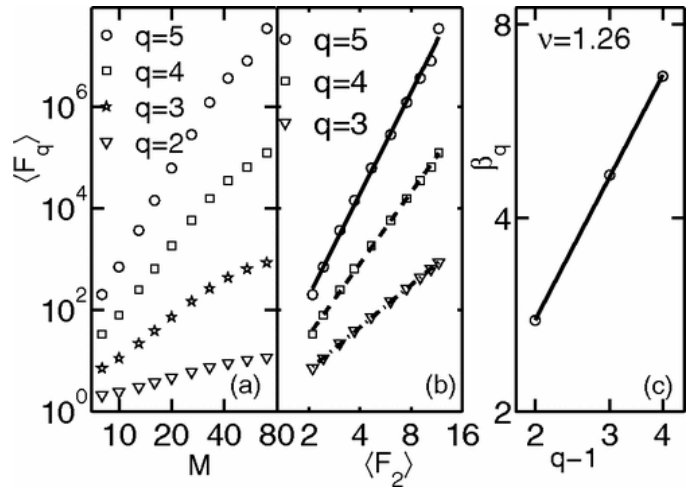

Figure C.3. Intermittency analysis for the quasi-critical case. [72].

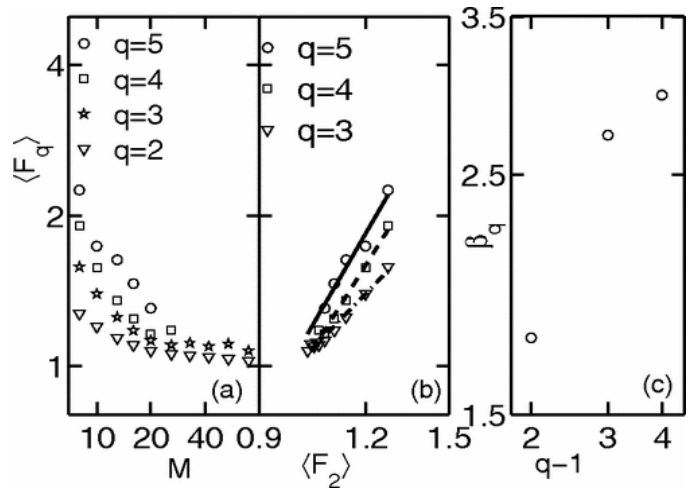

Figure C.4. Intermittency analysis for the non-critical case. [72].

In summary, the critical, quasi-critical, and pseudo-critical scenarios display scaling behaviour indicative of interesting fluctuations and criticality in the hadronization process, while the non-critical case lacks substantial deviations from random fluctuations and does not yield meaningful results. Deviations in experimental values could imply the presence of new physics or highlight potential shortcomings in the proposed theoretical models. Therefore, it emphasizes the importance of applying these measures to experimental data to explore and potentially uncover new aspects of particle physics at the LHC.

Appendix D

Data sets and run numbers

HIJING

Production name: LHC11a10a_bis

AOD: 162

Run numbers :

139510,139507,139505,139503,139465,139438,139437,139360,139329,139328,
139314,139310,139309,139173,139107,139105,139038,139037,139036,139029,
139028,138872,138871,138870,138837,138732,138730,138662,138653,138652,
138638,138624,138621,138583,138582,138579,138578,138534,138469,138442,
138439,138438,138396,138364,138275,138225,138201,138197,138192,138190,
137848,137844,137752,137751,137724,137722,137718,137704,137693,137692,
137691,137686,137685,137639,137638,137608,137595,137549,137544,137541,
137539,137531,137530,137443,137441,137440,137439,137434,137432,137431,
137243,137236,137235,137232,137231,37162,137161.

AMPT

Production name: LHC12a11a

AOD: 081

Run numbers: 137686,138534,138653,139038,139437

Experimental data

Production name: LHC10h

AOD: 160

Run Numbers :

Same run numbers as above.

Appendix E

Analysis in forward and backward pseudorapidity ranges

The analysis is performed by excluding the central pseudorapidity region near 0. This involved investigating two specific pseudorapidity ranges: one from 0.2 to 0.8 (forward side) and the other from -0.8 to -0.2 (backward side) with $\Delta\eta = 0.6$. The purpose of examining these windows was to look for any dependence of power-law behaviour on the central rapidity region. In both cases, multiplicity distributions are plotted, as shown in Fig. E.1(a). These distributions are subsequently compared with the default case, illustrated in Fig. E.1(b). The plots reveal that, in both pseudorapidity windows, the multiplicities are nearly identical but significantly smaller than those in the default scenario with $\Delta\eta = 1.6$.

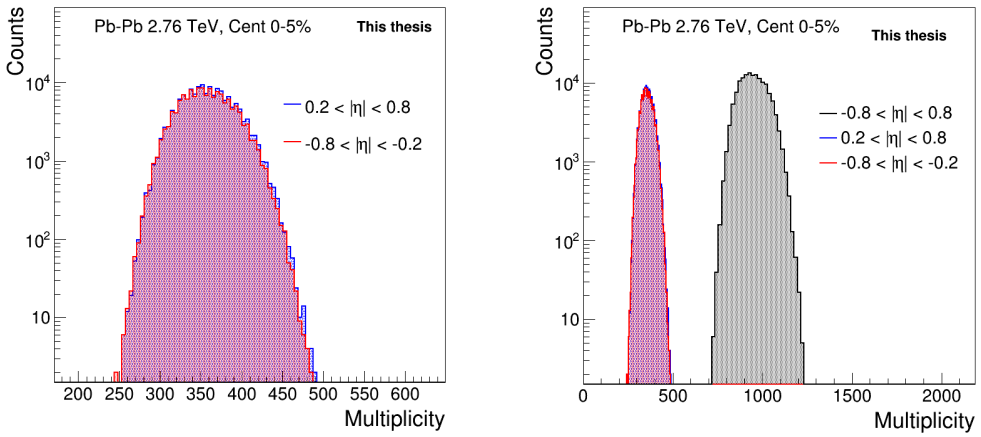

(a) (b)

Figure E.1. a) Multiplicity distributions in forward and backward pseudorapidity ranges b) Multiplicity distributions in forward and backward pseudorapidity ranges compared with the default full pseudorapidity range.

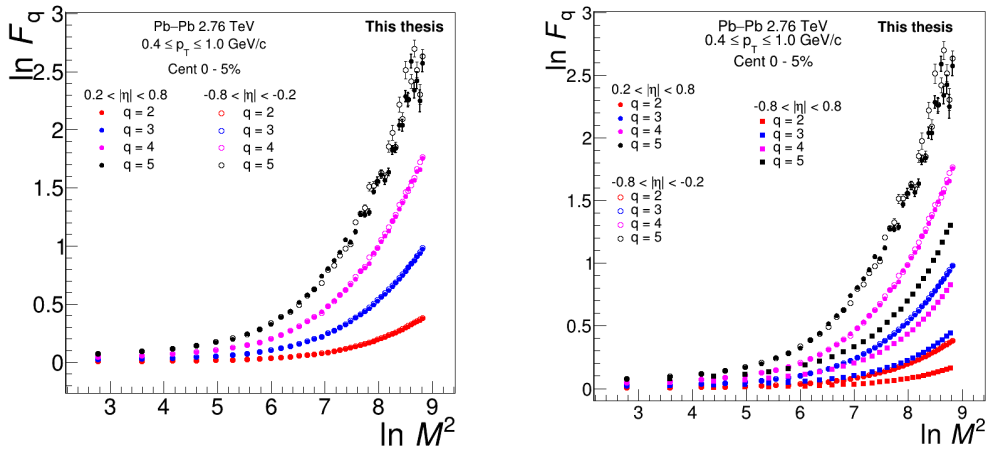

Figure E.2. a) Dependence of ln F_{q} on ln M^2 for q = 2, 3, 4 and 5 in forward and backward pseudorapidity ranges b) Dependence of ln F_{q} on ln M^2 for q = 2, 3, 4 and 5 in forward and backward pseudorapidity ranges compared with the default i.e. full pseudorapidity range for central Pb−Pb collisions at $\sqrt{s_{\mathrm{NN}}}$ = 2.76 TeV.

Normalized factorial moments $F_{\mathrm{q}}(M)$ are calculated and the $\ln F_{\mathrm{q}}$ versus $\ln M^2$ behaviour is given in Fig. E.2(a) for the two cases with $\Delta\eta = 0.6$. The charged particles show similar power-law behaviour in the forward and backward region with similar quantitative values. However, as shown in Fig. E.2(b) there is quantitative difference in the NFM values obtained from small and wide $\Delta\eta$ bins. The power-law behaviour shows similar trends both in $\Delta\eta = 1.6$ where $|\eta \leq 0.8$ and $\Delta\eta = 0.6$ where pseudorapidity ranges are $0.2 \leq \eta \leq 0.8$ and -0.8 $\leq \eta \leq$ -0.2. Power law growth signifies the intermittency in data. This study thus reveals that the scaling behaviour of NFMs is not due to fluctuations in η values near to 0.

List of Publications/Conferences

A. List of presentations/participation in conferences:

1. "*Charged particle erraticity in the AMPT model at LHC energies*"; **DAE-BRNS HEP Symposium 2020, NISER, India December 14-18, 2020**.

2. "*Intermittency Analysis of Toy Monte Carlo events*"; **50th International Symposium on Multiparticle Dynamics (ISMD2021), Virtual mode, July 12-16, 2021**.

3. "*Local multiplicity fluctuations in Pb-Pb collisions at* $\sqrt{s_{NN}}$ *= 2.76 TeV with ALICE at LHC* "; **29th International Conference on Ultra-relativistic Nucleus-Nucleus Collisions, April 4-10, 2022 Krakow, Poland**.

4. "*Event-by-event multiplicity fluctuations in Pb-Pb collisions at* $\sqrt{s_{NN}}$ *= 2.76 TeV with ALICE at LHC* "; **XI International Conference on New Frontiers in Physics, 30 August 2022 - 12 September 2022, Crete, Greece**.

5. "*Local multiplicity fluctuations in Pb-Pb collisions at* $\sqrt{s_{NN}}$ *= 2.76 TeV with ALICE at LHC* "; **XXV DAE-BRNS High Energy Physics Symposium 2022, December 12 - 16, 2022, IISER Mohali, India**.

6. "*Intermittency analysis of charged particles produced in Pb-Pb collisions at* $\sqrt{s_{NN}}$ *= 2.76 TeV with ALICE*"; **8th International Conference on Physics and Astrophysics of Quark Gluon Plasma (ICPAQGP-2023), February 07 - 10, 2023, Puri, Odisha, India**.

7. "*Factorial Moments and detector efficiencies: A Toy Model Study*"; **JK-Women Science Congress 2024, February 11 - 13, 2024, University**

of Jammu, India.

B. Work published/preprints as conference proceedings:

1. Sheetal Sharma and Ramni Gupta; "*Intermittency Analysis of Toy Monte Carlo Events*"; Submitted as proceedings of 50th International Symposium on Multiparticle Dynamics (ISMD), July 12-16, 2021; [https://scipost.org/SciPostPhysProc.10.024]

2. Sheetal Sharma and Ramni Gupta [ALICE]; "*Local multiplicity fluctuations in Pb−Pb collisions at* $\sqrt{s_{\rm NN}}$ *= 2.76 TeV with ALICE at the LHC*"; Submitted as proceedings of the XXV DAE-BRNS High Energy Physics (HEP) Symposium, December 12-16, 2022; [https://link.springer.com/chapter/10.1007/978-981-97-0289-3_221]

C. Paper Communicated

- Sheetal Sharma, Salman Khurshid Malik, Zarina Banoo and Ramni Gupta; "*Normalized factorial moments of spatial distributions of particles in high multiplicity events: A Toy model study*"; Submitted as article on arXiv:2309.07712 [Yet to be published]; [https://arxiv.org/abs/2309.07712]

D. ALICE internal analysis note

- Sheetal Sharma and Ramni Gupta; " *Scaling properties of local multiplicity fluctuations in Pb-Pb collisions at 2.76 TeV in ALICE* "; ALICE scientific note (not public);[https://alice-notes.web.cern.ch/node/996]

E. List of papers co-authored as ALICE Collaborator

1. S. Acharya,...,S. Sharma,...*et al.* [ALICE], Phys. Rev. C **109** (2024) no.6, 065202 doi:10.1103/PhysRevC.109.065202 [arXiv:2403.15213 [nucl-ex]].

2. S. Acharya,...,S. Sharma,...*et al.* [ALICE], Phys. Rev. Lett. **132** (2024) no.17, 172302 doi:10.1103/PhysRevLett.132.172302 [arXiv:2311.14357 [nucl-ex]].

3. S. Acharya,...,S. Sharma,...*et al.* [ALICE], Phys. Lett. B **853** (2024), 138665 doi:10.1016/j.physletb.2024.138665 [arXiv:2311.11786 [nucl-ex]].

4. S. Acharya,...,S. Sharma,...*et al.* [ALICE], Phys. Rev. Lett. **132** (2024) no.22, 222303 doi:10.1103/PhysRevLett.132.222303 [arXiv:2311.11792 [nucl-ex]].

5. S. Acharya,...,S. Sharma,...*et al.* [ALICE], JHEP **05** (2024), 184 doi:10.1007/JHEP05(2024)184 [arXiv:2310.10236 [hep-ex]].

6. S. Acharya,...,S. Sharma,...*et al.* [ALICE], JHEP **01**, 056 (2024) doi:10.1007/JHEP01(2024)056 [arXiv:2310.07490 [nucl-ex]].

7. S. Acharya,...,S. Sharma,...*et al.* [ALICE], JHEP **12**, 067 (2023) doi:10.1007/JHEP12(2023)067 [arXiv:2308.16123 [nucl-ex]].

8. S. Acharya,...,S. Sharma,...*et al.* [ALICE], Phys. Rev. D **108**, no.11, 112003 (2023) doi:10.1103/PhysRevD.108.112003 [arXiv:2308.04873 [hep-ex]].

9. S. Acharya,...,S. Sharma,...*et al.* [ALICE], JHEP **12**, 086 (2023) doi:10.1007/JHEP12(2023)086 [arXiv:2308.04877 [hep-ex]].

10. S. Acharya,...,S. Sharma,...*et al.* [ALICE], Eur. Phys. J. C **83**, no.12, 1123 (2023) doi:10.1140/epjc/s10052-023-12259-3 [arXiv:2307.14084 [nucl-ex]].

11. S. Acharya,...,S. Sharma,...*et al.* [ALICE], Phys. Lett. B **848**, 138337 (2024) doi:10.1016/j.physletb.2023.138337 [arXiv:2307.03603 [nucl-ex]].

12. S. Acharya,...,S. Sharma,...*et al.* [ALICE], Phys. Lett. B **845**, 138145 (2023) doi:10.1016/j.physletb.2023.138145 [arXiv:2305.19093 [nucl-ex]].

13. S. Acharya,...,S. Sharma,...*et al.* [ALICE], Phys. Rev. D **108**, no.11, 112004 (2023) doi:10.1103/PhysRevD.108.112004 [arXiv:2304.12403 [nucl-ex]].

14. S. Acharya,...,S. Sharma,...*et al.* [ALICE], JINST **18**, no.11, P11032 (2023) doi:10.1088/1748-0221/18/11/P11032 [arXiv:2303.15317 [physics.ins-det]].

15. S. Acharya,...,S. Sharma,...*et al.* [ALICE], Phys. Rev. C **108**, no.4, 045203 (2023) doi:10.1103/PhysRevC.108.045203 [arXiv:2303.13431 [hep-ex]].

16. S. Acharya,...,S. Sharma,...*et al.* [ALICE], Eur. Phys. J. A **59**, no.12, 298 (2023) doi:10.1140/epja/s10050-023-01139-9 [arXiv:2303.13448 [nucl-ex]].

17. S. Acharya,...,S. Sharma,...*et al.* [ALICE], JHEP **08**, 006 (2023) doi:10.1007/JHEP08(2023)006 [arXiv:2303.13349 [nucl-ex]].

18. S. Acharya,...,S. Sharma,...*et al.* [ALICE], Eur. Phys. J. C **83**, no.7, 661 (2023) doi:10.1140/epjc/s10052-023-11729-y [arXiv:2303.00590 [nucl-ex]].

19. S. Acharya,...,S. Sharma,...*et al.* [ALICE], Eur. Phys. J. C **83**, no.8, 741 (2023) doi:10.1140/epjc/s10052-023-11835-x [arXiv:2303.00591 [nucl-ex]].

20. S. Acharya,...,S. Sharma,...*et al.* [ALICE], Eur. Phys. J. C **83**, no.7, 576 (2023) doi:10.1140/epjc/s10052-023-11658-w [arXiv:2302.01234 [nucl-ex]].

21. S. Acharya,...,S. Sharma,...*et al.* [ALICE], Phys. Lett. B **846**, 137920 (2023) doi:10.1016/j.physletb.2023.137920 [arXiv:2212.06588 [nucl-ex]].

22. S. Acharya,...,S. Sharma,...*et al.* [ALICE], Phys. Lett. B **846**, 137795 (2023) doi:10.1016/j.physletb.2023.137795 [arXiv:2212.04777 [nucl-ex]].

23. S. Acharya,...,S. Sharma,...*et al.* [ALICE], Phys. Rev. D **108**, no.7, 072008 (2023) doi:10.1103/PhysRevD.108.072008 [arXiv:2211.15364 [nucl-ex]].

24. S. Acharya,...,S. Sharma,...*et al.* [ALICE], Phys. Lett. B **845**, 138110 (2023) doi:10.1016/j.physletb.2023.138110 [arXiv:2211.15326 [nucl-ex]].

25. S. Acharya,...,S. Sharma,...*et al.* [ALICE], Phys. Rev. C **108**, no.3, 034906 (2023) doi:10.1103/PhysRevC.108.034906 [arXiv:2211.13985 [nucl-ex]].

26. S. Acharya,...,S. Sharma,...*et al.* [ALICE], Eur. Phys. J. C **83**, no.6, 497 (2023) doi:10.1140/epjc/s10052-023-11614-8 [arXiv:2211.01197 [nucl-ex]].

27. S. Acharya,...,S. Sharma,...*et al.* [ALICE], Phys. Lett. B **846**, 137782 (2023) doi:10.1016/j.physletb.2023.137782 [arXiv:2210.08980 [nucl-ex]].

28. S. Acharya,...,S. Sharma,...*et al.* [ALICE], Phys. Rev. Lett. **131**, no.10, 102302 (2023) doi:10.1103/PhysRevLett.131.102302 [arXiv:2209.07360 [nucl-ex]].

29. S. Acharya,...,S. Sharma,...*et al.* [ALICE], JINST **18**, no.08, P08007 (2023) doi:10.1088/1748-0221/18/08/P08007 [arXiv:2209.04216 [physics.ins-det]].

30. S. Acharya,...,S. Sharma,...*et al.* [ALICE], Phys. Rev. Lett. **131**, no.19, 192301 (2023) doi:10.1103/PhysRevLett.131.192301 [arXiv:2208.04857 [nucl-ex]].

31. S. Acharya,...,S. Sharma,...*et al.* [ALICE], Phys. Lett. B **846**, 137644 (2023) doi:10.1016/j.physletb.2022.137644 [arXiv:2206.06216 [nucl-ex]].

32. S. Acharya,...,S. Sharma,...*et al.* [ALICE], JHEP **05**, 243 (2023) doi:10.1007/JHEP05(2023)243 [arXiv:2206.04587 [nucl-ex]].

33. S. Acharya,...,S. Sharma,...*et al.* [ALICE], Phys. Lett. B **844**, 137545 (2023) doi:10.1016/j.physletb.2022.137545 [arXiv:2206.03343 [nucl-ex]].

34. S. Acharya,...,S. Sharma,...*et al.* [ALICE], Eur. Phys. J. A **59**, no.7, 145 (2023) doi:10.1140/epja/s10050-023-00998-6 [arXiv:2206.03344 [nucl-ex]].

35. S. Acharya,...,S. Sharma,...*et al.* [ALICE], Eur. Phys. J. C **83**, no.4, 340 (2023) doi:10.1140/epjc/s10052-023-11476-0 [arXiv:2205.15176 [nucl-ex]].

36. S. Acharya,...,S. Sharma,...*et al.* [ALICE], Eur. Phys. J. C **83**, no.5, 351 (2023) doi:10.1140/epjc/s10052-023-11475-1 [arXiv:2205.13998 [nucl-ex]].

37. S. Acharya,...,S. Sharma,...*et al.* [ALICE], Phys. Lett. B **846**, 137625 (2023) doi:10.1016/j.physletb.2022.137625 [arXiv:2205.13993 [nucl-ex]].

38. S. Acharya,...,S. Sharma,...*et al.* [ALICE], Phys. Lett. B **846**, 137467 (2023) doi:10.1016/j.physletb.2022.137467 [arXiv:2204.10684 [nucl-ex]].

39. S. Acharya,...,S. Sharma,...*et al.* [ALICE], JHEP **05**, 036 (2023) doi:10.1007/JHEP05(2023)036 [arXiv:2204.10640 [nucl-ex]].

40. S. Acharya,...,S. Sharma,...*et al.* [ALICE], Phys. Lett. B **843**, 137649 (2023) doi:10.1016/j.physletb.2022.137649 [arXiv:2204.10157 [nucl-ex]].

41. S. Acharya,...,S. Sharma,...*et al.* [ALICE], Phys. Lett. B **845**, 137730 (2023) doi:10.1016/j.physletb.2023.137730 [arXiv:2204.10210 [nucl-ex]].

42. S. Acharya,...,S. Sharma,...*et al.* [ALICE], Phys. Lett. B **844**, 137223 (2023) doi:10.1016/j.physletb.2022.137223 [arXiv:2204.10258 [nucl-ex]].

43. S. Acharya,...,S. Sharma,...*et al.* [ALICE], Phys. Lett. B **846**, 137453 (2023) doi:10.1016/j.physletb.2022.137453 [arXiv:2204.10240 [nucl-ex]].

44. S. Acharya,...,S. Sharma,...*et al.* [ALICE], JHEP **05**, 244 (2023) doi:10.1007/JHEP05(2023)244 [arXiv:2204.10246 [nucl-ex]].

45. S. Acharya,...,S. Sharma,...*et al.* [ALICE], JHEP **06**, 147 (2023) doi:10.1007/JHEP06(2023)147 [arXiv:2204.10253 [nucl-ex]].

46. S. Acharya,...,S. Sharma,...*et al.* [ALICE], JHEP **05**, 245 (2023) doi:10.1007/JHEP05(2023)245 [arXiv:2204.10270 [nucl-ex]].

47. S. Acharya,...,S. Sharma,...*et al.* [ALICE], Eur. Phys. J. C **83**, no.6, 540 (2023) doi:10.1140/epjc/s10052-023-11449-3 [arXiv:2204.10263 [nucl-ex]].

48. S. Acharya,...,S. Sharma,...*et al.* [ALICE], JHEP **06**, 133 (2023) doi:10.1007/JHEP06(2023)133 [arXiv:2204.10167 [nucl-ex]].

49. S. Acharya,...,S. Sharma,...*et al.* [ALICE], Phys. Lett. B **846**, 137561 (2023) doi:10.1016/j.physletb.2022.137561 [arXiv:2204.10386 [nucl-ex]].

50. S. Acharya,...,S. Sharma,...*et al.* [ALICE], Phys. Rev. Lett. **131**, no.4, 042303 (2023) doi:10.1103/PhysRevLett.131.042303 [arXiv:2204.10171 [nucl-ex]].

51. S. Acharya,...,S. Sharma,...*et al.* [ALICE], Phys. Rev. Lett. **131**, no.4, 041901 (2023) doi:10.1103/PhysRevLett.131.041901 [arXiv:2204.10166 [nucl-ex]].

52. S. Acharya,...,S. Sharma,...*et al.* [ALICE], Nature Phys. **19**, no.1, 61-71 (2023) doi:10.1038/s41567-022-01804-8 [arXiv:2202.01549 [nucl-ex]].

53. S. Acharya,...,S. Sharma,...*et al.* [ALICE], JHEP **12**, 126 (2022) doi:10.1007/JHEP12(2022)126 [arXiv:2202.00815 [nucl-ex]].

54. S. Acharya,...,S. Sharma,...*et al.* [ALICE], Phys. Lett. B **832**, 137242 (2022) doi:10.1016/j.physletb.2022.137242 [arXiv:2112.09482 [nucl-ex]].

55. S. Acharya,...,S. Sharma,...*et al.* [ALICE], Eur. Phys. J. C **83**, no.1, 61 (2023) doi:10.1140/epjc/s10052-022-10896-8 [arXiv:2109.15240 [nucl-ex]].

56. S. Acharya,...,S. Sharma,...*et al.* [ALICE], JHEP **05**, 061 (2022) doi:10.1007/JHEP05(2022)061 [arXiv:2107.11303 [nucl-ex]].

57. S. Acharya,...,S. Sharma,...*et al.* [ALICE], Eur. Phys. J. C **81**, no.10, 945 (2021) doi:10.1140/epjc/s10052-021-09678-5 [arXiv:2107.11209 [nucl-ex]].

58. S. Acharya,...,S. Sharma,...*et al.* [ALICE], Phys. Rev. Lett. **127**, no.17, 172301 (2021) doi:10.1103/PhysRevLett.127.172301 [arXiv:2105.05578 [nucl-ex]].

59. S. Acharya,...,S. Sharma,...*et al.* [ALICE], JHEP **06**, 011 (2022) doi:10.1007/JHEP06(2022)011 [arXiv:2105.04957 [nucl-ex]].

60. S. Acharya,...,S. Sharma,...*et al.* [ALICE], Phys. Lett. B **833**, 137272 (2022) doi:10.1016/j.physletb.2022.137272 [arXiv:2104.04427 [nucl-ex]].

61. S. Acharya,...,S. Sharma,...*et al.* [ALICE], Eur. Phys. J. C **81**, no.8, 712 (2021) doi:10.1140/epjc/s10052-021-09437-6 [arXiv:2101.04577 [nucl-ex]].

62. S. Acharya,...,S. Sharma,...*et al.* [ALICE], JHEP **05**, 290 (2021) doi:10.1007/JHEP05(2021)290 [arXiv:2101.03110 [nucl-ex]].

63. S. Acharya,...,S. Sharma,...*et al.* [ALICE], Phys. Lett. B **822**, 136579 (2021) doi:10.1016/j.physletb.2021.136579 [arXiv:2011.05758 [nucl-ex]].

64. S. Acharya,...,S. Sharma,...*et al.* [ALICE], JHEP **02**, 002 (2021) doi:10.1007/JHEP02(2021)002 [arXiv:2008.04806 [nucl-ex]].

65. S. Acharya,...,S. Sharma,...*et al.* [ALICE], JHEP **10**, 141 (2020) doi:10.1007/JHEP10(2020)141 [arXiv:2005.14518 [nucl-ex]].

66. S. Acharya,...,S. Sharma,...*et al.* [ALICE], JHEP **09**, 160 (2020) doi:10.1007/JHEP09(2020)160 [arXiv:2005.14640 [nucl-ex]].

67. S. Acharya,...,S. Sharma,...*et al.* [ALICE], Phys. Rev. C **102**, no.5, 055203 (2020) doi:10.1103/PhysRevC.102.055203 [arXiv:2005.14639 [nucl-ex]].

68. S. Acharya,...,S. Sharma,...*et al.* [ALICE], Phys. Rev. Lett. **125**, no.16, 162001 (2020) doi:10.1103/PhysRevLett.125.162001 [arXiv:2005.11122 [nucl-ex]].

69. S. Acharya,...,S. Sharma,...*et al.* [ALICE], Eur. Phys. J. C **81**, no.3, 256 (2021) doi:10.1140/epjc/s10052-020-08690-5 [arXiv:2005.11120 [nucl-ex]].

70. S. Acharya,...,S. Sharma,...*et al.* [ALICE], Phys. Rev. Lett. **126**, no.16, 162001 (2021) doi:10.1103/PhysRevLett.126.162001 [arXiv:2005.11130 [nucl-ex]].

71. S. Acharya,...,S. Sharma,...*et al.* [ALICE], Phys. Lett. B **813**, 136054 (2021) doi:10.1016/j.physletb.2020.136054 [arXiv:2005.11131 [nucl-ex]].

72. S. Acharya,...,S. Sharma,...*et al.* [ALICE], Phys. Lett. B **815**, 136146 (2021) doi:10.1016/j.physletb.2021.136146 [arXiv:2005.11128 [nucl-ex]].

73. S. Acharya,...,S. Sharma,...*et al.* [ALICE], JHEP **09**, 162 (2020) doi:10.1007/JHEP09(2020)162 [arXiv:2004.12673 [nucl-ex]].

74. S. Acharya,...,S. Sharma,...*et al.* [ALICE], Phys. Lett. B **811**, 135849 (2020) doi:10.1016/j.physletb.2020.135849 [arXiv:2004.08018 [nucl-ex]].

75. S. Acharya,...,S. Sharma,...*et al.* [ALICE], Eur. Phys. J. C **80**, no.8, 693 (2020) doi:10.1140/epjc/s10052-020-8125-1 [arXiv:2003.02394 [nucl-ex]].

76. S. Acharya,...,S. Sharma,...*et al.* [ALICE], JHEP **06**, 035 (2020) doi:10.1007/JHEP06(2020)035 [arXiv:2002.10897 [nucl-ex]].

Data taking shifts for ALICE

I visited CERN in 2022 to take part in the data taking shifts for ALICE. Below are the details:

- **Visit Duration**: 13 March 2022 to 9 May 2022.
- **Purpose**: Participated in data-taking shifts for ALICE.
  - **Training Shifts**: 29−31 March 2022.
  - **Actual Shifts**:
    * 12−17 April 2022
    * 2−7 May 2022

I have also participated in online shifts for ALICE commissioning in 2021. Below are the details:

- Training shifts: 14−16 September 2021
- Actual Shifts: 23−25 September 2021

Service work

The ALICE service work system is a program within the ALICE experiment at CERN, where collaborators contribute to important tasks and services that ensure the smooth operation and maintenance of the experiment's detectors, data acquisition systems, and overall infrastructure. I have been involved in:

1. Quality Control (QC) for the Transition Radiation Detector (TRD)
   - Period: 01-01-2022 to 31-12-2023.
2. Operating the Hyperloop system.
   - Period: 01-01-2024 to 31-12-2024.

Intermittency Analysis of Toy Monte Carlo Events

Sheetal Sharma and Ramni Gupta*

Department of Physics, University of Jammu, India

* Ramni.Gupta@cern.ch

50th International Symposium on Multiparticle Dynamics (ISMD2021)
12-16 July 2021
doi:10.21468/SciPostPhysProc.10

Abstract

Event-by-event intermittency analysis of Toy Monte Carlo events is performed in the scenario of high multiplicity events as is the case at recent colliders RHIC and LHC for AA collisions. A power law behaviour of Normalized Factorial Moments (NFM), F_q as function of number of bins (M) known as intermittency, is a signature of self-similar fluctuations. Dependence of NFM on the detector efficiencies and on the presence of fluctuations have been studied. Results presented here provide a baseline to the experimental results and clarity on the application of efficiency corrections to the experimental data.

Received 25-10-2021
Accepted 14-03-2022
Published 11-08-2022
doi:10.21468/SciPostPhysProc.10.024

1 Introduction

Localized fluctuations in the charged particle production at LHC are proposed to be studied to characterize the multiparticle production and the quark-hadron phase transition [1]. QCD predicts large dynamical fluctuations of various measureables as one of the signatures of critical point, quark-hadron and hadron-quark phase transition. A study of spatial patterns of the charged particles in the phase space using normalized factorial moments (NFM) is one of the techniques to characterize phase transition and the multiparticle production mechanism [2–4]. Normalized factorial moments (F_q) of bin multiplicities as function of varying bin size resolution are proposed to be studied for q $\geq$ 2 [1]. For dynamical fluctuations $F_q > 1$ and is observed to show power-law behaviour with increasing M for self similar fluctuations and this phenomenon is known as intermittency. Here intermittency analysis is performed for the Toy Monte Carlo (ToyModel) events as baseline study.

2 Method of Analysis

A sample of 250K high multiplicity Toy Monte Carlo events are generated with two parameters for the tracks corresponding to pseudorapidity (η) and azimuthal angle (ϕ) such that $|\eta| \leq 0.8$

and $0 \leq \phi \leq 6.28$. Intermittency analysis (as in [5]) is performed in two dimensional (η, ϕ) phase space partitioned in $M \times M$ bins, with M = 4 to 82. The q^{th} order normalized factorial moment (F_q) is defined as

$$F_q(M) = \frac{\frac{1}{N}\sum_{e=1}^{N}\frac{1}{M}\sum_{i=1}^{M} f_q(n_{ie})}{\left(\frac{1}{N}\sum_{e=1}^{N}\frac{1}{M}\sum_{i=1}^{M} f_1(n_{ie})\right)^q}, \tag{1}$$

where $f_q(n_{ie}) = \Pi_{j=0}^{q-1}(n_{ie} - j)$, n_{ie} is the bin multiplicity in the i^{th} bin of e^{th} event. $q \geq 2$ is order of the moment and takes positive integer values. $F_q(M)$ shows power law dependence on M as $F_q(M) \propto M^{\phi_q}$ with $\phi_q > 0$ in case there are fluctuations in the bin multiplicities [5]. This scaling behaviour is referred to as *intermittency* and ϕ_q as intermittency index. With second order NFM (q = 2), the sensitivity of this analysis methodology to gauge bin-to-bin fluctuations and the resilience to detector inefficiencies has been studied in the present work.

3 Observations

Normalized factorial moments for q = 2 are determined for Toy Monte Carlo events (ToyModel) using Eq.1. It is observed that for all M, $F_2(M) > 1$ (Fig.1, black filled circles). Also F_2 values are independent of number of bins (M). Toy Monte Carlo events do not show any scaling behaviour and hence no intermittency.

For sensitivity check of the analysis methodology a modified sample of events is created from the ToyModel events, using two different approaches. In the first method five percent tracks are added randomly in some phase space bins and an equal number of tracks are removed from rest of the region. In the second method, in a similar fashion five percent tracks are added in some phase space bins but no tracks are removed. For both samples so obtained, intermittency analysis is performed and it is observed that $F_2 > 1$. However F_2 is observed to depend on M (Fig.1). At higher M region F_2 shows has linear growth with M. This establishes that intermittency analysis methodology is sensitive to the particle density fluctuations.

Calculations for the observables are affected by the detector effects and hence do not give true value. If ϵ_i defines the detector efficiency in the i^{th} bin then corrected NFM is taken as

$$F_q(M) = \frac{\frac{1}{N}\sum_{e=1}^{N}\frac{1}{M}\sum_{i=1}^{M}\frac{f_q(n_{ie})}{\epsilon_i^q}}{\left(\frac{1}{N}\sum_{e=1}^{N}\frac{1}{M}\sum_{i=1}^{M}\frac{f_1(n_{ie})}{\epsilon_i}\right)^q}. \tag{2}$$

From the ToyModel events, which may be called ToyModel(true), two samples of events equivalent to what is measured by the detectors after applying reconstruction routine are obtained. First sample is created by randomly removing 20% of tracks from the acceptance region of each event. The sample so obtained, say ToyModel(U), is 80% of the ToyModel(true) and has uniform efficiency across the acceptance region. For events with non-binomial type efficiencies, 20% particles are removed from some specific phase space regions of each event. This sample of events, say ToyModel(NU), is also 80% of the original events but with different efficiencies across the acceptance region.

Normalized factorial moments are determined for the three samples of events using Eq.1 and corrected NFM are determined for ToyModel(U) and ToyModel(NU) using Eq.2. It is

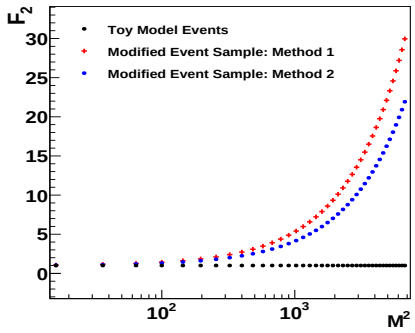

Figure 1: F_2 vs M^2, depicting sensitivity of analysis technique to gauge bin-to-bin fluctuations in the ToyModel events.

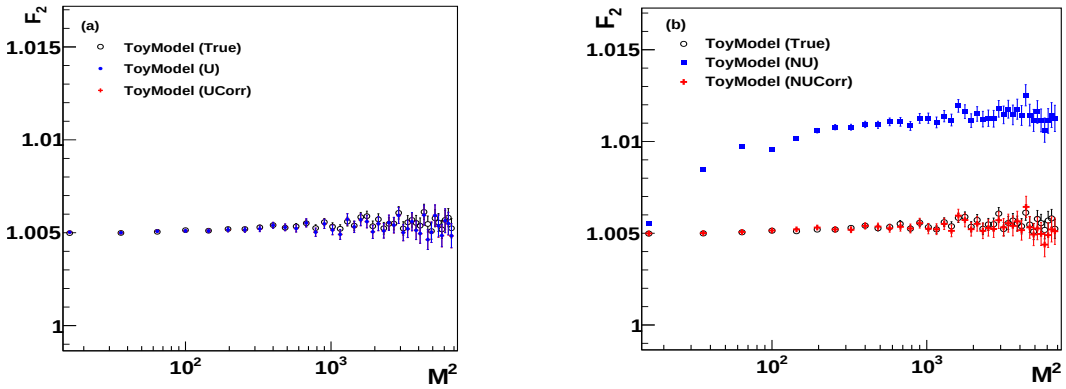

Figure 2: F_2 vs M^2 plot in case of (a)binomial type efficiencies and (b)non-binomial type efficiencies.

observed that $F_2^{(true)}(M) \approx F_2^{(U)}(M) \approx F_2^{(Ucorr)}(M)$ as is shown in Fig.2(a). However as in Fig.2(b) $F_2^{(true)}(M) \neq F_2^{(NU)}(M)$ (black open circle and blue solid square markers), that is any change in the true track values, introduced differently in different phase space regions, the NFM (Eq.1) do not give true value. Whereas $F_2^{(true)}(M) \approx F_2^{(NUcorr)}(M)$ (Fig.2(b)) implying that with corrected NFM calculated using Eq.2 the true NFM are reproduced. Thus the NFM are robust against binomial detector efficiencies but for non-binomial detector efficiencies, to obtain true NFM, formula (Eq.2) with bin efficiency correction values must be used.

4 Conclusions

Intermittency analysis is performed for high multiplicity Toy Monte Carlo events. Analysis technique is observed to be suitable to look for dynamical fluctuations in the multiplicity distributions. NFM as defined in Eq.1 are observed to be robust against the binomial detector efficiencies. However NFM should be corrected for detector effects if efficiencies are non-binomial/non-Gaussian in the acceptance region before any conclusions be drawn.

Acknowledgements

Author(s) are thankful to Igor Altsybeev, Mesut Arslandok and Tapan Nayak for the discussions and suggesstions that helped in the completion of this study.

Author contributions R.G. designed the model and the computational framework. Both R.G. and S.S. performed the analysis and worked to bring out this manuscript.

Funding information The author(s) received no financial support for the research, authorship and/or publication of this work.

References

[1] R. C. Hwa and C. B. Yang, *Local Multiplicity Fluctuations as a Signature of Critical Hadronization at LHC*, Phys. Rev. C **85**, 044914 (2012), doi:10.1103/PhysRevC.85.044914.

[2] A. Bialas and R. Peschanski, *Moments of rapidity distributions as a measure of short-range fluctuations in high-energy collisions*, Nucl. Phys. B **273**, 703 (1986), doi:10.1016/0550-3213(86)90386-X.

[3] R. C. Hwa and C. B. Yang, *Observable Properties of Quark-Hadron Phase Transition at the Large Hadron Collider*, Acta Phys. Polon. B **48**, 23 (2017), doi:10.5506/APhysPolB.48.23.

[4] W. Kittel and E. A. De Wolf, *Soft Multihadron Dynamics*, World Scientific, Singapore (2005).

[5] R. Sharma and R. Gupta, *Scaling Properties of Multiplicity Fluctuations in the AMPT Model*, Adv. High Energy Phys. 6283801 (2018), doi:10.1155/2018/6283801.

INDIAN INSTITUTE OF SCIENCE EDUCATION AND RESEARCH MOHALI
(Established by the Ministry of Education, Govt. of India)
Knowledge City, Sector 81, S. A. S. Nagar, Manauli PO 140306, Punjab, India

Certificate

On behalf of the local organizing committee, this is to certify that

Sheetal Sharma (University of Jammu)

presented a poster titled

Local multiplicity fluctuations in Pb−Pb collisions at $\sqrt{s_{\rm NN}}$ *= 2.76 TeV with ALICE at the LHC* [Abstract ID 258]

at the **XXV DAE-BRNS High Energy Physics Symposium 2022**.

The XXV DAE-BRNS high energy physics symposium (*silver jubilee edition*) was held from 12-16 December 2022 at Indian Institute of Science Education and Research Mohali, Punjab, India. The symposium is a premier event held every two years, supported by the Board of Research in Nuclear Sciences (BRNS), Department of Atomic Energy (DAE), India. The deliberations, from both experimental and theoretical perspectives, covered a variety of topics in Astroparticle Physics, Cosmology, Dark matter, Flavor physics, Higgs, Heavy-ion, LHC physics, Neutrino, Societal applications and related areas.

Ambresh.

Dr. Ambresh Shivaji, Convener,
XXV DAE-BRNS HEP Symposium,
Indian Institute of Science Education and Research Mohali,
Sector 81, Knowledge City, SAS Nagar,
Punjab-140306, India

September 2, 2021

ISMD 2021 certificate of attendance and presentation

We certify that Sheetal Sharma is principal author of the poster "Intermittency Analysis of Toy Monte Carlo events" (https://indico.cern.ch/event/848680/contributions/4434194/), presented online at ISMD 2021 from 12–16 July 2021.

Regards,

Dr Andy Buckley

Chair, ISMD 2021 Local Organising Committee,
andy.buckley@cern.ch